TECHNISCHE UNIVERSITÄT MÜNCHEN

TUM School of Natural Sciences

PEROVSKITE AND ORGANIC SOLAR CELLS STUDIED IN SPACE

Lennart Klaus Reb

Vollständiger Abdruck der von der TUM School of Natural Sciences der Technischen Universität München zur Erlangung des akademischen Grades eines

Doktors der Naturwissenschaften (Dr. rer. nat.)

genehmigten Dissertation.

Vorsitz:	Prof. Dr. Andreas Weiler
Prüfer*innen der Dissertation:	1. Prof. Dr. Peter Müller-Buschbaum
	2. Prof. Dr. Aliaksandr S. Bandarenka

Die Dissertation wurde am 30.10.2023 bei der Technischen Universität München eingereicht und durch die TUM School of Natural Sciences am 08.12.2023 angenommen.

One Ring to carry them all.
One Ring to launch them.
One Ring to measure them all,
and to the bright space Sun expose them.
In the Field of Rocket Science,
where Photovoltaics are rising.

Dedicated to my Grandfather Eugen

Abstract

Perovskite solar cells have faced unprecedented developments in the last decade. They are efficient, scalable, lightweight, and flexible. Here, a solar cell space experiment for a suborbital rocket is developed and flown. Electrical characterization of perovskite and organic solar cells is successfully performed during a spaceflight. Solar cell performance parameters are derived and correlated with solar irradiance. Postflight X-ray scattering measurements reveal stable structures.

Zusammenfassung

Perowskit-Solarzellen haben in der letzten Dekade eine beispiellose Entwicklung erlebt. Sie sind effizient, skalierbar, leicht und flexibel. Hier wird ein Solarzellen-Weltraumexperiment für eine suborbitale Rakete entwickelt und geflogen. Die elektrische Charakterisierung von Perowskit und organischen Solarzellen wird erfolgreich im Weltall durchgeführt. Die Leistungsparameter werden mit der Sonneneinstrahlung korreliert. Röntgenstreuungsmessung nach dem Flug zeigt stabile Strukturen.

Contents

List of abbreviations

2-ME	2-methoxyethanol, $C_3H_8O_2$
ADC	analog-digital converter
AFM	atomic force microscopy
AM	air mass
ASTM	American Society for Testing and Materials
CAD	computer-assisted drawing
CB	chlorobenzene, C_6H_5Cl
DAC	digital-analog converter
DAQ	data acquisition system
DI water	deionized water
DLR	Deutsches Zentrum für Luft- und Raumfahrt (German aerospace center)
DLR-MP	DLR institute for material physics
DMF	N,N-dimethylformamide, C_3H_7NO
DMSO	dimethyl sulfoxide, $(C_2H_3)_2SO$
DWBA	distorted wave Born approximation
EQE	external quantum efficiency
FF	fill factor
FTO	fluorine doped tin oxide
FWHM	full width at half maximum
GISAXS	grazing-incidence small-angle X-ray scattering
GIWAXS	grazing-incidence wide-angle X-ray scattering
GPS	global positioning system
HCl	hydrochloric acid
HOMO	highest occupied molecular orbital
HOPV	hybrid and organic photovoltaic
I-V	current-voltage (characteristics)
IMU	inertial measurement unit
INSIGHT	in-situ grazing incidence X-ray scattering heuristic tool
IPA	isopropyl alcohol, C_3H_8O
ITO	indium doped tin oxide
LED	light emitting diode
Li-TFSI	lithium bis(trifluoromethane)-sulfonimide

LL	log-likelihood
LMA	local monodisperse approximation
LO	lift-off
LUMO	lowest unoccupied molecular orbital
MAPHEUS	Materialphysikalische Experimente unter Schwerelosigkeit (material physics experiments at zero gravity)
MC	Monte Carlo
MCMC	Monte-Carlo Markow chain
MLE	maximum likelihood estimate
MPP	maximum power point
NVC	non-volatile coordinating solvent
NVS	non-volatile solvent
OHSCIS	organic and hybrid solar cells in space
P3HT	poly(3-hexyl-thiophene), $(C_{10}H_{14}S)_n$
PCBM	[6,6]-phenyl-C_{61}-butyric acid methyl ester
PCE	power conversion efficiency
PEEK	polyether ether ketone
PL	photoluminescence
PTFE	polytetrafluoroethylene
RT	room temperature
SDD	sample-detector distance
SEM	scanning electron microscopy
SLD	scattering length density
SODS	start of data acquisition
SOE	start of experiment
spiro-OMeTAD	2,2',7,7'-tetrakis(N,N di-*p*-methoxyphenyl-amine)9,9'-spiro-bi-fluorene
tBP	4-tert-butyl-pyridine, $C_9H_{13}N$
TTIP	titanium tetra isopropoxide, $TI\{C_{12}H_{28}O\}_4$
UV	ultra violet
VNS	volatile non-coordinating solvent
VS	volatile solvent
XRD	X-ray diffraction
XRR	X-ray reflectivity
µg	microgravity

1 Introduction

Perovskite and organic thin-film solar cells are candidates to become the next generation of solar cells. Their young technologies benefit from advances in the physical and chemical understanding of kinetic processes during nano self-assembling. This led to new materials and thin-film processing strategies for tuning nanostructure and morphology. In turn, this impacts charge transport and surface defect passivation and improves the quality of the final thin-film solar cell devices threefold – performance, reproducibility, and stability.

With a focus on performance, organic photovoltaics' certified power-conversion efficiency (PCE) has already surpassed 18 %, and recently, even 19.3 % have been reached [1, 2]. Such notable progress within the last years became possible due to the synthesis of new polymers and small molecules, new techniques of layer treatments, and changes in device architecture, such as ternary all-polymer solar cells [3, 4, 5]. In the field of perovskite photovoltaics, the first publication of solar cells using perovskite as the light-absorbing material dates back to 2009 [6]. Architecture, processing, and chemical improvements empowered the young perovskite technology to break through 20 % solar-cell efficiency within a few years [7]. Currently, the record perovskite solar cell is reported with a certified PCE of 25.7 % – a to silicon-based photovoltaics comparable value – using elaborated strategies of interface passivation [1, 8, 9, 10, 11]. Less than 15 years ago, perovskite solar cells emerged – now they reach efficiencies similar to silicon-based photovoltaics, a matured technology with a head start of more than 60 years. In Fig. 1.1a, a perovskite stand-alone farm with a size of more than 4 m^2 is shown. IT retained about 80 % of the peak power of above 250 W after more than eight months of operation in a field test, showing that relatively large-scale panels (single panel 11x11 cm^2) can already achieve notable long-term stability [12]. In organic solar cells, simple solution-processed UV filters and protective buffer layers promoted projected lifetimes of decades in organic non-fullerene acceptor solar cells [13].

Organic and perovskite semiconductor technologies are solution-processable. On the one hand, this asset creates challenges due to the specific demands of controlling crystallization and assembly that require rigorous optimization for achieving high device reproducibility with the desired morphology. On the other hand, wet-chemical processing enables scalable manufacturing techniques such as blade coating and slot-die printing in ambient conditions [13, 14, 15, 16, 17, 18]. Also, the wet-chemical low-temperature device fabrication processes allow the use of ultra-thin polymer substrates, creating plastic-foil-based solar panels with high flexibility (bending radii of 1 mm or below) [19, 20]. Using flexible substrates is challenging for other solar cell technologies due to high temperatures during manufacturing or additional expensive production steps. Solar

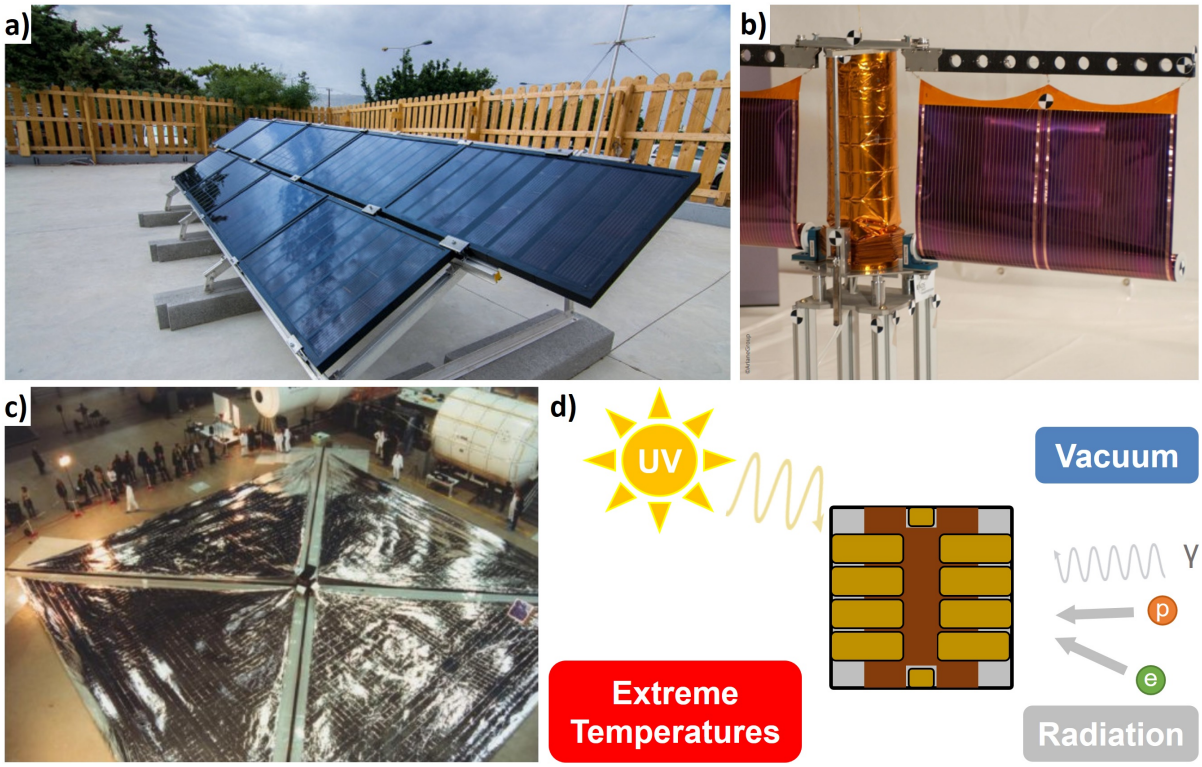

Figure 1.1: a) A rooftop perovskite solar farm [12]. Photograph from Graphene-perovskite solar farm trial up and running in Greece (perovskite-info.com). Accessed 12.07.2023. b) Deployment mechanism for a flexible thin-film solar panel by the Arianegroup. Accessed 12.07.2023. c) A large solar sail by the German Aerospace Center. Accessed 12.07.2023. d) Main environmental influences on a solar cell in space.

energy harvesting, in combination with colorful plastic foils, opens up applications for novel device integrations [21].

The features mentioned above make perovskite and organic solar cells an exciting technology for space applications primarily due to their lightweight and flexibility when processed on ultra-thin plastic foils [22]. While the PCE is an essential number for terrestrial solar cells, it is more appropriate to consider the power-per-weight on the solar panel system level due to the rocket launch, where all is about saving weight. The power-per-weight is defined as the electric power output per weight at standard test conditions and measured in power per gram, [$\mathrm{W\,g^{-1}}$]. Thus, the thinner the entire solar cell module can be manufactured, the more power-per-weight will be achieved. Therefore, fabrication methods and material systems that allow a decrease in the overall mass of the final solar panels have high potential. As an example, current state-of-the-art silicon/germanium-based solar cells or III-V triple-junction GaInP/GaAs/GaInAs modules reach maximum power-per-weight values of 1-3 $\mathrm{W\,g^{-1}}$ on the solar cell level [23, 24, 25]. There have been several studies investigating novel material thin-film solar cells on ultra-thin substrates, with highest power-per-weight values reported about a magnitude higher, reaching up to 30 $\mathrm{W\,g^{-1}}$ for a perovskite solar cell on μm-thin plastic foils [19, 20, 21, 26, 27, 28, 29, 30].

Also, flexible tandem solar cells experienced promising development and have an even higher power-per-weight potential due to higher theoretical efficiencies [30, 31]. A double-junction all-perovskite tandem solar cell module recently surpassed 26 % PCE, while upscaling of this technology is simultaneously investigated [32, 33, 34].

Here, it is essential to emphasize that the weight of the mounting framework drives the total module weight of conventional solar modules. This includes interconnects and packaging, attenuators, small motors, and unfolding mechanisms. Also, structural stabilizations increase the weight for twofold reasons: to withstand the vibrations and accelerations during launch and to provide stiffness for the unfolded panels to reduce resonances. In the numerical comparisons above, all these factors are not considered. Simply changing the solar cell from comparably thick and heavy silicon to thin and light perovskite or organic materials, not much weight can be saved on the module level, and currently, it does not outweigh the risk of potential losses due to limited lifetimes. Perovskite and organic solar cells might play off their advantages only in combination with novel principles and systems for deployment. Plastic-foil-based solar panels might be transported as a roll that is unfolded and stabilized by inflation without the need for additional framework or attenuators (cf. Fig. 1.1b), or they are packed and unfolded similarly to solar sails with a minimum of supporting structure (cf. Fig. 1.1c). Using semitransparency or customized, e.g., fan-like shapes, thermal management under intense solar power could be achieved automatically [35]. Genuinely flexible thin-film solar cells must challenge space solar panels' methodology and fundamental conception of being stiff, rigid, and heavy.

Another aspect of the novel material solar cells is the direct manufacturing of these solar cells in space at their desired place of application. For example, during the NASA Artemis program, the possibility of perovskite solar cell manufacturing on the moon is considered [36]. The very low material requirement necessary, e.g., for evaporation-based solar cells, could be much lower compared to the terrestrial processing with extra mass requirements for carrying these solar panels; in other words, this could be a way of ultra-dense packing for minimized transport weight of these solar cells.

The novel material solar cells must be better qualified for space use before the abovementioned developments in the engineering of deployment systems become relevant. In space, solar cells face harsh environment conditions (see Fig. 1.1d) with extreme temperature cycles, hard UV irradiation from the extraterrestrial AM0 solar spectrum (136.6 mW cm^{-2}), cosmic particle irradiation, ultra-high vacuum, and a lack of gravity [37, 38, 39]. All these conditions deviate significantly from the terrestrial conditions commonly used in perovskite and organic solar cell testing protocols.

Consequently, the first step towards space is mimicking specific space conditions selectively and characterizing the solar cell's behavior exposed to this simulated environment in terrestrial tests. Our group was one of the first to perform such testing of organic solar cells in a simulated space environment in 2014. In detail, the organic solar cells were exposed to AM0 irradiation in vacuum with surprising results regarding the solar cell stability. Their stability was better

than expected, possibly due to the absence of air and hence oxygen radicals [40]. Another group successfully stabilized perovskite solar cells against UV irradiation using a layer to redshift the photons (reduce their ionizing power) [41]. It is well known that perovskite solar cells undergo moisture-induced degradation, a major stability issue evaded in space [42]. While the absence of air can prevent degradation pathways in perovskite and organic solar cells, vacuum conditions could induce the outgassing of volatile species. We observed that mixed halide mixed cation perovskite solar cells show material instability in vacuum under illumination, causing phase segregation of the perovskite [43]. Including an additive during processing, this effect can be retarded in standard conditions, but its action in space vacuum is unknown [44]. Vacuum, in combination with illumination, seems to cause outgassing and ion accumulation in perovskite solar cells, and another route to prevent this is to optimize the solar cell architecture [45].

Appropriate encapsulation will be essential to achieve long-term stable devices [46]. A recent report promises excellent encapsulation, using a μm-thick SiO_2 barrier. The amorphous glass was thermally evaporated atop the solar cell and acted as a diffusion barrier [47]. In contrast to conventional resin-based encapsulation, this approach does not multiply the solar cell thickness and thus preserves flexibility, promising high adaptability for various application schemes [47, 48]. Stress testing of devices with this barrier layer by exposing them to heat ($\approx 75\,^{\circ}\mathrm{C}$) and vacuum for several months showed retainment of more than 90 % of their initial efficiency [49]. Arguably, the temperature differences in Earth's orbits and repetitive cycling put high thermal stress on the solar cell materials [50]. In early work, thermal cycling ($\pm 80\,^{\circ}\mathrm{C}$) of perovskite solar cells showed reduced efficiency at low temperatures during cycling, but after the experiment, the PCE recovered [51]. Temperature cycling puts the perovskite layer under stress because of a large mismatch of the thermal expansion coefficient of perovskite and glass [52, 53]. After repeating temperature cycling 200 times, perovskite solar cells maintained over 90% of their initial PCE [54].

Due to cosmic particle irradiation and high-energy photon irradiation, terrestrial stability tests of novel material solar cells under artificial irradiation have been performed. Here, perovskite solar cells demonstrated stability against high-energy proton irradiation and showed self-healing, an interesting feature, especially for strong-radiation exposure missions or orbits [55, 56, 57, 58]. In these terrestrial tests, they exceeded the stability threshold of crystalline silicon or triple-junction solar cells; however, actual space conditions are different, and the transferability of the results might be limited [56, 57, 58, 59]. For this reason, testing protocols developed for conventional solar cells need to be adapted for novel thin-film solar cells. Using lower energy protons for the soft and thin materials is recommended to avoid these self-healing effects [60].

Due to various cross effects as described above, results achieved via terrestrial testing need to be interpreted carefully, since there could be a complex interplay between different environmental conditions during space exposure. This makes simulating the solar cell behavior in actual space conditions on Earth very challenging, apart from being hard to mimic all environmental conditions simultaneously.

A very attractive and complementary approach to specialized terrestrial tests is near-space experiments [61]. In this second step to space, stratospheric balloons carry the solar cells and expose them to near-space conditions at altitudes of about 30 km for several hours; usually, the solar cells can be retrieved for post-flight analyses. During the experiment, the solar cells are exposed to the solar spectrum close to the AM0 spectrum far up in the atmosphere. In combination with the low air pressure and reduced thermal exchange with the surroundings, important environmental parameters come arguably close to real space conditions. Our group performed a stratospheric balloon flight with organic solar cells (P3HT:PCBM bulk-heterojunction) in the course of the Move-on Mission 2017. Data acquisition was successful, and the solar cells functioned during the mission. Cardinaletti et al. could show the functionality and energy harvesting of perovskite and organic solar cells during a balloon flight of several hours [46]. A similar experiment was performed with perovskite solar cells and detailed tracking of the photovoltaic parameters during the flight [62]. In a more recent balloon-based experiment, flexible organic solar cells were tested, reaching a power-per-weight of approximately $3.3\,\mathrm{W\,g^{-1}}$ on $38\,\mu$m-thick PET substrates [63]. These tests prove remarkable effectiveness, particularly for perovskite and organic solar cell applications in near-space environment. Although these near-space tests provide insights into the solar cell behavior in near-space environment, they are not sufficient in demonstrating the actual performance of the technologies in space. Therefore, additional steps must be taken to transport and evaluate the solar cells in space.

In this regard, a recent publication investigated the influence of 10-month space exposure on perovskite thin films on the International Space Station. The encouraging results show that the perovskite layers did not significantly degrade (i.e., maintained their initial black color), and the quantitative optoelectronic characterization affirmed the theoretical expectations that space stressors are manageable [64]. However, the perovskite films have not undergone characterization during the experiment. Unfortunately, no information is available concerning solar cell performance during space exposure. In particular, the solar-cell characterization in space is required, after experiencing the entire circumstances of transport, rocket launch, while exposed to space conditions. Currently, there is no information regarding the behavior of perovskite and organic thin-film solar cells in space. Hence, it is imperative to conduct tests in space, even for a short duration, to showcase the feasibility of employing new technologies in space and confirm their readiness – are they candidates for becoming future space solar panels? Such experiments can be a stepping stone for future orbital missions to assess their long-term stability in operational conditions.

Sounding rockets are the perfect choice for this third step because they reach orbital altitudes of over 200 km, leaving Earth's atmosphere and exposing the payload to space conditions. These rockets have rate control systems that ensure stable payload orientation and determinable irradiation conditions for the solar cells. The micro-gravity time of several minutes allows for several subsequent measurement cycles of a single solar cell under various illumination and temperature conditions. Although the time spent in space is relatively short, one strength of such rocket-based experiments lies in the ability to test the harsh launching conditions and the

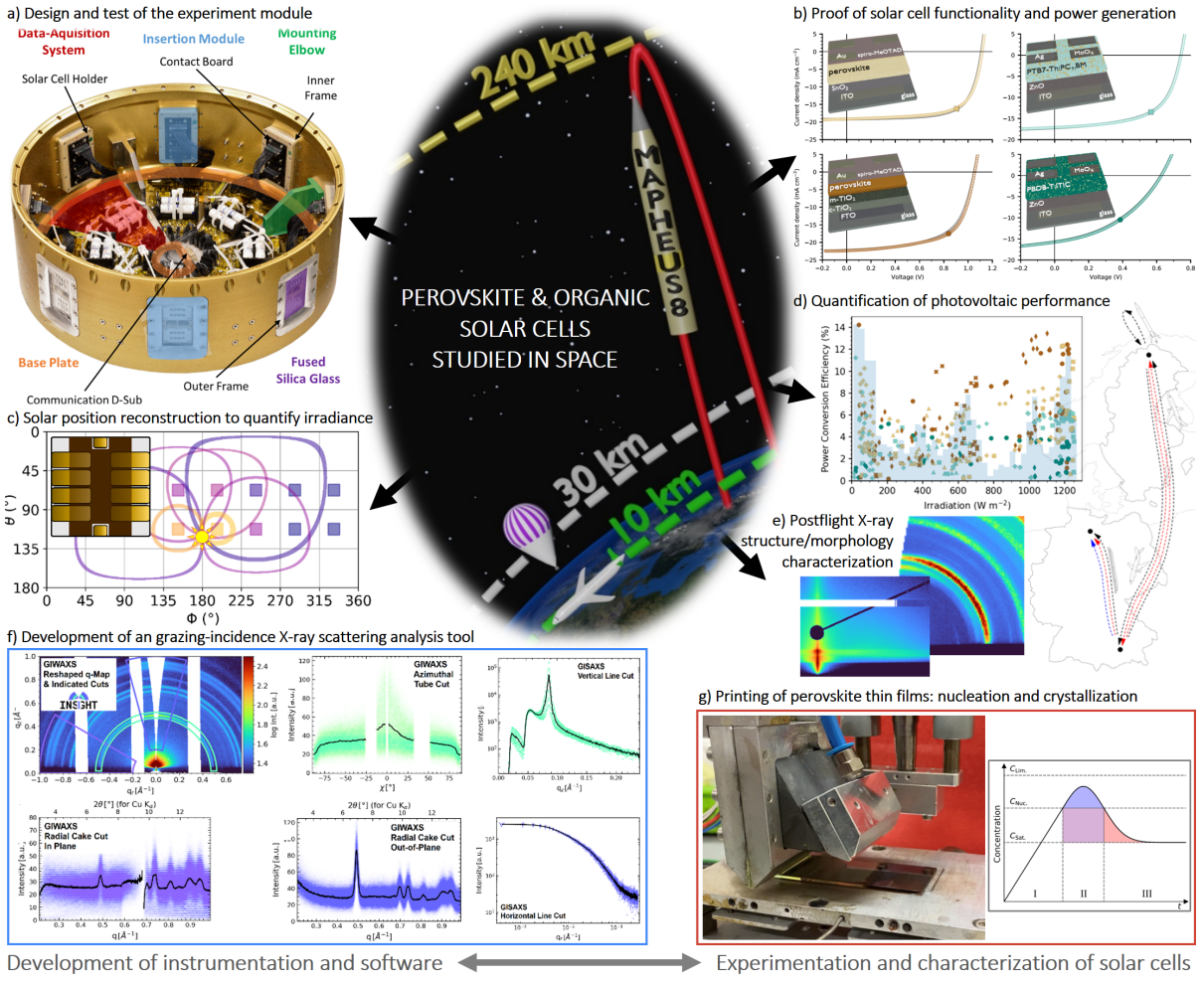

Figure 1.2: Overview of the projects covered in this Ph.D. thesis. For details, see text.

transportation and handling processes on Earth prior to launch. In addition, characterizing them *in situ* delivers valuable information that can guide future experiments. These sounding rocket experiments closely resemble orbital missions and serve as a stepping stone toward a full orbital demonstration. Conventional space experiments do not plan reentry with subsequent recovery, apart from sample return options at the International Space Station that are hardly available [64]. In contrast, these suborbital experiments usually allow for retrieval of the payload, including the solar cells. This advantage over orbital demonstrations allows for studying changes induced by space exposure and transport stresses and comparing the returned solar cells with reference solar cells postflight.

This thesis addresses a range of essential questions regarding the suitability of perovskite and organic solar cells for space applications in the context of a rocket launch. It seeks to determine whether the hardware can withstand the intense conditions of the launch and thereafter function and perform measurements nominally, including data acquisition and storage. Additionally, it aims to assess the resilience of the solar cells during transportation, handling, and the rocket launch itself, particularly concerning the extreme vibrations and accelerations experienced dur-

ing the lift-off of a sub-orbital rocket. The thesis also investigates the mechanical stability of the electrical contact: Can the goal of electrical characterization of perovskite and organic solar cells be achieved in space conditions? If so, this thesis assesses the proof of functionality and power generation of the solar cells beyond an altitude of 100 km. It explores the performance of solar cells under space conditions, particularly by attempting to quantify photovoltaic parameters such as the PCE in space conditions. The thesis also considers how solar cells perform in relation to different solar irradiation and whether they exhibit similar behavior to terrestrial tests, ultimately determining if they meet performance expectations and can reach their potential in space. Lastly, the thesis examines the condition of the solar cells after retrieval, looking for any morphological or structural changes during postflight characterization.

In Fig. 1.2, a graphical overview of the content of this thesis is presented, with the central project being the sounding rocket flight experiment to study perovskite and organic solar cells in space. The thesis is organized as follows: In Chapter 2, the theoretical background of solar cells is presented. The theory of nucleation and crystallization is introduced, including additional information about scalable perovskite manufacturing with the slot-die printing process (Fig. 1.2g). Then, the theory of thin-film characterization with a focus on Grazing-Incidence Small-Angle X-ray Scattering (GISAXS) and Grazing-Incidence Wide-Angle X-ray Scattering (GIWAXS) is given. In Chapter 3, experimental laboratory solar cell manufacturing and characterization methods are described. Herein, the newly developed GISAXS/GIWAXS data processing tool INSIGHT is briefly introduced, including concepts and features for data evaluation (Fig. 1.2f).

The first result Chapter 4 details the development, construction, and testing of the Organic and Hybrid Solar Cells In Space (OHSCIS) measurement setup, designed for the electrical characterization of novel material thin film solar cells and their incorporation in the sounding rocket during the scientific campaign MAPHEUS-8 (Fig. 1.2a). Herein, the first results of the maiden flight focus on the data acquisition technique and the flight conditions. In Chapter 5, the attitude determination during the rocket flight using the ambient light sensors is discussed with the solar irradiance reconstruction on individual solar cells as the main result (Fig. 1.2c). In Chapter 6, a detailed analysis of the performance of the space solar cells is given. The results obtained with a focus on solar cell characterization during the first-ever space-flight of perovskite and organic solar cells prove not only their functionality but also electrical power generation at different irradiation conditions (Fig. 1.2b). Using the results from the previous chapter, solar irradiation parameters are combined with photovoltaic performance to investigate correlations (Fig. 1.2d). In the last result Chapter 7, postflight GISAXS/GIWAXS studies are performed. Potential influences of the space environment on the solar cell nanostructure are revealed and discussed before concluding the thesis in Chapter 8.

2 Theoretical Background

This chapter introduces the theoretical concepts of this thesis. In Section 2.2, aspects of semiconducting hybrid perovskites, their structural and optoelectronic properties, and the principle of perovskite solar cells are described. In Section 2.3, fundamentals of nucleation and crystallization are introduced and applied to the thin-film coating methods of one-step anti-solvent spin coating and the meniscus-guided slot-die coating using air-knife solvent quenching. Section 2.4 gives a detailed introduction to the principles of elastic X-ray scattering on thin films, focusing on Grazing-Incidence scattering geometry.[1]

2.1 Solar Spectrum

Our sun fuses hydrogen to helium in its central region, producing heat radiated away through thermal black body radiation. Planck's law well describes the spectral radiance,

$$B(\lambda) = \frac{2hc^2}{\lambda^5 \left[\exp(\frac{hc}{k_B \lambda T}) - 1\right]}, \tag{2.1}$$

for a black body (emissivity=1) with a surface temperature of around 5780 K. Here, c is the speed of light, h is the Planck constant, and k_B is the Boltzmann constant. In the present case, the spectral radiance $B(\lambda)$ gives the power at a given wavelength per emitting surface area and per solid angle, [W m^{-2} nm^{-1} sr^{-1}], which is a directional quantity. Since thermal radiation is isotropic, the spectral irradiance or flux density crossing the unit area into a hemisphere is $I = \pi B$ with the unit [W m^{-2} nm^{-1}]. On the solar surface, light effectively comes from a hemisphere; in Earth's distance, the sun behaves in good approximation as a point source, and $B(\lambda)$ is the correct description [65].

On the way to the Earth's surface, the sunlight is subjected to spectral losses due to scattering and absorption by the Earth's atmosphere. UV light is primarily absorbed, blue light is scattered by elastic Rayleigh (& Mie) scattering, and towards the infrared, vibrational absorption bands by trace gases and water vapor occur. Thus, not all solar light of the extraterrestrial solar spectrum reaches Earth's surface. The light attenuation depends on the path through the atmosphere and is a function of geodetic latitude. To quantify atmospheric influences, the air-mass factor (AM)

[1] With the aim to create a lively language, derivations frequently use "we" in this chapter. This shall not imply the invention of the presented content.

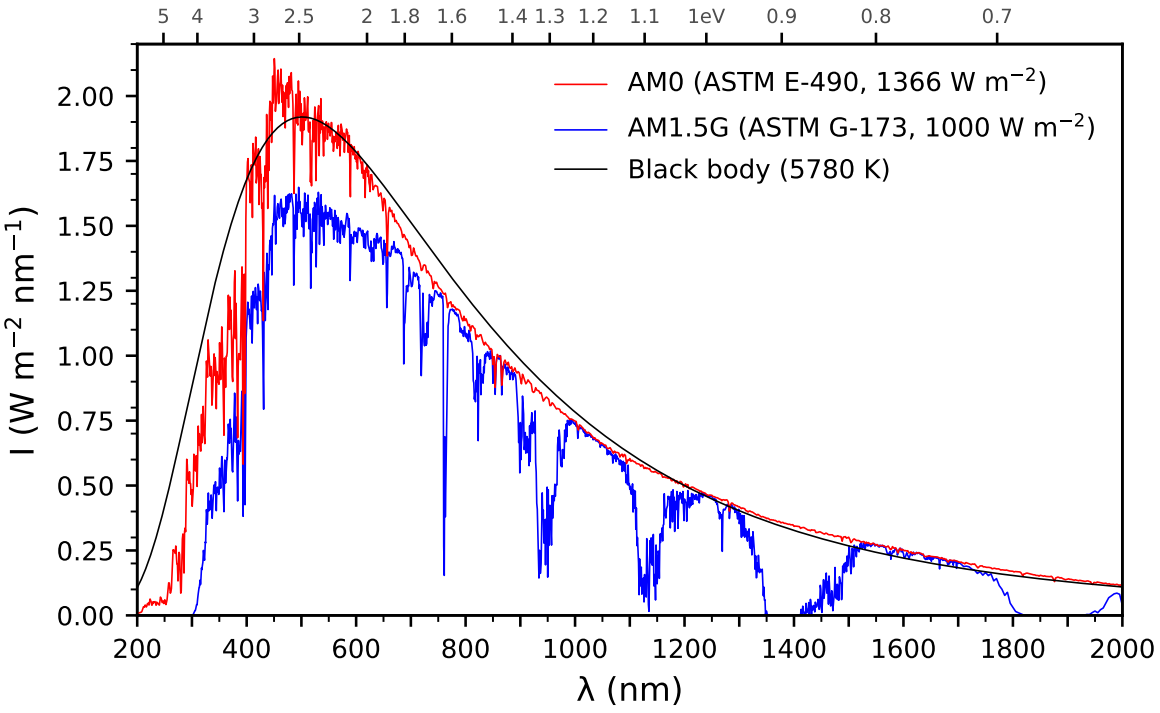

Figure 2.1: Spectral irradiance I (or spectral flux density) of the ASTM E-490 AM0 extraterrestrial spectrum (red) corresponding to the solar constant of 1366 W m^{-2}, and of the ASTM G-173 AM1.5G terrestrial spectrum (blue) corresponding to an irradiance of 1000 W m^{-2}. The black solid line shows the spectral irradiance following Planck's law in eq. 2.1 of an ideal black body of solar size in Earth's distance with a temperature of 5780 K.

is introduced in the naming convention of solar spectra to resemble an effective atmospheric attenuation cross-section for sunlight. It is a function of latitude angle ϕ,

$$\mathrm{AM} = \frac{1}{\cos\phi}. \tag{2.2}$$

Thus, an AM1 corresponds to perpendicular sunshine, whereas an AM1.5 corresponds to a latitude of around 47°. AM0 is used for the extraterrestrial solar spectrum, where no atmospheric attenuation occurs.

The most useful solar spectra are shown in Fig. 2.1. The AM0 extraterrestrial spectrum is shown in red, and the blackbody spectrum (intensity scaled to Earth's distance to the sun) is a black line. Some absorption from the Fraunhofer lines in the blue/UV region can be seen, but the high wavelength tail closely follows the blackbody curve. Spectrally integrating the AM0 spectrum, one yields the total power per square meter received at Earth's distance, the solar constant of approximately 1366 W m^{-2}. Temporal fluctuations due to the solar activity cycle and the ellipticity of Earth's orbit lie within a few percent. This solar spectrum resembles the solar spectrum outside Earth's atmosphere and thus is of relevance for space applications.

The AM1.5G reference spectrum is shown in blue, where a significant reduction of the UV

and visible light is visible. There are regions in the infrared where absorption bands make the atmosphere opaque. The AM1.5G ('G' for global) is a standardized spectrum defined by the American Society for Testing and Materials (ASTM) using specified standard atmospheric conditions at sea level at 47° latitude and a solar light receiving surface to be inclined by 37° to the horizon towards the sun [39]. Integrating the AM1.5G spectrum amounts to 1000 W m^{-2} or 100 mW cm^{-2}. The spectrum is frequently used for (non-concentrator) photovoltaics where the 1000 W m^{-2} is a handy value. Solar simulators attempt to resemble this spectrum closely to enable representative testing of solar devices at standardized conditions.

2.2 Semiconducting Hybrid Perovskite Solar Cells

The perovskite success story is based on the intriguing properties of this new photovoltaic material that are touched on below (for an extensive review, see e.g. Jena et al. (2019) [66]).

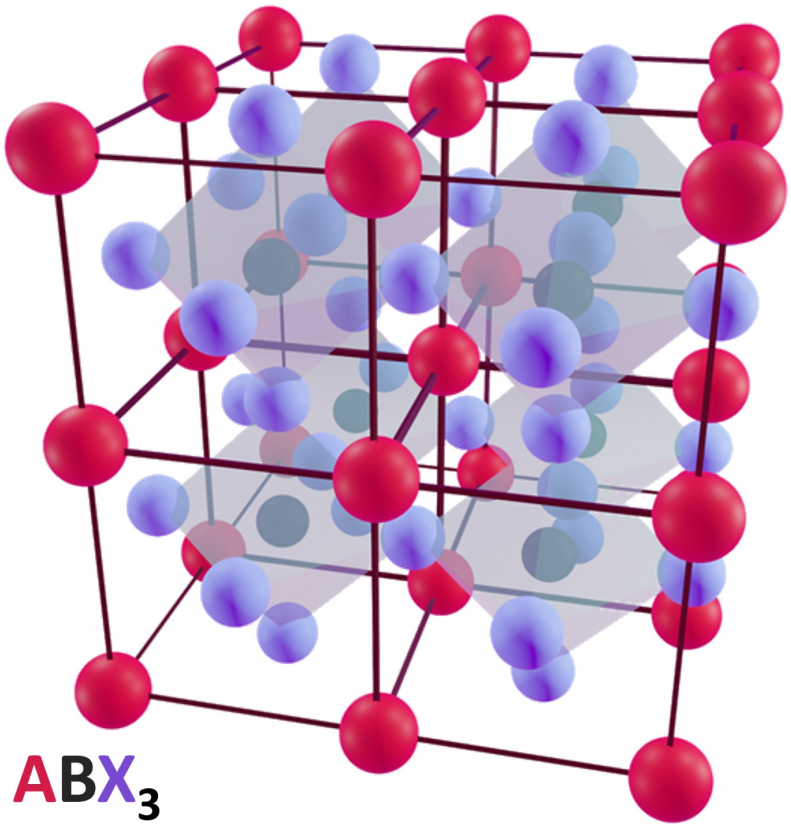

Figure 2.2: Cubic perovskite crystal structure ABX_3 where the A-site cation (red) resides in the cuboctahedral voids of a corner-sharing 3D network of $[BX_6]^{4-}$ octahedra (blue octahedra with blue X-site anions at the corners and the black double-charged B-site cation in the center). Figure adapted from Lukas Bauer's Bachelor thesis [67].

2.2.1 Perovskite Structural Properties

Perovskite is a material class with a perovskite crystal structure. The perovskite crystal structure ABX_3 is commonly found in calcium titanate, an abundant mineral with the chemical formula $CaTiO_3$. Many combinations of chemical elements crystallize in the perovskite crystal structure, where the relative ionic radii of the three ions influence the crystal structure as predicted by the Goldschmidt tolerance factor t: [68]

$$t = \frac{r_A + r_X}{\sqrt{2}(r_B + r_X)}, \tag{2.3}$$

where the ideal value of $t = 1$ results in a cubic crystal structure, shown in Fig. 2.2. For $0.8 < t < 0.9$, a distorted perovskite structure with a rhombohedral, tetragonal, or orthorhombic crystal structure is most likely to form; in the range $0.9 < t < 1$, perovskite tends to form cubic structures; for $t > 1$, a hexagonal perovskite phase is formed [69].

For the applications in solar cells, commonly used elements or molecules for the A-site are methylammonium ($[CH_3NH_3]^+$, MA^+), formamidinium ($[NH_2CHNH_2]^+$, FA^+), or cesium (Cs^+). The B-Site is frequently occupied by lead cations (Pb^{2+}) or tin cations (Sn^{2+}). The X-site is established by halide anions such as chlorine (Cl^-), bromine (Br^-), or iodine (I^-) [70]. Interchangeability of the chemical constituents gives rise to various perovskite compositions and structures with different properties, such as tunable bandgap [71].

2.2.2 Developments of Perovskite Solar Cells

Since the very first publication about organometallic methylammoniumtrihalogenoplumbates ($MAPbI_3$ and $MAPbBr_3$) in the cubic perovskite crystal structure, it took more than forty years for the first solar cell that made use of this material as the photoactive light absorber in 2009 [6, 72]. These first solar cells made use of $MAPbI_3$ and $MAPbBr_3$ perovskites as sensitizers, i.e., as light-absorbing material in contact with a mesoporous TiO_2 scaffold, a semiconducting metal oxide that has been commonly used in dye-sensitized solar cells [73]. Since then, multiple structural improvements of the perovskite solar cell absorber layer and architecture have been undertaken as illustrated in Fig. 2.3.

While these first perovskite solar cells showed power-conversion efficiencies (PCE) of only 3.8 %, the introduction of the electron-blocking material Spiro-MeOTAD[2] boosted PCEs to around 10 % [74, 75]. Still, control of the morphology during crystallization has been challenging and limiting the performance of $MAPbI_3$ solar cells until 2013; the sequential deposition further boosted power conversion efficiencies to around 15 % [76]. Using transient absorption and photoluminescence-quenching or impedance spectroscopy measurements to shed light on the general working principle of the solar cells, considerable charge carrier diffusion lengths of 1 μm were found [77, 78]. This is a remarkable value for a polycrystalline material with many defects.

[2] 2,2',7,7'-Tetrakis(N,N-di-p-methoxyphenylamine)-9,9'-spirobifluorene.

Further improvements were based on the introduction of the more stable formamidinium cation (FA^+) that replaces the methylammonium cation (MA^+), but pure ($FAPbI_3$) perovskite turned out to be unstable. In particular, a spontaneous phase transition at room temperature from the desired optically active α perovskite phase to the δ non-perovskite phase [79, 80, 81]. Interestingly, substituting a portion of MA^+ with FA^+ changes the crystal orientation and growth direction of the perovskite polycrystals that, in turn, influence the electronic properties of the layer [82]. A mixed cation mixed halide perovskite was formed where the introduction of around 15 % of $MAPbBr_3$ stabilized $FAPbI_3$ to achieve devices with 18 % PCE [83]. The one-step anti-solvent spin-coating technique was used for these high efficiencies, forcing perovskite nucleation and crystallization to achieve uniform, dense thin films. A simplified planar architecture discarded the mesoscopic TiO_2 scaffold in favor of a compact SnO_2 layer, yielding similar efficiencies [84]. From this on, further fine-tuning of the perovskite composition and selective layer (TiO_2, SnO_2, and Spiro-MeOTAD) optimizations in terms of doping or processing strategies made it possible to reach 20 % PCEs [85]. For example, it turned out that balancing the stoichiometry and aiming for a small PbI_2-excess in the precursor stoichiometry is essential to maximize device efficiency and improve device stability, likely due to a trade-off of defect passivation and ion migration [86]. Changes in stoichiometry influence charge-carrier mobility in the

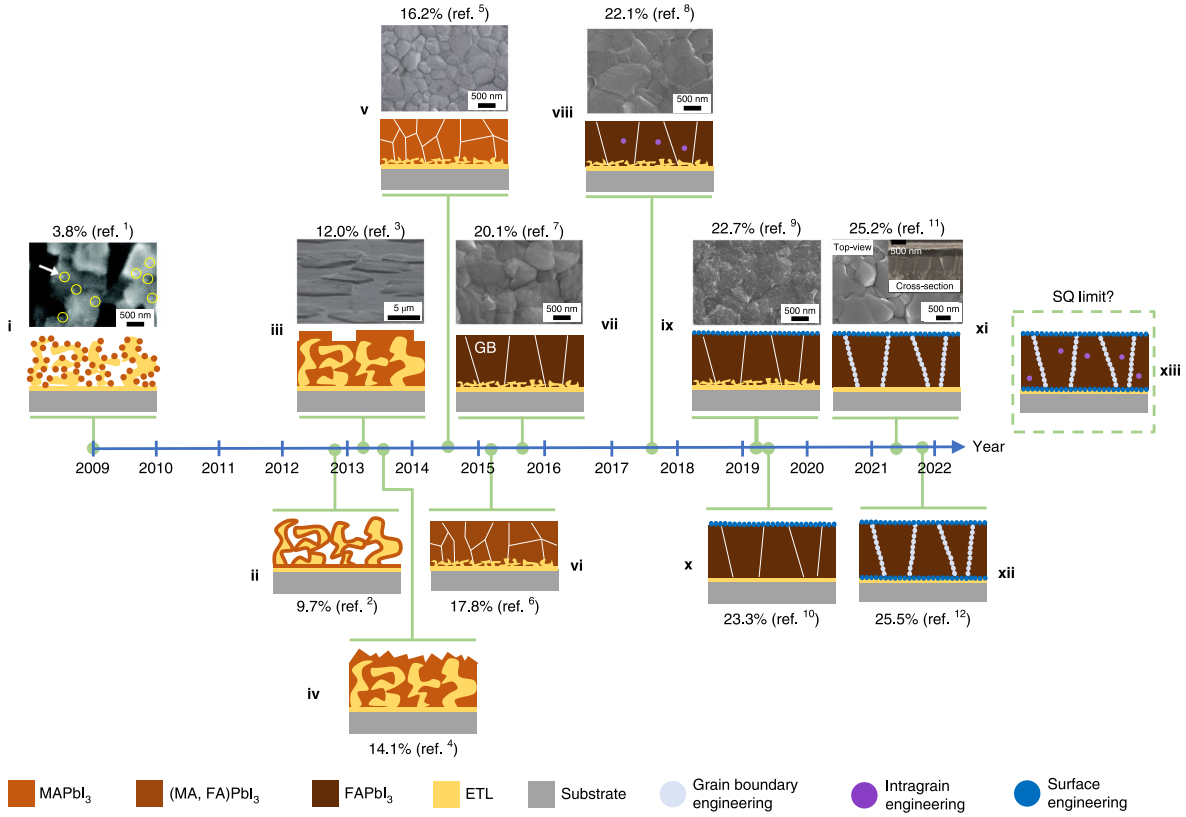

Figure 2.3: Timeline of the key developments of perovskite solar cells from their advent until today. Reproduced from Zhou et al. with permission [7]. Copyright © 2022 Springer Nature.

perovskite layer. Also, grain size, energetic disorder, and self-doping are extrinsic effects that define fundamental limits in mixed perovskites [87]. It is a complex interplay of nonradiative recombination centers (traps) and lattice vibrations (phonons) that determines charge-carrier and ion dynamics [88]. For example, the electron-phonon coupling is essential to understand degradation pathways during charge carrier cooling towards the band edges [89].

However, these mixed-cation mixed-halide perovskites turned out to be intrinsically unstable under illumination. Light-induced demixing of bromine- and iodine-rich phases quickly deteriorated the long-term stability of these devices [90]. Some groups found this problem related to cations, while others claimed defects to assist the process, and others held structural origins accountable for the observed phase segregation [91, 92, 93]. Indeed, there seem to be different effects at the same time. In short circuit conditions under illumination, photogenerated defects seem to assist ion migration and make it the dominant degradation effect. In contrast, in open-circuit conditions, photogenerated radicals create nonradiative recombination centers when charges accumulate [94]. Furthermore, light-induced phase segregation in vacuum is further accelerated, likely to mitigate illumination-induced microstrain in the crystals [43]. Research on the elemental $MAPbI_3$ composition revealed that Frenkel defects seem responsible for the deterioration of device performance [95].

Lately, iterations including band-alignment and interface passivation, phase stabilization of the $FAPbI_3$ perovskite layer, and optimization of light-harvesting lead to certified 25.4 % PCE making use of a conformal SnO_2 layer [96]. Surface defects have early been claimed to be responsible for recombinations. Still, in recent years, the power of interface, grain boundary, and inside-grain passivation was understood for device performance and stability [7, 97]. For example, potassium iodide can passivate grain boundaries by adding it to the precursor [98]. "Washing" the SnO_2 surface with potassium improved the interface between the SnO_2 hole-blocking layer and the perovskite layer [99]. Currently, the record perovskite solar cell with reported certified 25.7 % efficiency made use of volatile alkylammonium chloride additives in the antisolvent as surface passivation and to maximize grain size and crystallinity of the perovskite layer [11].

2.2.3 Perovskite Solar Cell Working Principle

Electron energy levels in materials with long-range order (i.e., periodicity) are described by their band structure (see Fig. 2.4). Semiconductors are materials with a band gap E_g, i.e., an energetically forbidden region between the electronic ground state (valence band) and the excited energy state (conduction band) of energy of a few electron volts (eV).

In the valence band, electrons are locally bound, and electrons in the conduction band are delocalized and can move. Einstein's photo effect, i.e., the excitation of electrons by absorption of photons can excite an electron in a semiconductor if the photon energy exceeds the band gap energy, [100]

$$E_{ph} = \frac{hc}{\lambda} > E_g = E_{VB} - E_{CB}. \tag{2.4}$$

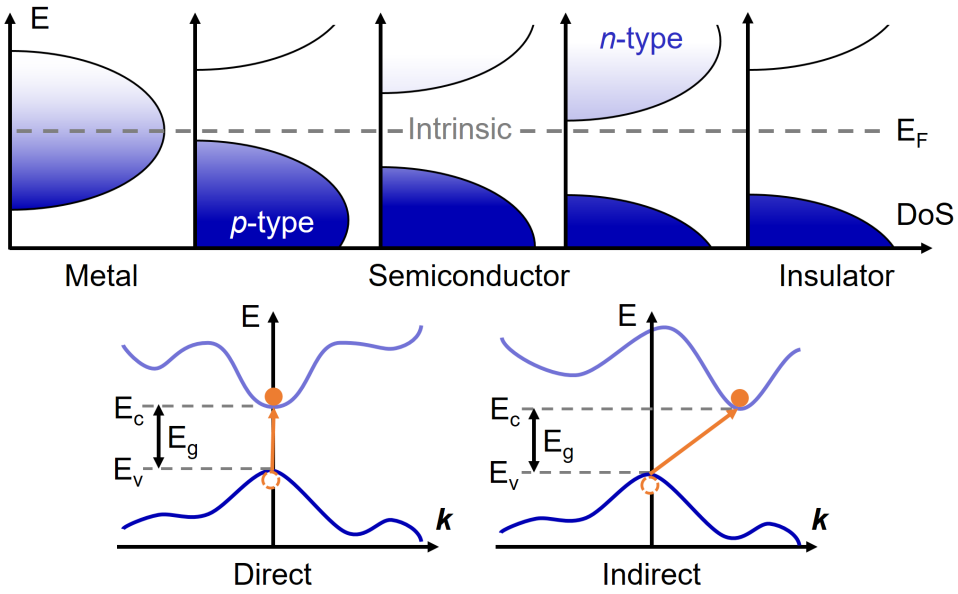

Figure 2.4: Band diagram of semiconductors. Top: The different position of the band edges with respect to the Fermi energy level E_g gives rise to different material properties. Electron population is indicated with blue-shaded regions in the density of states (DoS). For semiconductors, the Fermi energy level E_F is located between two bands (the upper conduction and lower valence band). The energy gap between the bands is called the band gap. Upon increase of Fermi energy levels relative to the band positions, a population of the bands is present at non-zero temperature (indicated by colors). The semiconductor type varies from p-type (charge transport by holes in valence band) to n-type (charge transport by electrons in conduction band) via intrinsic (charge transport in both bands via respective species); the type corresponds to the majority charge carrier polarity. The lower graphs show the band structure in reciprocal space (Brillouin zone) for a direct semiconductor (left) and an indirect semiconductor (right). For the excitation of an electron from the valence to the conduction band in the direct semiconductor, no additional momentum transfer via a phonon is required. In the indirect semiconductor, electron excitation requires momentum exchange with the crystal lattice.

In that case, a temporary, bound photoexcited electron-hole pair (exciton) emerges and excess energy is thermalized. The exciton and its binding energy are quantum mechanically similarly described as a hydrogen atom, except that the lower so-called effective masses $m^*_{h,e}$ of hole and electron result in lower binding energies. Perovskites are materials with a high dielectric constant ϵ_r. Therefore, Coulomb interaction is screened, substantially reducing the binding energy. Thus excitons in perovskites can be well described as Mott-Wannier excitons with a binding energy of

$$E_{\text{bind}} = E_R \frac{\mu^*}{\mu_H} \frac{1}{\epsilon_r^2} \tag{2.5}$$

where E_R is the Rydberg energy, μ^* is the reduced effective mass of the exciton system, μ_H the effective mass of a hydrogen atom. Consequently, $E_{\text{bind}} \approx 20$ meV, i.e., in the order of thermal energy $k_B T$, which causes spontaneous exciton dissociation at room temperature. In this regard, metal halide perovskites behave similarly to inorganic semiconductors where exciton

dissociation happens quasi-instantaneous and automatically. However, perovskite excitons play an essential role due to phonon-exciton coupling [87, 88, 101].

Here, the different nature of organic semiconductors shall be briefly introduced. In organic semiconductors, photons within a specific energy range (no absorption edge present) create an exciton (inside the so-called donor) with a binding energy of up to 1 eV. This localized Frenkel exciton has limited mobility, requiring conjugated electronic structures for moderate delocalization of the excited state and polaron 'hopping' via the Förster resonance energy transfer [102]. Correspondingly, exciton diffusion lengths of only a few nm require the interface to another material (acceptor) with different energy levels to achieve exciton dissociation at the interface and transfer the electron to the acceptor. This concept of the bulk heterojunction using a blend of acceptor and donor material creates free charge carriers in either material. Recently, there have been new approaches enabling quasi-one-dimensional transport of excitons or increasing exciton lifetime in organic semiconductors, where engineering of functional group and acceptor-donor-like stacking paves the way towards tailored excitonic coupling and charge carrier transport properties [103].

In perovskites, thermalization in the conduction and valence band takes place on much faster time scales than the recombination of charges, thus the populating species in either band are thermalized and can be described in good approximation with their respective quasi-Fermi energy levels

$$n_{e,h} = D_{\mathrm{CB,VB}} \exp\left(-\frac{|E^{\mathrm{CB,VB}} - E_F^{\mathrm{CB,VB}}|}{k_B T}\right) \tag{2.6}$$

where $D_{\mathrm{CB,VB}}$ are the densities of states, $E^{\mathrm{CB,VB}}$ and $E_F^{\mathrm{CB,VB}}$ are the energy levels and Fermi energy levels of the conduction band and valence band, respectively. Undoped perovskites are intrinsic semiconductors (see Fig. 2.4). They must be in contact with a *p*-type and an *n*-type semiconductor on either side to establish a *p-i-n* or *n-i-p* junction for efficient photovoltaic devices. Here, *p* and *n* refer to the doping of the adjacent semiconductors, which defines their majority charge carrier species (holes/electrons).

While for a classical (silicon) *p-n* junction, there are schematic drawings in nearly every semiconductor textbook, there is much less available for typical perovskite junctions. Schlipf introduced a self-contained drawing in his dissertation for this purpose that covers all relevant aspects, shown in Fig 2.5 [104]. In Fig. 2.5a) typical *n-i-p* perovskite device architectures can be seen. The solar cell is built up layer by layer on top of the transparent substrate, from which side the light is coming in. Here, both perovskite solar cell architectures used in this thesis are shown. On the left is the planar, and on the right is the mesoscopic version, where perovskite is backfilled into a mesoporous scaffold of the layer below. In Fig. 2.5c) the band energy level diagram of an *n-i-p* junction can be seen for different bias conditions during illumination. To discuss the three special cases, we first introduce the two charge transport mechanisms inside

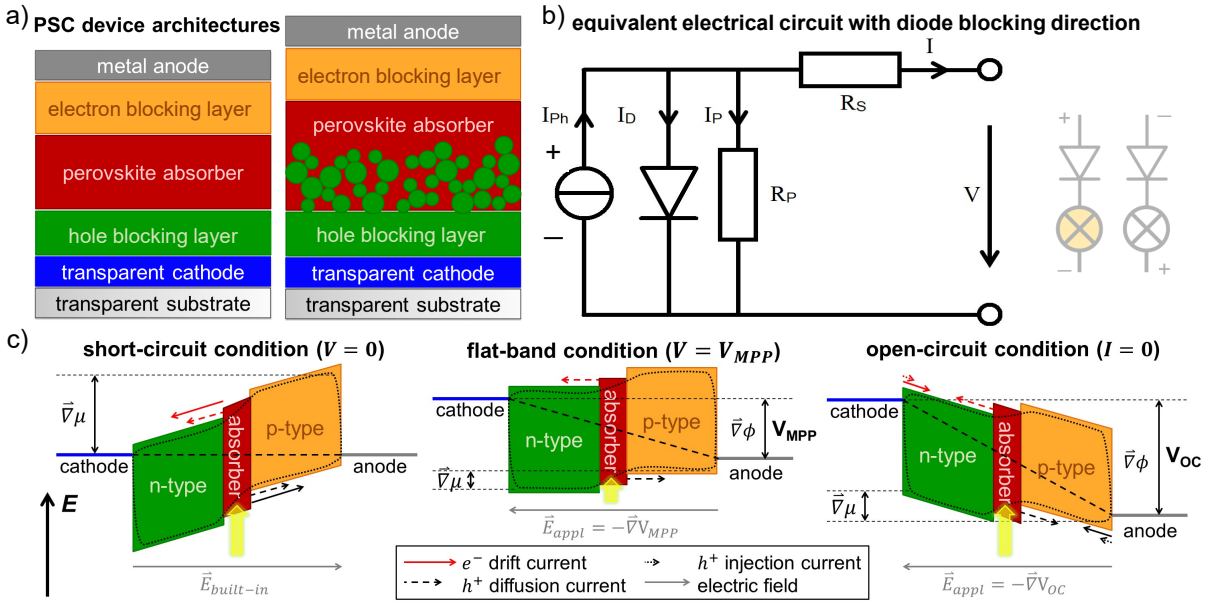

Figure 2.5: Perovskite solar cell. a) Device architecture. The left architecture shows the planar n-i-p structure and the mesoscopic n-i-p structure on the right. Sun enters from the lower side. b) Equivalent electrical circuit diagram consisting of a power source, ideal diode, and resistor in parallel with an additional series resistor. c) Band diagram of the n-i-p junction in short-circuit condition, in flat-band condition, and in open-circuit condition from left to right (details see text). a) and c) are reused from Johannes Schlipf's Ph.D. thesis [104].

the junction: drift and diffusion. Drift is charge movement induced by an external electrical field, i.e., a gradient of the electrical potential ϕ that results in a current,

$$\mathbf{j}_{\text{drift}} = -\sigma \nabla \phi, \tag{2.7}$$

with the conductivity σ. Diffusion occurs due to the random (thermal) motion of particles. In the case of non-uniform particle distribution, a gradient of the chemical potential $\mu_{e/h}$ (a particle density gradient) causes a net current

$$\mathbf{j}_{\text{diffusion}} = \pm \frac{\sigma_{e/h}}{e} \nabla \mu_{e/h}. \tag{2.8}$$

according to Fick's law where $\sigma_{e/h}$ is the diffusion coefficient [105]. Note that for the drift, consideration of accumulation of holes or electrons does not change the current flow direction, while for the diffusion, the sign is sensitive to the type of charge ($-$ for holes). Adding these two effects together results in the net force acting on single charges due to the gradient of the combined electrochemical potential, which is identical to the quasi-Fermi energy levels $E_F^{\text{CB,VB}}$ at $T = 0\,\text{K}$ [105]. One considers the three special cases in Fig. 2.5c):

- **The electron pump.** To begin with, the band diagram on the left is in short-circuit condition. Here, the cathode and anode are connected, which prevents the accumulation of charges and creates a flat Fermi level over the junction. The connection of Fermi levels of n- and p-type (dashed line) creates band bending of valence and conduction band over

the junction. The black dotted lines are the quasi-Fermi levels and correspond to the position of the valence and conduction bands, respectively. The band bending creates a built-in electrical field in either band that causes drift currents over the junction $\mathbf{j}_{\text{drift}}$. The intrinsic absorber acts as a light pump transporting electrons from the valence band and injecting them into the conduction band. Electrons drift in the built-in field towards the cathode and holes toward the anode. Diffusion due to chemical potential gradients $\nabla\mu$ – ergo due to charge carrier concentration gradients (the free charges are created in the intrinsic absorber) – is directed towards the electrodes (electrons to the cathode, holes to the anode), i.e., in the same direction as the drift occurs.

- **Drift-diffusion balance**. In the case of the open-circuit condition on the right of Fig. 2.5c), a static equilibrium is reached without any flow of charges. Imagine the pump on the left where the connection between the cathode and anode is released. Electrons will first continue drifting and diffuse to the cathode, thereby charging the left side by increasing its potential. This reduces the strength of the built-in electrical field as charges pile up. Similarly, holes pile up in the *p*-type/anode interface (since in the conductive anode electrons are the majority charge carriers, holes recombine with electrons at that interface, the wording "holes move through the anode" should be avoided). Eventually, an equilibrium is reached when the charging of the junction reaches an equilibrium where drift transport in one direction and diffusion in the opposite direction balance each other. As a result, a steady charge distribution is achieved with the maximum potential between the electrodes of either Fermi level $V_{\text{OC}} = (E_F^{\text{CB}} - E_F^{\text{VB}})/e$.
- **Leveling off - diffusion-induced charge flow**. This flat-band condition is the desired operation mode of solar cells, shown in the central diagram in Fig. 2.5. Here cathode and anode are connected via a resistor (finite load); thus, charges move through the junction, while simultaneously a potential is present. In this intermediate case, a specific space charge builds up to counteract the built-in electrical field. This eliminates any drift in the junction. The only transport mechanism left is (chemical potential) diffusion due to charge concentration gradients, in the flat-band condition.[3] In the flat-band condition, a certain potential difference between the cathode and anode is established, which can be identified with the maximum power point (MPP) voltage V_{MPP}, which is the typical mode of solar cell operation explained below. The important takeaway message is that solar cells operate in a regime that is diffusion-dominated movement of charges and not drift-dominated transport.

[3] Due to the absorber conduction band being energetically below the conduction band of the *p*-type, electrons cannot diffuse into the *p*-type semiconductor. The same holds for holes, which do not diffuse into the *n*-type semiconductor. Therefore, these layers are the so-called selective charge blocking layers since they effectively *block* the diffusion into them. This is the main reason why it is important to speak about blocking layers and not about transport layers of the opposite species. Transport is related to conductivity (which requires an external force to create drift), and diffusion is induced by concentration gradients. In the flat-band condition, no drift is present, thus the main mechanism of the adjacent layers is to block the diffusion of charges in one direction.

2.2.4 Diode Equation and Detailed Balance

Ideal p-n junctions obey the Shockley equation of an ideal diode

$$I_D = I_0 \left[\exp\left(\frac{eV}{k_B T} \right) - 1 \right] \tag{2.9}$$

with I_0 being the dark current or diode-leakage current (indicative of recombination processes), e the electron charge, k_B the Boltzmann constant, and T the temperature. In Fig. 2.5b) the equivalent circuit diagram of a solar cell is shown. For the moment, we neglect the resistors R_p and R_s and only consider a photocurrent source I_{Ph} due to illumination together with the diode. I_{Ph} is directed in the diode blocking direction, i.e., reverse to the natural let-through direction of the diode (cf. band diagrams in Fig. 2.5c). In Fig. 2.5b) on the right, the definition of diode blocking and let-through direction are indicated in grey and the technical diode sign is oriented as the architectures in Fig. 2.5a). Note that in the diagrams in Fig. 2.5c) we extract electrons on the cathode side, susceptible to flow back through the diode in the equivalent circuit Fig. 2.5b) and contribute to the leakage current. Thus we can set up the characteristic equation where the output current is the photocurrent minus the diode-leakage current.

$$I = I_{Ph} - I_D = I_{Ph} - I_0 \left[\exp\left(\frac{eV}{k_B T} \right) - 1 \right] \tag{2.10}$$

where, for large enough photocurrents, a positive effective current I can be extracted at positive voltages, and the solar cell creates power.

Some charges are lost during transport at resistances of the solar cell (interfaces, blocking layers, intrinsic absorber layer), which can be modeled in the equivalent electrical circuit diagram by adding a resistor in series R_S to the photodiode. A parallel resistor R_P (sometimes called shunt resistance) with finite Ohmic resistance models parasitic currents that 'shunt' the solar cell, such as surface currents, pin-holes, or grain boundaries [105]. If an external output terminal voltage V is measured, the inner voltage V_i across the photodiode must be the output voltage plus the voltage lost across the series resistor $V_i = V + IR_S$. Considering the parallel resistor, a leakage current $I_P = V_i/R_P$ reduces the total current. These effects lead to the characteristic equation

$$I = I_{Ph} - I_D - I_P = I_{Ph} - I_0 \left\{ \exp\left[\frac{e(V + IR_S)}{k_B T} \right] - 1 \right\} - \frac{V + IR_S}{R_P}. \tag{2.11}$$

This version of the equation does assume strictly positive currents. This equation includes a single diode, whereas, for more realistic descriptions, multiple parallel diodes might be necessary [105]. The diode equation is a transcendental equation, meaning that it is not possible to express the current as an analytic function of the voltage and vice-versa. Therefore, iterative numerical approaches are necessary to model measured I-V solar cell characteristics. A common way to extract detailed information of the I-V solar cell measurement is *via* using drift-diffusion models such as SCAPS for modeling polycrystalline semiconductor solar cells [106].[4] However, a first-order approach allows extracting values for the series and parallel resistances by the derivative of the diode equation at the two special points $V = 0$ and $V = V_{OC}$ (at $I = 0$). These

[4] See also Simiconductor, https://research.edm.uhasselt.be/simiconductor/, accessed 10.10.2023.

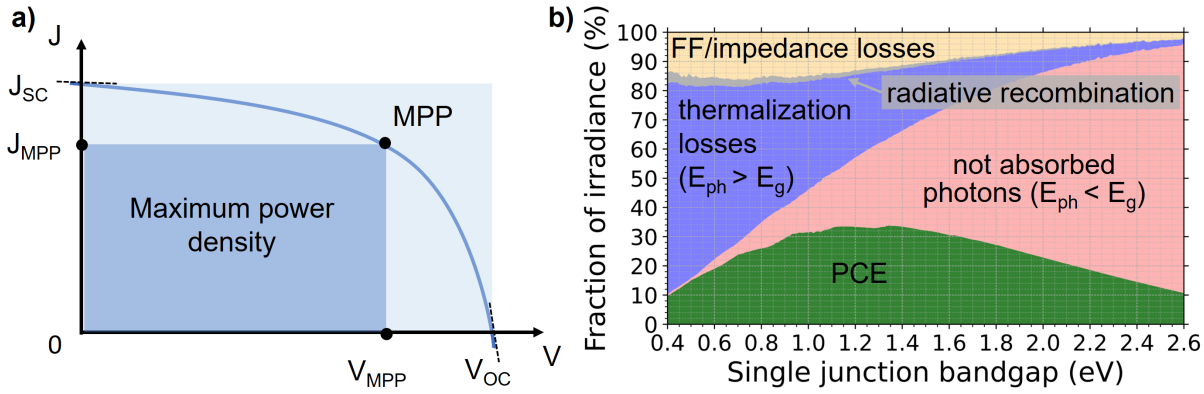

Figure 2.6: a) Solar cell current-density voltage characteristic with marks at the important locations. The inner dark rectangle defined by the maximum power point (MPP) represents the maximum extractable solar cell power. b) Detailed balance limit after Shockley and Queisser. The graph shows percentages of usable electric power (green area), losses due to below-bandgap photon energies (red), losses due to thermalization to the band edges of absorbed photons (blue), radiative recombination losses (grey), and FF losses (yellow). Steven J. Byrnes is acknowledged for straightforward calculations in Python of the detailed balance limit in his GitHub repository. Code adapted.

two special points at the equivalent circuit can be imagined as follows. At V_{OC} holds $I = 0$, thus the internal voltage equals the external voltage $V_i = V_{OC}$. If applying an additional small positive bias $\mathrm{d}V$, the resulting current will flow across R_S and the diode (which has low internal resistance at V_{OC}), giving $\mathrm{d}V \approx R_S \mathrm{d}I$. For the other case at I_{SC}, the voltage is zero and when applying a small positive bias, the diode will block the flow (high internal resistance at $V \approx 0$), and the resulting current will flow across R_S and R_P, thus $\mathrm{d}V = (R_P + R_S)\mathrm{d}I$. Summarized holds

$$R_S = \left(\left. \frac{dI}{dV} \right|_{V=V_{OC}} \right)^{-1} ; R_P = \left(\left. \frac{dI}{dV} \right|_{V=0} \right)^{-1} - R_S. \tag{2.12}$$

For an optimal photovoltaic device, parasitic losses are minimized, thus $R_S \to 0$ and $R_P \to \infty$.

The maximum power of a solar cell can be extracted at the maximum power point (cf. Fig. 2.6a), where the product of voltage and current is maximal. The ratio of this maximum power and the incident light power $P_L = I_L A$ is defined as the power conversion efficiency PCE or η of a photovoltaic device

$$\mathrm{PCE} = \frac{P_{MPP}}{P_L} = \frac{V_{MPP} I_{MPP}}{I_L A}. \tag{2.13}$$

According to Equation 2.12, this has direct implications for the slope of the I-V curve at $V = 0\,V$ and $V = V_{OC}$, which in turn influences the *rectangularity* of the diode curve. This resembles the fill factor (FF), which is defined as

$$\mathrm{FF} = \frac{P_{MPP}}{V_{OC} J_{SC}} = \frac{V_{MPP} I_{MPP}}{V_{OC} I_{SC}}. \tag{2.14}$$

The efficiency

$$\mathrm{PCE} \propto V_{OC} J_{SC} \mathrm{FF}, \tag{2.15}$$

is proportional to the product of open-circuit voltage, short-circuit current, and fill factor.

In order to estimate the maximum theoretical PCE, the different loss mechanisms that occur under specific assumptions must be considered. First, the perovskite layer absorbs only photons with large enough energy (cf. Eq. 2.4). All photons of below-band gap energy are lost (red in Fig. 2.6b). Second, photons absorbed with energy above the band gap are absorbed, but the excess energy is lost (purple in Fig. 2.6b). These two loss mechanisms are the most significant losses for perovskite solar cells with band gaps far above 1 eV. The optimum bandgap is a trade-off between being small enough to harvest more photons and large enough to weigh each photon with enough energy (eV_{OC}). We can calculate the total charge-generated current of a solar cell by spectrally integrating the number of absorbed (above band gap) photons and weighing them with the bandgap energy. Here is made use of the solar cell-specific external quantum efficiency (EQE), which is a spectral measure of the probability of a photon being absorbed by photoexcitation of the cell (for Shockley-Queisser 0 below and 1 above the band gap),

$$J_{gen.} = e \int \mathrm{EQE}(\lambda) I_{Ph}(\lambda) \mathrm{d}\lambda. \tag{2.16}$$

where $I_{Ph}(\lambda)$ is the spectral photon number per area and time.

Understanding the origin of the third loss component (yellow area) in Fig. 2.6b requires the detailed balance limit by Shockley and Queisser [107], who presented the first complete thermodynamic framework to derive the maximum possible photovoltaic parameters of an idealized solar cell, where they radiatively balance photon absorption and emission. In their concept, the solar cell (without bias in dark environment) emits black body radiation B_T, which can be interpreted as radiative recombination based on the so-called thermal voltage $V_T = e/k_bT$. In the case of illumination, an increased free charge carrier density causes quasi-Fermi splitting (ideally) equal to the solar cell voltage V. This, in turn, enhances the radiative recombination rate B_T by a factor of $[\exp(V/V_T) - 1]$ according to kinetic theory. The maximum current of the solar cell is the generated current minus the lost current due to radiative recombinations (no other recombinations assumed),

$$J = J_{gen.} - B_T[\exp(V/V_T) - 1]. \tag{2.17}$$

These radiative recombinations lose charges that otherwise could be used for photovoltaic power production and lower the maximum current. This function connects current density and voltage and the short circuit current density J_{SC} for $V = 0$ as well as the open-circuit voltage V_{OC} for $J = 0$ can be calculated by inverting the equation, $V_{OC} = V_T[\ln(J_{gen.}/B_T) + 1]$.

The last effect is called impedance matching by Shockley & Queisser is related to the FF introduced above. Due to the limited rectangularity of the J-V curve, the nominal power $J_{SC}V_{OC}$ can, in practice, not be reached. According to Eq. 2.17, the FF is a function of temperature and a function of the number of the photo-generated current density $J_{gen.}$ that depends on band gap and light spectrum.

From the graph in Fig. 2.6b, a maximum PCE of about 30 % and an FF of about 90 % for an 1.6 eV band gap solar cell can be read. The overall maximum possible PCE of 33 % is reached for a band gap of about 1.35 eV. For tandem cells with multiple absorber layers or concentrator cells, higher efficiencies are achievable than covered by the calculation [108]. The Shockley-Queisser detailed balance is based on the assumption of thermal equilibrium and constant temperature of the solar cells. Recently, work about theoretical performance parameters for variable temperatures has been published, showing that the heat-transfer coefficient and the solar concentration have implications for the optimal band gap of the solar cell [109].

2.3 Perovskite Crystal Growth and Thin-Film Crystallization

In this thesis, solution processing of perovskite precursors is used to obtain thin films for photovoltaic applications. To understand the physics taking part in this crystallization process, basic principles of nucleation and growth are introduced first using an energetic perspective. Thereafter, classical nucleation and growth models are discussed. Then, the transfer of these concepts to the application for (scalable) perovskite processing is made in terms of the effects taking place during one-step anti-solvent spin coating. The coordination of solvents with the perovskite constituents is explained with a summary of the state-of-the-art knowledge of solvent engineering for scalable perovskite processing from solution.

Before introducing theory, a short motivation for this section is appropriate since perovskite crystallization is closely related to the progress of perovskite technology in the last decade. The final macroscopic film is determined by physical and chemical processes and effects during film formation in self-assembled nano-scale films. In the past years, literature reached a consensus about the basic four steps, including their underlying principles involved in the process of high-quality thin perovskite film formation [110, 111], in brief (more details below): In the first step, a perovskite precursor is distributed on the substrate. In the second step, solvent drying occurs, bringing the solution to its solubility limit. In the third step, solution supersaturation is achieved by a quenching method to trigger nucleation and initiate crystal growth. In the fourth and last step, crystalline colloids grow, and perovskite grains form in the film.

Controlling the crystallization of perovskite is the key to achieving high-quality thin films. Film quality includes microstructure, such as crystallinity, crystal grain sizes, grain size distributions, grain boundaries, grain interfaces, and crystal defects, as well as macrostructure, such as homogeneity, absence of pin-holes, surface roughness, and film morphology. Understanding the influence of film micro- and macrostructure on device functionality and stability has become increasingly important in the last years [112]. For example, the perovskite crystal orientation at the interfaces influences the charge transfer to the blocking layers [113]. The charge-carrier dynamics are influenced by the crystal structure and intrinsic material stability is limited by defects because they mediate degradation pathways [7, 101, 112]. Therefore, the processes involved in nucleation, growth, and solution processing are covered in the following subsections.

2.3.1 Gibbs' Picture of Nucleation and Growth

The term nucleation refers to the stochastic creation of nuclei in a metastable system such as supersaturated solutions. This spontaneous process occurs when reaching the critical concentration and does not require any external help. Under certain circumstances, as detailed as follows, the nucleation process becomes energetically favorable and thus an energetic consideration is advised. For this, the Gibbs free energy G_1 of a homogeneous liquid-phase system of volume V_L and of an identical system G_2 are introduced, where in the latter system a solid spherical nucleus of radius r with volume $V_S = 4/3\pi r^3$ and surface $A = 4\pi r^2$ is present inside. Then holds

$$G_1 = V_L G_V^L \tag{2.18}$$

$$G_2 = (V_L - V_S)G_V^L + V_S G_V^S + A\gamma \tag{2.19}$$

where G_V^L, G_V^S are the volumetric free energies in the liquid and solid phase and γ the areal free energy. The energetic change from system 1 to system 2 is then:

$$\Delta G(r) = G_2 - G_1 = V_S\left(G_V^S - G_V^L\right) + A\gamma = \underbrace{\frac{4}{3}\pi r^3\left(G_V^S - G_V^L\right)}_{\Delta G_V} + \underbrace{4\pi r^2\gamma}_{\Delta G_S} \tag{2.20}$$

Here, γ is always positive because the increasing interface area is energetically unfavored, and the first term is negative because $G_V^S < G_V^L$ because the solid phase has a lower energy. In Fig. 2.7a), the trend of the change of effective system energy is shown as a function of nucleus radius r. While for smaller radii, the surface term ΔG_S dominates, the volume term ΔG_V becomes

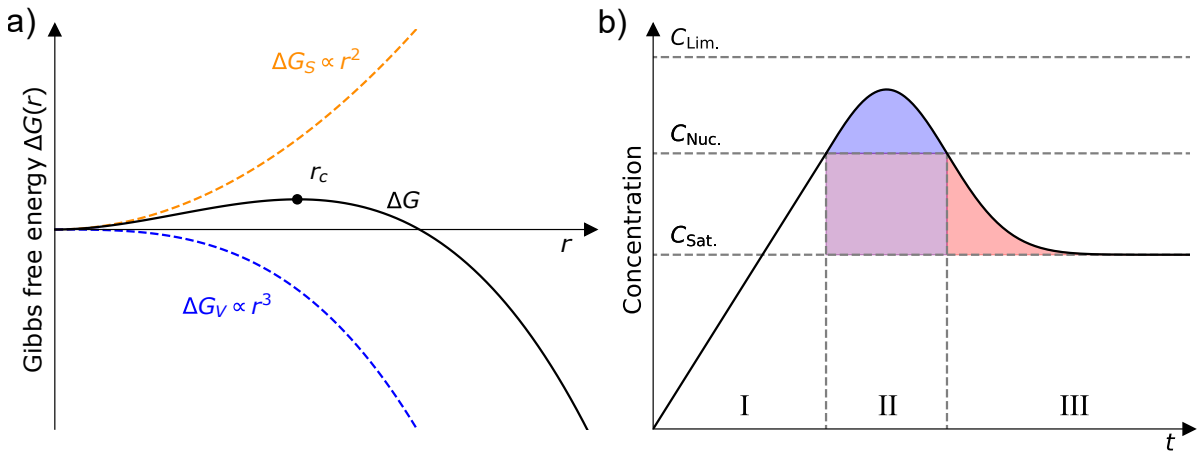

Figure 2.7: a) Gibbs free energy ΔG as a function of r with the resulting instability peak at r_c as a trade-off between the areal free energy ΔG_V and the volumetric free energy ΔG_V. For $r > r_c$, nucleation becomes energetically favorable. Figure adapted from Andrea Vitaloni's Master thesis [114]. b) The LaMer model with the three phases: I concentration increase until nucleation onset, II rapid nucleation until the concentration decreases below nucleation threshold, and III growth of existing nuclei until the solution eventually reaches saturation concentration. Note that in phase II nucleation and growth of stable nuclei coexists.

dominant at larger radii due to the larger exponent of r. By setting the derivative to zero, the critical radius $r_c = 2\gamma / \left(G_V^S - G_V^L\right)$ can be obtained where the nucleation is energetically maximally suppressed. Nuclei of larger radii are thermodynamically stable, and their growth is energetically favored.

Frequently terms homogeneous or heterogeneous nucleation can be found The process investigated above treats homogeneous nucleation [115]. The term homogeneous originates from the fact that this nucleation process occurs in a well-mixed, i.e. homogeneous, solution without any impurities or solid surfaces that aid the nucleation process. Heterogeneous nucleation, in contrast, happens at pre-existent nucleation seeds that could be foreign phases, surfaces (solution-substrate interface), or other species inside the solution like colloids [110]. Here, also earlier-formed nuclei can act as attachment points, comparable to the growth of snowflakes. Both processes follow the same logic, however, for heterogeneous nucleation, preexistent seeds effectively reduce the liquid-solid interface area, thereby reducing the magnitude of the interfacial (surface) term and, consequently, the critical radius.

We can compute the free energy barrier $\Delta G(r_c)$ that, in turn, enters the nucleation rate equation according to classical nucleation theory

$$R \propto \exp\left(-\frac{\Delta G(r_c)}{k_B T}\right), \tag{2.21}$$

where the Boltzmann distribution can be connected to the cluster energy states similar to in statistical mechanics [116].

2.3.2 Johnson-Mehl-Avrami-Kolmogorov Equation and the LaMer Model

The Johnson–Mehl–Avrami–Kolmogorov equation can model the kinetics of nucleation and growth that expresses the transformed fraction of material as a function of time as

$$f(t) = 1 - \exp\left(-kt^n\right) \tag{2.22}$$

where k is a temperature-dependent nucleation/growth rate constant related to R above, and n is the Avrami exponent taking values from 1 to 4, which is related to the dimensionality of growth [117]. This kinetic model assumes spherical nuclei shapes, stochastic nucleation within the untransformed fraction, and non-directed growth. Heuristically, $n = 4$ means that at early times the number of nucleation seeds increases linearly, as does the radius of existing nuclei (volume cubic), and hence a total volume increase $\propto t^4$. As time continues, the growth rate reaches a maximum, and as the converted ratio increases, less material is left for nucleation/growth. This slows down the process, asymptotically reaching 100 % conversion. The result is an S-like shape typical for logistic functions.

A successor of this model is the so-called LaMer model (see Fig. 2.7b), originally developed to explain the (homogeneous) nucleation and growth of monodisperse nanoparticles in solution in 1950 [118]. Here the crystallization process can be separated into three phases. First, a phase

of rise of the concentration to the critical supersaturation, then a short nucleation phase, and a final growth phase, where concentration changes control each of the three phases. In phase I, the concentration in the solute continuously increases beyond the saturation concentration (e.g., by reducing solubility or solvent) until reaching the critical concentration $C_{\text{Nuc.}}$ in the end. Due to the absence of nucleation seeds and the lack of a solid phase, the system crosses saturation concentration without any effects since growth is energetically hindered, as explained above. In phase II, the concentration exceeds $C_{\text{Nuc.}}$, causing rapid (homogeneous) nucleation. A classical diffusive growth coexists. However, LaMer considers timescales of nucleation to be close to instantaneous, effectively suppressing diffusive growth and making nucleation the dominant process consuming the solute. The solute forms nuclei reducing the concentration quickly until it declines below $C_{\text{Nuc.}}$. Then it enters phase III, where the concentration is still supersaturated above the solubility limit $C_{\text{Sat.}}$ but below the critical concentration $C_{\text{Nuc.}}$. Therefore, nucleation is inefficient in this phase; pre-existing thermodynamically stable nuclei grow by monomer addition in a purely diffusive growth process [110]. Eventually, the equilibrium settles at saturation concentration without further net crystal growth. The solid phase and the saturated liquid phase coexist.

2.3.3 One Step Anti-Solvent Spin Coating

The theoretical concept of nucleation and growth can now be transferred to the processing of perovskite from an ink (precursor) to a solid perovskite film. In 2014, the first publication of the today-called anti-solvent method appeared [119]. Here, the ”good” solvent (dissolves perovskite easily) is washed away with a ”bad” solvent (does not dissolve perovskite), to artificially reach the critical perovskite concentration and to trigger nucleation in the film. In the laboratory, the process is performed as follows: During one-step anti-solvent spin coating, the perovskite precursor is first dropped on the substrate. The subsequent spinning of the substrate establishes an equilibrium between radial centrifugal forces and surface tension, removing excess solution, and the remaining precursor creates a thin homogeneous film. Further spinning thins the film by evaporation (not crystallizing yet!). A few seconds before the end of spinning the anti-solvent is flushed onto the spinning substrate, with an abrupt change of the film’s color. Already in these early works, coordinating solvent was added to the ink (see next paragraph), and intermediate phases were reported [120]. Within the following three years, this anti-solvent method was optimized by various research groups, increasing the perovskite solar cell efficiency from 15 % to over 22 % [121]. Making use of in-situ synchrotron investigations, rapid nucleation during anti-solvent dropping could be identified to form the initial perovskite clusters that act as seeds for the following crystal growth upon thermal decomposition of the solvent complexes (intermediate phase) during annealing [122, 123]. Even today, the record perovskite solar cells are still produced with this technique [11].

Understanding the processes that occur during this anti-solvent method became important when research focused more and more on scalable deposition processes, as can be read in these

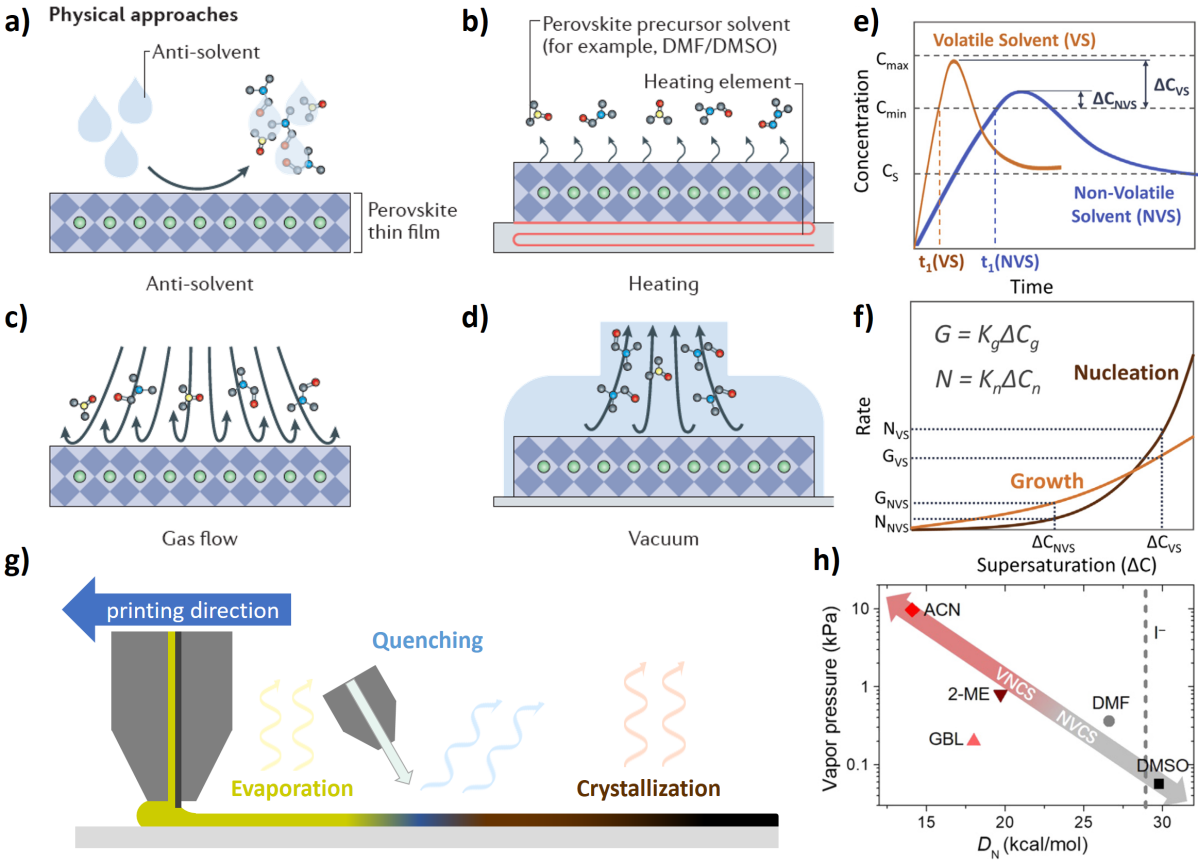

Figure 2.8: Overview of concepts covered in this section. a)-d) shows the four solvent quenching methods used during perovskite fabrication to initiate nucleation. Reproduced from Li et al. with permission [15]. Copyright © 2018 Springer Nature. e)+f) shows the qualitative effect of solvent volatility on nucleation and growth using the principles of the LaMer model (details see text). Reproduced from Wu et al. under the Creative Commons license [124]. Copyright © 2021 The Author(s). Published by Elsevier. g) schematically shows the four stages of perovskite film formation (for blade-assisted slot-die coating with air-quenching): I deposition, II evaporation, III quenching, and IV crystallization. h) shows the concept of volatile non-coordinating solvents and non-volatile coordinating solvents as described by their Gutmann Donor number D_N and vapor pressure at RT (details see text). Reproduced from Deng et al. under the Creative Commons license [125]. Copyright © 2019 The Author(s). Published by the American Association for the Advancement of Science.

highly recommended reviews and perspectives with the focus on solution engineering and scalable perovskite processing [15, 124, 126]. This was initiated because the anti-solvent spin-coating method's scalability is limited, and anti-solvent dipping or spraying turned out to be a technically challenging process or has not been tried for continuous fabrication yet [15, 126]. However, the anti-solvent method is only one of the so-called solvent-quenching approaches that can trigger nucleation [15]. In Fig. 2.8a)-d), the four main used methods are shown, where heating b) gas flow c) or vacuum d) are options to quickly remove the solvent from the deposited wet layer. They all require rapid (within sub-second timescales) removal of large solvent fractions to enter the nucleation regime. But why do we need nucleation at all?

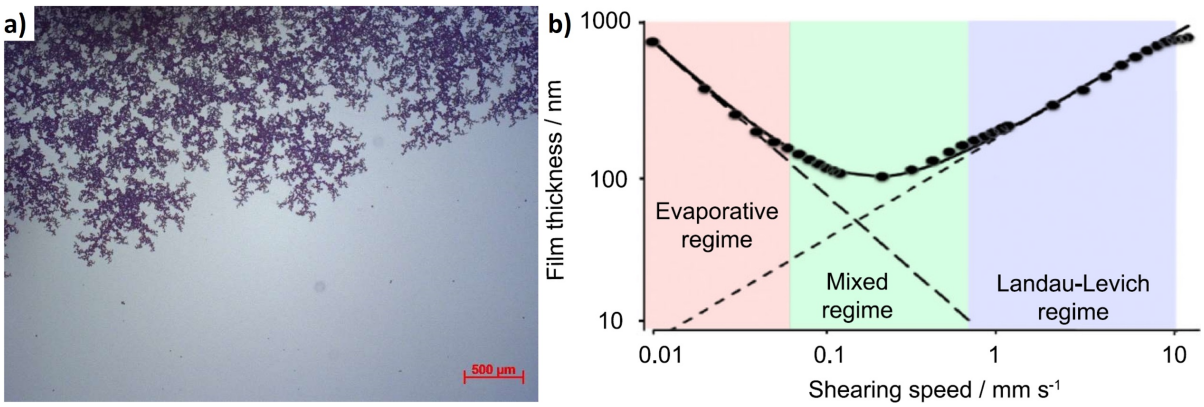

Figure 2.9: a) Optical microscopy from the glass slide side onto a slot-die-coated perovskite film. The top region shows dendritic growth due to heterogeneous nucleation beginning from the substrate. The lower region shows the desired homogeneous, nucleation-dominated morphology. Reprinted with permission from Ternes et al. [130]. Copyright © 2022 American Chemical Society. b) Evaporative, mixed, and Landau-Levich printing regime. Dots show measurements, and the straight dashed lines are theoretical predictions for either regime. Adapted from Gu et al. with permission under the Creative Commons license [132]. Copyright © 2018 The Author(s). Published by Springer Nature.

2.3.4 Nucleation Dominated Growth for Homogeneous Perovskite Layers

In Fig. 2.8e&f, the LaMer model for two different perovskite inks is shown. In e), the orange curve shows the qualitative behavior of a perovskite ink concentration over time for a volatile, quickly evaporating solvent. The maximum concentration reached above the onset of nucleation ΔC_{VS} is large, leading to a dominant nucleation process seen in f). In contrast, a non-volatile, slowly evaporating solvent (blue curve in e) shows only a small ΔC_{NVS}, causing 'some' nucleation while the crystallization is still growth-dominated. As a result, the film derived from the volatile precursor ink will show many tiny homogeneous crystal seeds while the non-volatile precursor will show few large crystals. In principle, having few large crystals is beneficial for charge carrier transport due to reduced interfacial areas between grains and fewer grain boundaries, so this should be favorable. However, in this growth-dominated regime, perovskites frequently enter *heterogeneous* growth, i.e., perovskite crystals grow preferentially, form dendritic structures or islands, create voids or pinholes with an undesirable discontinuous microstructure (see Fig. 2.9a)) [15, 119, 124, 127, 128, 129, 130, 131]. Therefore, the maxim is to grow large, *homogeneous* crystals in a dense film by initially triggering a high degree of nucleation in the films and then increasing the growth time window by a combination of volatile and retarding non-volatile solvents.

2.3.5 Solvent Coordination and Intermediate Phase

Already in 2014, the strongly coordinating solvent dimethyl sulfoxide (DMSO) was found to create an intermediate perovskite phase in the deposited layer after quenching but before annealing [120]. In recent years and still today, state-of-the-art perovskite layers have been derived

from a co-solvent mix made of dimethylformamide (DMF) and DMSO [7, 11, 85]. Progress in the understanding of the influence of solvent coordination on perovskite formation began in the late 2010s when the ability of the solvent to coordinate with Pb^{2+} cations was related to the Gutmann donor number [133]. Here, the Gutmann donor number is a quantitative measure of Lewis basicity, i.e., the ability to solvate cations [134]. Solvent complexes form colloidal dispersion of chemically and structurally diverse plumboiodide species, such as $[PbI_3]^-$, $[PbI_4]^{2-}$, and following this scheme higher orders, coordinated with MA^+ and the coordinating solvent [135]. Building upon this work, the concept of a volatile non-coordinating (VNC) and non-volatile coordinating (NVC) two-solvent system for tailoring the solvent-perovskite coordination in the precursor (see Fig. 2.8h) was introduced [125]. The basic principle behind this is to optimize the ratio of VNC and NVC solvents to the present fabrication conditions that, on the one hand, the perovskite nucleates uniformly upon VNC solvent removal and, on the other hand, has enough residual NVC solvent to grow large crystals in a smooth dense film. Here, other solution parameters, such as the solution concentration, strongly influence the solvent complexes inside the solution and therefore have direct relevance for the subsequent processing [135]. In the end, usually, an annealing step is included (see Fig. 2.8g) where the solvent-solute complexes of the NVC solvent are broken, the residual solvent evaporates slowly, and the perovskite crystal formation is completed [123, 124]. In the final stage, so-called Ostwald ripening likely plays a role in crystal growth and grain coarsening [126], either mediated by residual solvents in the film or by volatile additives such as MACl, MABr, or general alkylammonium-chlorides (that can also act as nucleation seeds in the first steps) that prolong the time for crystallization and thus lead to larger crystallite sizes in the final film [11, 15, 126, 136, 137]. Ostwald ripening refers to the diffusive (i.e., slow) transfer of material from a small crystallite to a larger crystallite due to an energetically favorable final state (decrease of surface volume - see Gibbs principle above in subsection 2.3.1).

The previous subsections provided concepts of perovskite crystallization and details of the quenching mechanism during one-step anti-solvent spin coating. Here, this knowledge shall be conceptually transferred to scalable perovskite fabrication. In particular, it aims to introduce the theory behind scalable printing methods and to answer how the quenching principle can be transferred to continuous processing. There are multiple different scalable deposition methods investigated in the literature. Namely, roll-to-roll compatible methods such as blade, slot-die, meniscus, spray coating, inkjet, and screen printing can produce perovskite solar cell modules of hundreds of cm^2 [13, 14, 15, 138, 139, 140, 141]. As one example, using the perovskite semi-transparency of thinner layers combined with transparent electrodes led to a scalable bi-facial module with an impressive area of 781 cm^2 and an efficiency of 11.9 % [142] as shown in Fig. 2.10.

2.3.6 Scalable Perovskite Fabrication

Upscaling solution-processed perovskite is a requirement for high-throughput processing [126, 143]. This work's scalable method of interest is the so-called blade-assisted slot-die coating using

air-knife solvent quenching. Slot-die coating is a highly efficient process for material efficiency and roll-to-roll compatibility for printing on flexible substrates [15, 18, 144, 145]. The thin slit in the print head allows to resupply ink of the meniscus by pumping new ink from the print head. However, compared to blade coating, one drawback of the slot-die coating method is the rather complex setup, making it unpractical for developing new ink chemistries [15, 124, 144]. Slot-die coating and blade coating share common principles for their techniques. They make use of the meniscus, i.e., a liquid bead, that is formed on and moved across the substrate to spread precursor ink to form *wet* thin films (see Fig. 2.8g). The meniscus is attached to the blade and the substrate by capillary forces. The film thickness is a function of the concentration of the ink, the gap height, i.e. the distance between blade and substrate, solution rheology (including viscosity, and surface tension), and the relative movement speed of the meniscus to the substrate. The optimal printing parameters for high-quality results can be found in the operating window, where competing effects are balanced to create a stable dynamic coating process. The operating limits are determined by a complex set of competing forces acting on the coating bead. This includes capillary, viscous, gravitational, applied vacuum pressure, inertial, and elastic forces that also depend on geometric variables and material properties [146]. To a certain extent, the operating limits for slot-die coating can be solved by making approximations and obtaining analytical models. For more accurate descriptions, a numerical solution of the

Figure 2.10: Bifacial semitransparent large-scale perovskite module by Imec [142]. Photograph from Imec unveils 781 cm^2 bifacial perovskite solar panel with 11.9 % efficiency (pv-magazine.com), accessed 12.07.2023.

2-D Navier-Stokes system is required [146, 147]. Due to the blade-assisted process used in our group, literature dealing with doctor blade coating delivers an appropriate theoretical framework for process optimization (see [148] for an extensive review). The flow solution for coating a flat plate with a liquid was solved initially by Landau & Levich in 1942 by using matched asymptotic expansions of different regimes of the upward and downward meniscus [149]. The thickness d of the wet-coated film (in the Landau-Levich regime) behaves as

$$d \propto h \left(\frac{\eta v}{\gamma} \right)^{\frac{2}{3}} = h \, (\mathrm{Ca})^{\frac{2}{3}} \, , \tag{2.23}$$

where h is the gap height, η is the ink viscosity, γ the surface tension, v is the printing velocity in the Landau-Levich regime (cf. Fig. 2.9b) [148, 150]. Here, the capillary number Ca has been introduced, which is a measure of the relative strength of viscous drag forces (nominator) versus surface tension (denominator) and thus determines the dynamic contact angle of the meniscus and the substrate. Interestingly, increasing printing speed in the Landau-Levich regime increases the layer thickness, since viscous drag forces become stronger. This effectively drags out the liquid volume from the meniscus [148]. Coating in the Landau-Levich regime is advantageous in contrast to the (slow) evaporative regime (see Fig. 2.9b) for several reasons. First, the coating speed is higher, which is desirable for scalability. Second, a wet film and a large enough processing window enable solution flow and diffusion after printing, leveling off potential inhomogeneities in the wet film. Third, since quenching is a consecutive but independent process, both processes can be optimized independently, reducing the entire process's complexity.

The solvent quenching method of interest in this work is solvent removal via an air knife that blows nitrogen (or dry air) over the wet-coated substrate to trigger nucleation. Air-knife-based quenching is abundantly used for scalable perovskite processing [13, 111, 125, 130, 151, 152]. In particular, Ternes et al. (2022) delivered an extensive model that incorporates printing and the complex gas-quenching process in their remarkable publication "fully gas-phase controlled drying" [130]. In detail, mass and heat transfer of the airflow are linked in the model with printing speed, air velocity, and other parameters (using a two-solvent system). As a note, due to the above-mentioned printing in the Landau-Levich regime, the air knife is usually spatially separated from the meniscus, and the airstream is directed away from the meniscus. Otherwise, the fluid dynamics at the downstream meniscus, i.e., the wet film deposition, would be influenced by the drying airstream, unnecessarily entangling separate processes [13, 125, 130, 153]. From the experimental comparison of the parameter space, the perovskite film appearance (whitish color growth dominated, black mirror-like nucleation dominated) is used as a proxy to define criteria for the optimal application of air-quenching as a function of printing parameters.

In detail, there is a quite determined threshold of heat or mass transfer in a short application time window, with a divergent influence on the final film morphology. In other words, a slight difference in drying rate around the threshold significantly affects the final dry film [130]. This makes the appropriate design of the air knife mandatory to maximize the laminarity of the airflow because turbulence not only reduces the airstream capability of solvent removal but also

causes flow instabilities that lead to undesirable fluctuations of the quenching effectiveness during processing with inhomogeneities in the resulting film. Please refer to Christoph Lindenmeir's Master thesis for a detailed discussion of the design and testing procedure of the air knife, including optimization of the printing parameters for thin perovskite films [154].

Likely, there cannot be too much nucleation during solvent quenching. The presence of solvent complexes, residual solvents, or volatile material-species mediate Ostwald ripening effects that act especially efficiently for large relative grain size differences since diffusion of monomers or smaller particles is faster than for larger particles [110]. Because of this, if there are 'too many' small crystallites due to strong quenching at the beginning of the Ostwald ripening process, their number will decline quickly and approach the grain size distribution of a similar film with weaker nucleation. This is in agreement with theoretical predictions: For a particular system, a universal stationary grain size distribution is automatically established, and the average radius of the distribution increases with time [155]. On the other hand, insufficient homogeneous nucleation makes heterogeneous nucleation and growth more probable, causing undesired film properties such as dendritic growth and poor coverage [81, 111, 130, 156]. Thus, the process engineering maxim should be to quench the films as ideally as possible to yield the best possible nucleation-dominated morphology. Then the crystal size is ideally controlled by tuning the time of the growth process and Ostwald-ripening, e.g. by increasing the fraction of coordinating solvent or modifying the annealing procedure [125, 157, 158].

2.4 Scattering Techniques

This section introduces the theoretical concepts behind X-ray diffraction (XRD), Grazing-Incidence Wide-Angle X-ray Scattering (GIWAXS), and Grazing-Incidence Wide-Angle X-ray Scattering (GISAXS). It is intended to be an easy-to-read, explanatory description with intuitive comparisons breaking down the processes to the fundamentals and shall guide the reader to the experimental and data-analysis concepts behind GIWAXS and GISAXS in a heuristic way. For an extensive overview of the application of X-ray scattering to perovskites, including a detailed methodological description and typical pitfalls, see Tan et al. [159]. For an introductory-level textbook on X-ray scattering, see e.g. "Elementary scattering theory" by D. S. Sivia, for greater depth and mathematical rigor and a focus on crystal diffraction, see "The diffraction of X-rays by crystals" by C. Giacovazzo [160, 161], where many of the fundamental concepts presented here can be found. Multiple sections cover topics starting with the Laue condition, Bragg-equation, experimental geometry of Bragg-Brentano XRD and GIWAXS, the concepts of orientation sphere, in-plane powders, the missing wedge, and closes with Lorentz representation, pole figures, and close with texture quantification for GIWAXS. The chapter aims to outline typical pitfalls related to the nature of the missing wedge and misunderstandings related to in-plane powders and the Lorentz factor. In-depth details about the mathematical framework of the model used frequently in our group for GISAXS analysis can be found in previous Ph.D. theses [104, 162]. Here in the last section, intuitive access will be provided by outlining similarities

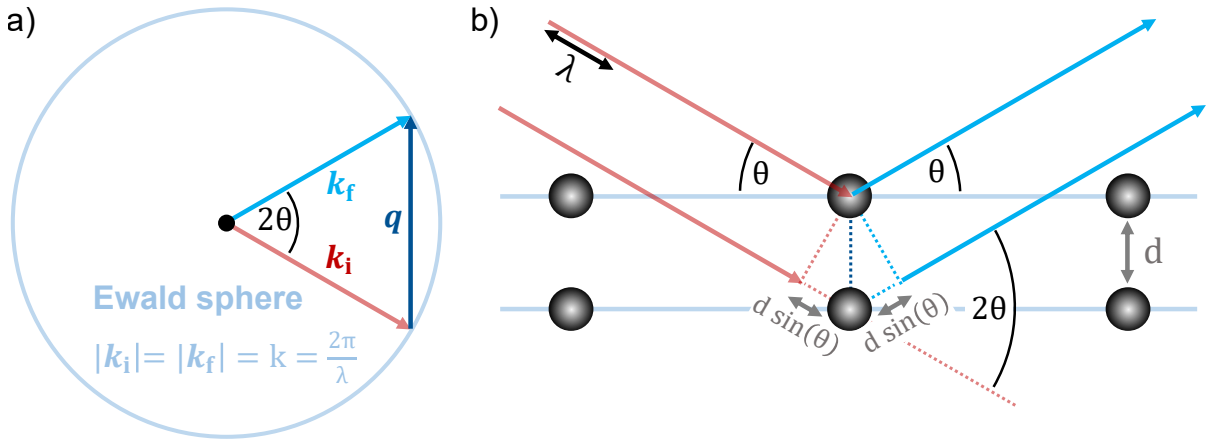

Figure 2.11: Scattering basics. $\mathbf{k}_i$ is the incident/initial wave vector, $\mathbf{k}_f$ is the forthgoing/final wave vector after a scattering event and 2θ is the total scattering angle. a) Elastic condition and Ewald sphere. Here, $\mathbf{q}$ is the momentum transfer $\mathbf{q} = \mathbf{k_f} - \mathbf{k_i}$. b) Illustration of the Bragg condition. Scattering centers (atom electron cloud positions) define lattice planes. The path difference between the two red incoming beams (of the wavefronts) and blue outgoing beams is indicated.

between GISAXS and the phenomena of diffraction and interference at optical slits and gratings, together with a hands-on explanation of the commonly used mathematical approximations.

2.4.1 Elastic Scattering and Reciprocal Space

The scattering theory introduced here is based on elastic scattering. An incident monochromatic and coherent X-ray plane wave creates a time-dependent electrical field at position $\mathbf{r}$ of

$$\mathbf{E}(\mathbf{r}, t) = \mathbf{E}_0 \exp\left[i(\mathbf{k_i}\mathbf{r} - \omega t)\right], \tag{2.24}$$

where $\mathbf{E}_0$ is the amplitude, the exponential describes a propagating wave with wave vector $\mathbf{k}_i$ and the angular frequency ω. Similar to an externally driven and damped oscillator, the external field forces (Coulomb force) electron clouds around atoms to oscillate along the electrical field direction of the incident wave. The oscillation of charges emits dipole emission according to a Hertz dipole (with specific emission characteristics) as a spherical wave. Since the oscillation occurs with the same frequency as the external electromagnetic field, the re-emitted (scattered) wave has the same frequency, hence the same wavelength and wave vector length

$$|\mathbf{k_f}| = |\mathbf{k_i}| = \frac{2\pi}{\lambda}, \tag{2.25}$$

which is the definition of elastic scattering. Here, the momentum transfer is defined as

$$\mathbf{q} = \mathbf{k_f} - \mathbf{k_i}. \tag{2.26}$$

The scattered signal is sensitive to the distribution of the electrons in the material described by the electron density $\rho(\mathbf{r})$. For an ordered crystal structure, the electron density can be defined

as a periodic repetition of the atomic electron density in space (mathematical folding). The scattered intensity is proportional to the squared modulus of the so-called (crystal) structure factor

$$I(\mathbf{q}) \propto |f_{\text{crystal}}(\mathbf{q})|^2, \tag{2.27}$$

where $f_{\text{crystal}}(\mathbf{q})$ is the Fourier transformation of the crystal electron density. Mathematical folding becomes a product in the Fourier transformation. The Fourier transformation of the crystal electron density is the product of the Fourier transformation of the unit cell electron density, and the Fourier transformation of the discrete lattice sum [160]

$$f_{\text{crystal}}(\mathbf{q}) = \underbrace{\sum_{n_1,n_2,n_3} \exp\left[i\mathbf{q}\left(n_1\mathbf{a}_1 + n_2\mathbf{a}_2 + n_3\mathbf{a}_3\right)\right]}_{\text{Lattice sum}} \cdot \underbrace{\int \rho(\mathbf{r}) e^{i\mathbf{q}\mathbf{r}} dV}_{\text{Unit cell structure factor}} \tag{2.28}$$

where ρ the electron density in the unit cell, $n_1, n_2, n_3 \in \mathbb{N}_0$, and $\mathbf{a}_1, \mathbf{a}_2, \mathbf{a}_3$ are the (real space) lattice vectors. The lattice sum contributes to the scattering when terms of different unit cells add up coherently, i.e. when the exponent phase fulfills (see an example in the next subsection):

$$\mathbf{q}\left(n_1\mathbf{a}_1 + n_2\mathbf{a}_2 + n_3\mathbf{a}_3\right) = \text{const.} + 2\pi n, \tag{2.29}$$

where n is an integer. This is achieved when

$$\mathbf{q} = h\mathbf{b}_1 + k\mathbf{b}_2 + l\mathbf{b}_3 \overset{\text{def}}{=} \mathbf{G_{hkl}}, \tag{2.30}$$

where $h, k, l \in \mathbb{N}_0$ are the Miller indices, and $\mathbf{b}_i$ are the reciprocal space (basis) vectors; $\mathbf{G_{hkl}}$ is the reciprocal lattice vector. The reciprocal basis vectors are defined *via* the real space basis vectors as

$$\mathbf{b}_i \overset{\text{def}}{=} \frac{2\pi\, \mathbf{a}_j \times \mathbf{a}_k}{\mathbf{a}_i \cdot (\mathbf{a}_j \times \mathbf{a}_k)}, \tag{2.31}$$

with cyclic permutations of i, j, k. This way they satisfy the relation with the real-space basis vectors

$$\mathbf{b}_i \cdot \mathbf{a}_j = 2\pi\delta_{ij}, \tag{2.32}$$

where the Kronecker delta takes the value $\delta_{ij} = 1$ for $i = j$ and 0 otherwise.

2.4.2 Laue Condition for Constructive Interference

The Laue condition states that there is constructive interference if the spherical waves emitted from different atom positions are in phase at a certain distant point $\mathbf{R}$. In other words, there is constructive interference if, for atom 1 at position $\mathbf{r}_1$ and another atom 2 at position $\mathbf{r}_2$, the phase difference of the emitted waves at a point $\mathbf{R}$ is a multiple of 2π at the same time. Here, we consider the phase shift due to the incident wave and the emitted wave, i.e., the total phase

difference is the sum of both phase shifts. In the case of constructive interference, we then state the phases of atoms 1 and 2 and the phase difference as

$$\begin{aligned}\phi_1 &= \mathbf{k_i}\mathbf{r}_1 + \mathbf{k_f}(\mathbf{R} - \mathbf{r}_1)\\ \phi_2 &= \mathbf{k_i}\mathbf{r}_2 + \mathbf{k_f}(\mathbf{R} - \mathbf{r}_2)\\ \Delta\phi &= \phi_1 - \phi_2 = \mathbf{k_i}\mathbf{r}_1 + \mathbf{k_f}(\mathbf{R} - \mathbf{r}_1) - \mathbf{k_i}\mathbf{r}_2 - \mathbf{k_f}(\mathbf{R} - \mathbf{r}_2)\\ &= \underbrace{(\mathbf{k_f} - \mathbf{k_i})}_{\mathbf{q}}\underbrace{(\mathbf{r}_2 - \mathbf{r}_1)}_{\Delta\mathbf{r}} \overset{!}{=} 2n\pi \text{ with } n \in \mathbb{N}_0,\end{aligned} \tag{2.33}$$

which is independent of $\mathbf{R}$ and only a function of the momentum transfer $\mathbf{q}$ and the relative position of both atoms $\Delta\mathbf{r}$.
For the periodic arrangement of atoms in real space, we can write per construction above $\mathbf{G}\Delta\mathbf{r} = 2n\pi$ for $\Delta\mathbf{r}$ being the vector between two real-space lattice points. Thus, the Laue condition can be written as (cf. [161]):

$$\mathbf{q} = \mathbf{G} \text{ with } |\mathbf{G}| = \frac{2n\pi}{d}, \tag{2.34}$$

where $\mathbf{q}$ is the momentum transfer from incident to final wave vector and d is the real space lattice plane distance.

2.4.3 Equivalence of Laue and Bragg

In Fig.2.11a, the elastic scattering condition is shown that leads to the Ewald sphere [161]. Here, the total scattering angle is defined to be 2θ. For elastic scattering, every possible scattering vector $\mathbf{k}_f$ points onto the surface of the so-called Ewald sphere with radius k. From the triangular relation of the vectors $\mathbf{k}_f = \mathbf{k}_i + \mathbf{q}$ we obtain by squaring the equation

$$\mathbf{k}_f^2 = \mathbf{k}_i^2 + \mathbf{q}^2 + 2\mathbf{k}_i\mathbf{q}. \tag{2.35}$$

Using the elastic condition, $\mathbf{k}_f^2 = \mathbf{k}_i^2$ we yield

$$\mathbf{k}_i\mathbf{q} = -\frac{1}{2}q^2. \tag{2.36}$$

At the same time, making use of the definition of the scalar product

$$\cos(2\theta) = \frac{\mathbf{k}_i\mathbf{k}_f}{|\mathbf{k}_i||\mathbf{k}_f|} = \frac{\mathbf{k}_i(\mathbf{k}_i + \mathbf{q})}{k^2} = 1 + \frac{\mathbf{k}_i\mathbf{q}}{k^2}, \tag{2.37}$$

and rearranging and solving the equation (using the trigonometric identity), we yield

$$\mathbf{k}_i\mathbf{q} = k^2\left[\cos(2\theta) - 1\right] = -2k^2\sin^2\theta. \tag{2.38}$$

We can now combine eq. 2.36 with eq. 2.38 and obtain

$$\begin{aligned}\frac{1}{2}q^2 &= 2k^2\sin^2\theta\\ q &= 2k\sin\theta\\ &= \frac{4\pi}{\lambda}\sin\theta.\end{aligned} \tag{2.39}$$

By making use of the scalar Laue condition ($q = 2n\pi/d$) we get

$$\begin{aligned} \frac{2n\pi}{d} &= \frac{4\pi}{\lambda}\sin\theta \\ n\lambda &= 2d\sin\theta, \end{aligned} \tag{2.40}$$

the Bragg equation [163]. So what happened? We showed equality of the requirement of phase matching (Laue) and the requirement of path length differences to be multiples of the wavelength, where the latter is the assumption for the classical way of deriving Bragg's equation from Fig. 2.11b, where parallel planes cause are envisioned to cause specular reflections [160]. This equality shall help to simplify considerations because a certain perspective in reciprocal space (Laue) has its equivalent in real space (Bragg). Both pictures must lead to the same conclusion, which can be used to cross-check considerations.

2.4.4 Getting the Geometry Right

In Fig. 2.12, a rich schematic drawing contains all geometrical information to understand the measurement principles of (Bragg-Brentano) X-Ray Diffraction and GIWAXS. Scattered information of the sample is naturally presented in reciprocal space. A natural choice of the sample's coordinate system uses the sample plane normal that defines the q_z-direction. The q_x- and

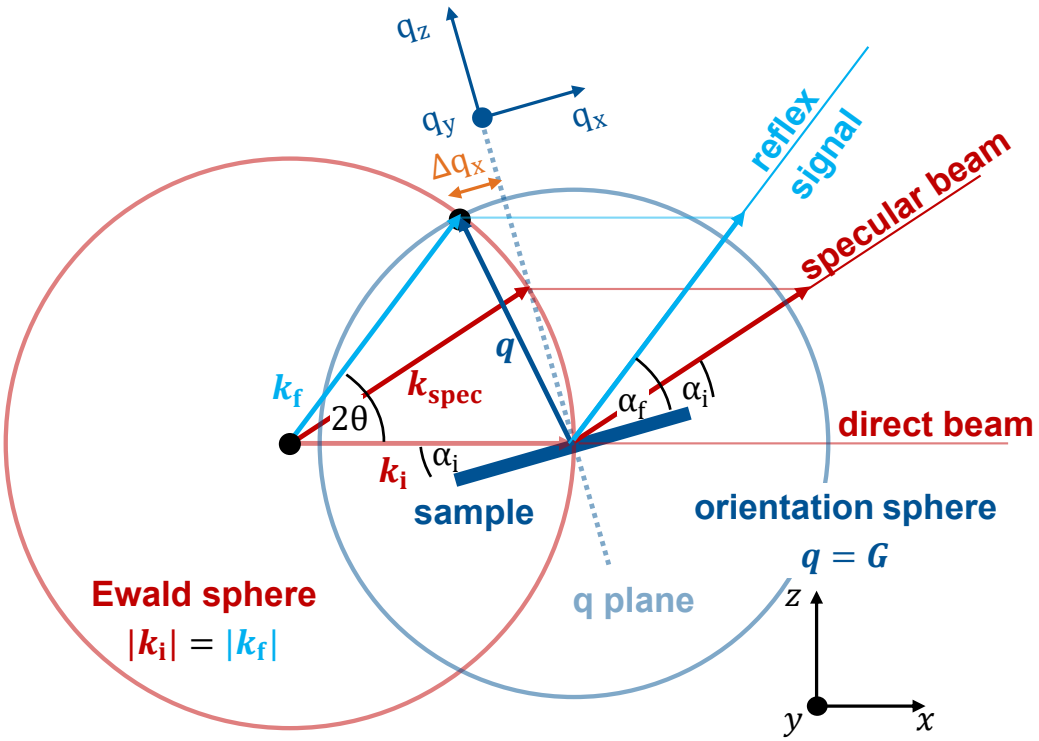

Figure 2.12: Scattering geometry for thin-film samples with extensive angular and coordinate definitions. It shows a cut along the plane defined by the sample normal and incident beam direction (the scattering plane, $\phi = 0$). A detailed explanation can be found in the text.

q_y-direction are in the sample plane, and due to the sample symmetry, their azimuth angle is arbitrary but, per convention, rotated in a way around q_z that q_x points along (along, the beam is not parallel to q_x – see below or in Fig. 2.12) the direct beam direction.

The geometry is briefly explained by following the beam path. The incident (direct) X-ray beam travels along the (real-space) x-coordinate direction (labeled with $\mathbf{k_i}$). The sample is tilted relatively to the incident angle by α_i. Also, the reciprocal space coordinate system is rotated by α_i with respect to the real-space coordinate system. The direct beam hits the sample on the surface, where we locate the origin of the reciprocal space coordinate system, which is translated along q_z in Fig. 2.12 for clarity of the drawing. Specular sample reflection (exit-angle equals incident angle) is indicated with $\mathbf{k}_{\text{spec}}$ and from the drawing, one can see that $\mathbf{q}_{\text{spec}} || \hat{e}_{q_z}$, i.e., the momentum transfer for the specular beam is purely in q_z-direction (see also the vector parallelogram). These definitions hold for the scattering geometries used for XRD and GIWAXS explained in the following paragraphs.

2.4.5 X-Ray Diffraction

Classical X-ray diffraction (XRD) is a standard tool for quick phase analysis of crystalline materials. One of the most common measurement configurations for thin films is the so-called Bragg-Brentano geometry, where the incident X-ray beam impinges under an angle Θ. At the same time, the point detector is tilted similarly with Θ relative to the sample surface plane (total scattering angle 2Θ). This geometry is shown in Fig. 2.13. Using the same angle for

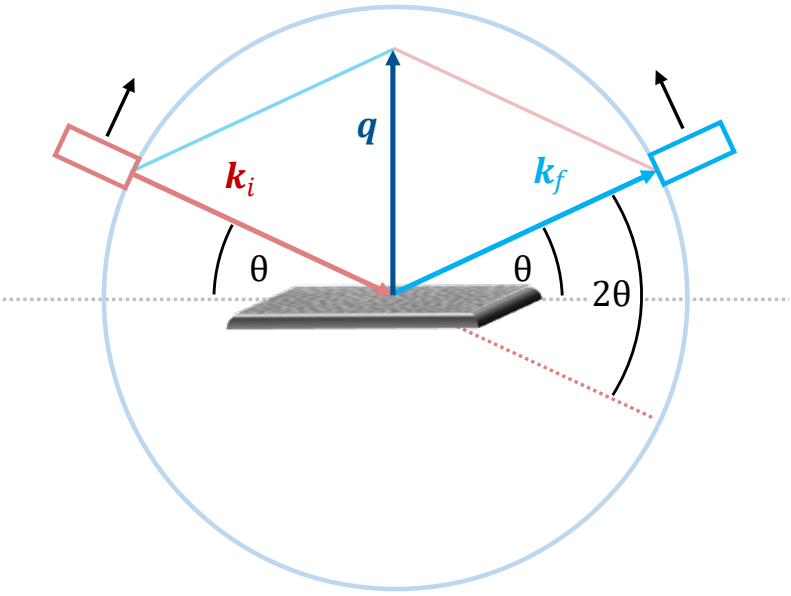

Figure 2.13: Geometry for (Bragg-Brentano) X-ray diffraction experiments. Measurements are performed in the local-specular condition, i.e. the incident angle of and the exit angle of the scattered signal that is registered (frequently by a point detector) are equal. Hence, only momentum transfer along the sample normal is probed. By varying θ, the q_z-range is probed.

the source and detector means the measurement is carried out in the local specular condition. The momentum transfer is purely in the q_z direction, meaning that only the part of the sample contributes to the signal where crystal lattice planes are parallel to the substrate. In a typical measurement, the X-ray source and the detector are simultaneously moved upwards along the circle indicated in Fig. 2.13, maintaining the symmetric position relative to the sample while increasing Θ. Consequently, scanning along increasing Θ corresponds to scanning along increasing momentum transfers q_z.

Here, a short paragraph shall summarize some possibilities for the interpretation of the crystallographic scattering data. Based on the momentum transfer where crystallographic reflexes occur, crystal lattices and thereof crystal phases can be identified [164]. Finite crystal size gives rise to a line broadening of the reflex, independent of instrumental broadening, that can be used to for crystal size quantification [165]. Using the entire diffractogram, Rietveld refinement can be used to quantify phases, quantify crystal sizes, and also deduce crystal (micro) strain in so-called Williamson-Hall plots [161, 166]. To a certain extent, grain size analysis can be adapted to grazing-incidence scattering with area detectors that will be introduced in the next paragraph [167].

2.4.6 Grazing-Incidence Wide-Angle X-Ray Scattering

GIWAXS is a powerful technique used to investigate the crystalline structure and molecular orientation in thin films. It is similar to XRD, probing parts of the reciprocal space (see Fig. 2.16), but it utilizes a two-dimensional detector to collect multiple Bragg reflexes from (poly-)crystalline samples in a single exposure frame. The typical grazing-incidence geometry (same for GISAXS) can be seen in Fig. 2.14. Each reflex contains valuable crystallographic information that can be analyzed to quantify the molecular or crystalline preferred orientation (texture). In terms of the orientation sphere, GIWAXS probes the entire orientation sphere volume intersecting with the Ewald sphere surface within a single measurement. However, the inaccessible region in Fig. 2.16 on the right side of pure q_z cannot be probed (as explained above), making XRD and GIWAXS excellent complementary tools. GIWAXS single frame acquisition times go down below 0.1 s at brilliant synchrotron sources, offering the unique opportunity to investigate fast processes. This can be done in real time by following e.g. the perovskite phase formation during deposition or annealing or degradation and crystal growth or ordering [43, 123].

We can read the momentum transfer vector from Fig. 2.12 and Fig. 2.14 to find

$$\mathbf{q} = \mathbf{k_f} - \mathbf{k_i} = \frac{2\pi}{\lambda} \begin{pmatrix} \cos\alpha_f \, \cos\phi - \cos\alpha_i \\ \cos\alpha_f \, \sin\phi \\ \sin\alpha_i + \sin\alpha_f \end{pmatrix}, \tag{2.41}$$

where ϕ is the out-of-scattering plane angle. Fig. 2.12 shows the plane for slicing at $\phi = 0$. Strictly right-handed coordinate systems are used in this work. Using left-handed coordinate systems is equivalent to a change of the sign of q_y, mirroring the scattering pattern, but does not

change the underlying physics creating the pattern (due to sample symmetry – in-plane powder).[5] Historically, the introduction of left-handed systems evolved from the desire to draw the q_y-direction towards the right side of the detector as usual for GISAXS, likely adding confusion to the already complex geometry [168, 169].

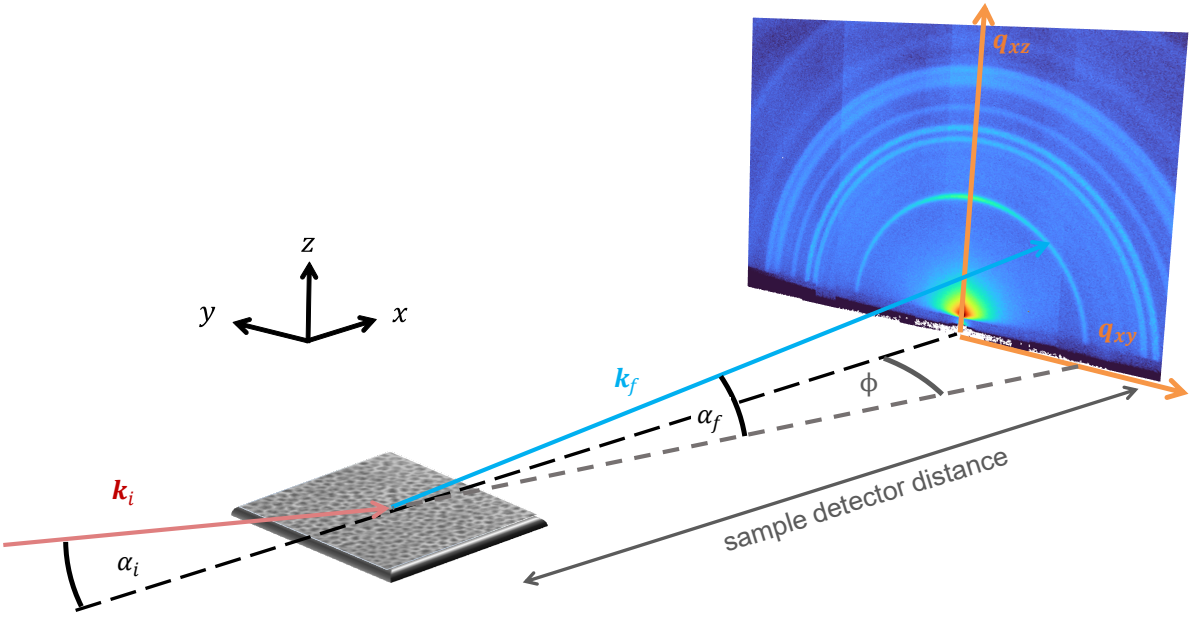

Figure 2.14: Sketch of the geometry for GIWAXS and GISAXS experiments. The X-ray beam hits the sample at a shallow incident angle and the scattered signal is detected by a 2-D detector. In this particular figure, the detector pattern was collected in a simultaneous GISAXS/GIWAXS measurement mode, where simultaneously the Scherrer- or Bragg crystal rings of wide-angle scattering and the central bright Yoneda region of diffuse small-angle scattering could be collected due to the choice of intermediate sample detector distance and high spatial resolution of the detector used. The left-right detector pattern was folded with INSIGHT to cover detector gaps [170]. The rich detector image is a courtesy of Julian E. Heger.

2.4.7 Concept of the Orientation Sphere

The so-called orientation sphere used to describe the crystallographic information of the investigated sample is shown in Fig. 2.12 with the origin of the reciprocal space coordinate system as the center. We consider the surface of the sphere only, containing the orientation information for a specific (hkl) reflex (the reflex momentum transfer is the radius of the sphere). The entire orientation sphere volume comprises the information of all reflexes that are inside, i.e. for smaller momentum transfers. For a powder, reflexes can occur in any direction because there will 'always' be a single crystallite oriented in a way to fulfill the scattering condition (see also [171] for additional information). Possible momentum transfers that fulfill the Laue

[5] Keeping the q_z-direction parallel with the sample normal and requiring q_y-direction towards the right side would require q_x to point away from the detector. This is physically not meaningful since then scattering out of the beam would *increase* the value of q_x.

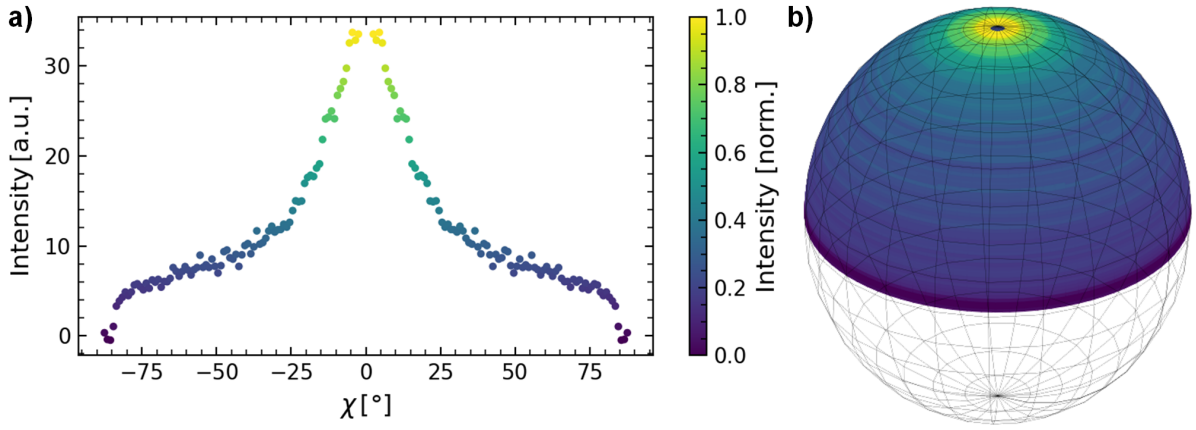

Figure 2.15: Illustration of the orientation sphere. a) a radially integrated azimuthal GIWAXS line cut after local background subtraction (cf. Section 3.3.1, Fig. 3.7) with a perceptively uniform color code in linear scale. For a 2-D powder, the line cut probes parts of the orientation sphere and can be used for reconstructing the orientation sphere surface b) of the reflex. Note that the missing wedge creates an open region at the polar region, which only covers a negligible fraction of the entire surface of the orientation sphere. Also, the strong face-on texture seen in the strong peak in a) only covers a tiny region of the entire sphere - illustrating the concept behind the Lorentz factor for pole figure representation (see text).

condition $|\mathbf{q}| = |\mathbf{G}_{\mathrm{hkl}}|$ of a certain (hkl) reflex point onto the orientation sphere surface and give rise to scattering of the corresponding lattice planes.[6] The word 'orientation' here signifies that for this reflex, the preferred orientation (also called texture) of corresponding lattice planes can be quantified later by analyzing the reflex intensities in different directions (i.e., on different sphere locations). Measuring the intensity distribution of the spherical surface, one can deduce the orientation distribution of all crystallites that contribute to this specific reflex. For the presented scattering geometry in Fig. 2.12, however, we cannot access the total orientation sphere with this single measurement: For the emergence of reflex signal, the momentum transfer needs to point on the Ewald sphere (elastic condition) and orientation sphere (Laue condition) simultaneously. Hence, for fixed scattering geometry as in GIWAXS, we can only detect signals for the intersection of both sphere surfaces, that is, geometrically, a ring in reciprocal space (origin of Scherrer rings). In the sliced representation Fig. 2.12, this ring is reduced to two points where the two circles intersect. The signal of an exit ray $\mathbf{k}_f$ (2Θ exit angle relative to the incident angle) probes the orientation sphere at the upper intersection point. We can calculate the components of $\mathbf{q}$ by using Eq. 2.41, i.e., deduce the reciprocal coordinates from the real space angles.

[6] Note that for a single crystal, the Laue condition is stated in a vectorial way since we observe a discrete reflex in a specific direction. For a crystal powder, the same reflex occurs in multiple directions simultaneously, the scalar notation is used.

2.4.8 What are In-Plane Powders?

After introducing the requirements for constructive scattering and the typical geometries used, we can move the attention to the actual interpretation of the scattered signal. Before that, the definition of the so-called in-plane powder shall be clarified [172]. Powders are considered to consist of randomly, hence isotropically, oriented crystals and thus show a rotational invariance for any rotation angle around arbitrary rotation axes – the scattered information is supposed to be independent of sample orientation [173]. This has been historically used by the Debye-Scherrer method [174].[7] In that case, a specific reflex results in an ideal ring of scattered signal on a flat 2-D detector behind the sample. Statistically, an equal number of constructive scatterers (crystallites) are oriented in each direction, giving rise (if fulfilling the scattering condition) to an equally strong scattered signal along the ring. In this case, the scattering pattern is independent of the orientation of the isotropic powder.

This, however, does not hold for samples that are thin films. For thin films, a variation of the incident X-rays' incident angle typically changes the species of crystallites that are perceptible to create scattering. At the same time, a rotation of the thin film around its plane-normal direction as the rotation axis does not change the scattering pattern. This means it is not a 3-D powder (as pure powder samples are) but a 2-D powder with reduced symmetry. Here, the expression "in-plane" indicates that any in-plane rotation (that does not alter the plane inclination) does not change the scattered information. The term in-plane powder is used for thin-film samples that fulfill this reduced symmetry. This is typically true for films grown without a preferential in-plane direction, such as spin-coated films. Any in-plane rotation does not influence the crystal distribution and, consequently, the expected scattering pattern since the statistical crystallite distribution is invariant under azimuthal rotations. In fair approximation, also (vertically) sprayed and printed films behave as in-plane powders. In contrast, lithographic, epitaxially-grown, and sputtered films might show a rotational dependence on the scattered information. In the case of asymmetric effects acting on the sample, e.g., by establishing a directed gradient during processing, they are no in-plane powders since the powder aligns somehow in a direction – the scattering pattern is subjected to changes upon in-plane rotations.

As an important note, distinguishing between a 3-D (isotropic powder) and 2-D (in-plane powder) symmetric sample does not infer anything about texture, i.e., preferential orientation in the sample. To understand the difference, we can imagine a set of cubes or dice in a Gedanken-experiment:

- **3-D powder**: We hold the randomly oriented cubes in our hands. They will be distributed randomly, some face-on, some edge-on, some corner-on. We will always find cubes with a specific orientation. No matter from which point we inspect the cubes, their ensemble looks statistically the same.
- **isotropic 2-D powder**: We let the cubes fall onto a *lawn*. They will be distributed randomly, some face-on, some edge on some corner on. We will always find cubes with a

[7] Link to the original publication, accessed 30.07.2023.

specific orientation. No matter from which side (walking around the cubes, watching from a certain fixed height) we inspect them, their ensemble looks statistically the same. If we bend down and investigate the ensemble from a lower height, the ensemble still looks the same. It is a powder confined to a plane.

- **2-D powder with preferential orientation**: We let the cubes fall onto *flat* ground. They will be distributed randomly, but all lie on the ground face-on (preferential orientation). No matter from which side (walking around the cubes, watching from a certain fixed height) we inspect them, their ensemble looks statistically the same - it still is a 2-D powder. If we bend down, the ensemble looks different - the side faces become better visible, but the top face becomes less. This is the result of having the preferred face-on orientation of the cubes.
- **no 2-D powder**: We let the cubes fall onto a *grooved* floor. They will be arranged somewhat aligned with their edges parallel to the grooves. Now we walk around the cubes, and their arrangement will change with our relative orientation to the grooves. Also, bending down changes the appearance - no symmetry that we can use here is present anymore!

Now, the powder ensembles with different symmetries can be related to the implications for the orientation sphere. For a 3-D powder, the crystal orientation inside the powder is isotropic. We can assign a constant value (proportional to the number of crystal unit cells oriented in the respective direction) for the entire orientation sphere surface (a single reflex). Thus a single measurement of any direction $\mathbf{k}_f$ pointing on the orientation sphere surface is sufficient to probe the entire surface. The same constant surface value of the orientation sphere holds for an isotropic 2-D (in-plane) powder. Still, to extract material quantities using pole figures and quantification (shown below), more concepts are required. For a non-isotropic 2-D powder, the orientation sphere surface value is a function of latitude. As discussed above, the azimuthal rotations of the sample (and the orientation sphere that rotates with the sample) make no difference due to the rotational symmetry around qz. Therefore, we need a measurement for each latitude to reconstruct the entire orientation sphere surface. For completeness, for specific samples without 2-D powder symmetry (see above or imagine a single crystal without special symmetry), we need to map the orientation sphere completely to obtain the complete crystallographic orientation information for a single reflex.

2.4.9 In-Plane Powders Empower $\mathbf{q_r}$

For 2-D powders, we can use the azimuthal symmetry of the orientation sphere - there is an equivalence of q_x and q_y. Mathematically speaking, we construct one orthogonal direction to q_z that contains the total in-plane distance from the origin,

$$q_r = \pm\sqrt{q_x^2 + q_y^2} \tag{2.42}$$

where we explicitly make use of the in-plane symmetry. Here, a short explanation of the $\pm$ sign is given. In literature, the $+$ sign is usually used, and then $q_r > 0$ is a natural consequence of non-zero q_x. To be more precise here, a non-zero q_x implies $|q_r| > 0$, where $q_r < 0$ is certainly allowed. However, the negative q_r-branch contains the same information due to symmetry. What we effectively do here is to collapse the 3-D orientation sphere volume to a 2-D plane without loss of information. This 2-D plane can be visualized in Fig. 2.12, called 'q plane' (in GIWAXS, this is sometimes called q map or q_r-q_z plane). We can think of an in-plane rotation where all momentum transfer vectors $\mathbf{q}$ pointing on the sphere surface of the sphere are rotated around q_z into the q plane. In contrast to a simple but (physically) wrong projection, this coordinate transformation conserves the in-plane length of $\mathbf{q}$. This 'folding' of the orientation sphere onto the q plane also gives rise to the well-known missing wedge seen on the latter.

2.4.10 Curved Detectors Don't Help

In Fig. 2.12 one can see that a specific momentum transfer in the q_x direction is attributed to this reflex signal. This non-zero q_x is true for any possible direction $\mathbf{k}_f$ except for the direct beam (no momentum transfer) and the specular beam (only transfer in q_z-direction). With the new representation by constructing the q_r-q_z plane, we realize that non-zero q_x determines non-zero q_r according to eq. 2.42. This creates an inner inaccessible region of small q_r, except for the direct- and specular beam, unique points where $q_r = 0$ holds. This is the reason for the so-called missing wedge above the specular beam and additionally for the missing eye[8] that is present in addition between the direct- and specular beam (for $\alpha_i \neq 0$ obviously). In Fig. 2.16, the accessible region is shown on the right GIWAXS image. It is important to highlight that this inaccessible region is not the result of "not having a curved detector", but it is a result of mapping a 3D sphere volume onto a 2D surface in reciprocal space for representative purposes under conservation of the length of the momentum transfer $\mathbf{q}$ according to Equation 2.42. One can think of it similarly as for the interrupted Goode homolosine world map with an equal-area property that made possible "cutting" the map like an "orange peel" [175].[9]

2.4.11 Calculating the Missing Wedge

Here, the missing wedge is calculated, specifically the functional relationship of q_r and q_z along the wedge. Using the freshly introduced coordinate $q_r = \pm(\cos\alpha_f - \cos\alpha_i)$ (combining Eq. 2.42 and Eq. 2.41), we can write

$$\begin{pmatrix} q_r \\ q_z \end{pmatrix} = \frac{2\pi}{\lambda} \begin{pmatrix} \pm(\cos\alpha_f - \cos\alpha_i) \\ \sin\alpha_i + \sin\alpha_f \end{pmatrix} = \underbrace{\frac{2\pi}{\lambda} \begin{pmatrix} \mp\cos\alpha_i \\ \sin\alpha_i \end{pmatrix}}_{\text{const.}} + \underbrace{\frac{2\pi}{\lambda} \begin{pmatrix} \pm\cos\alpha_f \\ \sin\alpha_f \end{pmatrix}}_{\text{(Ewald) sphere}} \tag{2.43}$$

[8] Despite an extensive literature research the description of the central missing region or a specific name for it could not be found.

[9] Due to geometric and attenuation effects, the intensities of the scattered signal require a correction that is discussed in detail elsewhere [104, 172, 176].

where we can identify the second term as a circle (Ewald sphere) in the q_r-q_z map (parametrized with α_f) with the first term being a constant (center of the circle). By bringing the constant to the left side and building the square norm, we retrieve

$$\left(q_r \pm \frac{2\pi}{\lambda}\cos\alpha_i\right)^2 + \left(q_z - \frac{2\pi}{\lambda}\sin\alpha_i\right)^2 = \left(\frac{2\pi}{\lambda}\right)^2. \tag{2.44}$$

Solving for q_z we can express it as a function of q_r for fixed λ, α_i.

$$q_z = \frac{2\pi}{\lambda}\sin\alpha_i \pm \sqrt{\left(\frac{2\pi}{\lambda}\right)^2 - \left(q_r \pm \frac{2\pi}{\lambda}\cos\alpha_i\right)^2}, \tag{2.45}$$

which describes the functional dependence of the missing wedge border seen in Fig. 2.16. For the special case $\alpha_i = 0$ it reduces to

$$q_z = \pm\sqrt{\left(\frac{2\pi}{\lambda}\right)^2 - \left(q_r \pm \frac{2\pi}{\lambda}\right)^2}, \tag{2.46}$$

i.e. two circles around $(\pm 2\pi/\lambda|0)$ with radius $2\pi/\lambda$ that touch each other at the direct beam $(0|0)$. Every scattering vector $\mathbf{q}$ with a non-zero q_y component lies inside the circles above, filling their area. For non-zero α_i, the circle centers move vertically and towards each other, maintaining the direct beam point as one intersection point and the specular beam as the second intersection point. The new region between these two points, enclosed by both circles (missing eye) is not accessible due to non-zero q_x. A way to geometrically think of the transformation is the following in Fig. 2.12: The rotation of the q-vector pointing to the Ewald sphere surface into the q-plane around the q_z-axes naturally creates the inaccessible regions of missing wedge and missing eye. In other words – the missing wedge and missing eye region directly show the curvature of the Ewald sphere. For highly oriented samples with a strong reflex peak inside the missing wedge, the peak information is not accessible. However, by measuring at different incident angles, the information can be reconstructed [171].

Alternatively, X-ray diffraction can be used to obtain the missing information as a complementary measurement. In XRD in Bragg-Brentano geometry (local specular condition, q_z probed), the orientation sphere is probed at its north pole, and scanning Θ corresponds to the vertical slab in Fig. 2.16 on the left side.[10] With Θ, q_z increases, and gradually larger orientation spheres are probed.

2.4.12 Lorentz Factor for Pole Figure Representation

In the past, there has been plenty of confusion about the Lorentz 'correction' of thin film 2-D powder scattering [178]. First, it should be emphasized that it should *never* be called Lorentz 'correction' because the word correction implies an error or effect that needs to be corrected. In contrast to the typical corrections on the way to reshaped GIWAXS q-maps where physical

[10] Note that non-zero beam divergence, nonideal monochromaticity, and other effects that can be subsumed as instrumental broadening smear out the theoretically infinitesimally thin vertical line in the q plane [177].

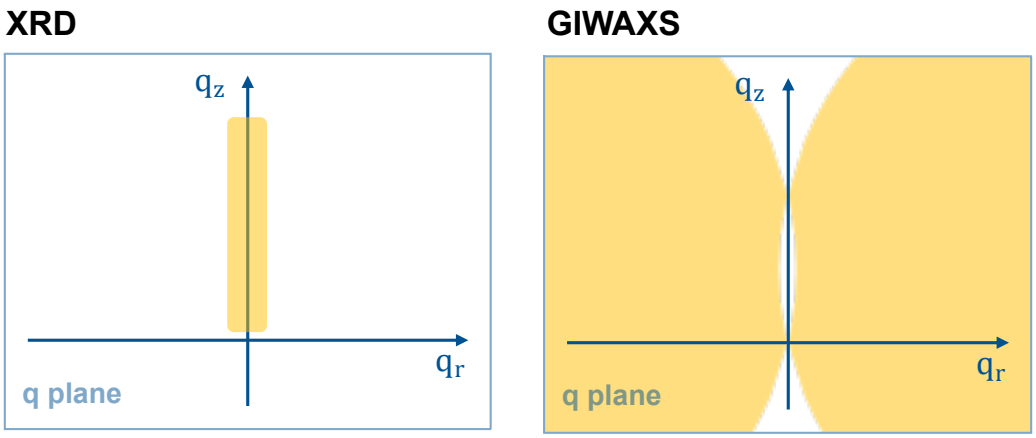

Figure 2.16: Sketch of the accessible region for X-ray diffraction measurements in the Bragg-Brentano (scanning θ in local specular condition) geometry on the left and for GIWAXS measurements (fixed geometry) on the right. Note that the signal with $q_r = 0$ in GIWAXS is only accessible at the direct beam in the origin and at the specular beam, with the missing eye between them and the missing wedges outside of these two special points. The pattern on the right is the pedant to the Ewald sphere intersecting the q-plane in Fig. 2.12 with left-right symmetry and thus determined by wavelength and incident angle.

effects require "corrections", the Lorentz factor is used for a specific representation.[11] Thus, we should better speak about the Lorentz factor used for the pole figure representation of radially integrated azimuthal (tube) cuts [171]. For using the Lorentz factor the presence of 2-D powders is required!

Likely, most of the confusion about the Lorentz factor ($\sin(\chi)$) stems from the resulting multiplication with zero at $\chi = 0°$. The quick but false conclusion is that there are no crystallites oriented in this face-on (for cubic systems) orientation because the resulting pole figure shows a value of 0. Another question is why multiply isotropic scattering data with a 'correction' – then it does not appear isotropic anymore. The following paragraph tries to explain the correct reasoning.

A pole figure is a specific representation of the orientation sphere to move from showing the scattering intensity (from the q-maps extracted radially integrated azimuthal tube cut) to quantifying the crystal material in the sample of a specific orientation. For details of the concept of the orientation sphere, see above. An isotropically oriented crystalline sample (a 2-D powder with randomized crystal orientation) is characterized by an orientation sphere with the same intensity all over its surface. When we collect a GIWAXS pattern of such a sample and show the q_r-q_z intensity maps, we find a ring of constant intensity for all χ-angles. So why should we now multiply this constant with a sine, and why should the material quantity be zero at $\chi = 0°$? The counter-question is: How much area of the sphere surface can we find at a certain infinitesimal $d\chi$ at the angle χ? Or in other words, how does the circumference of our spherical surface scale with latitude? The answer for this is 'with $\sin(\chi)$' as it is for classical integration in spherical coordinate systems: To account for the change of the size of the infinitesimal volume

[11] It is not the Lorentz factor of special relativity meant here.

integration element, this scaling factor is introduced (it is the Jacobian determinant of a unit sphere). Neither the scattered intensity is zero at $\chi = 0°$, nor the number of crystals is zero, but the area of the orientation sphere surface at the north pole becomes zero (which remains zero for finite values on the orientation sphere).

To put this into context with an illustrative analogy: Imagine Earth from far away in space. Earth has a thin shell of isotropic atmosphere, and in projection, we see a ring of atmosphere of equal thickness everywhere, at the equator, similarly as at the north pole. We now ask for the distribution of the atmosphere as a function of Earth's latitude. Obviously, in equatorial regions (e.g. from the equator to 20° north) there is a large fraction of Earth's atmosphere while there is a small fraction in the polar region (e.g. 70°-90° north), simply because there is much more surface area closer to the equator. Please refer also to Fig. 2.15 for an illustration of this effect. We can state that most of Earth's atmosphere is located in equatorial regions and only a few in polar regions, despite having an isotropic atmosphere. Similarly only probe a ring of the entire orientation sphere (cf. Fig. 2.12 and see also [173] for a short discussion in the Supplemental Information therein).

Another important message is that any texture, i.e., any oriented signal that comes on top of an isotropic signal in tube cuts, cannot be interpreted in terms of crystallite number compared to crystallites creating the isotropic signal without using pole figures. For example, a strong peak in the region around $X = 0°$ does not relate to a high content of crystallites with this specific orientation (small Lorentz weight). Vice-versa, even weak peaks at large X-angles result from a significant quantity of crystallites with that orientation (large Lorentz weight).

2.4.13 Effective Beam-Direction Correction

For transmission experiments such as WAXS or SAXS and for powder-XRD measurements, the scattered signal is commonly interpreted by its angle or q-value relative to the direct beam, where multiple scattering events are not treated in the first order (Born) approximation. For GISAXS and GIWAXS however, the incident beam penetrates the film at angles close to or similar to the critical angle of the materials. Especially for the analysis of reflexes at small q-values, i.e. of small deflection angles, effects of refraction inside the probed volume and reflection at the substrate-film interface are considered to improve the quality of data treatment. This is done for GISAXS in the framework of the distorted-wave Born approximation. For GIWAXS, usually, there is no correction done but assumed that the direct beam travels unaltered inside the probed material and all scattered signal is scattered off the direct beam. However, in the following, different typical scenarios, their implications for later data treatment, and how the precision and quality of GIWAXS analysis can be augmented with the effective beam-direction correction are discussed.

In the schematic drawing in Fig.2.17, the X-ray beam path is shown for an exaggerated incident angle and a material critical angle for making the effects visible. Usually, we use the simplification of the direct beam simply penetrating the sample in a straight way without

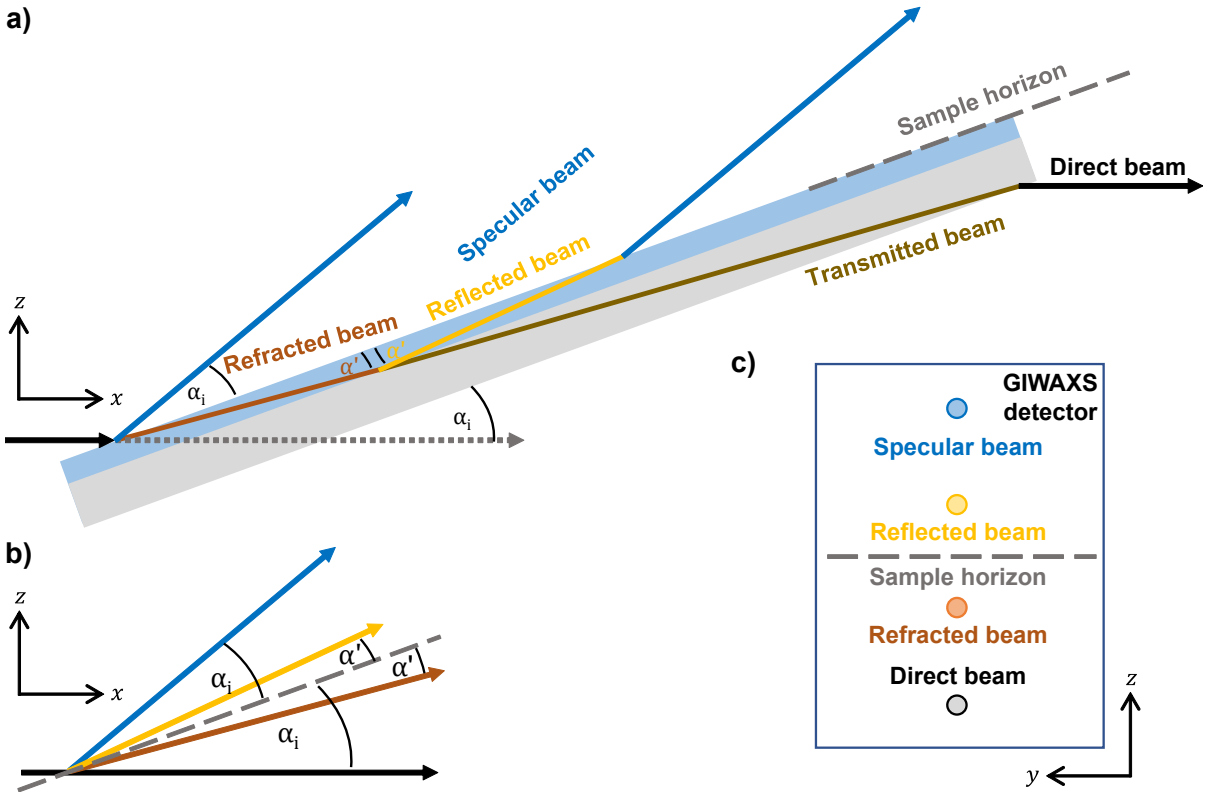

Figure 2.17: Schematic illustration of the special directions during a grazing-incidence experiment relevant for the wide-angle scattering (within the Born-approximation). a) The direct beam gets partially reflected (specular beam) and refracted (refracted beam) into the thin film (blue layer) that should be probed. Reflection (yellow) on the substrate (gray layer) leads to outcoupling back in the direction of the specular beam. b) Summary of the four special directions, symmetrically arranged around the horizon (dashed). The lateral shift can usually be neglected and effectively only the different beam directions matter as seen in c) where the directions of pointing of the different parts of the beam are shown. Note that the (substrate) reflected and refracted beam travel in the material in the indicated directions but do usually not appear on the detector.

considering any refraction and thus without considering a lateral (z-direction) shift of the direct beam position. This neglection of the lateral direction can be made safely, since for a typical substrate of 1 mm-thickness the lateral shift is not more than substrate thickness and thus amounts to few pixels, usually still well covered within the direct beam stop.

Considering the optical path of the direct beam, it is first transmitted from air/vacuum $n = 1$ to the material with $n' = 1-\delta+i\beta$ with $\delta, \beta \ll 1$ where usually $\beta \ll \delta$ (β is related to absorption in the complex refractive index). In this case, Snellius' law states that [160]

$$n_i \sin\gamma_i = n' \sin\gamma' \tag{2.47}$$

where the incident and transmitted angles γ_i, γ' are defined with respect to the interface normal. This becomes, by using the complementary angles α and $\cos\alpha = \sin(\alpha - 90°)$ and using $n_i = 1$,

$$1\cos\alpha_i = (1-\delta+i\beta)\cos\alpha'. \tag{2.48}$$

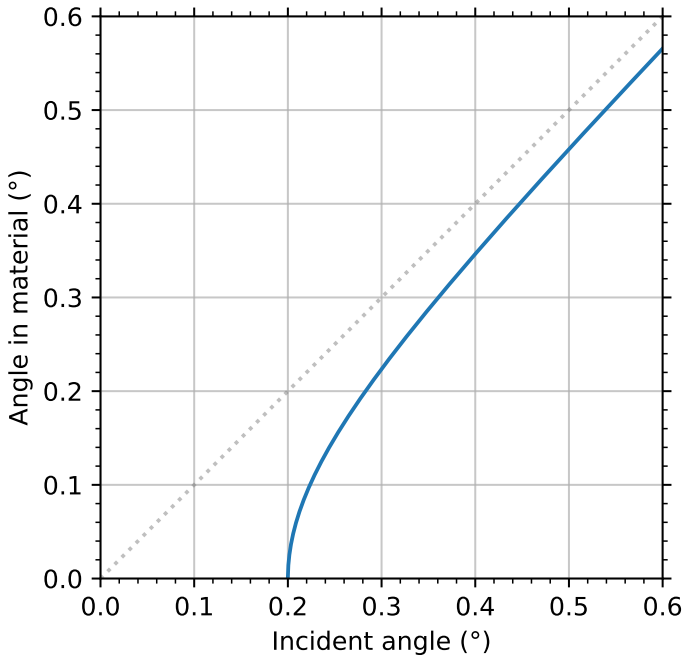

Figure 2.18: The transmitted angle in the material as a function of the incident angle for a material critical angle of 0.2° according to Eq. 2.50 as a blue line. The grey dashed line shows the equality of the incident and transmitted angle, which is the usually implicitly used approximation that breaks down when the incident angle approaches the critical angle.

Using the Taylor expansion for small angles, $\cos x \approx 1 - \frac{x^2}{2}$, this becomes

$$1 - \frac{\alpha_i^2}{2} = (1 - \delta + i\beta)\left(1 - \frac{\alpha'^2}{2}\right) \tag{2.49}$$

which can be solved for the transmitted angle neglecting higher order terms, yielding

$$\alpha' = \sqrt{\alpha_i^2 - \underbrace{2\delta}_{\alpha_{\text{crit}}^2} + 2i\beta}. \tag{2.50}$$

Assuming absorption to be small, which is usually ensured when probing away from elemental X-ray absorption edges, β can be omitted, and we see that the transmitted angle in the film is a hyperbolic function of the incident angle and thus below $\alpha_i - \alpha_{\text{crit}}$. We can also see that for incident angles approaching the material-specific critical angle, the transmitted beam angle approaches zero, i.e. the beam travels parallel to the thin film surface direction. As a note, with β in Eq. 2.50 the the penetration depth of the evanescent wave can be derived for surface-sensitive measurements with the incident beam impinging below the critical angle [179, 180]. In Fig. 2.18, the transmitted angle is plotted versus the incident angle for a critical angle of 0.2°, which is a typical magnitude for the critical angle that depends on the materials used and the X-ray wavelength. For incident angles only slightly larger than the material critical angle,

the transmitted angle in the film is very low, i.e., the beam travels close to parallel to the film. Besides obvious implications for the penetration depth, which is covered in detail in other works (see e.g. [179, 180]), here the implications for the resulting scattering of the crystalline phase in the film are pointed out. Similar as for the Debye-Scherrer principle where one always assumes to find crystals in the "right" orientation to give rise to constructive diffraction fulfilling Bragg's law, we should consider the refracted beam as the principal direction from which the scattering of the beam originates. In other words, the center of the Bragg reflex rings is not the direct beam but the refracted beam in red in Fig. 2.17. The deviation of the transmitted beam direction from the direct beam direction is just a few centigrades for the incident angle fairly above the critical angle, i.e. for example, for an incident angle of 0.4° (see Fig. 2.18). However, when measuring close to the critical angle this effect becomes more pronounced and one might want to take it into account during data analysis by setting the cut-center 'somewhat' (see below) above the direct beam. In literature, an approach of modeling the transmitted and the reflected beam, the 'two-beam approximation' had been used earlier for simulating Grazing-Incidence X-ray Diffraction patterns [181].

It becomes even more complex when measuring materials with a lower critical angle than their substrate, such as an organic film on a piece of a silicon wafer. Here, to maximize the scattered signal, one wants to use an incident angle above the critical angle of the thin film but below the critical angle of the substrate to maximize the reflected signal off the substrate (dynamic regime) [182]. In this case, the reflected beam has an intensity of similar magnitude to the refracted beam (apart from reflection and absorption losses). Hence, the GIWAXS signal originates from both refracted and reflected beams with similar intensities, shifting the effective beam direction further upwards. If there were no losses of the reflected beam, the vertical height of the sample horizon should be the correct choice for the effective cut center (cf. Fig. 2.17). However, in reality, one will need to adjust the cut center to be placed between the refracted beam and the sample horizon because the relative strength of the refracted and reflected beam is not known and is hard to estimate.[12]

So how to include this entire reasoning in the data analysis? First, calculate the q_z value of the transmitted beam and the horizon. Second, optimize the cut center directly using the scattering data that are to be analyzed. Third, plausibility check the present scenario and its consequences on the effective beam direction by comparing it with the calculations from the first step. For example, Fig. 2.19 shows the innermost region of the $q_r - q_z$ map of a crystalline thin polymer film on top of a silicon wafer. The crystalline signal at $q \approx 0.3\text{Å}^{-1}$ forms a ring that is superimposed with the smeared vertical signal of the Yoneda region (see below). The incident angle of 0.11 ° is slightly above the polymer critical angle but below the substrate critical angle, i.e. the measurement is performed in the dynamic regime. Two cuts are shown, one for the direct beam as the cut center, and one for the cut center shifted upwards to the horizon. Focusing on the right side of the cut, clearly, the cut around the direct beam shows an offset

[12]The cut center cannot be adjusted in the current version of GIXSGUI (1.7.3) [172], but in INSIGHT.

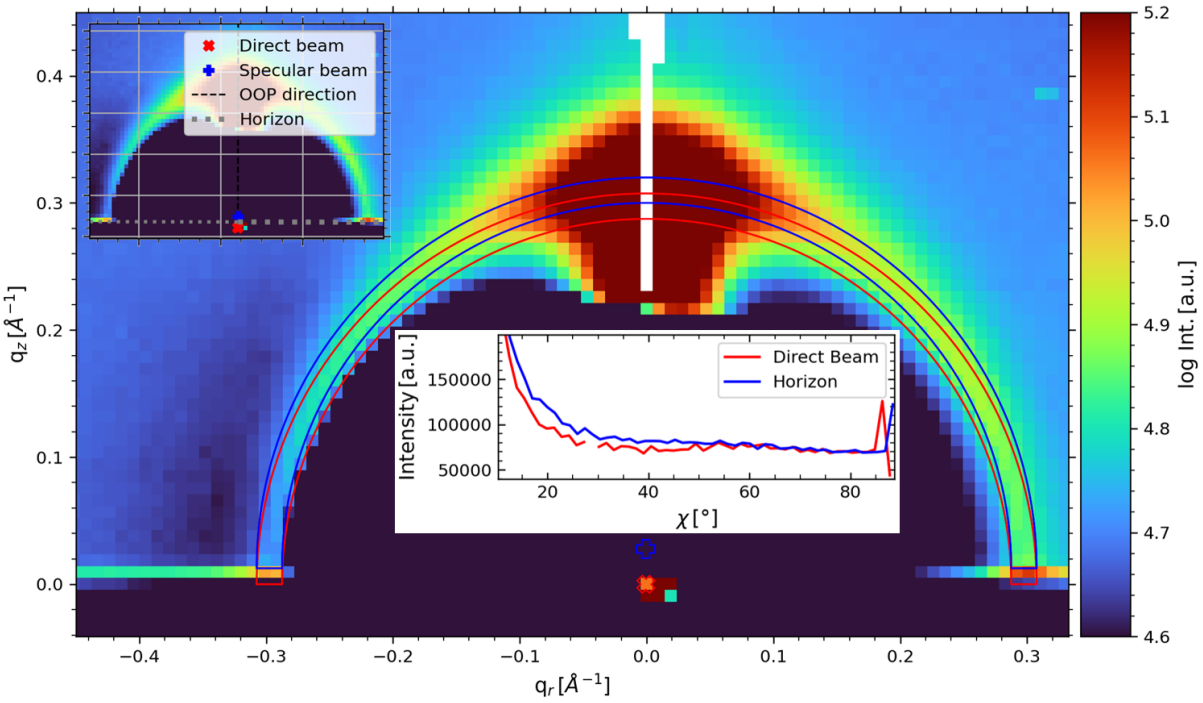

Figure 2.19: Inner region of the $q_r - q_z$ map of a crystalline thin polymer film on top of a silicon wafer. The top left inset shows the raw detector pattern including the direct and specular beam as well as the horizon and vertical direction to assess the quality of geometrical refinement of this scattering data. In the main graph, two radially integrated azimuthal tube cuts with the same q range but different cut centers are shown. The red cut uses the direct beam position $q_r = q_z = 0$ as the center, whereas the blue cut uses $q_r = 0$ and the horizon height $q_z = \frac{2\pi}{\lambda}\sin(\alpha_i) \approx 0.013\,\text{Å}^{-1}$ as the cut center. The positions of the direct and specular beams are indicated with the non-filled cross and plus symbols in the large graph. The white background inset graph shows the resulting binned line cut data for positive χ-values, i.e. the right part of the rings. Note that the beamstop is in a non-ideal position, shielding parts of the crystalline signal in the left part of the ring.

to the scattered signal. This discrepancy is alleviated when observing the cut with the shifted center. Also in the linecut data, no artificial peak at around $\chi = 60°$ is visible if using the shifted center. Furthermore, the horizontal line of enhanced scattering signal directly at the horizon contributes physically correctly at $\chi = 90°$ and not at lower angles. This line of piled-up intensity at the horizon occurs solely for scattering in the dynamic regime, showing that there is a strong evanescent wave present parallel to the substrate (horizon).

2.4.14 Grazing-Incidence Small-Angle X-Ray Scattering

For the modeling of GISAXS data performed by our group, we frequently use software initially developed by Christoph Schaffer that allows interpreting complex scattering data to extract trends or quantify sizes inside the thin films [162]. Here in this thesis, the focus lies on the essential concepts that shall allow for understanding GISAXS scattering in an intuitive way. For a detailed mathematical discussion of the model, Christoph Schaffer's and Johannes Schlipf's

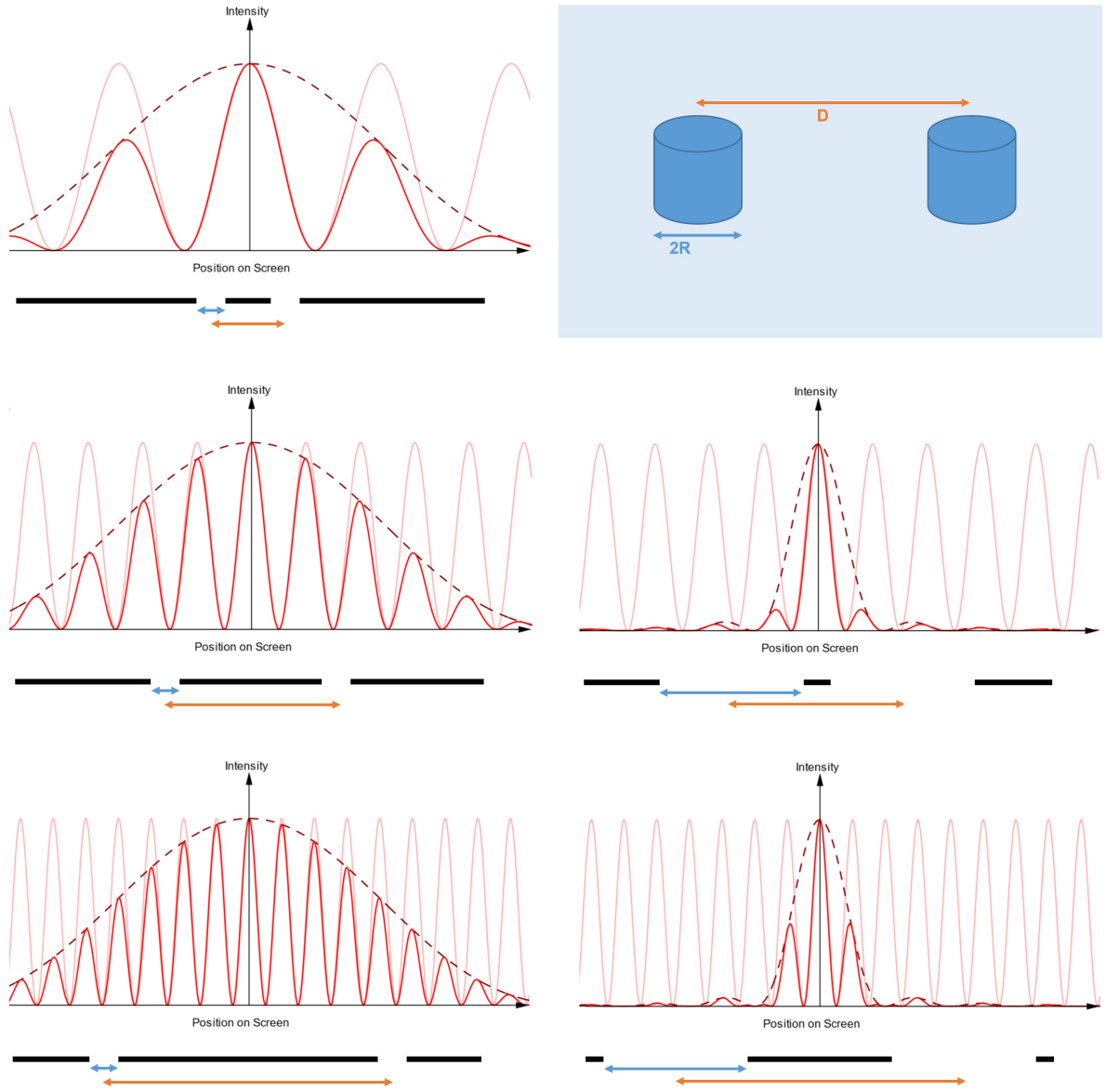

Figure 2.20: Diffraction and interference at slits. The top right blue box shows the definition of radius (R) of (in this case) cylindrical form factors that are structured in the distance (D) – the basic concept of modeling GISAXS as described in the text, which is related to the concept of diffraction and interference at slits shown in this figure. The other panels show the combined diffraction and interference pattern (red solid line) of a double slit where the dashed lines are the single slit diffraction (relying on the slit form factor) and the semi-transparent lines are interference as a result of the periodicity of the slit positions (relying on the structure factor). Below each graph, the corresponding slit geometry is black, with colored arrows indicating the slit size and slit distance. From top to bottom, the distance (D) increases, and the slit size (2R) increases from left to right. Interference patterns are produced with GeoGebra – Double Slit Interference, accessed 16.07.2023.

theses are recommended for further reading to build a solid theoretical framework for understanding the principles of GISAXS and of our GISAXS model [104, 162]. Apart from this, the

publications by Peter Müller-Buschbaum are encouraged reading because they embed the mathematical principles in a broader context, which allows building connections from theory to the concrete application [168, 169, 183].

Classical Double Slit Experiment

In Fig. 2.20, the basic principle of diffraction and interference at a double slit is recaptured. These effects require coherent monochromatic electromagnetic plane waves with wavelengths of a size corresponding to the slit dimensions. The detector pattern that can be observed results from the Fourier transformation of the geometry of the slits, which includes the shape of a single slit and the structural arrangement of all the slits. In this context, thinking in frequencies and reminding the basic principle behind Fourier transformations is advisable: The interference pattern is directly related to the Fourier transformation of the geometry of the slits. To describe a small real-space object with Fourier components in reciprocal space (also known as frequency domain), small real-space wavelengths are required, i.e., high frequencies in reciprocal space. If the real-space object is large, Fourier components of larger wavelengths, i.e., lower frequencies, are sufficient (the Fourier components in the frequency are closer to zero, more peaked in the center). This principle can be transferred to the left side of Fig. 2.20. From top to bottom, the distance of the slits increases while the interference pattern shrinks. The peaks move closer together, and their distance decreases. From left to right, the slit size increases, followed by a decrease in the size of the diffraction pattern.

The interplay of single-slit diffraction and slit interference can be inspected more closely. In Fig. 2.20, moving the left column downwards, the slit position changes (distance increases), but the size of single slits is fixed. Therefore the diffraction pattern (dashed line) stays constant but the modulation of the interference pattern changes (peak distances decrease). In the typical GISAXS terminology, this is equivalent to having constant form factors, but the structure factor is modified. Moving from left to right in Fig. 2.20, the slit position remains constant, but the slit size increases. The interference pattern (semi-transparent line) stays the same, but the diffraction pattern responds reciprocally (peak width decreases). In this case, the structure factor is unaltered, but the form (factor) of the slits is modified. Since the underlying physical concept is the same, this basic behavior of diffraction and interference at slits is vital for interpreting GISAXS patterns.

Diffuse Scattering

The scattering intensity is proportional to the differential cross-section, given by

$$I(\mathbf{q}) \propto \frac{d\sigma}{d\Omega} = \frac{C\pi^2}{\lambda^4}\left(1-n^2\right)^2 |T_i|^2 |T_f|^2 F(\mathbf{q}) \propto F(\mathbf{q}), \tag{2.51}$$

where C is a scaling factor, λ is the X-ray wavelength and T_i, T_f are the Fresnel transmission coefficients [168]. For a fixed geometry, the scattered intensity is proportional to the diffuse

scattering factor $F(\mathbf{q})$ [183]. For N randomly oriented centrosymmetric objects, the diffuse scattering factor can be approximated with

$$F(\mathbf{q}) \propto NP(\mathbf{q})S(\mathbf{q}), \tag{2.52}$$

the isotropic form factor intensity of individual scattering objects $P(\mathbf{q})$ contains information on their shape, and the structure factor $S(\mathbf{q})$ describes their spatial arrangement [160]. Frequently, form factors for cylinders or spheres are used and described by analytic functions [162, 183]. $P(\mathbf{q})$ is the isotropic form factor intensity which is the orientational average of the squared modulus of the form factor amplitude,

$$P(\mathbf{q}) = \langle |f(\mathbf{q})|^2 \rangle. \tag{2.53}$$

The form factor amplitude, in turn, is defined as the 3-D Fourier transformation of the real-space electron density $\rho(\mathbf{r})$,

$$f(\mathbf{q}) = \int \rho(\mathbf{r}) e^{i\mathbf{q}\,\mathbf{r}} dV. \tag{2.54}$$

The structure factor contains information about the inter-particle arrangement [104]

$$S(\mathbf{q}) = \frac{1}{N_j} \left\langle \sum_j \sum_{j'} \exp\left[i\mathbf{q}\,(\mathbf{r}_j - \mathbf{r}_{j'}) \right] \right\rangle, \tag{2.55}$$

where j and j' are two scattering objects. In essence, the scattering intensity related to the diffuse scattering factor is observed, which is proportional to the product of the number of scattering objects, form factor, and structure factor of the scattering objects.

In 1963, the first publication of this diffuse (anomalous) scattering by Yoneda was published [184]. The scattering intensity observed in the later so-called Yoneda region was shown to be independent of the crystal phases of the material but connected to the material's critical angle, hence its electron density. Analyzing the information in this region was found to contain morphological information of the probed film [185]. But only within the last decades, the power of this method was fully exploited for application in soft material thin films [4, 168, 169, 183, 186].

Model & Approximations

In the course of modeling the scattering of hierarchically structured films, we usually make use of three decoupled polydisperse components of different sizes within the local monodisperse approximation in a 1-D paracrystal arrangement using the effective interface approximation in the framework of the distorted-wave Born approximation. The meaning of this sentence is explained below. There are several approximations and concepts used that use complex-seeming terminology that should be put in context for understanding the principles behind the GISAXS model used:[13]

[13] For an overview of the approximations including additional explanations also see Claudia Maria Palumbiny's dissertation [176].

- **1-D paracrystal approximation.** All scattering objects are arranged on a 1-D line. The structure factor describes the arrangement of scattering objects along a line. This is similar to the structure of a 1-D grating for the interference of (multiple) slits. In a paracrystal, local positional distortions of the lattice are included, i.e. the periodicity smears out for longer distances [187, 188]. This is included by assuming a normal distribution of distances entering the calculation for the structure factor.
- **Local monodisperse approximation.** Locally, the scattering objects are monodisperse. If looking at a particular spot of the sample, all scattering objects are of similar size. Therefore, there is no interference between scattering objects of different sizes. We can calculate the diffraction and interference of the scattering objects for this spot. At another spot, an ensemble of larger scattering objects might produce diffraction and interference with different form and structure factors. The scattering contributions from different spots are finally (incoherently) summed up. This approximation should not be confused with the *decoupling approximation* not used here [162].
- **Effective interface approximation.** No vertical structures are considered in the film. For cylindrical form factors, this corresponds to having an unspecified height. They are assumed tall enough that the cylinder faces do not enter the calculation (edge effects neglected) – the incident beam 'sees' ideal pillars. For spherical form factors, the object's shape has a height dependence included in the form factor. Still, only a single layer of objects is considered, i.e., without vertical spheres stacking. As a result, there is no interference in q_z-direction.
- **Distorted-wave Born approximation** The Born approximation assumes an unperturbed external electrical field at the position of the scattering object; the incident wave is 'ideal'. We can evaluate the resulting scattering at the object using the unperturbed incident wave. This is classical first-order (linear) perturbation theory to treat weak non-linear effects when the perturbation of the incident wave is small (weak scattering limit). If the perturbation of the incident wave becomes non-negligible, we need to evaluate the object's scattering using the perturbed (distorted) wave. In terms of perturbation theory, higher-order correction terms must be included. In GISAXS, reflection and scattering at interfaces become very efficient (the scattered wave amplitude becomes of the order of the incident wave amplitude), and waveguiding and dynamic effects make it a highly non-linear problem where multiple scattering events must be considered. One can think of a distortion of the incident wave by superimposing it with scattered waves. This distorted wave is then used as the external field to evaluate the scattering of an object.
  Due to this non-linearity, the scattering pattern of two thin layers of different materials on top of each other will not be the sum of scattering measured from the separate layers individually - the classical superposition does not hold!
- **Normally distributed form factor and structure sizes.** This is (soft) Gaussian blurring of the form factor radii and structure distances within one (monodisperse) component

to account for (limited) polydispersity. Instead of assuming single fixed radii and distances for the form factors and their structure, a normal distribution allows for slight variations in the geometry. Here, σ of the normal distribution of the form factor radii should be considerably small to avoid the size overlap of different components because otherwise, the local-monodisperse approximation breaks down. This smearing of radii and distances leads to a smearing of the diffraction and interference pattern – peaks are effectively broadened.

- **No structure factor is assumed.** There is no preferential distance of scattering objects; they align 'randomly', i.e., arranged in a way that neither constructive nor destructive interference modulation occurs. The resulting pattern is a function of the form factor only.

3 Methods

This chapter covers the experimental methods used in this thesis. In Section 3.1 the preparation of perovskite solar cells and organic solar cells for their space application is described. In Section 3.2 structural and morphological characterization methods are introduced. In Section 3.3, GIWAXS, and GISAXS measurement and evaluation details are explained. in Section 3.4, optoelectronic characterizations from UV-vis to External Quantum Efficiency measurements are presented.

3.1 Sample Preparation

In this section the preparation of perovskite solar cells for the MAPHEUS-8 flight in planar and mesoporous architecture is detailed and the achievements for slot-die printed solar cells in planar architecture are summarized. The organic solar cells part of the MAPHEUS-8 flight were manufactured by Christian L. Weindl and Goran I. Ivandekic according to the recipe of the best-performing solar cells described in the last sub-section. Here, their manufacturing is presented based on the publication "Perovskite and Organic Solar Cells on a Rocket Flight" [189]. In subsection 3.1.1 a list of the chemicals used for either solar cell type is listed, in subsection 3.1.2 processing of spin-coated high-efficiency solar cells for MAPHEUS-8 is introduced, in subsection 3.1.3 the modifications from to the high-efficiency spin-coated solar cells to the slot-die coated solar cells are explained.

3.1.1 Perovskite (Solar Cell) Materials

This subsection comprises a list of the chemicals used for manufacturing the space perovskite solar cells used for the MAPHEUS-8 flight. The chemicals are as follows in accordance with Benjamin Predeschly's Master-thesis work: [190]

The list contains several abbreviations or acronyms of the chemicals and materials in brackets to simplify the description in the next paragraph.

- TEC10 (1.1 mm), chemical vapor deposited fluorine-doped tin oxide on glass, sheet resistance 6 - 9 $\Omega\,\square^{-1}$, *Xop Glass*, Castellón, Spain
- ITOSOL12 (1.05 mm), *Solems S.A.*, Palaiseau, France
- Hydrochloric acid (HCl), 37 %, fuming, Rotipuran, *Carl Roth GmbH & Co. KG*, Karlsruhe, Germany

- Zinc powder, $\geq 98\,\%$, particle size $< 63\,\mu$m, *Carl Roth GmbH & Co. KG*, Karlsruhe, Germany
- Chlorobenzene (CB), C_6H_5Cl, *Sigma-Aldrich (Merck KGaA)*, Steinheim, Germany
- Lead iodide, PbI_2, 99 %, *Sigma-Aldrich (Merck KGaA)*, Steinheim, Germany
- Lead bromide, $PbBr_2$, $\geq 98\,\%$, *Alfa Aesar - Thermo Fisher (Kandel) GmbH*, Karlsruhe, Germany
- Methylammonium bromide (MABr), CH_3NH_3Br, *Dyesol*, Queanbeyan, Australia
- Formamidinium iodide (FAI), $HC(NH_2)_2I$, *Dyesol*, Queanbeyan, Australia
- N,N-dimethylformamide (DMF), C_3H_7NO, 99.8 %, *Sigma-Aldrich (Merck KGaA)*, Steinheim, Germany
- Dimethyl sulfoxide (DMSO), C_2H_6OS, 99.9 %, *Sigma-Aldrich (Merck KGaA)*, Steinheim, Germany
- 4-tert-butylpyridine (tBP), 96 %, *Sigma-Aldrich (Merck KGaA)*, Steinheim, Germany
- Tris(2-(1H-pyrazol-1-yl)-4-tert-butylpyridine)cobalt(III) tri[bis- (trifluoromethane) sulfonimide] (FK209), *Dyesol*, Queanbeyan, Australia
- Bis(trifluoromethane)sulfonimide lithium salt (LiTFSI), 99.95 %, *Sigma-Aldrich (Merck KGaA)*, Steinheim, Germany
- Titanium(IV) isopropoxide (TTIP), 97 %, *Sigma-Aldrich (Merck KGaA)*, Steinheim, Germany
- TiO_2 30 NR-D paste, *Dyesol*, Queanbeyan, Australia
- Acetonitrile, C_2H_3N, 99.8 %, *Sigma-Aldrich (Merck KGaA)*, Steinheim, Germany
- Isopropyl alcohol (IPA anhydrous), 2-propanol, C_3H_8O, 99.5 %, anhydrous, *Sigma-Aldrich (Merck KGaA)*, Steinheim, Germany
- 2,2',7,7'-tetrakis[N,N-di(4-methoxyphenyl)amino]–9,9'-spirobifluorene, spiro-OMeTAD (spiro), $\geq 99\,\%$, *Sigma-Aldrich (Merck KGaA)*, Steinheim, Germany

In the following, chemicals used for cleaning and additionally used materials are listed:

- Soda lime glasses, standard microscope slides, *Carl Roth GmbH & Co. KG*, Karlsruhe, Germany
- Silicon wafer, *Siltronic AG*, Burghausen, Germany
- Etch resistant adhesive tape (tesafilm), clear, $10\,m \times 15\,mm$, *tesa SE*, Norderstedt, Germany
- Detergent, Alconox, *Sigma-Aldrich (Merck KGaA)*, Steinheim, Germany
- Ethanol, $\geq 99.8\,\%$, Rotipuran, *Carl Roth GmbH & Co. KG*, Karlsruhe, Germany
- Acetone, $\geq 99.8\,\%$, Rotipuran, *Carl Roth GmbH & Co. KG*, Karlsruhe, Germany
- Isopropanol (IPA), $\geq 99.8\,\%$, Rotipuran, *Carl Roth GmbH & Co. KG*, Karlsruhe, Germany

- PTFE filter, 0.45 μm pore size, Rotilabo, *Carl Roth GmbH & Co. KG*, Karlsruhe, Germany

For the slot-die coated solar cells, the following chemicals have been used following Christoph Lindenmeir's Master thesis [154]:

- Substrates:
  - Soda-lime glass, microscope slides, *Carl Roth GmbH + Co. KG*, Karlsruhe, Germany
  - Patterned ITO soda lime glass slides, sheet resistance 9-15 Ω/sq, LT-G001, *Lumtec*
- Substrate cleaning:
  - Hellmanex© III, alkaline cleaning concentrate, *Hellma*
  - Ethanol, purity $\geq$ 99.8 %, *Carl Roth GmbH + Co. KG*, Karlsruhe, Germany
  - Acetone, purity $\geq$ 99.8 %, *Carl Roth GmbH + Co. KG*, Karlsruhe, Germany
  - Isopropanol, purity $\geq$ 99.8 %, *Carl Roth GmbH + Co. KG*, Karlsruhe, Germany
- Hole blocking layer:
  - Tin(IV) oxide (SnO_2), 15 % in H_2O colloidal dispersion, *Alfa Aesar*
  - DI-water, for synthesis
- Perovskite active layer:
  - Methylammonium iodide (MAI), CH_6IN, purity $\geq$ 99 %, *Sigma Aldrich (Merck KGaA)*, Steinheim, Germany
  - Methylammonium chloride (MACl), CH_6ClN, purity $\geq$ 99 %, *Sigma Aldrich (Merck KGaA)*, Steinheim, Germany
  - Formamidinium iodide (FAI), CH_5IN_2, purity $\geq$ 99 %, *Sigma Aldrich (Merck KGaA)*, Steinheim, Germany
  - Lead(II) iodide (PbI_2), purity $\geq$ 99.999 % trace metals basis, *Sigma Aldrich (Merck KGaA)*, Steinheim, Germany
  - 2-Methoxyethanol (2-ME), $CH_3OCH_2CH_2OH$, anhydrous, purity $\geq$ 99.8 %, *Sigma Aldrich (Merck KGaA)*, Steinheim, Germany
  - Dimethyl sulfoxide (DMSO), $(CH_3)_2SO$, anhydrous, purity $\geq$ 99.9 %, *Sigma Aldrich (Merck KGaA)*, Steinheim, Germany
- Electron blocking layer:
  - SHT-263 Solarpur© (Spiro-OMeTAD), $C_{81}H_{68}N_4O_8$, *Sigma Aldrich (Merck KGaA)*, Steinheim, Germany
  - LiTFSI, $CF_3SO_2NLiSO_2CF_3$, purity $\geq$ 99.95 %, *Sigma Aldrich (Merck KGaA)*, Steinheim, Germany
  - FK 209 Co(III) TFSI salt, $C_{42}H_{45}CoF_{18}O_{12}N_{12}S_6$, *Sigma Aldrich (Merck KGaA)*, Steinheim, Germany
  - Acetonitrile (ACN), CH_3CN, anhydrous, purity $\geq$ 99.8 %, *Sigma Aldrich (Merck KGaA)*, Steinheim, Germany

  - 4-tert-Butylpyridine (tBP), $C_9H_{13}N$, purity $\geq 98\,\%$, *Sigma Aldrich (Merck KGaA)*, Steinheim, Germany
  - Chlorobenzene (CB), C_6H_5Cl, purity $\geq 99.8\,\%$, *Sigma Aldrich (Merck KGaA)*, Steinheim, Germany
- Back contact electrodes:
  - Fine Gold 999.9/1000, *Goldkontor Hamburg GmbH*

3.1.2 Spin Coated High-Efficiency Perovskite Space Solar Cells

This subsection details the manufacturing of high-efficiency perovskite solar cells that were used for the space flight. The entire manufacturing process is schematically illustrated in Fig 3.1. Many details and tricks stated below were recommended by Dr. Renjun Guo, who invested a lot of time to achieve the high-quality perovskite layer we can spin coat today.

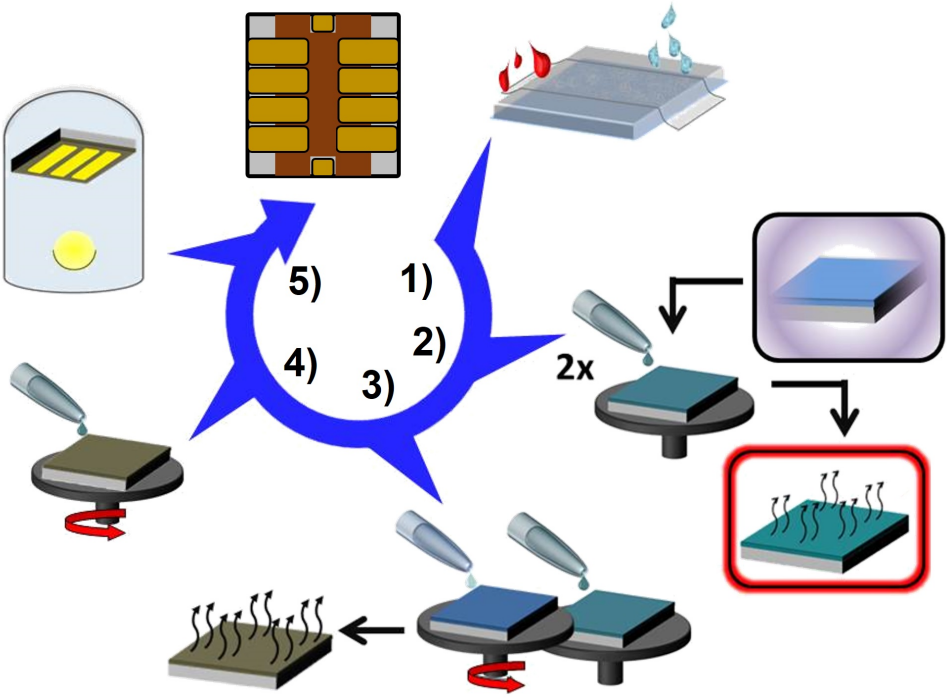

Figure 3.1: Fabrication steps of a mesoscopic perovskite solar cell: 1) Etching and cleaning the FTO-coated substrate. 2) Plasma treatment and spin-coating of the c- and m-TiO_2 layer with annealing and calcination after each deposition. 3) Transfer to the glovebox, subsequent precursor spin coating, and anti-solvent quenching, followed by annealing. 4) Dynamic spin coating of Spiro with oxygen-doping overnight. 5) Evaporation of the gold anode completes the final solar cell. For the planar architecture with SnO_2, step 2) is modified (see text). Adapted from Benjamin Predeschly's Master thesis [190].

Sample Etching & Cleaning

Before beginning with the fabrication of solar cells, it is advisable to measure the resistance of the ITO/FTO surface with a multimeter (side-side, same position for all substrates) because we found substantial variations from sample to sample. Samples of too-high resistances should be discarded (they still should be used for structural/morphological studies). Also, variations in the substrate size should be identified in the very beginning and corrected by using sandpaper to make sure those substrates will fit for example the evaporation holder. Then, the glass substrates are labeled with a diamond cutter at a corner of their glass side to later be able to distinguish the SCs from each other. This might seem time-consuming because they all are processed similarly; however, tracing back potential manufacturing influences (e.g. the sample order of spin coating) becomes possible.

The glass substrate's ITO/FTO is etched in the first step to achieve the desired geometry patterning for the solar cell layout. The protected area is covered by adhesive tape – it must be appropriately tightened to avoid etching of the underlying FTO. For the etching, zinc powder is applied to the uncovered areas, and a solution with 37 % HCl and deionized water (DI water) of ∼1:1 (vol.) is dripped onto the surface to etch the conductive oxide. Wiping with cotton buds avoids incomplete removal due to the manual distribution of zinc powder and acid. After that, rinsing the specimen with copious amounts of tap water removes residual acid. Also, the tape is removed under flowing water to avoid acid residuals affecting the covered area.

The organic cleaning procedure that follows begins with a mechanical cleaning with a toothbrush dipped in an aqueous Alconox/Hellmanex detergent solution. The substrates are scrubbed vigorously; the toothbrush is too soft to scratch or damage the ITO/FTO surface. Here, it is vital to protect the backside of the flexible substrates from scratches. The substrates are then placed in a PTFE sample holder and successively immersed in five cleaning solutions: first in the detergent, second in DI water, third in ethanol, fourth in acetone, and last in isopropanol (IPA). For each step, the specimens are rinsed with the respective solution before immersing and sonicating them for at least 10 minutes. Especially rinsing with DI water after sonication in detergent is crucial because otherwise, remanents of detergent create cloudy features on the substrates in a reaction with ethanol. After the last (IPA) step, the substrates are dried with an oil-free (nitrogen) air stream.[1] After drying, the samples can be stored in clean sealed boxes for later use.

Hole-Blocking Layer

The recipes presented here are optimized and validated in terms of their layer thickness, sufficiently thick to minimize shunting while being as thin as possible to keep the solar cell series resistance low (cf. 2.2.4) [191, 192]. Before the deposition of the hole-blocking layer, the

[1] The high nitrogen consumption in our group has been debated for years. In my experience, drying with a gentle nitrogen flow (low-pressure setting) gave the best and controllable cleaning results. Other drying methods, such as dry-spinning or heating them, could not reach the same high quality.

ITO/FTO areas need to be covered in the regions of the electrodes to optimize electrode contact stability and charge transport to the electrodes. For this, adhesive tape can be used and removed directly after spin-coating. One pitfall of taping is spin coating edge effects within a few mm of the tape towards the substrate center. This effect can be minimized by streamlining the electrode cover geometry using triangular tape pieces. This taping should be prepared in advance, before beginning with the plasma treatment.

In advance of the first spin-coating step, a cleaning and surface activation step in the form of a 10-minute oxygen plasma treatment (0.4 mbar, 250 W) is performed. For polar solutions, this reduces the contact angle and improves the wetting of the surface. Especially for FTO/ITO substrates, it is essential to minimize the time between plasma treatment and the deposition because the effect notably vanishes already after ∼30 minutes, while on pure, insulating glass samples, the effect holds longer.

The solution for the compact layer is prepared with a 2 M stock solution of fuming HCl in anhydrous IPA, of which 35 μl are further diluted with 2.5 ml anhydrous IPA. The diluted HCl is shaken for at least 10 min. In the meantime, 368 μl titanium(IV) isopropoxide (TTIP) is added into a stirring 2.5 ml anhydrous IPA solvent, resulting in a concentration of 0.43 M TTIP, and is left stirring for 10 min. Under vigorous stirring, the whole diluted HCl solution is dropwise added into the TTIP solution and then stirred for at least 1 h. During preparation, the solution has to be clear at all times. 200 μl of this final solution is dropped on an oxygen plasma-treated FTO substrate (air-blown on the spin coater to remove dust) and then spin-coated at 3500 rpm for 30s with a ramping time of 4 s (replace the pipette tip when crystallization occurs). The tape is removed, and the substrate is subsequently annealed at 150 $^{\circ}C$ for 15 min on a hot plate. During annealing, covering the samples is advisable to avoid dust from settling on them. The compact layer is sintered (air-interchange) at 450 °C for 1 h with a heating ramp of 375 °C h^{-1}.

On top of the compact TiO_2 layer, the mesoporous TiO_2 layer is deposited. The solution is prepared with the TiO_2 Dyesol 30 NR-D paste solved in ethanol 1:6 wt. and stirred overnight. After taping, plasma treatment, and dust removal by blowing the samples (see above) 200 μl are spin-coated with 4000 rpm for 30s with a ramping time of 2 s. The annealing temperature is 100 °C for 10 min. Sintering includes multiple steps similar to that reported in [85]: Sintering at °C for 5 min using a heating time of 5 min, at 325 °C for 5 min using a heating time of 15 min, and finally at 450 °C for 30 min using a heating time of 5 min. After the second sintering, as soon as the substrates are cooled down to ∼150 °C (they do not melt the plastic petri dish transport boxes anymore below this temperature), they are quickly transferred into a glove box with nitrogen atmosphere before the hygroscopic TiO_2 can adsorb any water.

The planar perovskite solar cell sample preparation is identical including the first plasma treatment. Then, a tin oxide layer is prepared by spin-coating the pure colloidal SnO_2 dispersion (Alfa Aesar) at 6000 rpm for 30 s using a ramping time of 6 s and subsequent annealing at 150 °C for 30 min. Here, it is essential to shake the dispersion in the large bottle for some minutes to achieve uniform mixing before extracting the desired amount of the dispersion in the personal

vial. Shaking the personal vial from time to time is advisable. Also for this layer, direct hot transfer into the glovebox is very important. Good quality compact blocking layers should be hardly visible – if features or particles are visible, filtering of the solution should be tried out or a new solution considered.

Perovskite Layer

The perovskite precursor solution is prepared and spin-coated inside the oxygen- and water-free glove box (<1 ppm). For the precursor solution, two 1.5 M solutions of $FAPbI_3$ and $MAPbBr_3$ are prepared in a mixture of DMF/DMSO 4:1 (vol.). Here, dissolving the lead salts in the solvents by applying moderate heat and then adding the lead salt solution to the organic salt is the typical procedure, allowing precise stoichiometry control. According to Saliba et al. (2018), these inorganic stock solutions can be stored for weeks and are added to the organic salt [85]. Another route is to directly mix the lead and organic salt in a vial (starting with the organic salt to minimize the weighing error of the heavy lead salt). The most reproducible results are achieved by following the latter steps and only using solutions prepared on the same day. Also, this successive addition in a single vial can accelerate the dissolution due to the presence of the organic cations that somehow aid complex formation. Further, the solutions are prepared with a 9 % lead excess. This means the lead salts are prepared with a 1.5 M concentration while the organic salt weights are reduced to match the desired stoichiometry. After complete dissolution, $FAPbI_3$ and $MAPbBr_3$ solutions are mixed in a 5:1 ratio (vol.). Filtering the solution is advisable to avoid any dust or particles on the substrate, but the solution should be clear even without filtering if the work is done cleanly and carefully. The final precursor solution, a $(FAPbI_3)_{0.87}(MAPbBr_3)_{0.17}$ perovskite ink, must be used on the same day.

The fabrication of the perovskite film is done *via* spin coating inside the glove box with the anti-solvent method. In the first step, the perovskite ink is dropped in the middle of the substrate. The mesoporous titania and the planar tin-oxide surfaces should show excellent wetting (no plasma in this step – see above!) of the perovskite precursor – 50 μl should result in a drop that automatically spreads to more than 1 cm diameter without spinning. [2] The perovskite ink is spin-coated at 6000 rpm for 30 s with the spin coater lid open. 5 s before the end, around 120 μl anti-solvent chlorobenzene (CB) is flushed onto the spinning substrate. The fast crystallization induced by CB results in a homogeneous, uniform, and flat thin film (compare 2.3.3). Here should be specified that anti-solvent flushing is a delicate process (see Taylor et al. 2021 for a detailed work [193]). First, classical pipette tips have an outlet too narrow to support the flushing with a proper stream. Therefore, tips of larger diameter are beneficial and preferred over cutting standard tips, which causes contamination and reduces reproducibility.

[2] It is advisable to minimize the amount of precursor used for the spin-coating process. It is not only convenient to save resources and to save time for cleaning, but it also is beneficial for the sample quality. It minimizes the undesired solvent atmosphere and thus improves film quality and inter-comparability amongst different samples within a batch. For perovskite, usually ~40 μl precursor solution is sufficient for complete coverage for well-working solar cells but even 20 μl give good enough coverage for thin film characterization.

Then, timing, pressure on the push-button, and good positioning, i.e. lateral position, height (∼1 cm), and angle of the pipette are essential to control the process.

Typical artifacts on the film appear as cracks (flushing too slow), holes (too fast), or strikes (not centered). By actively observing the anti-solvent stream during flushing one can directly assess the dropping quality – there is a supplemental demonstrating the process in [85]video. Also, the individual conditions, for example, spin coater geometry, define the airflow, and in turn, drying requires refinement of the spin coating parameters. Immediately after spinning, the substrate with now a semitransparent brownish film is placed on a hot plate at 100 °C for 40-60 min (covered to avoid dust). The samples should turn opaque black within some seconds of annealing, with a shiny mirror-like surface. After annealing, the samples are cooled down to room temperature

Electron-Blocking Layer & Gold Contacts

Dynamic spin coating is used to fabricate the electron-blocking layer spiro-OMeTAD. The recipe is slightly adapted from the paper "How to make over 20% Efficient Perovskite Solar Cells in Regular (n-i-p) and Inverted (p-i-n) Architectures" by Saliba et al. [85]. In detail, the spiro concentration is diluted to approximately 3/4 of the concentration (same holds for the additives) published in Saliba to achieve a similar thickness with our devices. Two different stock solutions are needed for the additives. The first one consists of 520 mg Li-TFSI dissolved in 1 ml of ACN (1.8 M). The second one is made from 375.8 mg FK209 dissolved in 1 ml of ACN (0.25 M). To prepare 1 ml of spiro solution, one needs to solvate 72.3 mg of spiro powder in 1 ml of CB. Then 4 μl of the FK209 stock solution, 17.43 μl of the Li stock solution, and 28.8 μl of tBP to the solution are added. Due to the low volumes used, it is advisable to wash the pipette tip in the precursor vial by pushing the volume out and back in the pipette tip multiple times to extract the complete additive volume. The solution with the additives must be prepared on the day of usage, while the FK209 and LiTFSI stock solutions can be stored for weeks. After spin-coating the spiro-MeOTAD precursor dynamically (similar dropping technique as used for the perovskite anti-solvent treatment, with open lid. Here, 30-50 μl are enough (complete coverage can be reached with $< 10\,\mu$l!) at 4000 rpm for 10 s, the substrates are stored in a desiccator filled with silica gel with a relative humidity of less than 10 % for one day to oxidize the spiro layer. The spiro layer should have a greenish-yellowish reflective color after spin coating – blue or purple indicates a too-thick layer. After the deposition of the blocking layer but before the electrode evaporation, the ITO/FTO pads must be exposed at the electrode position. The idea is that any contact pin piercing through the soft metal electrode still establishes good electrical contact since ITO/FTO is widely covered with the metal at the electrode. For the space solar cell, the spiro and the perovskite layer were removed by scratching the electrode positions with a PTFE tweezer.

The back electrode consists of a 160 nm thick thermally evaporated gold layer for the space solar cells. This is thicker than the usual 50-80 nm to improve the mechanical resistance of

the contacts. The gold is evaporated on the films using an evaporation mask for the solar cell geometry. The deposition of the electrode is done in an evaporation process with multiple steps: At first, up to a thickness of 2 nm a low rate of 0.2 $\mathring{A}\,s^{-1}$ is used to minimize the thermal stress on the spiro layer and to minimize penetration depth of the gold particles. Then, an intermediate rate of 1-2 $\mathring{A}\,s^{-1}$ is used to reach percolation and form good contacts of 30-50 nm total thickness. They are further stabilized with additional gold deposited with a ramp of 3-4 $\mathring{A}\,s^{-1}$ to yield a total thickness of 160 nm. Note that the largest passive aluminum cooling plate should be used to minimize the heat stress on the solar cells. Also, using a boat (with ~1 g of gold, but of course not using all of it) instead of a crucible is highly recommended to maximize the liquid gold puddle and hence the "evaporation rate to radiative heat transfer ratio" during evaporation.

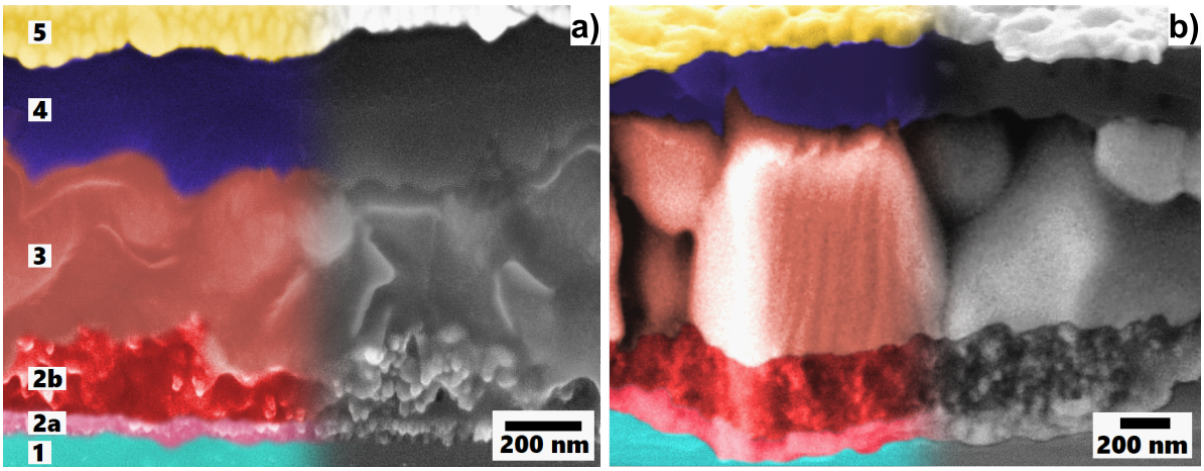

Figure 3.2: Crossection scanning electron microscopy images of perovskite solar cells in the n-i-p mesoscopic architecture. a) View of the solar cell after optimizing the fabrication steps, achieving more than 19 % efficiency. b) Early attempts of the same architecture yield around 8 % efficiency. Note the slightly different scale bar. Layers are 1) substrate, 2) compact TiO_2, 2b) mesoporous TiO_2, 3) perovskite, 4) spiro, and 5) gold anode. In b) The perovskite layer shows pronounced grain boundaries, and the interfaces to the charge selective layers show pronounced demarcations, i.e. the interlinking of the material is not as good as in a). Figure adapted from Benjamin Predeschly's master thesis [190].

Manufacturing Suggestions for Solar Cell Improvements

At the start of the project, the best perovskite solar cells reached an efficiency of about 8 %. After including many optimizations that are detailed above, more than double the efficiency has been achieved. Differences in the solar cell cross-section can be seen in Fig. 3.2, especially the changes in the granular structure of the perovskite and the improvement of interfaces. Absurdly, the two most important improvements of the solar cells were achieved by I) hot-transfer into the glovebox after finishing sintering of the TiO_2 blocking layer and II) spin coating perovskite and spiro with the lid open – such details are hard to find (some spin coaters do not even have lids), therefore rarely found in publications. Another important improvement was the gold thermal evaporation from a boat with a comparably large puddle and the introduction of passive cooling

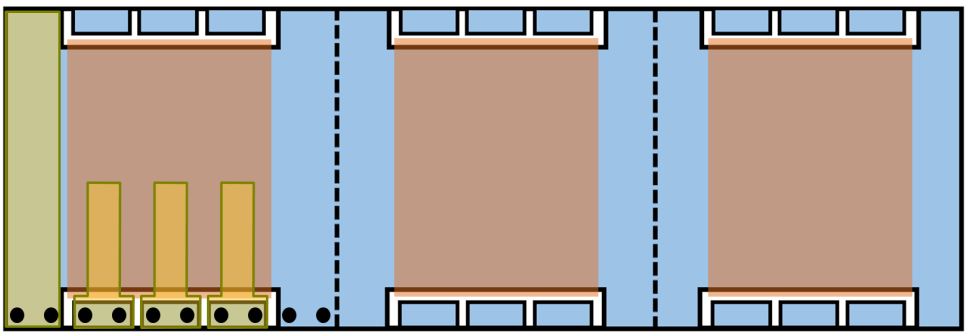

Figure 3.3: The six solar cell layout for a three-module slide for printed solar cells. In blue, the ITO patterning layout can be seen, with three pads on each side of the single modules, one for each top contact of the solar cell. The important central area of the solar cells is marked red, where no removal of the blocking, perovskite, or spiro layer takes place. The left module is shown in half-completion with the electrode contact points as black circles and half the cell covered with the gold electrodes in semi-transparent yellow. The upper part of the three gold fingers defines the active solar cell area where ITO, the other layers, and the gold overlap. On the left side, the stripe of gold is evaporated to extract charges from the bottom ITO. Note that removal of the blocking and perovskite layers must be done as shown in the schematic drawing – the gold stripe does not contact the (red) other layers. This minimizes the path for the electrons inside ITO to reach gold (decreasing series resistance and increasing the fill factor), which is one of the layout design maxims to optimize layout-dependent photovoltaic parameters [194].

plates. Also, the layer thicknesses we got were different than those reported in Saliba et al. [85]. We compensated for this by adjusting the perovskite spin coating program and diluting the spiro solution with more solvent.

In the cross-section SEM image of Figure 3.2c, thin films of a reference PSC of the same architecture with which type 20 % PCE can be achieved are shown. The cross-section demonstrates layers and their thicknesses close to the ones in Figure 3.2a. Between perovskite and mesoporous TiO_2 there is no sharp boundary visible in the SEM image that indicates a good backfilling of the mesoporous structure and therefore a good interface with a large contact area between these two layers. Due to that the extraction of charges can be improved and expedited by improved charge separation.

General suggestions for the fabrication of high-efficiency (perovskite) solar cells include

- preselect substrates
- label individual samples for error tracing
- use fresh solutions, in case of doubt – always filter
- try new chemicals
- pipette solution from the central region of the liquid, neither from the vial bottom nor the surface
- minimize dust by using bellows before every single deposition
- test at least one sample for solution deposition (test vacuum chuck, solution, warm-up)

- use surface tension to 'rescue' samples (if a dust grain occurs after dropping before spinning, try pushing it to the edge of the drop to let centrifugal forces expel the dirt)
- inspect the solution and the samples closely and with care – keep the eyes open all the time
- repeat spin coating on the very same sample (if it does not look good) – it can improve wetting or remove dust grains, there is nothing to lose
- stop immediately if results are not satisfactory during manufacturing – save your samples
- process all layers on a single day
- avoid (extrinsic) solvent atmosphere, e.g. someone printing in the fume hood while someone else using the spin coater
- take care of interfaces
- spin coat with the lid open for perovskites
- hot-transfer samples to the glove box

Some of these rules are specific to the used materials, architecture, and devices, and might require adaption for other recipes. Careful handling is advised for flexible substrates to avoid scratches on the backside and to protect the quite vulnerable ITO coating.

3.1.3 Printed Perovskite Solar Cells

Many steps are copied from the explanation above, only differences are explicitly stated here. The substrates for printed perovskite solar cells are patterned ITOs of 75x25 mm^2 size (and 25x25 mm^2 for spin-coated references) and thickness of $\sim$1 mm. In Fig. 3.3, a slide for printing with three modules in the six solar cell layout is shown. Here, the blue areas are covered with conductive oxide, and the contact points for the electrodes are indicated in one row on the bottom left as black circles. The blue isolated patches of conductive oxide at the electrodes improve electrode contact and mechanical stability.

As hole blocking layer, the colloidal dispersion of SnO_2 was mixed in a ratio of 1:4 with DI water. This solution was left to stir for proper mixing. After organic cleaning and plasma treatment, the solution is statically spin-coated for 30 seconds at 3000 rpm with an acceleration of ramping time 5 s. Depending on the size of the substrate, either 120 μl for a 25x25 mm^2 sample or 360 μl for a 75x25 mm^2 sample, are distributed on the substrate to achieve full wetting, even before the spinning. We found the diluted precursor solution using low rpm (compared to the pure recipe above) suitable for spin coating the large printing slides because at higher rpm the substrates continuously kept flying away and broke. After the spin coating process and before annealing, the wet SnO_2 layer was removed from the sides with thin-tip cotton tips (designated for makeup) dipped in DI water. The removed area should look like shown in Fig. 3.3, where the remaining coated area is colored orange. Wiping the regions instead of taping gave the best results for subsequent printing since tape resin residuals were shown to cause undesired effects on the meniscus during printing, and thereby have a detrimental effect on the film quality (see

Andrea Vitaloni's Master thesis [114]). The samples are annealed at 150 °C for 30 minutes and then hot-transferred to the glove box if not directly processed further. In contrast to spin-coated reference solar cells, perovskite printing on top of the SnO_2 (described in the next paragraph) leads to milky, cloudy perovskite films, and a bad-quality final solar cell device. Residuals on top of the SnO_2 film seem to be responsible for this effect since we found (see Christoph Lindenmeir's Master thesis [154]) substantial improvement upon 'washing' the SnO_2 layers in an additional spin-coating step with DI water (with a microdose of 0.05 M potassium chloride) for 30 seconds at 3000 rpm and ramping time of 2 seconds [96]. After drying for a few minutes on the hotplate at 100 °C, slot-die printed films reach (again) their mirror-like quality as when printed on glass.

The perovskite solution is prepared in a glovebox in a water- and oxygen-free (<1 ppm) nitrogen atmosphere. PbI_2 and MAI powders are stoichiometrically mixed, and 2-Methoxyethanol (2-ME) was added to reach a concentration of 0.4 M. After stirring for a few hours at room temperature it is dissolved. Before using the solution, a DMSO additive (20 mol%) is added. This corresponds to 14.44 μl per ml of solution with a concentration of 1 M, which was found to deliver the best results for MAPI solar cells derived from this solvent system [195]. It is essential to use the perovskite solution on the same day since aged 2-ME solutions (even without DMSO) created non-reproducible results. Manufacturing of the perovskite layers was exclusively performed outside the glove box in ambient conditions via spin coating (for the reference layers) and slot-die coating.

For spin coating, 70 μl of perovskite solution is dropped and coated at 4000 rpm and ramping time of 5 s for 35 s (lid closed). 6 s after the program starts, i.e. after reaching full speed, a nitrogen gun is directed towards the spinning center at a distance of ~5 cm to start the crystallization process by applying a nitrogen stream. It is important to highlight that only good film results are achieved if the crystallization onset is triggered by nitrogen blowing – just being two seconds too late causes poor and inhomogeneous film quality. The pressure of the N_2 gun is set to 1 bar and the gun must always be pressed to full strength to achieve reproducible N_2 flows. As for anti-solvent treatment, the N_2 gun must be aimed perpendicular to the substrate to avoid film defects. After spin coating, the film is annealed for 20 minutes at 100 °C, and then transferred to the glove box.

For slot-die coating, the setup used can be seen in Fig. 3.4. It was designed and built by Manuel A. Reus and has been used for printing thin films in our group for several different material classes – including organic semiconductors for organic solar cells, carbon nitrides, cellulose-nanofibril thin films to perovskite quantum dots [141, 196, 197, 198]. Its modular design allows for various tailored experiments, for example, in-situ photoluminescence measurements [67]. It consists of printer housing with horizontal and vertical motors. On these motors, the printhead and the air knife are fixed. The printing stage is heatable, has a vacuum chuck to hold the substrate in place, and is aligned by a 2-axis goniometer. Additionally, there is a syringe pump next to the housing. The motors and the syringe pump are controlled via computer software. To consistently print comparable samples, following a precise sequence with the printer is essential: First, clean and assemble the printhead, then connect the air knife to the printhead at a 30-

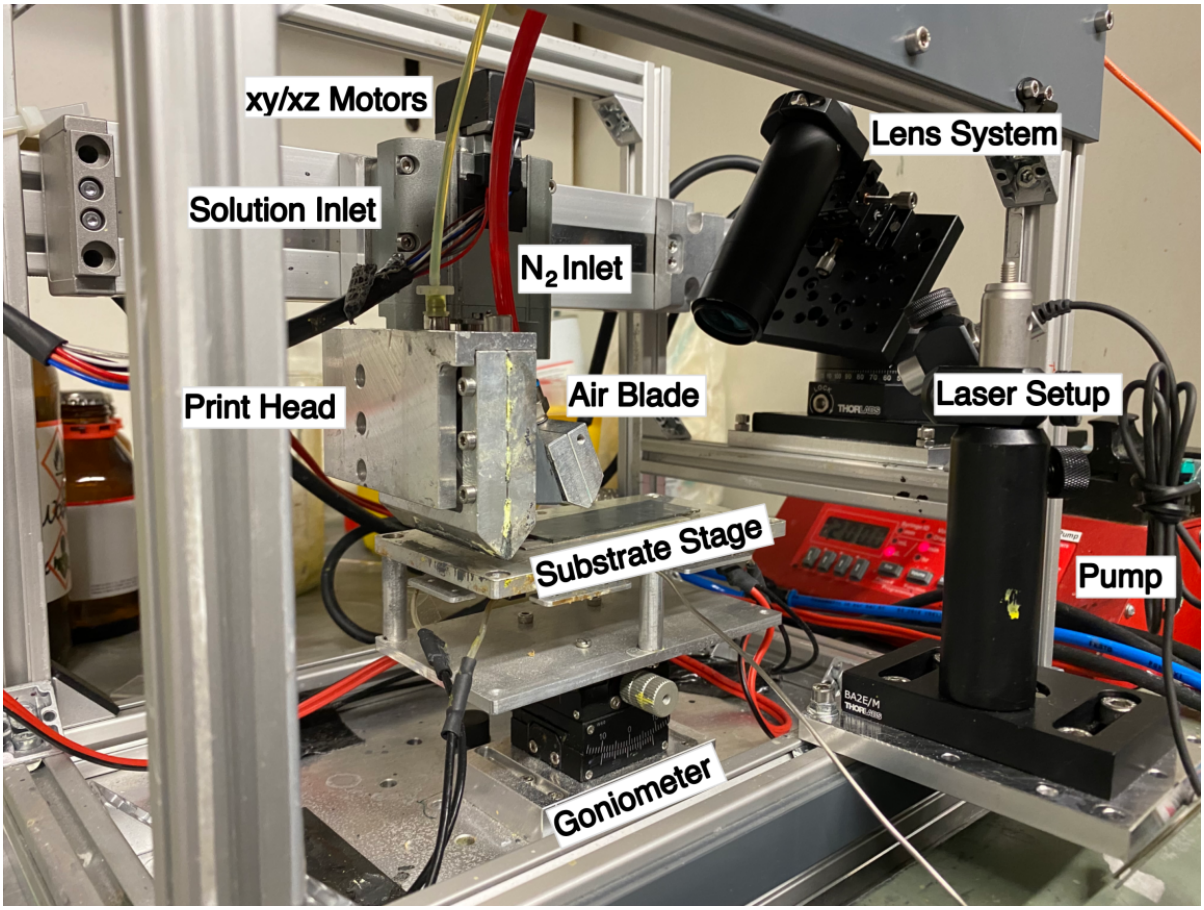

Figure 3.4: Photograph of the slot-die printer with labeled components. The mobile photoluminescence setup is currently installed for in-situ photoluminescence measurements.

degree angle and secure the printhead to the mount. Please refer to Christoph Lindenmeir's Master thesis for a detailed investigation of the design of the air knife, its positioning and flow optimization, and a simple but effective method to investigate and fine-tune the flow profile in the mount configuration [154].

A successful printing process should result in perovskite thin films of comparably high efficiency as known from spin-coating. The process after all the optimizations is shown in the different printing stages in Fig. 3.5. Usually, the following steps need to be performed: Connect the air blade to a nitrogen bottle and adjust the flow rate with the pressure gauge. Align the stage and print head height accurately by using a water level and the 2-axis goniometer of the stage to ensure a constant gap height across the substrate. Fill the PTFE tube with the solution and use the WinPump program to control the pump and MEXE02 to move the motors. When printing, either use the pump to form a meniscus between the printhead and substrate or a pipette for a controlled initial meniscus volume.[3] Turn on the air knife and start moving

[3]Please refer to Christoph Lindenmeir's Master thesis for a calculation of the appropriate flow rate based on the solution parameters, the printer geometry and parameters, and the final film thickness [154].

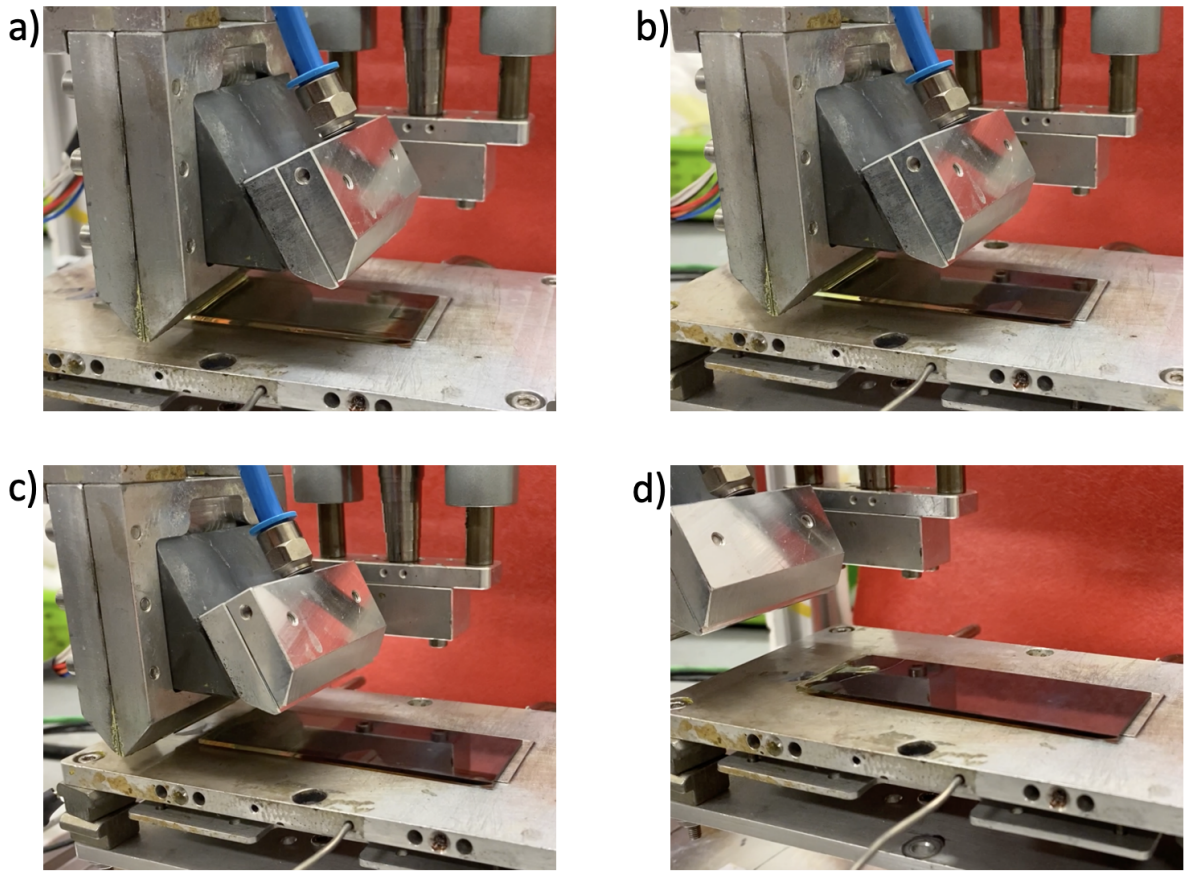

Figure 3.5: The optimized printing process of perovskite. Figure taken from Christoph Lindenmeir's Master thesis [154]. a) The meniscus has crossed more than half of the substrate, the drying begins on the rear side visible by the color change. b) The printhead drags along the stable meniscus, while a straight drying front is established. c) The printhead has left the substrate. d) The entire substrate has been dried. Note the liquid drop at the end of the substrate (see text).

the motors once the meniscus is formed. Catch the meniscus with a piece of paper when the printhead reaches the end of the substrate, and turn off the air knife when the drying front reaches the end to minimize solution backflow and avoid solution underneath the substrate (not shown in Fig. 3.5c,d). After finishing the perovskite layer, the slide is separated into squared pieces and the electron-blocking layer and the gold anode are deposited on the 25x25 mm^2 single pieces as described above.

3.1.4 Organic Space Solar Cell Preparation

This subsection describes the manufacturing of the organic solar cells used for the MAPHEUS-8 flight as described in [189]: Christian L. Weindl and Goran I. Ivandekic fabricated two types of organic solar cells with different absorber systems, namely the fullerene-based active layer with

PTB7- Th:$PC_{71}BM$[4] and the fullerene-free active layer PBDB-T:ITIC[5] in inverted architecture. Indium-doped tin oxide (ITO) coated substrates were patterned with zinc powder and HCl similarly as described above. After sonification for 15 min in each, Hellmanex solution, ethanol, acetone, and isopropanol, the substrates were dried with a nitrogen gas flow and plasma treated (10 min, 250 W). As hole-blocking layer, a zinc-oxide (ZnO) precursor solution of 500 mg zinc-acetate dihydrate (Sigma-Aldrich) in 5 mL 2-methoxyethanol (Sigma-Aldrich) plus 142 µL 2-aminoethanol (Sigma-Aldrich) was spin-coated at 4500 rpm for 30 s on top of the ITO coated substrates and annealed at 200°C for 1 h. After ZnO blocking layer fabrication, the substrates were transferred to a nitrogen-filled glove box. For the PBDB-T:ITIC (1-Material) photoactive layer, a precursor of 18 mg PBDB-T:ITIC (1:1 wt.) in 1 ml chlorobenzene (Sigma-Aldrich) was spin-coated dynamically at 1500 rpm for 3 s and 2500 rpm for 30 s with subsequent annealing at 150°C for 30 min. For the PTB7-Th:$PC_{71}BM$ (1-Material) photoactive layer, we followed Liao et al. [199]. A precursor of 35 mg PTB7-Th:$PC_{71}BM$ (1:1.5 wt.) in 1 ml chlorobenzene (Sigma-Aldrich) with additive 1,8-diiodooctane (3 % vol.) was spin-coated statically at 2000 rpm for 60 s. On top of the organic absorber layer, a 10 nm thick molybdenum oxide blocking layer and a 150 nm thick silver contact were thermally evaporated. After fabrication and prior to the launch, the solar cells were stored in the dark under an inert nitrogen atmosphere.

3.2 Real-Space Structural Characterization

3.2.1 Profilometry

With a profilometer, the roughness and thickness of a thin film can be determined. For our contact profilometer (Bruker $DektakXTStylusProfiler$) a thin needle (stylus) is lowered to the surface to touch it and then in a second step slowly dragged across the surface. A slight force keeps the needle in touch and vertical stylus displacements down to nm variations are recorded as a function of lateral position. The resulting profile can then be analyzed to quantify e.g. the surface roughness in a quick way.

To determine the film thickness using profilometry, thin scratches are made on the sample to remove the film down to the substrate. Measuring across the scratch allows us to estimate the relative height of the thin film surface compared to the substrate height. By doing this on several spots, an average and standard deviation allow for a precise estimate of the film thickness. Note that for spin-coated films, the central region of the sample should be used due to the Mexican hat profile of (larger) samples.

[4] Poly[4,8-bis(5-(2-ethylhexyl)thiophen-2-yl)benzo[1,2-b;4,5-b']dithiophene-2,6-diyl-alt-(4-(2-ethylhexyl)-3-fluoro-thieno[3,4-b]thiophene-)-2-carboxylate-2-6-diyl)]:[6,6]-phenyl-C71-butyric acid methyl ester.

[5] Poly[(2,6-(4,8-bis(5-(2-ethylhexyl)thiophen-2-yl)-benzo[1,2-b:4,5-b']dithiophene))-alt-(5,5-(1',3'-di-2-thienyl-5',7'-bis(2-ethylhexyl)benzo[1',2'-c:4',5'-c']dithiophene-4,8-dione)]: 3,9-bis(2-methylene-(3-(1,1-dicyano-methylene)-indanone))-5,5,11,11-tetrakis(4-hexylphenyl)-dithieno[2,3-d:2',3'-d']-s-indaceno[1,2-b:5,6-b']-dithiophene.

3.2.2 Optical Microscopy

Optical microscopy is one of the first characterization methods of thin films because it is sensible to film surface morphology, and homogeneity on the micrometer scale. Artifacts and non-phase pure regions can be identified, e.g. regions of heterogeneous growth with macroscopic dendrites (compare Section 2.3) can be seen. The spatial resolution d of a microscope depends on its numerical aperture NA, which is roughly speaking related to the opening angle of an optical system where light can enter or leave, giving the Abbe diffraction limit

$$d = \frac{\lambda}{2NA} \tag{3.1}$$

with λ being the wavelength [200]. Therefore, about 200 nm is the theoretical resolution limit [201].

For measurements, a Zeiss Axiolab A microscope is used with a PixeLink webcam to collect digital images. The relation between the magnification and the respective pixel size can be found in Tab. 3.1.

Magnification	Pixel size
2.5	6.26 μm
2.5	3.11 μm
10	0.82 μm
50	0.17 μm
100	82 nm

Table 3.1: Calibration parameters for different magnifications of the optical microscope.

3.2.3 Scanning Electron Microscopy

In a modern optical microscope, the resolution is not only limited by the optical system but also by the wavelength of the wave used as seen in formula 3.1. Since electrons have a much shorter de-Broglie wavelength than visible light, probing material with electrons allows a resolution down to 1 nm and below. A scanning electron microscope (SEM) uses electrons accelerated in an electric field and scans the focused electron beam over the sample. With an applied acceleration voltage V the kinetic energy and the momentum p of the electrons can be calculated, which in turn is related to the de-Broglie wavelength as [202]

$$\lambda_e = \frac{h}{p} = \frac{h}{\sqrt{2m_e eV}} \tag{3.2}$$

with the Planck's constant h, the electron mass m_e, and the elementary charge e. The typical acceleration potential of order 5 keV is low enough to neglect relativistic effects.

The electrons generated by an electron gun and are converged by an electromagnetic lens and deflected by scanning coils. This allows scanning line-by-line over the sample. The focused electron beam interacts with the surface of the sample, mainly secondary electrons and backscattered electrons but also characteristic X-rays are produced. Counting the (secondary) electrons with appropriate detectors, local structural, morphological, and chemical information is revealed [201]. An electrical grounding of the sample is beneficial, otherwise, impinging electrons are deflected from the charged surface. Therefore, it is beneficial to investigate layers on conductive substrates or to use conductive graphite tape. Primary electrons scatter inelastically with loosely bound electrons, which are emitted successively from the surface up to a depth of a few nanometers (primary electrons lose their energy during penetration) [201]. Secondary electrons hereby need kinetic energy higher than the work function of the material to escape and to be subsequently detected. Thus, elevated regions and materials with high electron densities create more secondary electrons, visualized by a brighter pixel of the corresponding 2D map. Therefore, SEM measurements are generally not suitable for detecting the topography of the probed layers. The SEM measurements were performed with an *NVision40 FIB-SEM* (*Carl Zeiss*) at the ZNN of the Walter-Schottky-Institut (WSI) of the Technical University of Munich.

3.3 Reciprocal-Space Structural Characterization

This section describes the structural characterization by means of GISAXS/GIWAXS in the course of the post-flight characterization of the space solar cells. They were performed at the DESY Synchrotron P03 beamline on the solar cells [203]. To avoid detector saturation, the solar cells were probed in between the metal electrodes in the vicinity of the active area. A beam of $23 \times 32\ \mu m^2$ shape with a monochromatic X-ray energy of 12.9 keV (corresponding to 0.961 $\AA$)

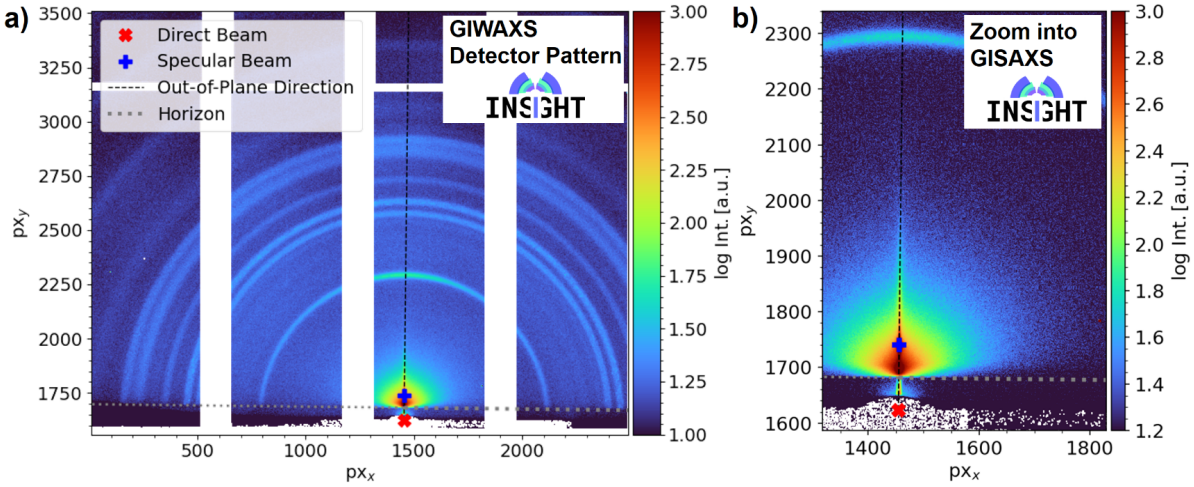

Figure 3.6: Exemplary raw 9M lambda detector mixed GISAXS/GIWAXS image with focus on the wide-angle region in a) and the small-angle region showing diffuse scattering in b). Geometry guidelines include the horizon and the vertical direction and the direct and specular beam positions are indicated by marks.

with a high brilliance impinged the samples at an incidence angle of 0.4°, which is above the critical angle of the involved materials, to probe the buried morphology and crystal structure in the bulk active layer of the solar cells.

The measurement geometry is shown in Fig. 2.14, where different detector configurations were used for GISAXS and GIWAXS, respectively. For GISAXS, a Dectris Pilatus 1M detector was used behind a vacuumed flight tube at a distance of 2701 mm. For GIWAXS, a Dectris Pilatus 300k detector was positioned at a distance of about 116 mm. Exemplary GIWAXS and GISAXS detector patterns can be seen in Fig. 3.6 with the polycrystalline rings and the diffuse scattering at the Yoneda region, respectively.

For data analysis, the Python-based software INSIGHT is used that Manuel A. Reus and I wrote together to process large data sets of in-situ measurements, to have full control of the analysis operations, to assess the unbinned data directly, and to customize evaluation depending on the system [170]. It puts the focus on efficient reduction of time-resolved data and the scripting-based workflow from raw data to the final graphs within a single script allows for modification of the data processing routine at any step within the process. Efficient computation shall enable the first data reduction directly at the beamline to assess the experiments' success.

3.3.1 Grazing-Incidence Wide-Angle X-ray Scattering

Data reduction was performed with the software INSIGHT, including typical GIWAXS geometrical and intensity corrections (solid-angle correction, detector pixel sensitivity correction, polarization correction, and air attenuation correction) [170, 172]. See our INSIGHT publication (currently in prep.) for an overview of the corrections, alternatively, in Jiang et al. (2015) and Claudia Palumbiny's thesis detailed explanations of the effects and corrections can be found [172, 176]. In recent work, Steele et al. published 'How to GIWAXS', a paper giving a broad overview of the methods and usage of the technique [204]. Since the footprint on top of the sample can move a distance of several mm, for GIWAXS analysis, an individual correction of the sample-detector distance was performed. For the perovskite solar cells, the (001) MAFA perovskite ring was corrected to q=1.0089 Å^{-1} [205]. The ITO peak position was used for correction for the organic solar cells [206]. A Si attenuation of 3.50 mm^{-1} and a horizontal polarization of 0.98 was used, and an air attenuation coefficient of 3.01 $\times$ 10^{-4} mm^{-1} was used for GIWAXS [207].

For the analysis of the GIWAXS data, radially-integrated azimuthal (tube) cuts and azimuthally-integrated radial (cake) cuts were performed in the qr-qz plane (compare Fig. 3.7). For the perovskite solar cells, tube cuts of the (001) perovskite Bragg peaks were performed by cutting the central 1 σ of the perovskite reflex and locally subtracting the intensity average of an inner and outer ring with 0.5 σ width in a distance to the reflex center of 2.5 σ on an angular grid of 60 points. For the PbI_2 Bragg peak, the central intensity within 1 sigma was locally

[5]The graining algorithm uses adaptive binning with irregular bins in q-direction, reflecting the grouped data points to avoid classical binning artifacts.

subtracted with inner/outer annuli with a width of 0.5 σ at a distance of 1.5 σ to the center. The resulting tube cuts were normalized to unity area. A half-circle sector cut that covered all scattering intensity (pseudo-XRD [123].) was performed and binned for further analysis. The resulting line-cuts were intensity normalized in the region 0.6-0.7 nm^{-1} where the data appeared flat and no significant features were in the vicinity, except stated differently. For the organic solar cells, sector cuts in out-of-plane (sample-plane) direction from -25° to +25° and in in-plane direction from 55° to 85° have been performed.

3.3.2 Grazing-Incidence Small-Angle X-ray Scattering

All the GISAXS data were reduced with the software INSIGHT [170]. For analysis of the GISAXS data, vertical and horizontal line cuts were performed (compare Fig. 3.8). An angular width of 0.02°, was used for the vertical line cuts. To maximize the signal arising from the polymer bulk-heterojunction active layer, the horizontal line cut was performed around the critical angle of the polymer ([184, 186]) within 0.095 to 0.115°, resulting in a cut-width of 6

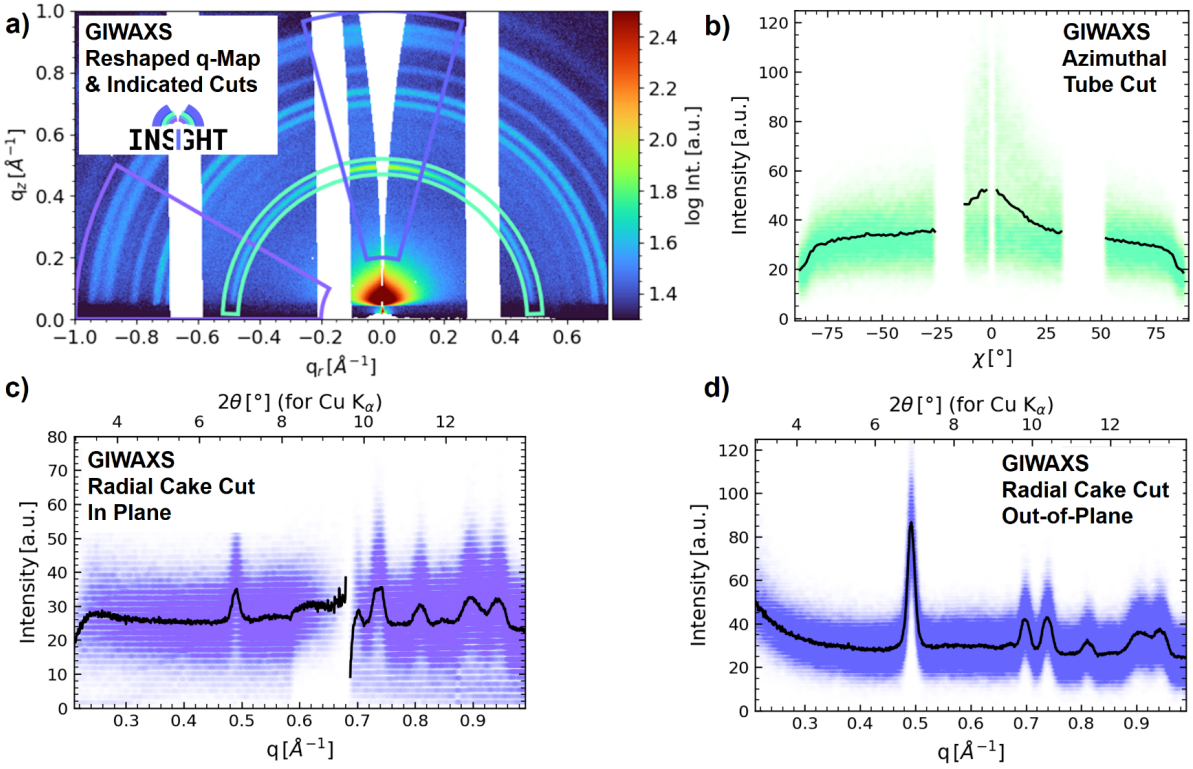

Figure 3.7: GIWAXS analysis of the image shown in Fig. 3.6a). In a) the reshaped q_r-q_z map is shown including GIWAXS-typical radially integrated azimuthal tube cut and azimuthally integrated radial cake cuts in color. b)-d) shows the corresponding cut data in the respective colors. The black solid line results from the binning of the raw data (every single colored point represents the data of one pixel). In the azimuthal tube cut, the same data as in the orientation sphere in Fig. 2.15 is shown.

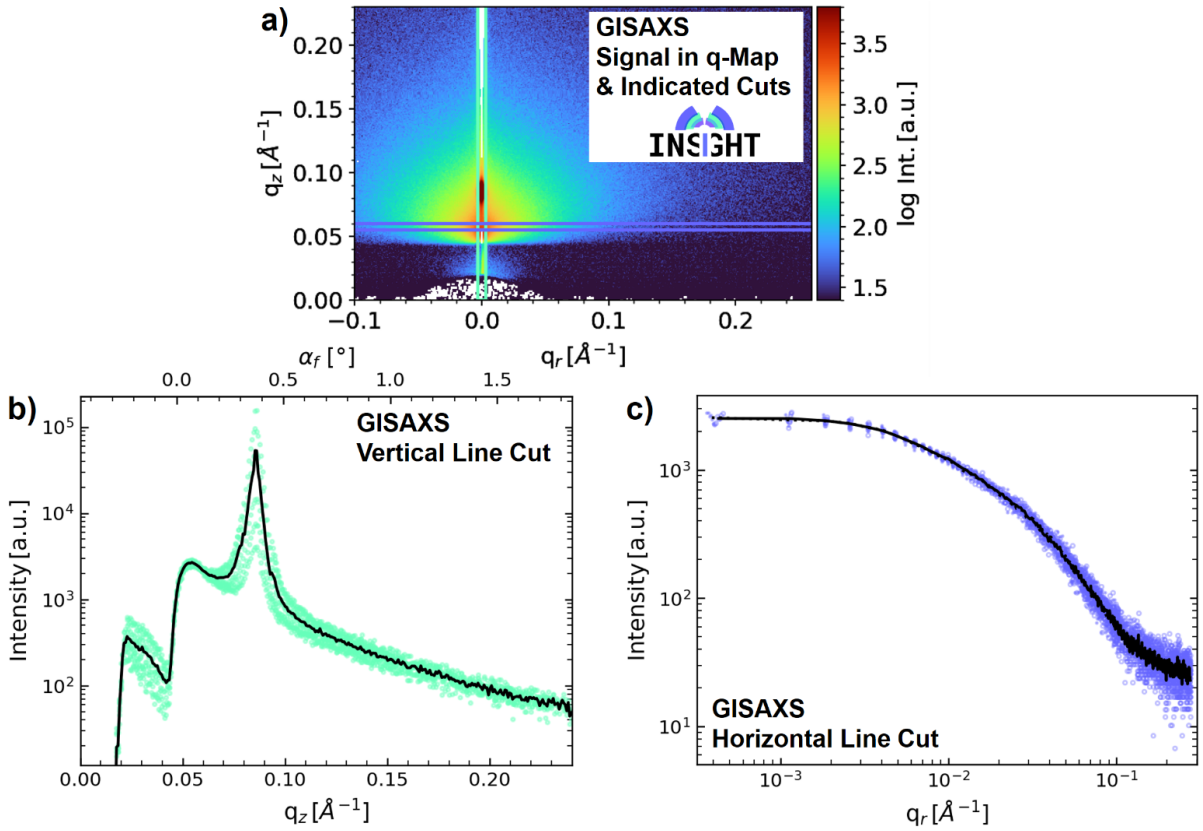

Figure 3.8: GISAXS analysis of the image shown in Fig. 3.6b). In a) the small-angle signal is shown with colored cut contours in vertical and horizontal directions; the corresponding linecuts are found in the respective figures in b) and c). Each colored point corresponds to one pixel intensity and the solid lines show the grained data[6]. Note that the horizontal axis of a) and c) is q_r instead of the usually seen q_y in GISAXS (the latter is a result of the small-angle approximation q_x=0, which is valid, but obsolete in INSIGHT since also q_x is consistently calculated). Using q_r or q_y is hardly distinct in the resulting horizontal line cut and does not influence any subsequent modeling, but INSIGHT offers also the possibility to explicitly cut in q_y if desired.

pixels, from which the arithmetic mean including standard deviation was determined for each pixel row.

The resulting line cut data was folded onto one side and then modeled (see Subsec. 2.4.14) in the framework of the distorted-wave Born approximation (DWBA) and the local-monodisperse approximation (LMA) of three decoupled cylindrical form factors in a 1-D paracrystalline structure, making use of the effective interface approximation (EIA) [186]. For the form factor sizes and the structure distance, normal distributions were included in the DWBA-based LMA. For the modeling of the perovskite solar cells, no structure factor was assumed, i.e., no further assumptions for the lateral distribution of the domains were needed [208]. The standard deviation of the size distribution of the form factors was fixed at $0.7\,\sigma$. For the modeling of the organic solar cells, structure factors were required to describe the measured data with the model. Where possible, the form factor standard deviation was fixed to similar values to maximize the com-

parability of the resulting model parameter values. As explained in earlier work, the number of scattering centers contributing to the respective GISAXS signal and the relative number of scattering centers was calculated from the model fits [208].

3.4 Optoelectronic Characterization

3.4.1 UV-Vis Spectroscopy

UV-vis spectroscopy is a technique to quantify absorption, transmission, and reflection within the UV (ultra-violet) and visible (and near-infrared) range. Usually, a deuterium gas discharge lamp is used to create a continuous spectrum in the UV range, and a tungsten halogen lamp for the higher wavelengths. A grating acts as a monochromator to select the wavelength and a set of lenses directs half of the beam toward the sample (probe beam) and a half to the reference via a beam splitter (reference beam). The baseline and 100% transmission are measured by using a totally blocked probe beam and a free probe beam (without the sample). For transmission measurements, typically an identical substrate is used in the reference beam in order to directly measure the relative transmission of the sample film compared to the reference substrate. This allows for canceling out the time-variability of the lamp intensity or spectral changes during the measurement.[7] The resulting measurement is the relative spectral transmission of sample $I(\lambda)$ and reference $I_0(\lambda)$,

$$T(\lambda) = \frac{I(\lambda)}{I_0(\lambda)}. \tag{3.3}$$

A frequent representation of UV-vis measurements uses the absorbance $A(\lambda)$, which is defined as the negative decadic logarithm of the transmission

$$A(\lambda) = -\log[T(\lambda)]. \tag{3.4}$$

The absorbance $A(\lambda)$ can be expressed via the Beer-Lambert law with the optical thickness of the material times the path distance inside the material $\tau l = \epsilon c l$, where the optical thickness is expressed by the molecular attenuation coefficient ϵ and the molar concentration c [209]. The absorbance is a unitless quantity and can be converted to transmission on the fly for plausibility checks ($A = 1$ corresponds to $T = 10\%$, $A = 2$ corresponds to $T = 1\,\%$, and so on). Note that the absorbance is something entirely different than the (physical) absorption (ranging from 0 to 1). Also, since absorbance is a direct function of the transmission, it cannot be distinguished between absorption and reflection of the sample. For this purpose, however, the concept of the integrating sphere allows us to directly measure spectral reflection and absorption. Also should be added, that measurements of (e.g.) perovskite precursor solutions are preferably done with short path lengths inside the cuvette, and in general diluted non-turbid solutions are required, otherwise Mie-scattering biases the results.

[7] It is advisable to control the calibration measurements by repeating the blocked sample beam and free sample beam measurement from time to time to avoid undesired artifacts and ensure high-quality measurements.

UV-vis absorbance measurements of semiconducting materials allow the extraction of information about the band gap of the probed material. For inorganic semiconductors, the so-called Tauc plot allows us to extract an approximate estimate of the band gap [210]. In these Tauc plots, polycrystalline or amorphous materials give rise to exponential sub-bandgap states that can be linked to the (energetic) disorder in the material (Urbach tail) [211].

The measurements done in this thesis are done using a Perkin Elmer Lambda 35 in transmission mode. A wavelength range from 280-1100 nm with a scan speed of 480 nm/min is used. Slits and grating settings are used to achieve a bandwidth of 1 nm and a measurement step size of 5 nm. For the fused silica measurements shown in Chapter 6, no reference was used in the reference beam path, the transmission measurements show the transmission of glass and soot.

3.4.2 External Quantum Efficiency Measurements

External Quantum Efficiency (EQE) describes the probability for a light quantum (photon) to generate electrical current in solar cell devices. Heuristically speaking, we want to know the amount of electrons generated per incoming photon at a given wavelength. 'External' here means that it is the measurement of the entire device, without correcting for lost photons due to reflection or transmission.[8]

In the Oriel Quantum Efficiency Measurement Kit (Newport, see Fig. 3.9), a broadband Xenon lamp spectrum is collimated and passes a filter and then a monochromator (Cornerstone, calibrated 8/2021, Newport) to shine monochromatic light (via a focus lens) on a test solar cell inside a closed dark chamber. With a slit assembly, the size of the beam on the solar cell can be adjusted. Reinhold manufactured a tiny pinhole slit with which the beam diameter at the focal plane (sample position) can be reduced to less than 2 mm in either direction which must be the **only mode of operation of the EQE**, as detailed below.

For EQE measurements, a stable silicon (photo)detector (DETL-L-SIUV-RC, calibration 8/2021, Newport Corp.) with a known spectral response (SR_{PD}) from the calibration file is used first. While scanning the wavelength with the monochromator, the resulting photocurrent is measured. In detail, a chopper together with a lock-in amplifier (Merlin Digital Lock-in Amplifier, Newport) is used to measure a clean current signal (noise or constant bias insensitive) in the photodetector which is amplified and converted to a voltage (using a pre-set gain) that is recorded. The systems are connected to a computer using the TRACQ BASIC software, which is utilized as the interface to control the measurements and acquire the data. After this, the measurement is repeated with a test solar cell. The spectral response of the test solar cell is then

$$SR_{T}(\lambda) = \frac{I_{T}(\lambda)}{I_{PD}} SR_{PD}(\lambda), \tag{3.5}$$

[8] By measuring reflection and transmission in addition, the Internal Quantum Efficiency can be determined by scaling the EQE with absorption. This is helpful to distinguish the loss mechanisms due to being sensitive to photoconversion properties only [105].

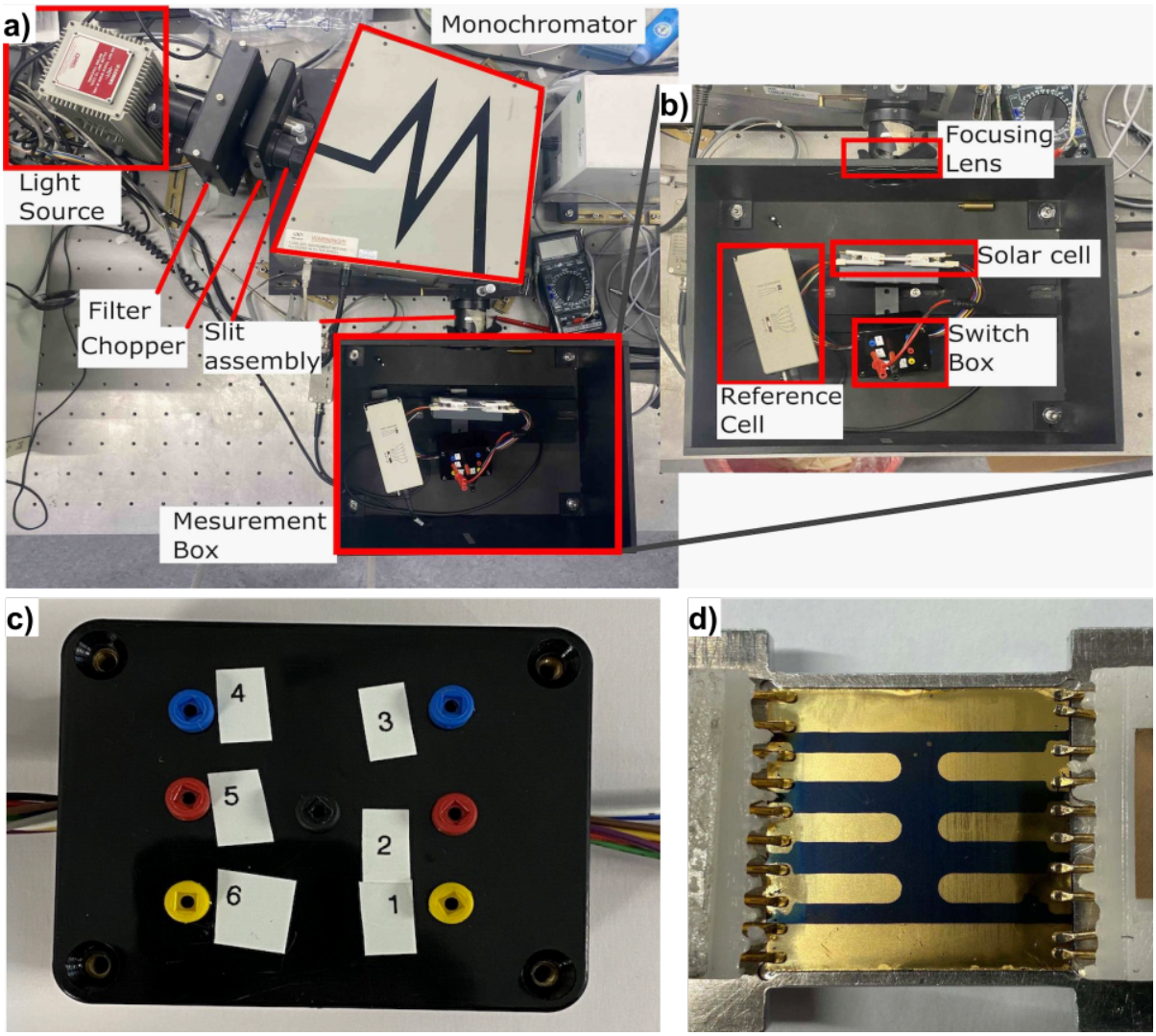

Figure 3.9: The External Quantum Efficiency measurement device after its movement into the glove box laboratory and reactivating it. a) The general components viewed from the top include a broadband light source, filter and choppers, monochromator, and measurement box. In the measurement box b) the Si reference cell or the test solar cell can be moved into the light beam. The switch box c) allows for selecting one solar cell of the six that make up a single module in the 6-layout, which can be seen in d) including the contacting clamps. Images reused from Paul Pucknus' Bachelor thesis [212].

where $I_{\mathrm{T}}(\lambda)$ and $I_{\mathrm{PD}}(\lambda)$ are the measured photocurrents of the test solar cell and the photodetector, respectively. For conciseness, internally the respective (amplified) voltages are used in the calculation.

This equation only holds if the entire monochromatic beam is recorded by a photodetector and test solar cell, respectively. Here should be clarified: Measurements performed this way are quantitative. The alternative method would be to use a beam larger than the active area of the photodetector and of the test solar cell and use the ratio of apertures as a current-scaling factor (comparing current densities). However, in practice, this is valid only for homogeneously

illuminated areas. For our EQE device, however, there are visible inhomogeneities within the beam area, These strong local light intensity differences of a factor of 2 or more make it hard to reproducibly align the test solar cell and photodetector at the same position. In addition, the position and strength of beam inhomogeneities are a function of the wavelength, rendering this method unreliable regarding the absolute current scaling. Therefore, it is strongly recommended to not use the latter method, but use measurements based on the full-beam exposure to ensure consistency for quantitative analysis. For more detail on this, and the general measurement process, please refer to Paul Pucknus' Bachelor Thesis [212].[9] Then, the spectral response is converted into the EQE via

$$\mathrm{EQE_R}(\lambda) = \mathrm{SR_R}(\lambda)\frac{hc}{e\lambda}. \tag{3.6}$$

The spectral response gives a wavelength-dependent quantity of extracted short-circuit current per incident light power, and the EQE describes the probability of generating a charge for one incident photon at a certain wavelength.

A test measurement was performed where the EQE of the calibrated Fraunhofer KG5 reference solar cell was measured and compared to the EQE according to the calibration data sheet and Eq. 3.6 (see Paul Pucknus' Bachelor Thesis [212]). As a result, the absolute average difference between the measurement and the Fraunhofer calibration file was less than 2 %, with a systematic offset toward higher values of the measurements. Likely explanations for the systematic offset are a reduced effective photodetector response due to cable resistances, a slightly higher gain in the amplifier for the test solar cells, or the measurement was performed on a spot where a reduced number of top-contact wires of the reference solar cells artificially increased the EQE beyond its large area average. As a last note, the automatic grating change should be changed from 400 nm to 430 nm to minimize artifacts introduced at the grating change and the abrupt beam intensity change.

3.4.3 Solar Simulator J-V Measurements

The probably most important characterization of solar cells is their electrical characterization under illumination. The collection of J-V curves allows us to assess photovoltaic parameters (cf. Section 2.2.4). For the laboratory measurements carried out in this work, a LOT Quantum Design LS0500 reflector Xenon light source is used with a spectral filter to match the AM1.5G solar spectrum. A photograph of the setup is shown in Fig. 3.10. It has an ABA classification,[10] which means an A-rated spectral match (a spectral power difference of less than 25 % within 100 nm bandwidth), a B-rated spatial uniformity (less than 5 % deviations within the illuminated area of 45 x 45 mm^2, and an A rated temporal stability (less than 0.5 % short-term fluctuations and less than 2 % long-term fluctuations).

[9] This attempt to use aperture scaling instead of full beam measurements is the main reason why the EQE could not be used for quantitative measurements but only for qualitative comparisons previously.

[10] A comprehensive overview of the different classification standards can be found on the Newport page, accessed 2023.07.24.

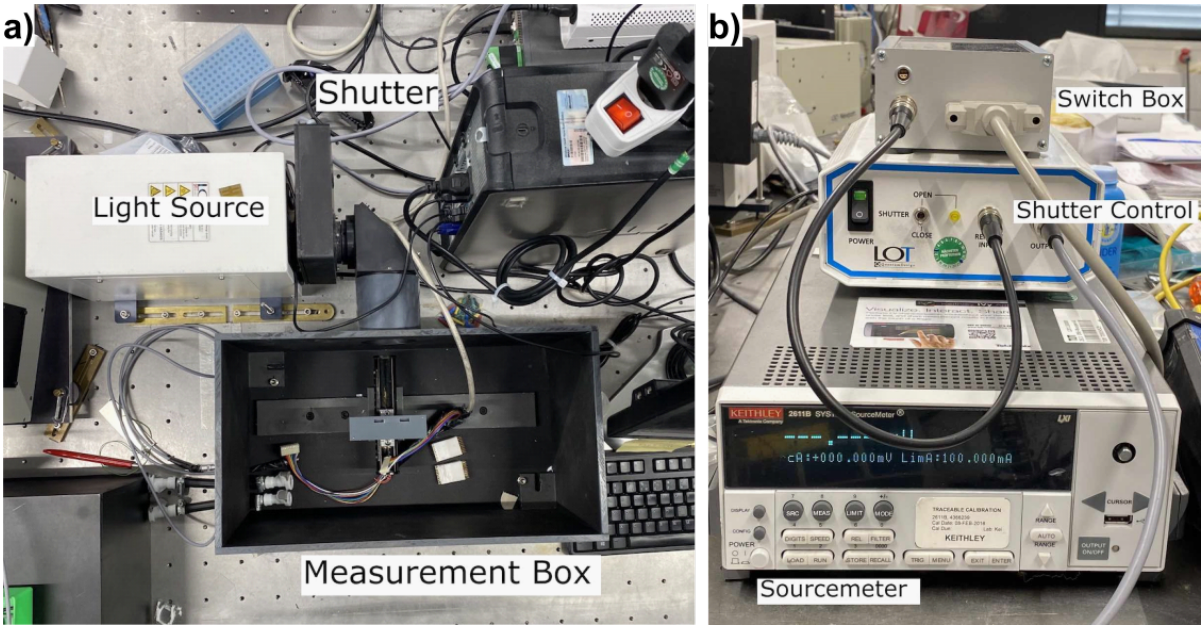

Figure 3.10: The solar simulator after the movement into the glove box laboratory. a) The Xenon light source can be closed by the shutter to enable dark-current solar cell measurements. The six solar cell layout module is connected via the clamps, similarly as shown in Fig. 3.9 via four-point contacting. Alternatively, the eight solar cell layout can be used by plugging in the copper holder designed by Johannes Schlipf ([104]). b) The measurements are performed by a Keithley 2611B source meter. Control of the Keithley, the shutter control, and the switch box (with relais to iterate through the different solar cells within a module) is done with Python-based computer software. Images reused from Paul Pucknus' Bachelor thesis [212].

Apart from the spectrum available from the manufacturer's datasheet, we measured the solar simulator spectrum in the central region of the light spot at the sample position with a CAS 140CT spectrometer from Instrument Systems, see Fig. 3.11 for the two graphs, together with the standard AMG1.5G solar spectrum and the EQE of the KG5-filtered silicon reference solar cell certified by Fraunhofer ISE in 2017.

This cell has been calibrated by Fraunhofer ISE: under ideal $1000\,\mathrm{W\,m^{-2}}$ AM1.5G exposure, it should give a short circuit current of $47.95\,\mathrm{mA}$.[11] By assuming a similar spectrum of our lamp and the AM1.5G spectrum, we can tune the lamp intensity to give a similar current reading on the Fraunhofer reference cell, which needs to be done for all measurements by tuning the lamp intensity after giving it about 30 minutes time to warm up and stabilize.

Here, the concept of spectral mismatch factor shall be introduced. Since the lamp spectrum and AM1.5G spectrum deviate, and the absorption characteristic of the reference cell and the test solar cell is distinct as well, there can be deviations in the current measurement of the test solar cell in the solar lamp spectrum. In other words, while for the reference cell, the lamp

[11] This value is calculated by first converting the Fraunhofer calibration spectral response ($\mathrm{SR}_R(\lambda)$) file to the $\mathrm{EQE}_R(\lambda)$ as in Eq. 3.6. In the second step integrating the reference $\mathrm{EQE_R}$ under AM1.5G via gives the (ideal) reference solar cell short-circuit current $\mathrm{I_{R,AM1.5G}} = \int \mathrm{EQE_R}(\lambda)\, E_{\mathrm{AM1.5G}}(\lambda) d\lambda$

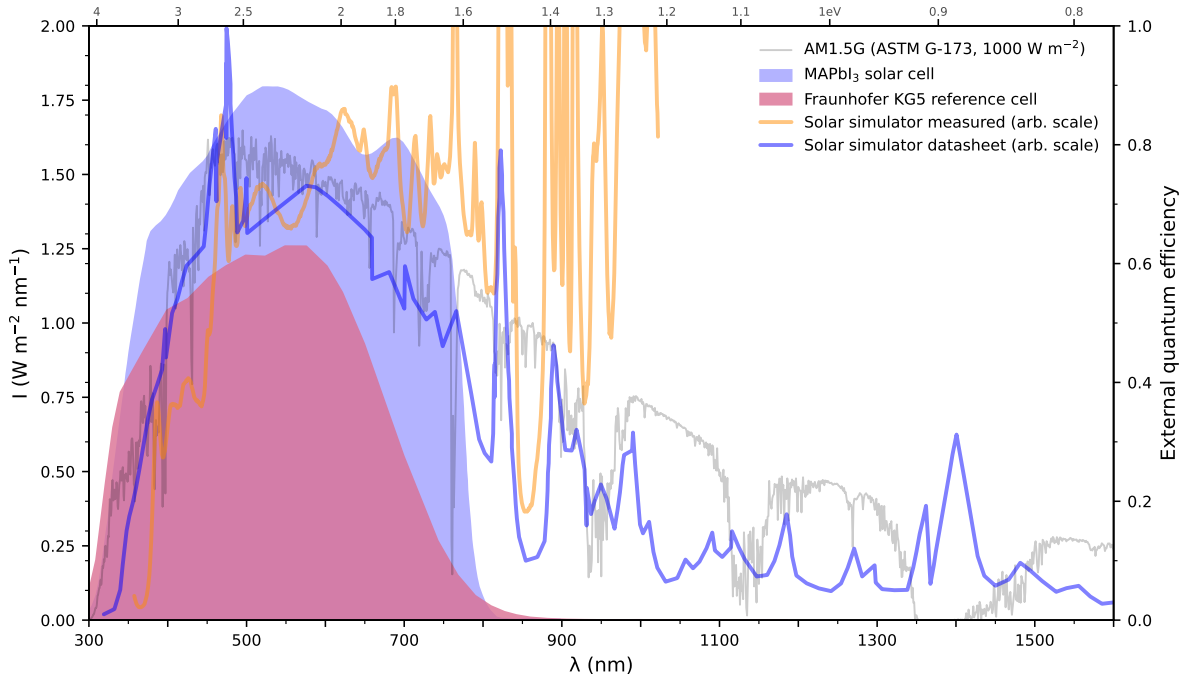

Figure 3.11: Spectra of the solar simulator. In the background, the AM1.5G standard spectrum is shown as a grey line. The solar simulator spectrum is measured with the spectrometer (see text) in orange and the manufacturer spectrum in blue in arbitrary scale. In addition, the purple and blue areas show the EQE of the Fraunhofer KG5 reference cell and a MAPI perovskite test solar cell, respectively.

might appear equally bright compared to the AM1.5G spectrum (reference cell measures same current), the lamp spectrum appears to have a different brightness for the test cell – due to the different EQE of the test cell, it converts a spectrally different ensemble of photons to charges, causing a different current. To calculate the spectral mismatch factor, one needs to have the following data (in the following the spectra are denoted with capital E to avoid confusion with the current symbol I):

- The AM1.5G standard spectrum $E_{\mathrm{AM1.5G}}$.
- The $\mathrm{EQE_T}(\lambda)$ of the test solar cell (measured in the EQE measurement device).
- The typical calibration current for the reference solar cell under AM1.5G of 47.95 mA.
- The (short-current) measurement of the reference solar cell in the solar simulator $\mathrm{I_{R,SoSi}}$.
- The (short-circuit) current of the test solar cell in the solar simulator $\mathrm{I_{T,SoSi}}$.

From the first two datasets, the test solar cell short-circuit current under AM1.5G can be calculated by integrating

$$I_{\mathrm{T,AM1.5G}} = \int \mathrm{EQE_T}(\lambda)\, E_{\mathrm{AM1.5G}}(\lambda) d\lambda. \tag{3.7}$$

We would measure this current for our test solar cell in the solar simulator if the spectrum were ideal, i.e. identical to the AM1.5G spectrum.

Then the ratio of test cell target $I_{\mathrm{T,AM1.5G}}$ and current measured $I_{\mathrm{T,SoSi}}$ is the mismatch factor M,

$$M = \frac{I_{\mathrm{T,AM1.5G}}}{I_{\mathrm{T,SoSi}}}, \tag{3.8}$$

which is the 'easy' form that we obtain for $I_{\mathrm{R,SoSi}} = I_{\mathrm{R,AM1.5G}}$, which is done by adjusting the solar simulator lamp to the calibration current of 47.95 mA. Without this constraint, the mismatch factor is more general

$$M = \frac{I_{\mathrm{T,AM1.5G}}}{I_{\mathrm{T,SoSi}}} \frac{I_{\mathrm{R,AM1.5G}}}{I_{\mathrm{R,SoSi}}}. \tag{3.9}$$

For the upper variant, we thus only need to first measure the test solar cell in the solar simulator with the lamp intensity calibrated to a reference solar cell current of 47.95 mA, and second calculate the test solar cell current under AM1.5G from the EQE measurement, to form the ratio in Eq. 3.8. One can also think of a current scaling factor that, if used for scaling the lamp intensity, results in an irradiance of 1 effective sun on the test cells. For good MAPI solar cells, Paul Pucknus performed the calculations in August 2022 and found a slightly lower current from the EQE integration than from the solar simulator measurement [212]. The current mismatch is less than 10 % ($M \geq 0.9$) – the measurement of the solar cell in the solar simulator slightly overestimates the current.

Inspecting the EQEs of reference and test solar cell in Fig. 3.11, the perovskite solar cell shows a relatively flat EQE extending towards higher wavelengths to roughly 700 nm. In comparison, the silicon reference cell EQE declines above 600 nm. In addition, the measured solar simulator spectrum is stronger in the range 600-700 nm than the AM1.5G. The perovskite solar cell can harvest this excess light from the spectral region better than the reference cell. This is likely one part of why the perovskite solar cell solar simulator current exceeds the EQE current. Here, an essential note for interpreting the mismatch factor in perovskite solar cells: The mismatch factor derived above assumes that the solar cell tested behaves the same during EQE and solar simulator measurements. However, the EQE setup using monochromatic light has a comparably small total light intensity compared to the standard 1 sun used in the solar simulator. Therefore, the charge density inside the perovskite solar cell is much higher in the solar simulator, which triggers dynamic effects that cause higher current measurements in the solar simulator compared to the EQE measurements [213]. Different effects might contribute to this discrepancy, one being the slow response of perovskite solar cells where the interaction of the chopper frequency with dynamics inside the solar cell might occur [213, 214].

For measurements, the solar cell is connected electrically in the copper holder (for 8 solar cell layout, active cooling possible) or the clamp holder (for 6 solar cell layout). Either holder is making use of 4-wire measurements to minimize parasitic resistances. While for the 8-layout each spring pin is connected with two wires (the measurement and the sensing wire), for the 6-layout each clamp finger is connected with a wire. Hence, contact resistances occurring between the pin and metal electrode are not mitigated in the 4-wire measurement of the 8-layout, while there is an actual 4-contact measurement for the 6-layout.

The sample chamber should be closed for measurements to avoid parasitic light from outside, especially for dark-current measurements. The solar cell is electrically connected to a Keithley 2611B Source Meter (Tektronix Inc.), which addresses individual solar cells of the module via the electronic relais box (Switch Box in Fig. 3.10). Here, the Keithley usually acts as a voltage source, biasing the solar cell to a specific voltage to measure the current as a function of voltage (Keithley is the current sink). Biasing the solar cell with a voltage is physically identical to connecting the solar cell to a specific load since, in the latter case, the voltage drop at the load is directly exerted on the solar cell. The advantage of the Keithley is that voltages outside the solar cell voltage range enable measuring the diode curve outside the quadrant to estimate series and parallel resistances (cf. Section 2.2.4). A computer communicates with Keithley via Python software and saves the recorded data. The measurement parameters and settings (e.g., sweep-voltage, direction, speed, solar cell selection, shutter, number of measuring loops, file directory). Also, a script has been developed to enable maximum power-point tracking.

4 Design of the OHSCIS Experiment

Most results shown in this chapter have been published in the article *An experiment for novel material thin-film solar cell characterization on sounding rocket flights* [215] (L. K. Reb et al., *The Review of scientific instruments* 92 (7):074501, 2021, doi:10.1063/5.0047346). Some results are reused from Benjamin Predeschly's Master thesis [190].

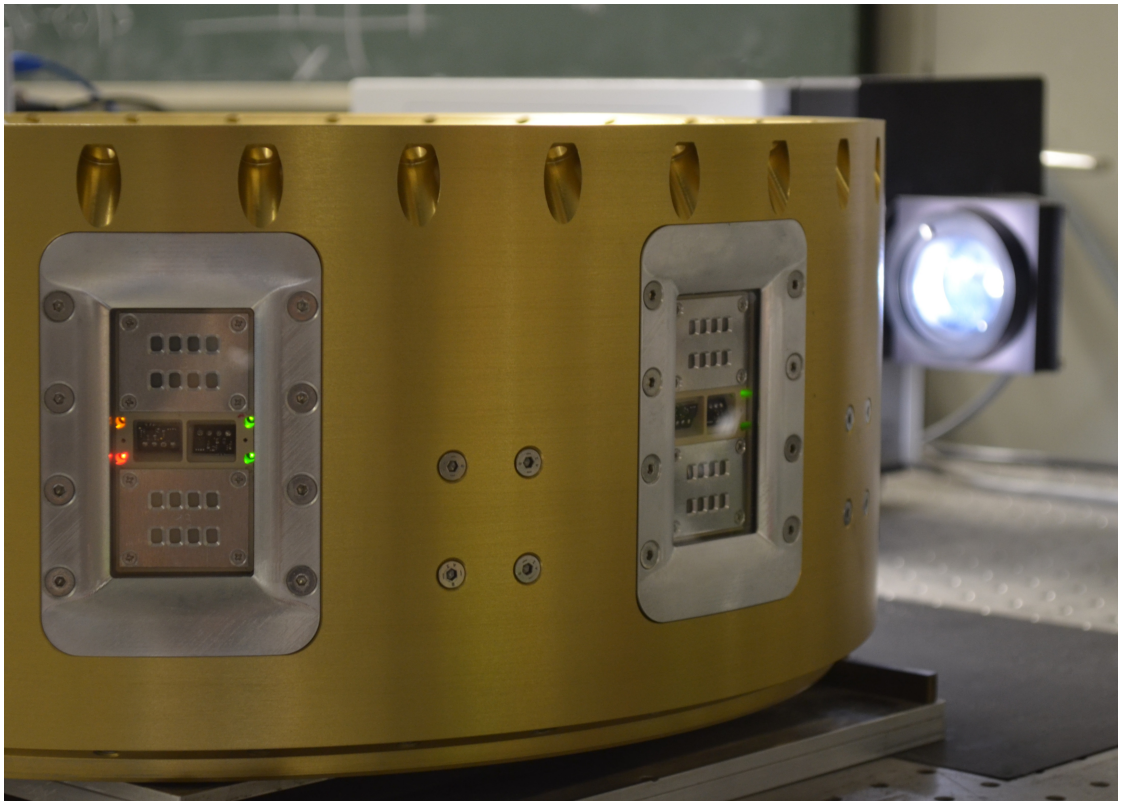

Figure 4.1: The OHSCIS experiment during solar simulator pre-tests in the laboratory.

This thesis focuses on studying perovskite (and organic) solar cells in space. In this course, the Organic and Hybrid Solar Cells In Space (OHSCIS) module has been developed to enable the testing of novel material thin-film solar cells on a sounding rocket flight. The following chapter details the development, construction, and validation testing of the OHSCIS measurement setup, seen in Fig. 4.1, designed for the electrical characterization of solar cells, and its incorporation in the sounding rocket in the course of the scientific campaign MAPHEUS-8. Measurement results obtained by the OHSCIS experiment during its maiden space flight are presented.

4.1 A Short Project History

The German aerospace center *Deutsches Zentrum fuer Luft- und Raumfahrt* (DLR) emerged as the ideal partner for this collaboration with its MAPHEUS program, where the acronym stands for *Materialphysikalische Experimente unter Schwerelosigkeit* - material science experiments in the absence of gravity. Within the MAPHEUS program, the DLR Institute of Material Physics (DLR-MP) and the DLR MORABA (Mobile Raketenbasis) launch sub-orbital rockets approximately once a year, carrying a couple of different and independent experiments as scientific payloads. These experiments need to fulfill mechanical and electrical requirements, i.e., they must follow norms for mechanical stacking and electrical connections, apart from being capable of coping with the conditions imposed upon the rocket flight.

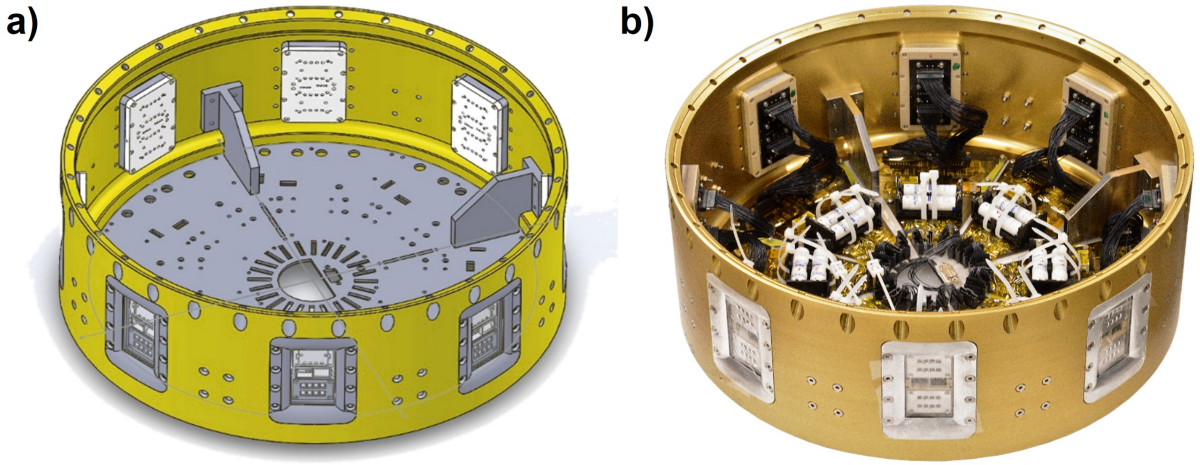

Figure 4.2: OHSCIS Experiment development. a) Computer-assisted drawing (CAD) sketch of the planned experiment module. The base plate with its many cut-outs and the mounting elbows are visible. b) Oblique-view photograph in the pre-flight configuration in Kiruna, Sweden. For a detailed description of the parts, see the next section.

The initial spark of the project was the first meeting between the Group of Functional Materials and the DLR-MP. Lukas Krempl and Sebastian Grott had successfully constructed and recently flown a stratospheric balloon experiment to measure organic solar cells during the flight. With this know-how, the next step toward space seemed within reach. The ad-hoc minimum requirements for the space experiment after the first meeting have been:

- diameter and threads of the ring must be compatible with MAPHEUS specifications
- electronic switching with service module signals according to requirements
- experiment must be flight-ready, i.e., planned, constructed, and tested within less than one year

Additional constraints imposed by the scientific goals of the solar cell experiment:

- symmetric design due to unpredictable payload orientation during the flight

- measure as many solar cells simultaneously as possible
- sunlight must reach the solar cells
- mechanical protection from hot gases during super-sonic ascent is required since the mantle usually reaches temperatures of 200 °C.
- late-access: solar cells must be mountable during the countdown to minimize exposure to terrestrial environment
- monitoring the space environment, and the solar position is crucial for later quantitative data processing

Due to the ambitious timeline, the entire project was conducted with the maxim to:

- recycle as many concepts and electrical components for the electronics of the successful balloon experiment
- keep it simple and stupid wherever possible to maximize fail-safety (KISS principle)
- maximize symmetry and, thereby, redundancy of the measurement setup and data collection

This large and complex project could only be managed by a group of people with clearly distributed roles. Many helpful suggestions from multiple sides make it impossible to provide a complete list of involved persons, but here, the distribution of the main work is briefly listed. My master's student Benjamin Predeschly and I were coping with the mechanical design, where Christoph Dreißigacker helped us with the module ring design and manufacturing to achieve the mechanical boundaries to the MAPHEUS specifications (ATEK/MAPHEUS-8 flight requirements plan [216]). Many mechanical parts were manufactured by the head of our precision mechanics workshop, Reinhold Funer, but some parts were processed at the central workshop in the basement, at the medicine technics workshop, and at the workshop at E15. The electronics were planned, prototyped, optimized, manufactured, programmed, and tested by Dr. Michael Böhmer, head of the Central Technology Laboratory at the Department of Physics. Michael, Benjamin, and I have been working closely together daily, where Michael's experience, ideas, recommendations, and connections greatly contributed to the experiment's success. During the campaign in Sweden, Sebastian Grott accompanied and helped me go through the entire procedure with valuable advice. Any analysis of sensor or measurement data of the experiment's electronics during the validation tests and of the data obtained in the spaceflight has been performed by myself. In the text below, the wording "we" includes but is not limited to the core executing team: Michael, Benjamin, and me.

According to all the considerations and constraints above, it was quickly decided against moving parts, so as not to use any removable mechanical covers or unfoldable solar cells. Discussions about pyro-separating metal covers on top of the solar cells were seriously discussed at that time, even though now they appear unrealistic in retrospect. Consequently, we decided to use glass windows that protect the solar cells but let light through. Initially, we considered using bent glasses with a similar shape as the module ring for better airflow along the payload with minimized turbulence, but they were too difficult to find and too expensive. These are just

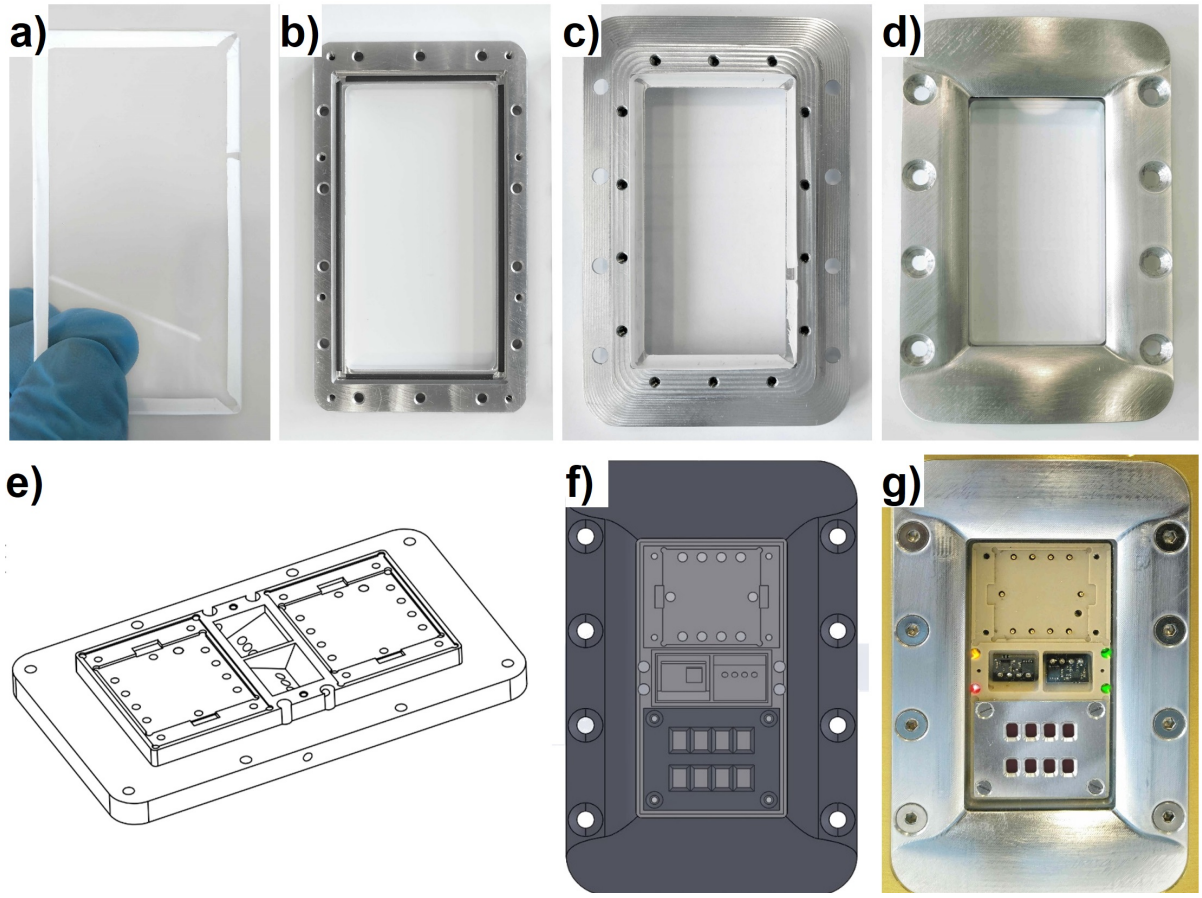

Figure 4.3: Assembly of a hatch insertion module. a) Fused silica wrapped with a PTFE band, b) outer frame with glass and c) inner frame with rubber stripes inserted, d) ready assembled framework, with a discernible bent surface of the outer frame. e) Excerpt of the construction plans of the PEEK solar cell holder. The solar cells are installed in the elevated socket, protruding into the inner frame to place the SCs as close as possible to the glass. f) CAD of a single hatch insertion module. g) Photograph of the assembled insertion module. Inspired by Benjamin Predeschly's Master thesis [190]. For a detailed description of the parts, see the text in the next section.

two examples to illustrate the design process at this early stage. No matter how far-fetched, any possible seemed to be a valid approach worth considering.

The point-symmetry requirement imposed by our solar cells gave rise to the idea of partitioning the electronics, i.e., having multiple copies of the same hardware around the ring. On the planning side, this reduced setup complexity, and manufacturing became simpler since the same components could be used multiple times around the ring. On the testing side, mechanical and software testing was enormously facilitated since a single partition could resemble the measurement behavior of the entire experiment. But then the question arises - what-fold symmetry is the way to go? How many solar cells can we reasonably arrange around the ring? How much space do we need for the electronics? Do we connect the solar cells to the electronics during

late access or design single plug-in modules that carry the solar cells and the electronic circuit boards?

The convergence solution, in the end, is a result of the implementation of the requirements: Rectangular glass windows with high mechanical stability, thermal robustness, and high light transmission must stand vertically in the experiment and be as slim as possible to minimize the reduction of load-bearing mantle circumference. Behind each window should be placed at least two solar cell modules for redundancy considerations that failure of a single module does not make an entire partition a failure. Placing three modules behind a window instead of two would increase the spatial requirements of measurement electronics, increase the larger glass window's fragility, reduce the module's statics, and increase total module height and weight, all driving the decision against pursuing this path.

After deciding on two solar cell modules (one on top of another) behind a single window and ordering the customized glass windows (see Fig. 4.3a), we converged on the electronic components and their possible arrangement. Michael realized that the spatial requirements of the electronic circuit boards would not fit through the mantle cut-out dimensions defined by the window dimensions. Hence, we pursued the route of fixing the electronic circuit boards inside the experiment with the requirement of connecting the insertion modules carrying the solar cells electrically during late access. Due to the circular setup, Michael decided to partition the electronics like a pizza, i.e., each pizza slice is one self-contained measurement setup. A natural choice was consequently to insert one large bottom plate inside the experiment to mount all the electronics on top of it. The spatial requirements of the printed circuit boards limited the symmetry to be not more than eight-fold. Six-fold would have been an option, but effectively reducing the solar cells in the payload. Another advantage of the eightfold symmetry is that typical sunshine illuminates three pairs of solar cells due to the 45°-symmetry while with 60°-symmetry (sixfold symmetry), only two pairs can be illuminated by the Sun.

The basic design converged and Benjamin and I began drawing the detailed technical parts (using Solidworks). Since some parts were already ordered, but other part dimensions were not determinable at this point, the design was a balancing act between concretizing the parts that all needed to fit together and fixing measures to advance the ordering/manufacturing process of the parts. For example, the hatch dimensions and screw positions needed to be set for manufacturing the module ring. However, the counterpart, the outer frame, was a part without determinable sizes, because we did not know how to fix glass windows in metal holders with stability as required for this kind of rocket flight (see Fig. 4.3a)-d) for the final implementation). We needed to set the screw positions that fix the solar cell holder to the frame appliance before we knew the final measures of the PCB connected to the solar cell holder on the back side or the position of the connection plugs. Therefore, especially at the beginning of the construction, some dimensions were defined based on educated guesses and in a way to maximize spatial availability for the remaining parts rather than a generalized optimization of the design (see Fig. 4.3f & g for the insertion module CAD technical drawing and the implementation). 3D printing turned out to be very helpful in the process of iterating solar cell holder prototypes, the arguably most

complex and functional mechanical part of the entire experiment (cf. Fig. 4.3e). This way, we could quickly iterate the part, estimate margins, update adjacent parts, and modify screw positions for the electronics. The entire process ended with the basic concept of the mechanical design of the ring, described in the following chapter.

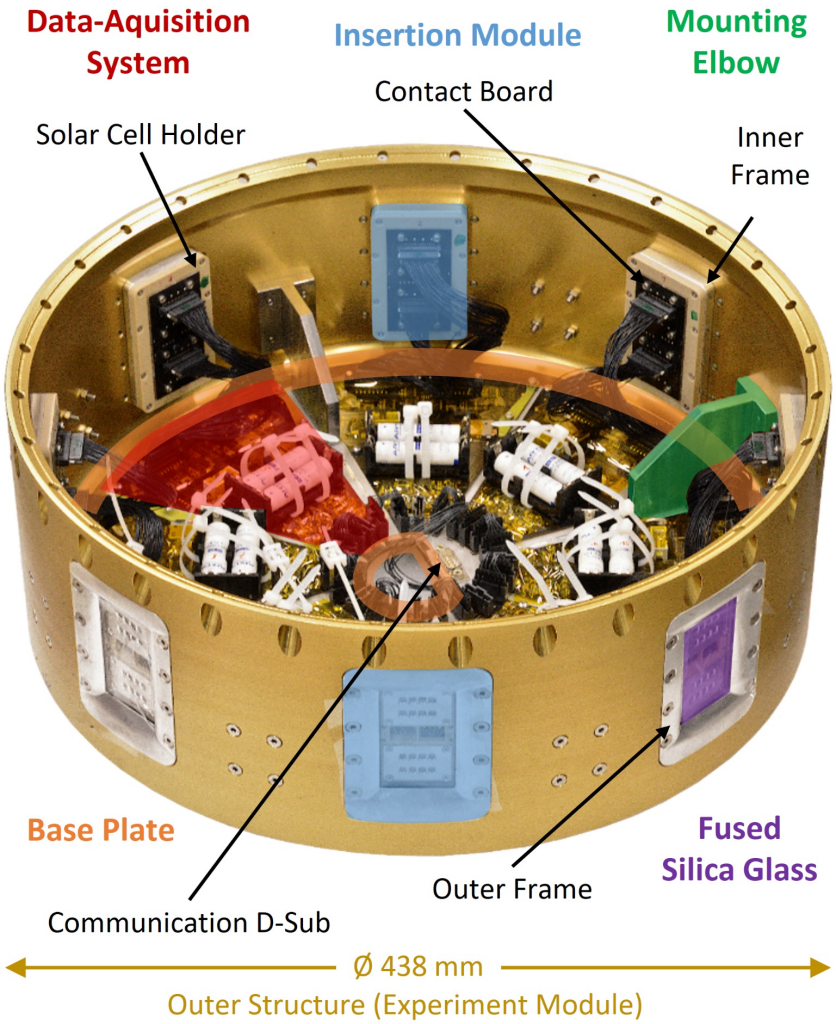

Figure 4.4: OHSCIS Experiment overview. Oblique-view photograph in the pre-flight configuration in Kiruna, Sweden, with colored assembly units: base plate (orange), mounting elbow (green), data-acquisition system (red), and insertion module (blue) with the fused silica glass (purple). Reproduced from Reb et al. with permission [215]. Copyright © 2021 The Author(s).

4.2 Mechanical Design

The experiment is integrated into an anodized aluminum ring with 438 mm (outer) diameter, a height of 170 mm, and a wall thickness of 8 mm. The rather thick wall compensates for structural weakening resulting from the eight cut-outs (hatches). The ring's height is minimized to save weight. In Fig. 4.4, an oblique-view photograph shows the complete OHSCIS experiment, where

different parts are indicated by color. Attached to the inner side of the ring, four stainless steel mounting elbows (green) are attached to the outer structure and center a 3 mm strong aluminum base plate (orange). Stainless steel is chosen here to provide the necessary mechanical strength and to reduce the thermal conduction towards the sensitive electronics, while the aluminum bottom plate works as a heat sink to passively cool the electronics in vacuum. A central cut-out in the bottom plate acts as cable feed-through for the communication cable bundle of the service module and other experiments. The eight symmetrically arranged rectangular hatches in the outer ring structure harbor insertion modules (blue). The insertion modules can be mounted and unmounted from the exterior to access the inner experiment and enable solar cell exchange in the assembled payload state before launch.

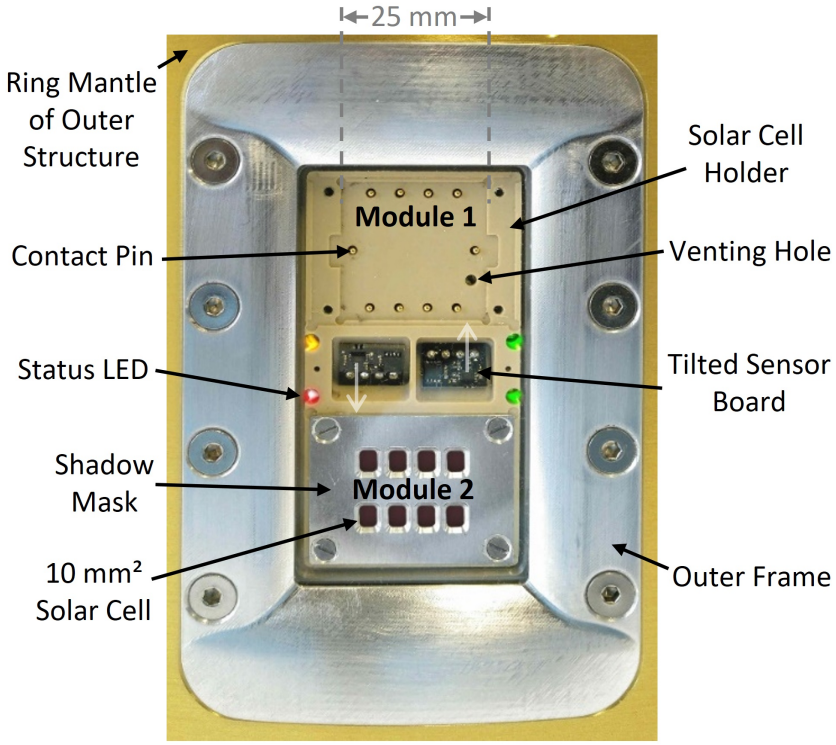

Figure 4.5: Outside close-up view of one of the eight hatches with the plugged-in insertion module. Behind the fused silica window (barely visible), the beige solar cell holder for two solar cell modules is visible. At module position 1 the spring pins for solar cell contacting are visible, in position 2 the shadow mask is assembled, defining eight solar cells with each 10 mm^2 aperture. Between the solar cell modules, two tilted sensor boards (one facing upwards, one facing downwards, indicated with the white arrows) are placed to collect illumination and temperature information. Reproduced from Reb et al. with permission [215], copyright 2021 the Authors.

Each insertion module comprises a fused silica window embedded in two aluminum frames and a solar cell holder, the key part of the insertion module. Fig. 4.5 shows a close-up photograph of the mounted insertion module from the outside. The outer aluminum frame is designed with two continuously varying radii in horizontal and vertical direction to allow for a smooth transition

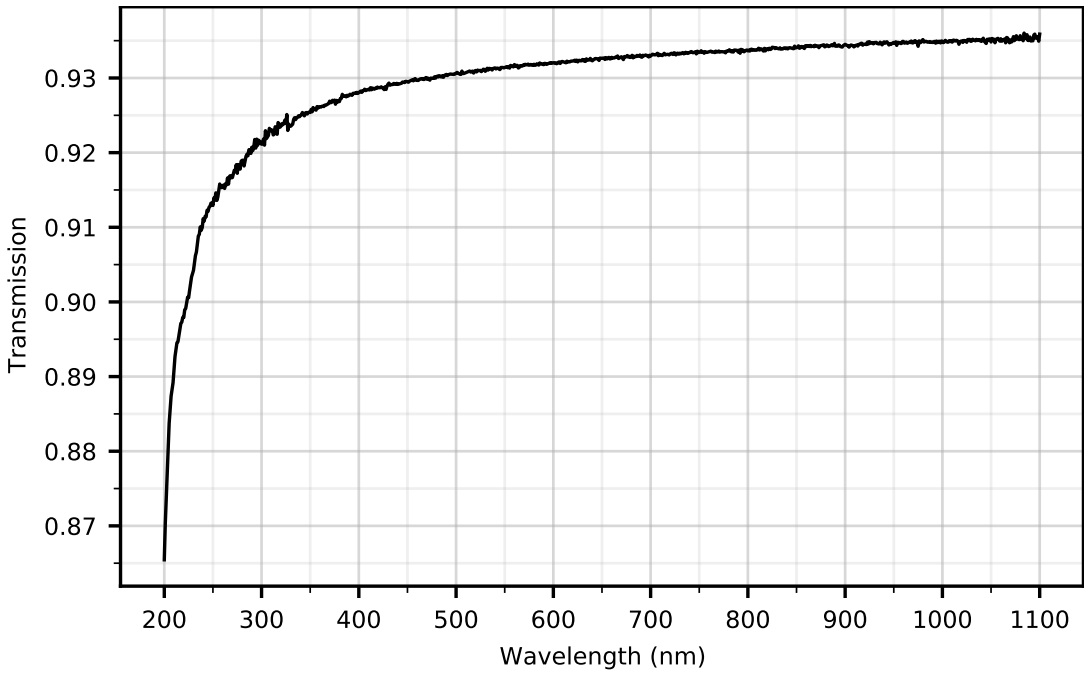

Figure 4.6: Transmission of the fused silica glass (JGS1). Reproduced from Reb et al. with permission [189]. Copyright © 2020 Elsevier.

between the cylindrical ring mantle and the flat window to minimize turbulences of the air-flow profile at the rocket surface during super-sonic flights and consequently friction and heat.

The windows with dimensions of 80x45x4 mm^3 with small bevels are made of fused silica glass (JGS1), a material with exceptional mechanical strength and high transmission across the entire AM0 solar spectrum including the UV-region [38]. In Fig. 4.6 the transmission of the fused silica glass can be found. Basically, the transmission curve shows negligible absorption, as the decline at lower wavelengths follows the expectation according to Fresnel reflection. According to Fig. 2.1 there is not much solar irradiance present below 300 nm, where the glass transmission is still fairly above 90%. The glass is enclosed by the outer frame using Teflon© tape as a thin buffer layer and fitted to the inner frame using an O-ring sealing. The O-ring sealing absorbs shocks, as well as vibrations, and compensates for mechanical material deformations and heat-induced material expansion during flight. In essence, the brittle glass does not touch any metal to minimize the chance of cracking.

The solar cell holder is a central part of the insertion module and is of particular importance for the entire experiment because it carries the scientific payload. It is made of polyether ether ketone (PEEK), a mechanically durable and heat-resistant polymer. The solar cell holder can be unscrewed from the inner frame to mount the solar cell modules. As a safety aspect, even in case of a breaking glass window during flight, the robust PEEK material would withstand the conditions during reentry to protect the inside of the payload from hot gas in-flow. Further, PEEK acts as a thermal and electrical insulator to protect the solar cells from the hot ring mantle during ascent and reentry and to avoid electrical short-circuiting of the solar cells, respectively.

One solar cell module is fixed to the upper and one to the lower module position, respectively, by mounting the aluminum shadow mask on top of the solar cell modules as shown for the lower position in the bottom part of Fig. 4.5. The aluminum mask also defines the apertures, i.e. the illuminated area of the eight individual solar cells of a single module. Indentations on the backside of the aluminum masks keep the solar cells in the correct position during mounting and increase mechanical fixation of the cells to avoid possible scratching of the metal electrodes during mounting. This also decreases further the solar cell distance to the fused silica window. The entire mechanical layout is designed to minimize the distance between solar cells and the outer mantle radius to minimize shadowing effects on the solar cells; e.g. the shadow masks have a distance to the fused silica of less than 1 mm.

In the middle of the solar cell holder, two small black printed circuit boards are placed, each carrying temperature (MAX31725) and light (BH1750FVI) sensors (Fig. 4.5). Those are tilted with an angle of 22.5° with respect to the solar cell surface, forming a relative angle of 45° between each other. Note that this is the same angle as provided by the eightfold azimuthal symmetry of neighboring insertion modules.

The four LEDs (two for status feedback and two for 3.3 and 5 V power supply display) are located on the printed circuit board (PCB) attached to the backside of the solar cell holder (right side in Fig. 4.7). Viewing channels in the solar cell holder allow one to look down at these LEDs and pressurize the void volume of the insertion module to the inside of the rocket. The PCB on the backside of the solar cell holder further carries spring pins to contact the solar cell electrodes. Because of the late access mounting of the solar cell modules, no rigid electrical contacting is possible. Therefore, the solar cell modules press onto gold-coated spring pins close to full stroke to maximize the grip between the pin and metal pad to ensure reliable low-ohmic electrical contacts.

4.3 Electronic Design

The electronic hardware and measurement software is planned, constructed, and programmed by Dr. Michael Böhmer, head of the Central Technology Laboratory at the Department of Physics. The eight identical data acquisition (DAQ) systems are located on pizza-slice-shaped PCBs to efficiently utilize the space inside the ring segment. Fig. 4.7 shows a photograph of one complete DAQ system on a PCB with colored highlighting of the system's partitioning of the electric circuit, together with a connected solar cell holder. Each DAQ includes batteries, micro controller (µC), data storage, and receives the service module signals. The design of the DAQ system strictly follows the KISS principle to keep it straightforward and simple, resulting in a system that includes many features to increase resiliency.

A successor of this DAQ system has been used for deployment and long-time monitoring of the STRAWb experiment in the Northern Pacific [217, 218]. The DAQs are designed on black PCBs and fixed on top of the base plate with an intermediate layer of ©Rogers foil to

ensure electrical insulation and thermal conduction to the bottom plate. The black color aims to provide increased radiative thermal coupling to the surroundings, i.e. to radiate heat away more efficiently.

A schematic overview of the DAQ system architecture is given in Fig. 4.8, and a listing of the main electrical components can be found in Table 4.1. The DAQ is powered by two AA 1.2 V NiMH batteries, which provide sufficient energy for several hours of operation. These rechargeable batteries do not contain liquid electrolytes which would cause problems at accelerations of the order of 10g and vacuum. They lasted for more than 10 hours in pre-tests. A DC/DC converter together with a dedicated charging circuit allows safe recharging of the system during the standby phase. During operation, the battery voltage is split into three independent power rails via highly efficient DC/DC converters, followed by low-dropout regulators to suppress high-frequency noise from the DC/DC converters. The main element of the DAQ is an 8-bit ATmega644PA µC. The environmental sensors as well as a chip for voltage/current consumption monitoring are connected to the µC by I^2C.

An SPI bus controls the solar cell measurement system (details in section 4.4 below) and carries the main data load during flight with fast and efficient data transfer. The rocket interface is implemented by optocouplers adapting the DLR design guidelines and allows one-way communication from the service module to the experiment. The in-flight signals of the service module are transferred to the inner pins (snap-in connectors), from where they are distributed to all eight identical DAQs. Using a specialized bootloader, the integrity of the program is

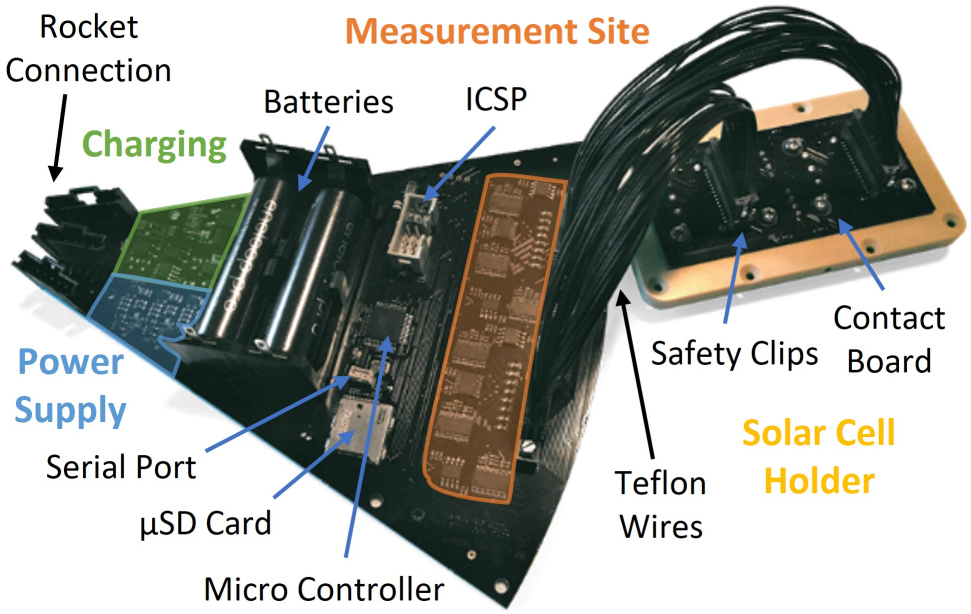

Figure 4.7: Photograph of a complete single DAQ system. The black pizza-slice-shaped PCB contains spatially separated electrical units of different purposes that are colored. The solar cell holder on the right is seen from the backside and connected via two snap-in connectors. Reproduced from Reb et al. with permission [215]. Copyright © 2021 The Author(s).

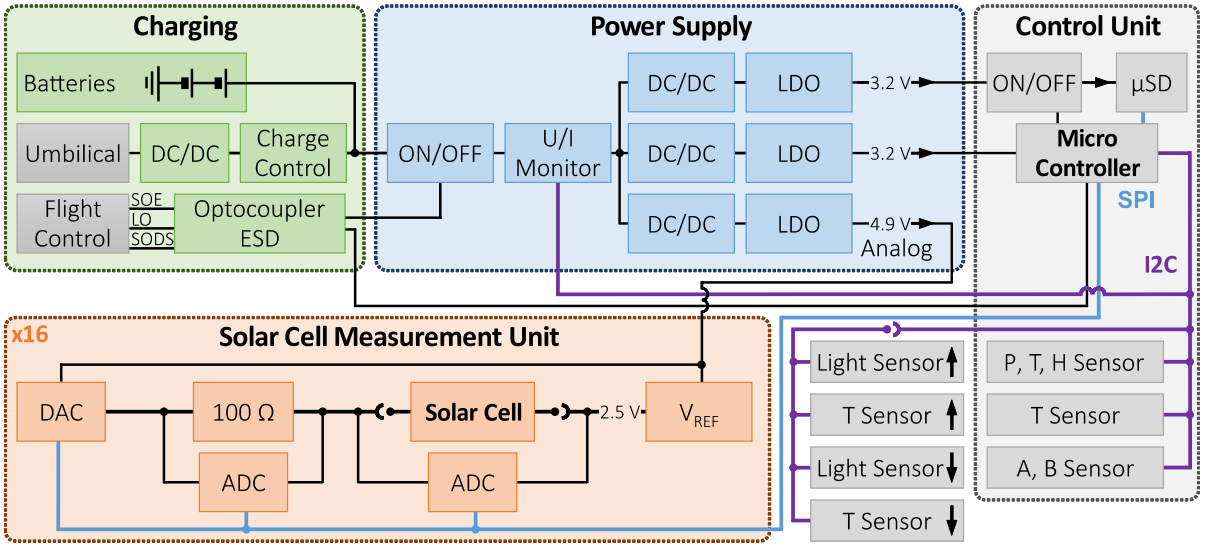

Figure 4.8: Electrical System Overview of each DAQ. The logical blocks can be divided into charging, power supply, control unit, and solar cell measurement unit and are colored in accordance with Fig. 4.7. Reproduced from Reb et al. with permission [215]. Copyright © 2021 The Author(s).

ensured, as well as golden image reflash in case of a µC FlashROM corruption during flight. The attached micro secure digital memory (µSD) card is supplied by a dedicated power rail to minimize power supply drops caused by write access to the file system. An integrated watchdog surveils the correct operation of the program and takes care of rebooting the system in case of a software failure (as well as logging such failures for later analysis). The main program enables timeline logging with granularities of 93 µs and 10 ms, to ensure synchronization between the eight DAQ systems on the bottom plate. The DAQ system monitors power consumption, temperature, humidity, and pressure on the PCB to provide basic environmental information inside the ring segment. Acceleration and magnetic field values (both in three axes) are also recorded during the measurements and provide a further option to synchronize the solar cell measurements of different segments post-flight. In addition, the temperature and light sensor data on the solar cell holder are frequently recorded.

The heart of the experiment is the electrical characterization of the solar cells. A schematic overview of the measurement principle is presented in Fig. 4.8. The DAQ system consists of two high-precision analog-digital converters (ADCs) (24-bit, internal oversampling), a constant voltage reference, and a digital-analog converter (DAC) (Fig. 4.8). The voltage reference provides a nominal voltage of 2.5 V as "virtual ground" to the solar cells. A high precision resistor of $(100 \pm 0.01)\ \Omega$ acts as a shunt for the current measurement while protecting the DAQ system in case of a short circuit inside one of the solar cells. This protection works as follows: In case of a short circuit, a voltage of say ± 1.5 V creates a current of 15 mA across the 100 Ω resistor which can be drained by voltage reference or the DAC, without overloading the components. The potential applied across the solar cell is defined by a DAC with an accessible output range between 0 V and 5 V.

Table 4.1: Main electrical components used in every single DAQ.

Components (#)	Model	Task	Features
Voltage Reference (2)	ADR431	Define virtual ground potential 2.5 V	source/sink max 30/20 mA, high precision
Digital-Analog Converter (2)	AD5676R	Sweep voltage to apply solar cell bias	16 bit, 15mA sink, buffered output
Analog-Digital Converter (6)	AD7193	Measure voltages at solar cell and shunt resistor	24 bit, gain1, 8fold oversampling and mean value calculation
Shunt Resistor (16)	APC1206	Enable high precision current measurements	0.01 % tolerance, limiting short circuit current
Micro Controller (1)	ATMEGA 644PA	Control DAQ, I^2C&SPI communication, data handling	11.0592MHz, 4kB RAM
DC/DC Converter (1)	LMZM23601, TI	Convert charging input to 5 V system voltage	Vout=5 V (max dropout 2 V), Vin≥7 for flexible charging
Charge Controller	LTC4060, Linear	Charge management for batteries	Simple configuration by pin strapping
Batteries (2)	VHAA LT 1700 CFG, Arts	Rechargeable power supply during flight	NiMH military-grade, vacuum and acceleration stability
Boost Converter (3)	TPS61322XX, TI	Convert battery voltages to system voltages of 1x3.3 V, 2x5 V power rails	6.5-µA quiescent current,1.8-A switch current boost converter, efficient drain of batteries
Low-Dropout Regulators (3)	TPS73601	Reduce high-frequency signal in power rails	Low dropout 75mV at full load
U/I Sensor (1)	INA219, TI	Monitor DAQ system power consumption	Autonomous measurements
Acceleration & Magnetic Field Sensor (1)	MC6470	Collect acceleration information	PCB bottom plate, three axes measurements
Temperature, Humidity & Pressure Sensor (1)	MS8607	Collect environmental information	PCB bottom plate
Temperature Sensor (2+1)	MAX31725	Collect temperature information	Sensor boards between solar cells, PCB bottom plate
Light Sensor (2)	BH1750FVI	Collect illumination information	on each sensor boards between solar cells, adaption of sensor integration time

With the virtual ground potential of 2.5 V, negative and positive voltages can be applied to the measurement circuit. Consequently, solar cells of different polarities can be measured in both forward and reverse directions. This approach simplifies the design of the DAQ circuit and allows the use of standard electrical components that work without negative auxiliary voltages. While the DAC applies a voltage to the circuit, the first ADC measures the voltage drop across the solar cell, referenced to the 2.5 V source. At the same time, the second ADC records the voltage across the high-precision resistor. The voltage is converted via Ohm's law, providing information about the amount of current flowing, as well as the direction. To accommodate for connector and cable resistances, four-point measurements are applied in the DAQ system.

4.4 Solar Cell Measurement Cycle

To maximize the number of measurements made during the flight, two identical measurement circuits are used in parallel to characterize two solar cells, one from each solar cell module, at the same time. Solar cells are defined here by sweeping the voltage across the cell in both directions, first from negative to positive voltages (forward) and then from positive to negative voltages (reverse/backward). Measuring the I-V characteristics in both directions is critical for solar cells that exhibit significant hysteresis, which is common in perovskite solar cells, especially during rapid voltage sweeps [219]. The file structure and data writing are discussed in detail below because they heavily influence the data acquisition routine described later.

The data storage is organized in a chunk structure. Each part of the data recorded is marked by a chunk byte, defining the logical content of the data chunk, a second byte carries information about the length and internal unit of data stored. This allows a simple unpacker to handle data, even in case of changes to the data stored inside the file (like adding or removing data chunks). This storage method automatically yields a small file size per measurement cycle, minimizing the risk of data loss in case of unexpected reboots during the measurement phase. In addition, a dedicated directory is used to store data sets, driven by the start-of-experiment signal (SOE). Overwriting of files is efficiently prevented, and no external access is needed between test cycles inside the launch tower. To guarantee a defined timing during the measurement cycle, file operations on the µSD card have to be scheduled carefully. As a compromise between the available SRAM storage inside the µC (2048 bytes) and the step size in the sweep, a data block size of 512 bytes has been chosen. As a beneficial side effect, block writings of this size are realized efficiently on the µSD FAT32 file system.

In Fig. 4.9, a flowchart of the measurement is presented. A full measurement cycle starts with opening a file for the swept data. Next, the file size is expanded to the final size of the file (13 blocks of 512 bytes, 6.5 kB), allocating the necessary sectors inside the µSD card in advance. A first data buffer is prepared by the DAQ, containing all sensor data, as well as information about the directory and file number. All values necessary for the sweep run are calculated and also stored inside the first buffer. For MAPHEUS-8, the lower and upper voltages $V_L = -0.4$ V,

$V_U = 1.35$ V are defined, respectively, and this range is covered with 240 equidistant steps for both for- and backward sweeps. The delay time between single steps is set to $\Delta t_D = 20$ ms and an additional waiting time at the upper return point V_U is $\Delta t_W = 200$ ms. These identical parameters are used for all solar cell measurements, but in principle, the DAC voltages can be controlled separately to measure e.g. solar cells of different polarity in the same solar cell holder.

These voltages are applied by the DAC to the measurement circuit, i.e. solar cell and high precision resistor in series, with respect to the virtual ground. The voltage drop measured at the solar cell does not depend solely on this external bias but also on the photo-generated current of the solar cell. The photo-current is drained into the DAC via the shunt resistor, causing a voltage drop which effectively pulls up the potential of the solar cell electrode connected to the resistor. Therefore, V_L is set low enough to measure the full I-V characteristic in the fourth quadrant including the short-circuit current of the solar cells also during strong solar AM0 illumination (to reach negative voltage bias at the solar cell). This is in large contrast to typical laboratory measurements done using the Keithley setup, where the set voltage is applied regardless of solar cell-specific behavior. The quite negative lower voltage $V_L = -0.4$ V is hence a trade-off between safety margin to safely capture the short-circuit current while not biasing the solar cells too far into their blocking direction (especially during dark conditions) which is known to cause

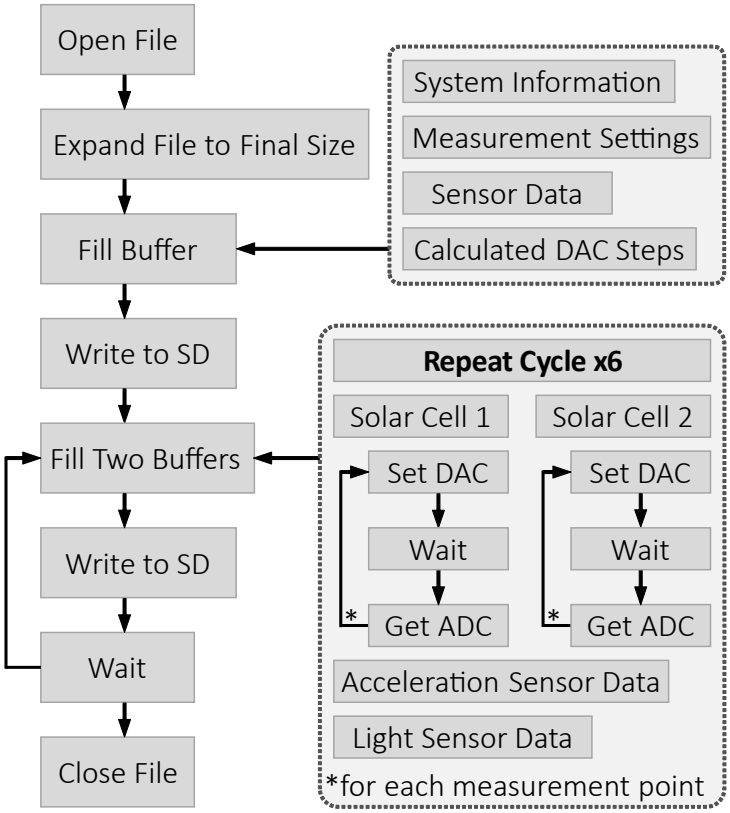

Figure 4.9: Flowchart of the measurement and data-flow organization. Reproduced from Reb et al. with permission [215]. Copyright © 2021 The Author(s).

potentially irreversible damage to the internal diode. In a similar reasoning, the upper voltage applied to the resistor and solar cell in series is $V_U = 1.35$ V. The solar cell V_{OC} is measured in any case as long as $V_{OC} < V_U$, since in this case the current flow (and hence the voltage drop) across the resistor is zero. However, in the case of dark measurements where the diode opens up at high positive bias, i.e. reduces its internal resistance, more voltage drops across the resistor, effectively reducing the maximum voltage bias applied to the solar cell in positive direction.

For efficient use of the data blocks, the solar cell measurement is split up into six parts, three parts for the forward sweep and three for the backward sweep, where each part consists of 80 measurement points. The parts are executed successively in a loop. At the beginning of each part, two data buffers (one for each solar cell) are prepared, and the light and temperature sensor data from the solar cell holder are written to the SD card. The remaining free space in the buffers is then filled with sweep data. For each data point, a new (pre-calculated) DAC value is set, the constant time-delay Δt_D applied to allow voltages to settle, and then ADC data for both the shunt resistor voltage and the solar cell voltage are measured. The internal oversampling of the ADC is used to reduce noise to a reasonable level. After filling the two buffers, the defined delay Δt_D is applied until repeating the loop with the next part of the sweep. This delay is used to write the block of acquired data from the buffers to the µSD card, while the delay is dynamically adjusted to compensate for the time needed to write the data block. In other words, the time necessary for data-writing is counted to ensure equidistant time steps between the measurement points despite the splitting up of measurements into blocks. After finishing the loops, the DAC pins are set to high impedance, the file is closed, and the DAQ system is prepared for the next sweep of the following two solar cells.

4.5 Operational Tests

The mechanical stability and environmental stability of the experiment and measurement system have been tested in advance of the flight. To test mechanical stability, the entire module performed a shaking test in-flight configuration with acceleration sensors attached to the experiment to monitor the accelerations at different module positions (see Fig. 4.10a). The results from the sine sweep in Fig. 4.10c reveal significant resonances at low frequency (strongest Eigenfrequency at 192.5 Hz) of the bottom plate, leading to strong accelerations in the central region. In the random-noise test using a motor-like vibration spectrum of the VSB-30, maximum accelerations of 41.8 g have been measured due to the superposition of multiple resonances. With this, the oscillation amplitude can be conservatively (assuming this acceleration to occur solely at the first resonance) calculated to be at most 0.29 mm.

However, at higher frequencies of 1 kHz and above, this is where typically strong engine vibrations occur, resonances are suppressed in the central region of the bottom plate. Fig. 4.10c) shows that accelerations on the bottom plate are significantly damped by more than a factor of two, roughly starting above 1000 Hz. Interestingly, the strongest vibrations in the random

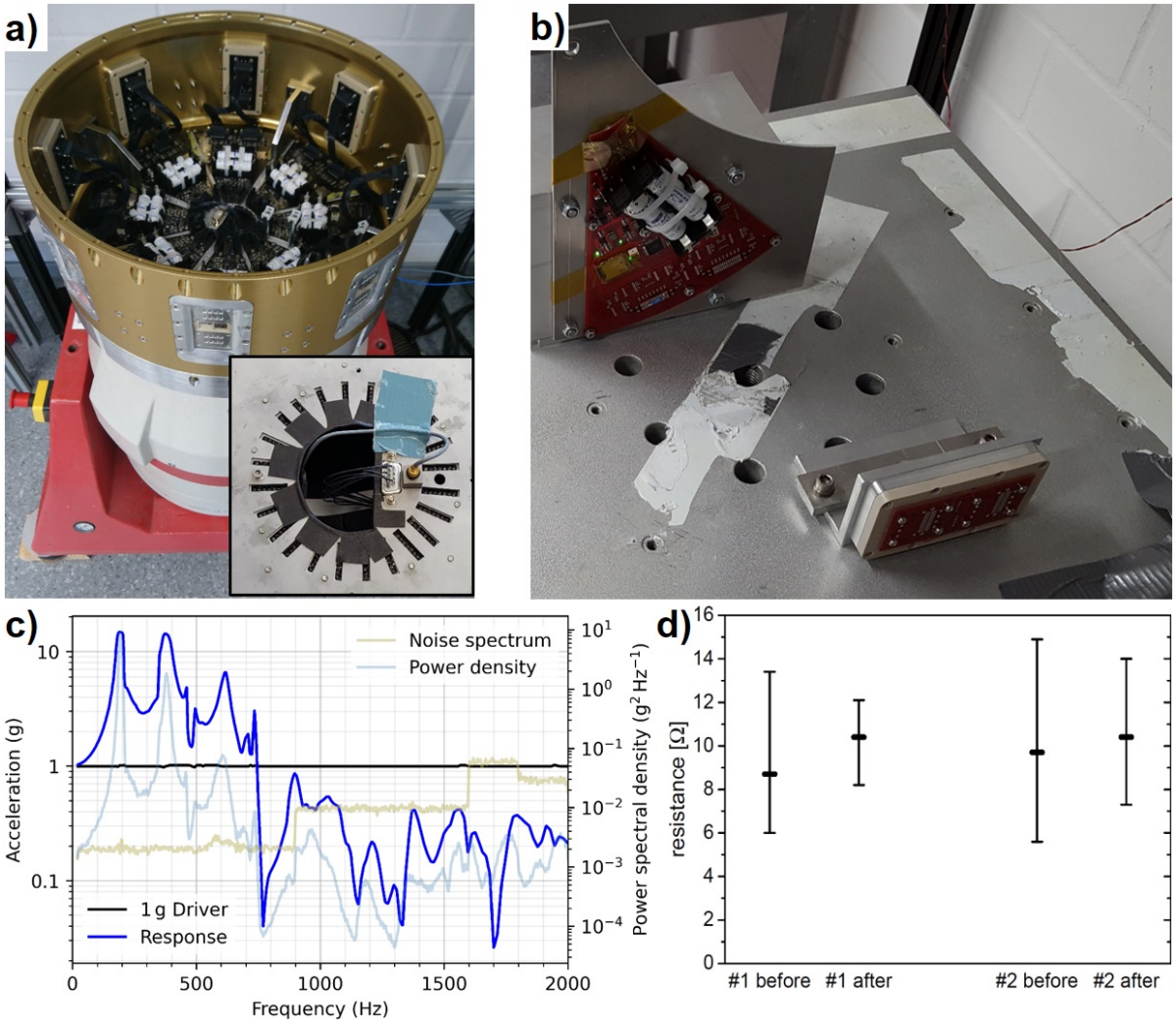

Figure 4.10: Composed graphic showing the two shaking tests. a) Photograph the complete experiment module mounted at the in-house shaker at DLR-MP. The inset shows the fixation of the acceleration sensor on the bottom plate in the center of the backside. b) Photograph by Christoph Dreißigacker of the shaking table at DLR-MP for the y-axis shaking of one (prototype) DAQ and one solar-cell holder with ohmic resistances for contacting tests (details see text). c) Left axis: Resonances of the experiment module acceleration measurements (solid line) from the sine-sweep with 1 g acceleration. Right axis: Semitransparent lines show the random noise test spectrum (olive color) according to the ATEK/MAPHEUS-8 flight requirements plan and the resulting power spectral density (steel blue color) [216]. Note the logarithmic y-scales. The d) Results of the contact resistance measurements before and after shaking along all three axes for two ohmic dummy modules. The average and min-max values of each module are shown. d) taken from Benjamin Predeschly's Master thesis [190].

noise profile that occur around 1700 Hz are maximally suppressed. This can be assessed more closely in the power spectral density (steel-blue line), which gives the energy distribution in different modes resulting from driving the shaker with the pseudo-engine vibration spectrum (olive semitransparent line). In the course of the shaking, the entire experiment was switched

on to test the vibrational stability of the electronics, especially of the batteries for the power supply. As a result of the test, the battery fixation was optimized by adding small pieces of solid rubber between the metal springs and their spacers. Also, we experienced an unexpected brownout (the system switches off due to insufficient battery voltage) in one DAQ during the shaking. By closer inspection, we found evidence of too high power consumption of this single DAQ and Dr. Michael Böhmer found and fixed the issue: one chip was not properly placed by the assembly machine. Similarly, during the later bench test, the switched-on experiment was shaken together with the entire payload. A loose screw from another experiment fell onto one of the DAQs, causing weird behavior during the shaking but no damage. This led to the coverage of the PCB electronics with insulating Kapton© foil for the flight, to avoid future short circuits while still keeping the chips accessible. These tests have proven the mechanical and electronic integrity of the experiment for the sounding rocket flight.

Due to the absence of convective cooling in space, thermal management via heat conduction is important to ensure a controlled temperature of the electronics during operation. The electronics dissipate heat to the aluminum bottom plate, hereby acting as a heat sink. To electrically isolate but thermally connect the DAQs to the plate, a thin layer of Rodgers© foil is inserted between the two parts. To test the concept of passive cooling, one complete DAQ system with a correspondingly-sized aluminum bottom plate has been inserted into a vacuum oven and preheated to 65 °C.

This temperature results from a first-order calculation using the following assumptions. First, the temperature difference between mantle and aluminum plate is constant $\Delta T = 100\,\mathrm{K}$, stainless steel thermal conductivity is $\lambda = 20\,\mathrm{W\,m^{-1}\,K^{-1}}$, and the effective elbow crosssection $A = 2 \cdot 10^{-3}\mathrm{m}^2$ and length $l = 0.05\,m$. Then the power of the conducted heat is

$$P_{\mathrm{cond.}} = \frac{A\lambda\Delta T}{l} \approx \frac{2 \cdot 10^{-3}\mathrm{m}^2 \cdot 20\,\mathrm{W\,m^{-1}K^{-1}} \cdot 100\,\mathrm{K}}{0.05\,\mathrm{m}} = 80\,\mathrm{W} \tag{4.1}$$

Second, the black body radiation received from an opaque emitter obtending a quarter of the 4π sphere at a temperature of 390 K is $P_{\mathrm{rad.}} \approx$10 W, and reemission of the module is neglected. A vacuum time t of around 7 minutes results in a total heat transfer of $Q = Pt \approx 90\,W \cdot 420\,s \approx$ 40 kWs. With a weight of the aluminum plate of $m_{\mathrm{BP}} \approx 1\,\mathrm{kg}$ (neglecting the stainless steel elbows and other parts) and a heat capacity of $c_{\mathrm{Al}} = 0.9\,\mathrm{kW\,kg^{-1}\,K^{-1}}$, the expected maximum temperature increase of the bottom plate can be estimated:

$$\Delta T_{\mathrm{BP}} = \frac{Q}{c_{\mathrm{Al}}\, m_{\mathrm{BP}}} = \frac{40\,\mathrm{kWs}}{0.9\,\mathrm{kW\,kg^{-1}\,K^{-1}} \cdot 1\,\mathrm{kg}} = 44\,\mathrm{K}. \tag{4.2}$$

Therefore, based on this simplified calculation using conservative numbers, the expectation is a maximum aluminum bottom plate temperature of around 65,°C at the end of the space measurement when reentering Earth's atmosphere. Consequently, space conditions were simulated by Benjamin Predeschly at a pressure of ∼1 mbar to limit convective cooling and a temperature of 65 °C for 10 min in the vacuum oven. One DAQ including an aluminum plate for passive cooling was switched on and inserted into the oven. After the test, visual inspection showed

functionality, and analyzing the data showed nominal data acquisition and agreement of the test conditions by reading 68 °C for more than 10 minutes. The DAQ operated during the entire test and collected sensor data as well as sweep measurements nominally.

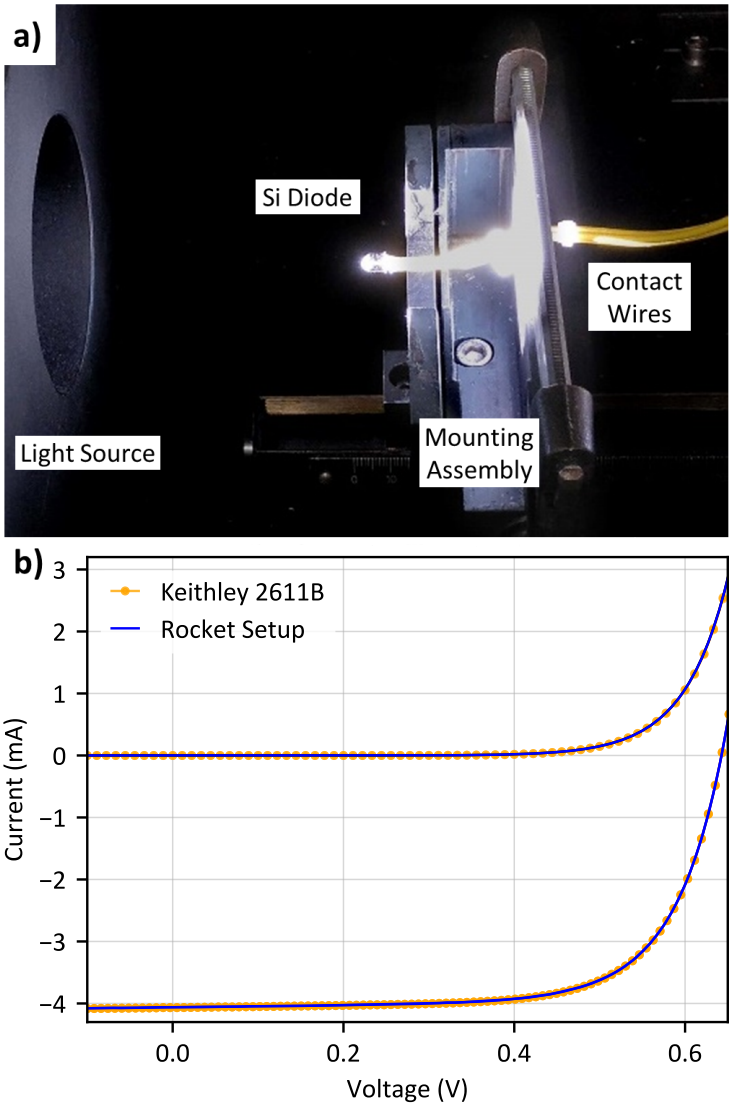

Figure 4.11: Validation of the DAQ measurement system with a stable silicon diode (BPW24R). a) Photograph of the laboratory experiment. b) Resulting measurements of illuminated (lower) and dark (upper) measurements of the Si diode obtained with laboratory (yellow points) and rocket (blue line) measurement systems. For both systems, forward and backward sweeps are shown but are not distinguishable. Reproduced from Reb et al. with permission [215]. Copyright © 2021 The Author(s).

Various scenarios have been tested to improve the defined handling during unexpected occurrences. These include different malfunctions such as instantaneous power loss, brown-out detection, loss of service system signals, the connection loss of sensors, µSD, and solar cells. Via detailed analysis of the system state during the tests and the data on the µSD afterward, exception handling on the software side is optimized to ensure reproducible behavior. This will

allow for a full time-line reconstruction in any case – for time synchronization of the data and therefore parallelization after the flight. A long-term test has shown that the maximum operation time can reach more than 12 hours. Even in the case of count-down prolongation, OHSCIS has enough power resources, consequently recharging in the launch tower is not mandatory, reducing external requirements. A key challenge in solar cell measurements is reliable electrical contacting. Already in the laboratory, there are various challenges to reaching a reproducible, low-ohmic contact between the electric measurement device and the nm-thin metal pads used as top electrodes for the solar cells. Regarding the strong vibrations and g-forces during launch, stable and immovable contacts are crucial to protect the metal pads and ensure electrical connection. A shaking test of a single solar cell holder mounted with test modules was conducted by Christoph Dreißigacker to simulate the launch vibrations and assess potential contact damage by the pin springs establishing the solar cell contacts (see photograph in Fig. 4.10b). Test modules have been ohmic resistances in the solar cell module layout, coated with a transparent conductive electrode and evaporated metal contact pads. The resistances before and after the test have been measured and investigated with the optical microscope. As a result, no scratching due to vibrations of the contacts could be found. The contact resistances did not show a systematic change, some contacts improved and some got worse. On average they got slightly worse but no significant deterioration of the contacts occurred (see Fig. 4.10d). To test the solar cell measurement circuit and to investigate the measurement precision of the DAQ system, the DAQ measurements were compared to the laboratory measurement device, consisting of a Keithley 2611B. A Si-photodiode (BPW24R) was mounted to the laboratory solar source to obtain defined and stable illumination. The diode has a highly stable I-V characteristic within a similar range as the solar cells. In Fig. 4.11a, a photograph of the experimental realization of these validation measurements is shown. Via four-point contacting the diode was electrically connected alternatingly to the OHSCIS DAQ and also to the Keithley, a laboratory measurement device usually employed for electrical characterization of solar cells. For both measurement systems, dark-current and illuminated measurements were acquired under laboratory solar simulator illumination with a Xenon lamp with 1 sun (AM1.5G). The temporal and spectral stability of the light source of the source is A classified according to IEC 60904-9 Ed. 2.0, i.e. that the short-term temporal intensity variability is within 2 %.

For the dark-current measurements, the hatch was closed to avoid any scattered light from reaching the Si-diode. For the illuminated measurements, a waiting time of several minutes lets the diode reach thermal equilibrium to minimize temperature influences on the diode characteristics. In Fig. 4.11b I-V diode characteristics were collected with the DAQ (rocket setup) and a Keithley (laboratory setup), respectively. Both have been measured forward and backward, for dark and illuminated conditions. The deviation of both measurement systems is negligible within the experimental error. The maximum absolute differences between the short-circuit current and the open-circuit voltage are 5 µA and 0.2 mV during illumination, respectively, which is in the low per mil range of the measured value. Assuming an ideally stable light source and the Keithley to produce ideal measurements, this deviation underlines the DAQ system's high

precision for excellent solar cell measurements during the sounding rocket flight. To further

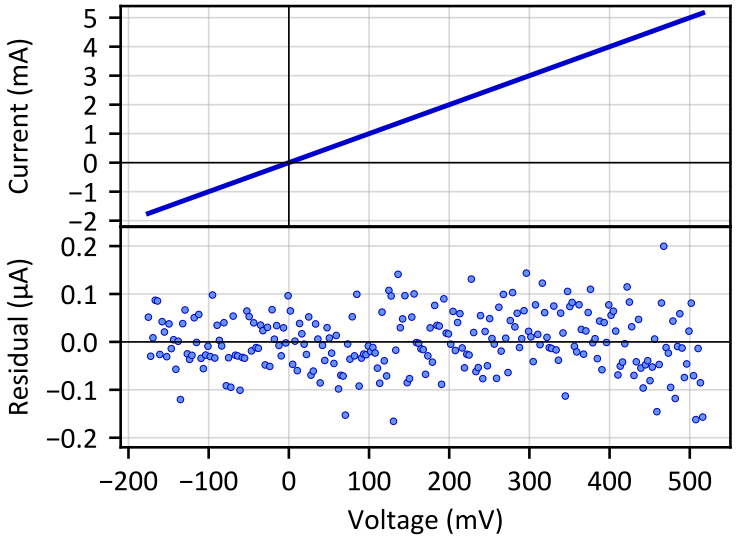

Figure 4.12: Current-voltage measurements of the high-precision 100 Ω resistor. On top the measurements, including the least-squares fit (100.03 Ω). The lower panel shows the residuum with random scatter within a band of 0.1 µA around the ideal zero line without evidence of a systematic trend. The standard deviation assuming a normal distribution amounts to $\sigma_I = 0.057$ µA.

quantify the measurement precision of the DAQ system, I-V measurements of a (100 ± 0.01) Ω resistor were collected and fitted with a least-square approach to obtain a resistance of 100.03 Ω from the inverse slope (see Fig. 4.12). By relating fit and measurement values, the sample standard deviation of the current measurements of σI = 0.057 µA results. Here, the test resistor has the same resistance as the shunt resistor, thereby resulting in a similar contribution of read-out noise of both ADCs to the measurement error estimation. In other words, this value can be considered as an upper limit of the standard error in the determination of the short-circuit current, since voltage read-out noise at the shunt resistor has a negligible contribution to the current measurement in short-circuit conditions. Equivalently, the voltage standard error of open-circuit measurements is determined by the read-out noise of the shunt resistor, and an upper limit of $\sigma_V = \sigma_I \cdot 100\,\Omega = 5.7$ µV is derived. Also, the absence of trends in the residuals of the measurements underlines negligible non-linearity of the DAQ within the measurement range.

4.6 Flight Experiment Procedure

A few hours before launch we mounted the solar cell modules into the solar cell holders and enclosed the solar cell holder with the outer window frames to obtain the complete insertion modules (see Fig. 4.13). During late access, the insertion modules were electrically connected via Samtec plugs with safety clips to the experiment module and integrated. The module windows

were covered with aluminum foil bags that fell off during launch (see Fig. 4.13e). At t-7 min (before lift-off, LO) the SOE for OHSCIS was set, used to cycle power to the experiment. See Table 4.2 for a detailed launch timeline with a focus on the important events before, during, and after the launch. At regular system start-up, the µC initiated ADC calibration and switched thereafter to measurement mode, recording five complete dark-current measurements for each solar cell before LO. Once activated by SOE, the DAQ system will work until shutdown by the low voltage lockout from the DC/DC converters, to make sure that during flight no accidental power-down is initiated.

At LO (T+0 s), the internal clock started counting, while the measurements continued without any interruption. At T+61 s the rate-control system of the service module achieved a stable orientation of the payload and thus the main microgravity (µg) measurement time began. This allows for a full measurement cycle of each solar cell until the SODS signal for OHSCIS was set at T+155 s. Upon receiving the signal, the internal time stamp was saved, the ongoing sweep was completed and written to the SD card. Thereafter an ADC re-calibration was initiated, and the calibration details were saved, and the measurement mode continued. During activated SODS, the sensor sensitivity of the gravitation sensors increased from a 16 g range to a 2 g range. The SODS off signal was set to T+425 s, which was recorded together with an internal timestamp

Table 4.2: Timeline of the Launch of ATEK/MAPHEUS-8 with a focus on OHSCIS.

time	Event
t−5 h	Unpacking of solar cells, preparation of insertion modules with solar cells
t−4 h	Electrical motor arming
t−3 h	Late access, integration of insertion modules
t−2 h	Mechanical motor arming
t−7 m	OHSCIS switch on, after ADC calibration begin with dark I-V measurements
T+0 s	Lift-off, signal for internal time stamp
T+12.5 s	Burn-out first stage
T+15 s	Ignition second stage
T+44 s	Burn-out second stage
T+57-61 s	De-spin, payload separation, rate-control activation
T+63 s	Begin µg phase, rate $< 1\,^{\circ}\,s^{-1}$
T+155 s	SODS signal for internal time stamp, re-calibration of ADC
T+251 s	Apogee 239 km
T+425 s	SODS signal for internal time stamp, data writing to new directory
T+432 s	End of µg phase
T+600 s	OHSCIS switch off
T+800 s	Payload touchdown
T+4 h	Payload disassembling, securing solar cells

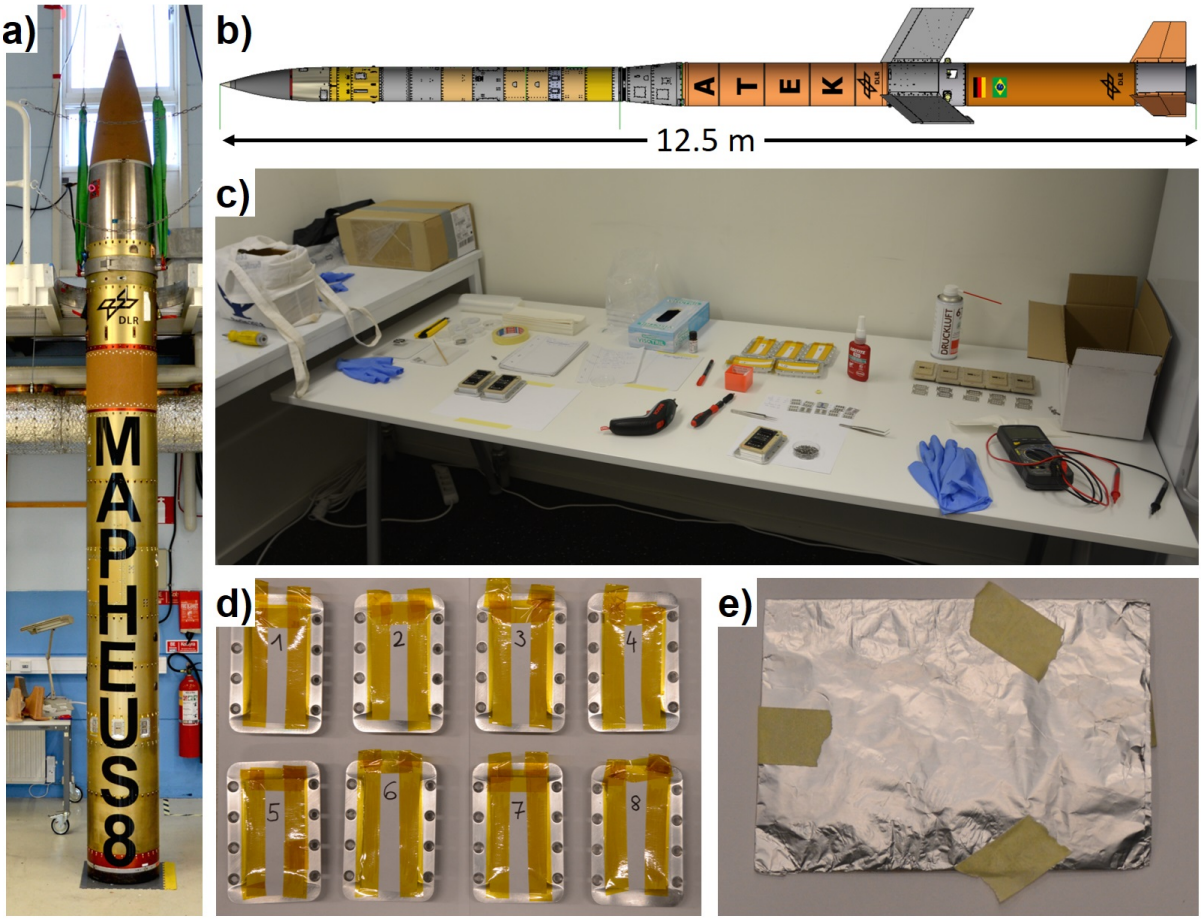

Figure 4.13: Prelaunch preparation. a) The assembled payload before transport to the launch tower. b) Drawing of the complete ATEK/MAPHEUS-8 rocket, adapted from the ATEK Flight Requirements Plan and reproduced with permission [216]. c) Insertion module/solar cell preparation desk. d) Prepared modules ready for late access. The removable covers protect the solar cells from light and the glass from dirt. e) One of the disposable protection covers mounted outside on the module windows during late access.

to have an additional external trigger for time synchronization of the eight DAQs. The I-V measurements continued until the experiment shutdown was triggered by SOE off at T+600 s. The onboard flight system safely switched off the DAQ system before payload touchdown for data protection.

4.7 Results

At payload recovery and disassembly, visual control of the experiment module confirms the full integrity of the mechanical parts, electrical parts, and solar cells. All eight glass windows were intact and the electrical connection appeared intact. Data extraction and conversion into ASCII files show that all eight segments steadily collected data and no exception occurred during the flight. In Fig. 4.14 the recorded acceleration in the vertical direction of all eight DAQs covering

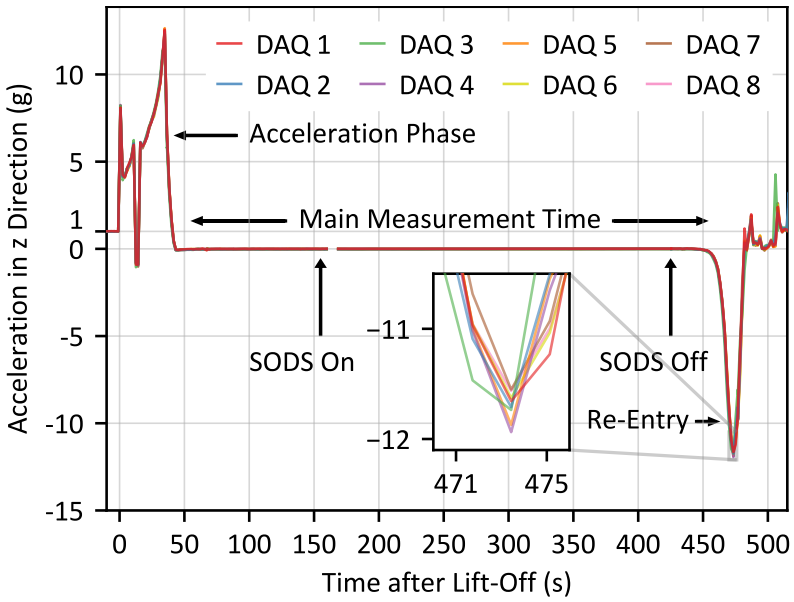

Figure 4.14: Acceleration sensor data in the vertical direction of all eight DAQ systems. The most important timeline events for OHSCIS are labeled in the graph. The superimposed curves of the different DAQs prove the time-synchronicity of the measurements. Reproduced from Reb et al. with permission [215]. Copyright © 2021 The Author(s).

the launch, main measurement time, and re-entry is shown. In the beginning, the acceleration phase of stages one and two is registered simultaneously by all eight segments, resulting in eight superimposed lines. At the strong re-entry de-acceleration at around T+470 s, all eight DAQs still show simultaneous acceleration measurements, indicating time synchronicity. In more detail, the SODS signals are registered by all eight segments simultaneously, in particular, at SODS off, the internal clocks of all eight segments are within a range of 0.01 s. The measurement asynchronicity, i.e. the time difference of the start of single measurements in the eight segments is limited to less than 0.7 s at this stage. This measurement asynchronicity presumably occurs due to cumulative time delays of single DAQs. These are caused by different write-access times of the very first buffer in each measurement, where no dynamic time adaption is used. The dynamic time adaption during the I-V acquisitions, however, prevents a larger total drift and guaranteed equidistant measurement acquisition within single solar cell sweeps in each segment. It is worth pointing out that this drift (measurement asynchronicity) is recorded, and thus it is possible to select the most synchronous measurement set at any time. The acceleration and light sensor data acquisitions both have a time resolution of around two seconds, more than double the maximum measurement asynchronicity, and thus need no further fine adjustment to be ideally parallelized. Therefore, all the sensor data and solar cell measurements acquired during the main measurement time are designated for in-depth analysis with parallelization and correlation of all the data obtained.

Fig. 4.15 presents the example of solar cell measurements obtained at the end of the µg phase measured in one segment for an organic and perovskite solar cell from modules 1 and

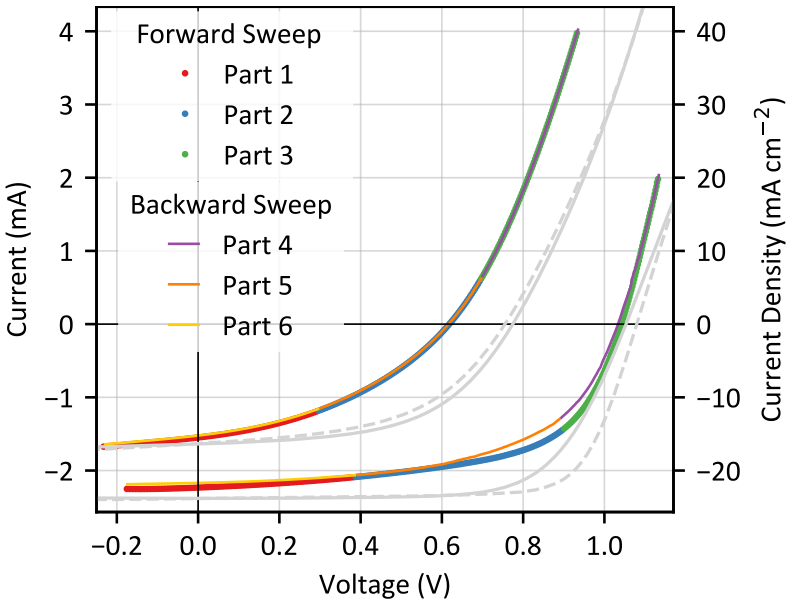

Figure 4.15: Solar cell measurements at the end of the main measurement time at T+405 s at an altitude of more than 100 km, collected for the segment with the strongest solar illumination at that moment (colored). The upper curves show the I-V characteristic of an organic solar cell and the lower curves for a hybrid perovskite solar cell. The colors allow distinguishing between different parts of the sweep measurement as they are collected in the buffer and written to the file. In addition, the corresponding reference measurements in laboratory conditions (1000 W cm^{-2}) of the same solar cell types from the same batch are shown in solid grey (forward sweep) and dashed grey (backward sweep). Reproduced from Reb et al. with permission [215]. Copyright © 2021 The Author(s).

2, respectively. Both solar cells show smooth I-V curves of diode-shape in both, forward and backward sweep directions. The different colors indicate the different data blocks according to the data structure explained above that are stitched together to obtain the complete I-V curves. Note that the lower voltage limit reached is different for the two solar cells, where the system with higher photocurrents effectively does not reach -0.2 V anymore due to the effect explained in Section 4.4 and similarly the upper voltage limit reached of less than 1 V for the cell of lower photocurrent. This highlights the necessity of systematic laboratory testing in advance of such a novel experiment and extrapolating knowledge in an educated way.

Before the flight, there has been an extensive discussion about the best size of the series resistor with the final choice of 100 Ω. A lower resistance was not reasonable due to the current sink restrictions of the electrical parts, as discussed above in Section 4.3. However, a larger resistor would have been possible in principle, with the following effects. First, in conditions of large photocurrent, the potential drop across the resistor would have been larger, shifting the lower accessible voltage limit of the solar cell to larger values. This would have required further lowering V_U below -0.4 V and thus operating the solar cells even stronger in their blocking direction at small photocurrents, which is not desired. Secondly, at small photocurrents, a higher voltage drop at the resistor would have decreased the upper accessible voltage across

the solar cell. These two effects both effectively reduce the available voltage range that can be measured for given sweep limits of the DAC. The theoretical improvement in the read-out quality of the voltage at the resistor due to larger voltages (larger signal/noise) did not balance out these facts. Therefore the resistor size was defined by the criterion 'as small as possible and as large as necessary'. Also, in this case, a current-voltage equilibrium at each measurement point could likely be reached quicker, since the settling of voltages occurs quicker when using smaller resistances in the system.

The I-V curves and the low noise of the measurements allow us to assess the details of the measurement setup. In particular, there is a stable and reliable electrical contact for both solar cells and the DAQ performs as in the pre-tests (cf. Fig. 4.11). The system proves nominal operation from single DAC and ADC acquisitions, data collection and storage, up to post-flight retrieval of the data. Both solar cells show clear diode-shaped I-V characteristics, proving the functionality of the charge-selective transporting layer. At the time of this measurement, the strongest solar illumination is detected for this segment with the photosensors, which is also supported by the strong photo-currents produced in both solar cells as seen by the vertical shift of the diode-shaped curves to negative currents. At this late stage of the flight, both organic and perovskite solar cells show significant power generation. Therefore, after traveling to the launch site, mounting and waiting in the payload, being exposed to the harsh conditions with strong mechanical stresses during launch, and more importantly, after a time of nearly 6 minutes in µg space conditions in orbital altitudes they still function well.

Table 4.3: Environmental and key performance parameters for the presented solar cell measurements.

Solar cell type	T	I	V_{oc}	J_{sc}	FF	V_{mpp}	J_{mpp}	P_{mpp}	PCE
	°C	W m-2	V	mA cm-2	%	V	mA cm-2	mW cm-2	%
In-flight									
Perovskite m-TiO_2, fw.	57	1214	1.04	22.32	59.3	0.81	16.97	13.79	11.4
PBDB-T:ITIC fw.	57	1214	0.62	15.49	39.2	0.37	10.03	3.75	3.1
Perovskite m-TiO_2, bw.	57	1200	1.03	21.69	56.6	0.76	16.70	12.67	10.6
PBDB-T:ITIC bw.	57	1200	0.62	15.22	39.0	0.37	9.83	3.66	3.0
Pre-flight									
Perovskite m-TiO_2, fw.	RT	1000	1.05	23.80	68.0	0.80	21.31	17.06	17.06
PBDB-T:ITIC fw.	RT	1000	0.77	16.39	54.0	0.54	12.68	6.85	6.85
Perovskite m-TiO_2, bw.	RT	1000	1.08	23.85	74.4	0.89	21.58	19.15	19.15
PBDB-T:ITIC bw.	RT	1000	0.76	16.32	50.7	0.51	12.23	6.25	6.25

The fourth quadrant, i.e. the region of negative currents and positive voltages, is covered

completely for both solar cell types, together with the important axes intersections giving short-circuit current at zero voltage and open-circuit voltage at zero current. The minimum and maximum voltage drop across the solar cells measured depend on their photo-current response as described in Section 4.4. For the organic solar cell, the forward and backward sweeps are superimposed with barely visible differences. This highlights the stable payload orientation at this phase of the flight, resulting in stable illumination conditions during this measurement of around 10 s, which is beneficial for an in-depth data evaluation. The perovskite solar cell measurement acquired at the same time shows hysteresis as manifested by the different shapes of the forward and backward sweep, which is well-known from terrestrial I-V measurements. This hysteresis is most pronounced in the vicinity of the maximum power point, i.e., the solar cell operation point where the product of voltage and current and, thus, power extraction is maximal. This underlines the importance of characterizing perovskite solar cells in both forward and backward directions also under space conditions. In Table 4.3 an overview of environmental parameters (temperature and light sensor measurements) together with the solar cell key performance parameters can be found. For completeness, the results of the reference measurements in the laboratory at standardized conditions, i.e., at room temperature (RT) and AM1.5G (1000 W m^{-2}), are included. The maximum extracted power densities of the presented in-flight measurements are 3.75 and 13.79 mW cm^{-2} for the organic and perovskite solar cell, respectively. Based on a solar irradiance measured of around 1200 W m^{-2}, this converts to a power-conversion efficiency (PCE) of more than 11 % and 3 %, respectively. The presentation of these single measurements shall be considered as the proof-of-principle; an extensive solar cell performance discussion can be found in Chapter 6.

4.8 Conclusion

The design scope of simplicity and reliability has shaped the OHSCIS experiment presented in this chapter. Maximizing the experiment symmetry and, thereby, the chance of strong solar irradiation onto the solar cells by using eight similar cut-outs and DAQs enables the experiment to collect a high number of solar cell measurements and thus to use the limited flight time efficiently for high-level scientific insights. The one-way communication from the service module simplifies the maintenance before the start and during flight and maximizes the fail-safety on the software side. Accordingly, the electronic design is optimized for high data throughput while maintaining high resilience. For the electrical characterization of the solar cells, noise is suppressed, and adaptive timing guarantees precise measurements. The measurement data is complemented with detailed monitoring of temperature and irradiation parameters to derive a full picture of the environmental conditions present for the solar cells. The experiment passed all pre-tests and performed the flight onboard MAPHEUS-8 successfully without any defects. The analysis shows that data acquisition was successful during the entire flight for all eight segments and that the data is time-synchronized. The mechanical design avoided thermal stress for the DAQs and protected the solar cells, which were measured nominally and proved operational

by generating power at the end of the µg phase. OHSCIS was recovered completely, and no experiment modifications are needed for future sounding rocket flights. The versatile design allows for easy adaption of the experiment to solar cells of different polarities or measurement requirements as well as different solar cell layouts. This offers the possibility to investigate the suitability of further novel material solar cell types for their use in space. Thereby it provides an ideal test platform for all kinds of solar cells in future flight experiments.

5 Solar Irradiance Determination Using Ambient Light Sensors

> The results shown in this chapter have been published in the article *Attitude determination in space with ambient light sensors using machine learning for solar cell characterization* [220] (L. K. Reb et al., *Solar RRL* 6 (11):2200537, 2022, doi:10.1002/solr.202200537).

The last chapter introduced the OHSCIS experiment with many technical and electronic details necessary to perform reliable solar cell measurements in space environment. One essential environmental parameter missing so far to embed the solar cell performances in a quantitative context is the solar irradiance that was received by individual solar cells during the flight.

This chapter details the measured sensor brightnesses and how to use these measurements with mathematical and numerical modeling of the physical irradiance conditions making use of Bayesian optimization to retrieve time-resolved solar irradiance values for each of the eight sectors during the entire time in space. In Section 5.1, background information about the ambient light sensors and their measurements are given as well as the basic idea that allows reconstructing the solar position by parallelizing the simultaneous measurements of multiple light sensors that are facing in different directions. In Section 5.2, the mathematical framework for the radiation model is developed, in Section 5.3 the numerical optimization approach is described and thereafter in Section 5.4, the results are presented and discussed, followed by a short conclusion.

5.1 Ambient Light Sensor Positioning and Measurements

As was described in Section 4.2, the OHSCIS module (Fig. 4.4) contains eight hatches each 45° azimuthally arranged. They are covered with fused silica glass (n=1.46 at λ= 550 nm) that has negligible absorption in the visible range but gives rise to angular-dependent Fresnel reflection.

In between the solar cell modules, two tilted sensor boards are located, one facing up and one facing down by 22.5° relative to the solar cell surface plane. Each sensor board has one I^2C temperature sensor and light sensor of type BH1750FVI (see Table 4.1). Thus each hatch contains two ambient light sensors that steadily collect illumination measurements during the flight (Fig. 4.5) [221]. The special feature of the two sensors is that one sensor is rotated upwards by 22.5° and the other one downwards by 22.5° as indicated in Fig. 5.1a), creating an effective

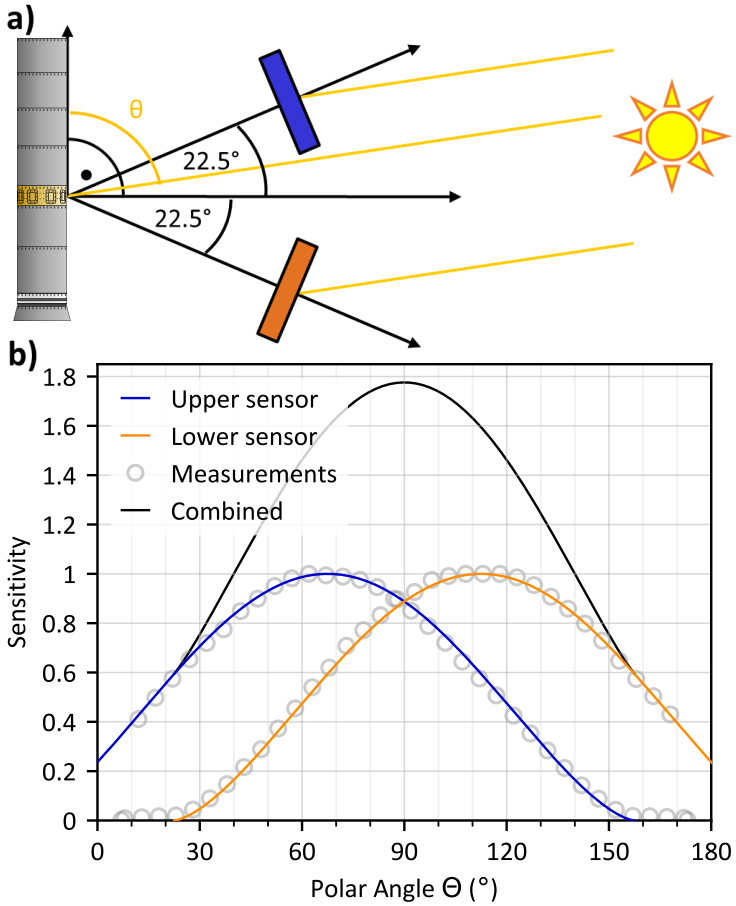

Figure 5.1: View direction of the light sensors. a) Schematic presentation of the orientation of the light sensors with respect to the solar cell surface normal. One sensor is facing slightly upwards (blue), and one is facing downwards (orange). The image of the payload is adapted from the ATEK Flight Requirements Plan and reproduced with permission [216]. b) The angular sensitivity curves of the light sensors. Grey circles are laboratory test measurements, which can be approximated with analytic functions (colored lines) within a presumed measurement accuracy of a few degrees. Taking the response function of both sensors together, their sum behaves like a single light sensor facing towards Θ=90°, i.e., in solar cell surface normal orientation. Reproduced from Reb et al. with permission [215]. Copyright © 2021 The Author(s).

viewing angle of 45° between the two sensors. In combination with the eight hatches with the 45° angle between neighboring hatches, each of the in total 16 light sensors of the OHSCIS module is oriented in a distinct spatial direction. Summing up the angular response of both light sensors of a single hatch (Fig. 5.1b), the result is an angular response curve that peaks for normal incident light onto the solar cells. In other words, summing up the light sensor response gives a total signal that can be interpreted as a single sensor facing in the solar cell direction, thereby referencing the solar irradiance on a relative scale. In addition, the tilt allows us to measure the differential illumination strength to obtain relative changes that contain further

information about the solar position. In the sketch in Fig. 5.1a), the blue light sensor would receive more sunlight, resulting in a stronger response than measured by the orange sensor.

The light sensors are designed for terrestrial illumination measurement purposes and thus are expected to saturate under strong AM0 irradiation, the solar irradiation spectrum with around 1366 W m^{-2} in space, according to the ASTM E-490 spectrum [38, 39]. To quantify expected

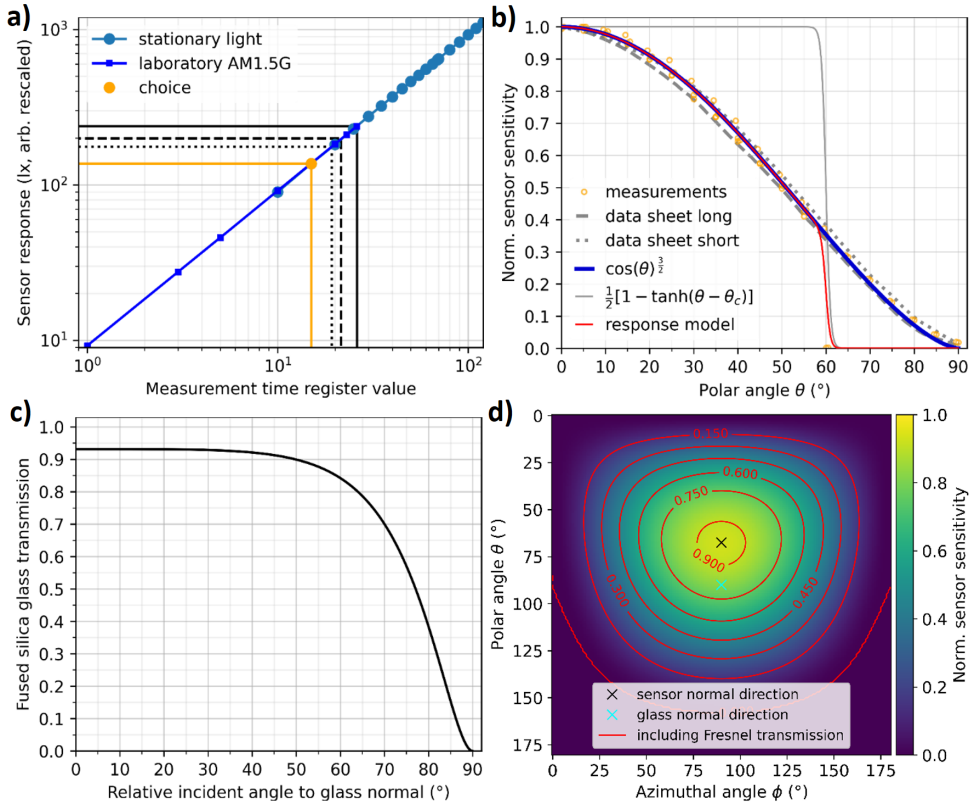

Figure 5.2: Light sensor properties and angular response modeling. a) Measured linear correlation of sensor measurement time and response for ambient light and a strong laboratory light source. The black solid line shows the maximum register value that can be used without causing sensor saturation in laboratory AM1.5G measurements. The dashed black line shows the maximum register value that can be used for AM0 without saturation from folding the AM0 spectrum with the spectral sensor response. The dotted black line results from scaling the saturation register threshold measured with the AM1.5G lamp to the AM0 spectrum. The solid orange line is the choice for the space flight with a one-third safety margin. Note the double-logarithmic representation. b) Angular light sensor response as measured in the lab, extracted from manufacturer datasheet and approximated with a cosine to the power of $\frac{3}{2}$ (blue). On top the sigmoidal function that suppresses the response above the cutoff angle is added, resulting in the total sensor response model (red). c) Angular fused silica transmission derived from Fresnel equations for n=1.46. d) Effective sensor response angular contour plot including sensor response (without sigmoidal function) and Fresnel transmission. The contour lines are no circles since the glass transmission peaks at angles different than the peak of the sensor sensitivity and due to the cylindrical Mercator projection that distorts regions at high latitudes. Reproduced from Reb et al. with permission [220].

saturation, the sensor spectral sensitivity curve (extracted from the sensor datasheet) is folded with the AM0 solar spectrum, which results in possible maximum brightness measurements of 88331 lx in the sensor configuration of lowest sensitivity (default high-brightness measurement-time register value of 31), while the 16-bit measurement range is effectively limited to 65535 lx [221]. Thus, the measurement-time register value is decreased further down to 15 to avoid possible saturation for the sensor application in space with a safety margin of around 1/3 of the available measurement range as a compromise of safety and proper use of large parts of the possible sensitivity scale for accurate measurements. Fig. 5.2a shows the linearity of the measurement-time register value to sensor brightness response for stable light sources in our laboratory. This graph and the results of this work allow for fine-tuning the measurement-time register value for improved accuracy for future flights of the OHSCIS module.

In this work, the focus lies on the sensor measurements acquired during stable payload configuration, i.e. selecting approximately the µ-gravity time of the flight of MAPHEUS-8. During flight, the cameras could capture both, the Sun and Earth horizon, even simultaneously, which was not possible in earlier flights[222]. Good solar position and Earth horizon tracking at different times of the flight by the cameras have been the key for the high precision of attitude determination in Braun et al.'s work. This, in turn, is the solid ground to interpret the results of this work. Our dataset includes all light sensor measurements starting with the first at around T+60.5 s (after lift-off) after activation of the rate-control system. Included are the measurements at T+444.4 s as the last measurement, before payload spin-up became too strong, yielding a total number of 256 measurements of all 16 sensors that are time-synchronized. This way, as many reliable measurements as available are included with the goal of maximizing the amount of data for model training. As a convention, each of the 256 measurements is called a (single) frame. For the selected data, the payload shows a sufficiently stable orientation, i.e. within the measurement time asynchrony of the 16 light sensors (of up to 0.7 s in the dataset), the payload orientation change effective angle is strictly below 1° [215]. Thus this does not influence the solar triangulation results within their accuracy. Each single sensor measurement in the dataset is an integer number ranging from 0 to 31776, the minimum and maximum registered brightness value by the light sensors during flight.

Parallelization of the light sensor data recorded by all eight DAQ systems enables the reconstruction of the solar position, which in turn allows deriving the irradiation intensity reaching the solar cells for power conversion efficiency analysis. For this, the radiation model will be defined in the upcoming section.

5.2 Radiation Model

To model the brightness values measured by the sensors, we need a) to define the sensor response function, b) consider further effects that have an impact on the model, e.g. angle-dependent

fused silica transmission or geometrical shadowing of the light sensors, and c) to incorporate all these relations into a coordinate system together with the definition of the light source(s).

The sensor sensitivity is described as a function of the incident angle onto the sensor, which is measured relative to the sensor surface normal or sensor viewing direction. To find a functional dependence of incident angle and sensor response, the sensor sensitivity curves are extracted from the sensor datasheet for vertical and horizontal directions and execute laboratory measurements for various incident angles with the light sensors in our labs with a fixed and stable light source (Fig. 5.2b). Comparing the extracted and measured sensor sensitivity curves, one finds a good agreement within a few degrees or percent, which is the attributed measurement error of single sensor measurements. The validation measurements lie in between the range of the curves extracted from the datasheet. The empirical and extracted data strongly agree with a cosine function to the power of $\frac{3}{2}$. Therefore, for numerical simplification in our calculations, the sensor sensitivity curve is modeled as

$$R_S(\alpha) = \cos^{\frac{3}{2}}(\alpha) \tag{5.1}$$

with the incident angle α. Deviations in the shape of our simplified sensor model and the intrinsic functional behavior are small. However, there might be systematic sensor misalignment properties that are estimated to be of order 1°. In laboratory tests, no inter-sensor sensitivity variations were detected, however, such systematic sensitivity sensor differences would add to measurement uncertainty. Also, sensor read-out noise adds on top to the measurement uncertainty. For 1000 W m^{-2} irradiance, a standard measurement error of 0.1 % is determined. However, the effective measurement error can become more pronounced for lower signal-to-noise ratios in faint conditions. All these effects add up to potential measurement uncertainties discussed in the next section.

A closer look at the measurements in Fig. 5.2b) shows a quick cutoff of the sensor response caused by the onset of geometrical shadowing effects above certain incident angles. This effect occurs due to shadowing by the rocket payload, i.e., only in one direction along the vertical axis for a sensor. To include this cutoff behavior in the modeling in an easy way, the cutoff angle α_c is defined to be identical in all directions and extends the sensor response model with a sigmoidal function

$$R_{S,\text{eff}}(\alpha) = \cos^{\frac{3}{2}}(\alpha)\text{Sig}\left(\alpha, \alpha_c\right), \tag{5.2}$$

where the sigmoidal function

$$\text{Sig}\left(\alpha, \alpha_c\right) = \frac{1}{2}\left\{1 + \tanh\left[\frac{\gamma(\alpha - \alpha_c)}{2}\right]\right\} \tag{5.3}$$

is defined to be close to 1 below α_c, 0.5 at α_c, and close to 0 above α_c (cf. Fig. 5.2b) with the slope γ. The (smooth) sigmoidal function instead of e.g., a (binary) Heavyside step function is used to be compatible with gradient-based optimization methods. $\gamma = 0.88$ is set to let the sigmoidal function decrease from 0.9 to 0.1 within 5°, which roughly corresponds to the estimated geometrical shadowing range.

A light ray is transmitted through the glass before arriving at the sensor. The glass transmission follows Fresnel's equations since glass absorption is negligible in the optical range where the solar spectrum and sensor sensitivity peak (550 nm, see Fig. 5.3 and compare Fig. 4.6). Correspondingly, a refractive index of n=1.46 is used for the fused silica. The effective glass

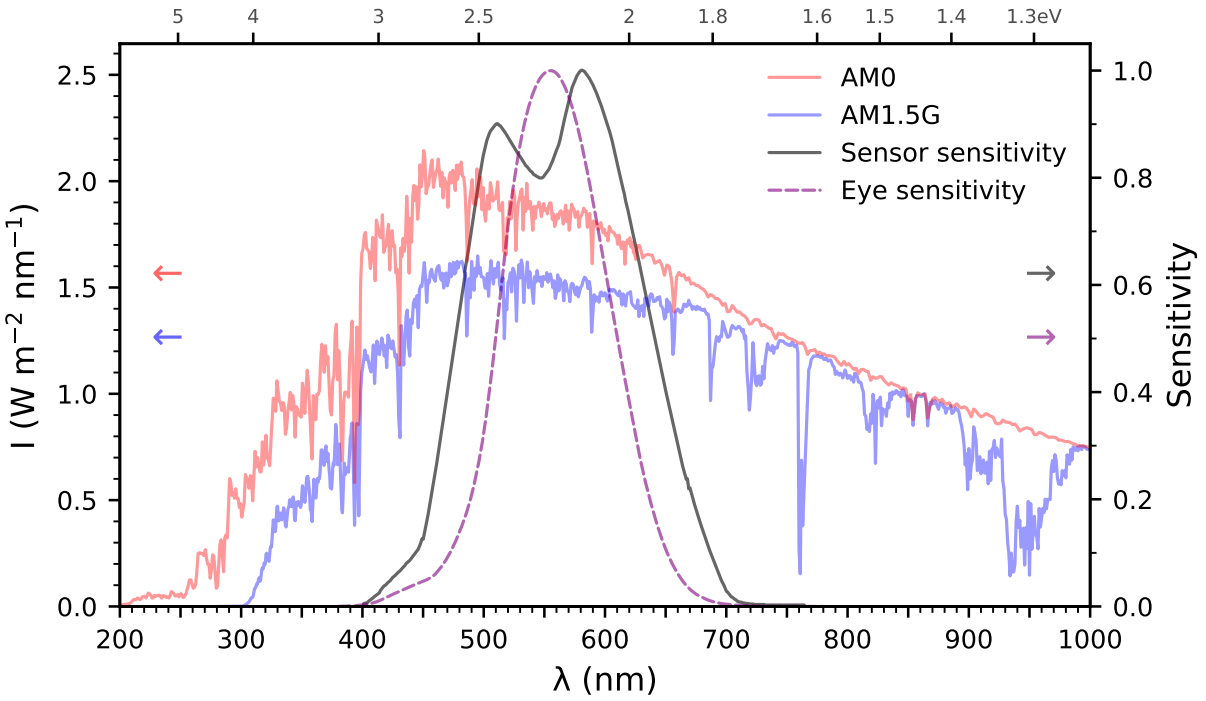

Figure 5.3: Spectral quantities and peak-normalized sensitivity curves. Solar spectrum AM0 in space (red) and solar spectrum AM1.5G on Earth's surface (blue)[38]. Light sensor sensitivity curve extracted from [221] in dotted purple and, as a comparison, human eye sensitivity as a solid black line. Reproduced from Reb et al. with permission [220]. Copyright © 2022 Wiley.

reflection coefficients of light of different polarization concerning the plane of incidence are:

$$R_{\perp} = \left[\frac{n_1 \cos(\alpha_1) - n_2 \cos(\alpha_2)}{n_1 \cos(\alpha_1) + n_2 \cos(\alpha_2)}\right]^2 \text{ and} \tag{5.4}$$

$$R_{\parallel} = \left[\frac{n_2 \cos(\alpha_1) - n_1 \cos(\alpha_2)}{n_2 \cos(\alpha_1) + n_1 \cos(\alpha_2)}\right]^2, \tag{5.5}$$

where n_1 and α_1 are the refractive index and incident angle (to the surface normal) of a light ray inside the initial medium, n_2 and α_2 in the final medium, respectively. Since for the transmission from vacuum to glass and back from glass to vacuum the n_1 and n_2, as well as α_1 and α_2, are exchanged, respectively, and the expressions for reflection are squared and hence symmetric functions, we can write the effective glass transmission as

$$T = \left(1 - \frac{R_{\perp} + R_{\parallel}}{2}\right)^2 \tag{5.6}$$

The refracted angle is expressed via Snells' law via incident angle and the refractive indices,

$$\alpha_2 = \arcsin\left[\frac{n_1 \sin(\alpha_1)}{n_2}\right] \tag{5.7}$$

and thus derive the angle-dependent fused silica transmission $T(\alpha_1)$ in Fig. 5.2c). Note that the incident angle of the light ray on the glass differs from the incident angle of the sensor. For the description of the geometry, a spherical coordinate system is used to make use of the azimuthal symmetry of the OHSCIS module to define a certain direction with the azimuthal angle ϕ and the polar angle θ:

$$\mathbf{r}(\phi,\theta) = \begin{pmatrix} \cos(\phi)\sin(\theta) \\ \sin(\phi)\sin(\theta) \\ \cos(\theta) \end{pmatrix} \tag{5.8}$$

The definitions of the coordinate system follow the coordinate system convention of the Mobile Rocket Base (MoRaBa),[1] i.e., the payload points always towards $\theta = 0°$, a radial direction of the cylindrical OHSCIS module mantle surface corresponds to $\theta = 90°$, see Fig. 5.4.

Thus, the eight window normal directions are

$$(\phi_i|\theta_i) = (16.875° + 45° \cdot i \,|\, 90°) \text{ with } i \in \mathbb{N}. \tag{5.9}$$

Accordingly, the sensor ϕ_i coordinates are the same, and $\theta_i = 67.5°, 112.5°$ for upward- and downward-oriented light sensors, respectively. First, a point source is defined by its position $\mathbf{r}$. The effective incident angle between a ray direction $\mathbf{r}$ and surface normal direction $\mathbf{n}$ is then calculated via the scalar product

$$\alpha = \arccos\left(\frac{\mathbf{r}\cdot\mathbf{n}}{|\mathbf{r}||\mathbf{n}|}\right) \tag{5.10}$$

Combining Equations 5.2- 5.7 to account for total solar brightness, sensor angular sensitivity, shadowing effects, and angular-dependent glass transmission, the response of a specific sensor to the light source is calculated as

$$R_{total}(A, \alpha_c, \mathbf{n}_s, \mathbf{n}_g, \mathbf{r}) = R_{total}(A, \alpha_c, \phi_s, \theta_s, \phi_g, \theta_g, \phi, \theta) = L\, R_s(\alpha_s) \mathrm{Sig}\,(\alpha_s, \alpha_c)\, T(\alpha_g) \tag{5.11}$$

with the sensor normal direction $\mathbf{n}_s$, glass normal direction $\mathbf{n}_g$, and the derived incident angles α_s and α_g onto a sensor and the glass, respectively. Here, L is introduced, the global scaling value that refers to the brightness of the light source.

An example simulation of a point source together with sensor response is shown in Fig. 5.5a, which illustrates how multiple sensors can be used together for point-source triangulation. For modeling the solar irradiation (the Sun-only model) onto each of the 16 light sensors for a given solar position, the Sun is described as a point-like light source. In reality, the Sun's angular diameter of around 1° makes it an extended source. However, within fair reasoning, the solar ray divergence does not affect our model description. For a given set of parameters, $L, \alpha_c, \phi, \theta$, the sensor response for each of the 16 light sensors is calculated to obtain a sensor simulation for the given parameters that can describe a single frame.

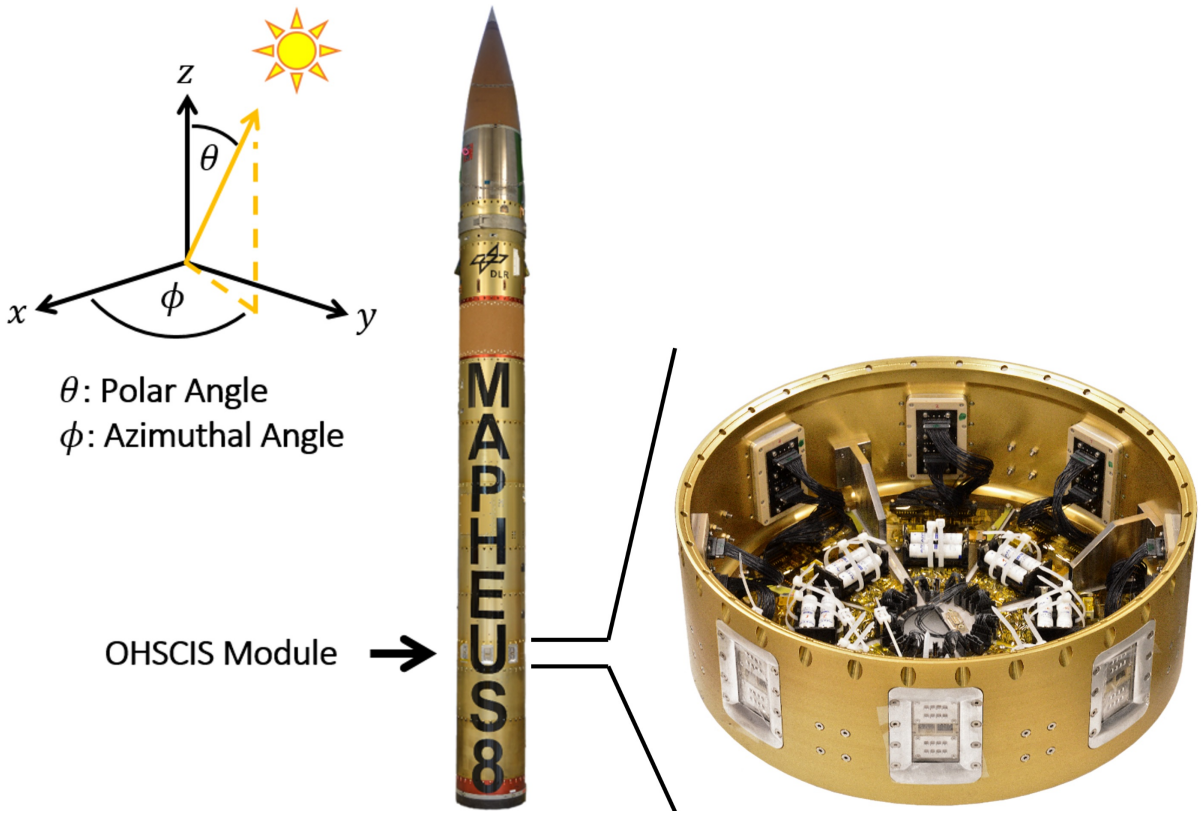

Figure 5.4: Schematic illustration of the polar coordinates used in this work with the rocket tip pointing towards +z-direction. In the photograph of the MAPHEUS-8 payload, the position of the OHSCIS module is marked (located at the "U"). Reproduced from Reb et al. with permission [220]. Copyright © 2022 Wiley.

In a refinement step for the model (Sun+Earth model), Earth is included as a second irradiation source. Earth is hereby modeled as an extended source where the following assumptions are applied (see Fig. 5.6). First, Earth subtends a semisphere, i.e., a solid angle of 2π. Second, the semisphere is approximated by a discrete number of angularly equally distributed points, i.e. with regular spacing between them. To achieve this, the special Icosahedron, a convex regular polyhedron with 20 faces that are equilateral triangles, is used. These points of known coordinates allow quick iterative doubling of points by creating new points in the center of nearest neighbors. The new points again produce smaller equilateral triangles. This way, a reasonable number of points to describe Earth within a few iterations can be reached. Third, all these points act as point sources with equal brightness. This is equivalent to assuming Earth to be an ideal and homogeneous Lambertian emitter. Each point is contributing to the sensor response as described above. The orientation of the semisphere can be described with its "normal" direction $\mathbf{n}_e$. This direction is the same as the normal direction of an infinite plane that covers the very same semisphere. In other words, Earth's normal direction points towards Earth's center. This

[1]MoRaBa stands for "Mobile Raketenbasis", DLR-Oberpfaffenhofen, department of Space Operations and Astronaut Training.

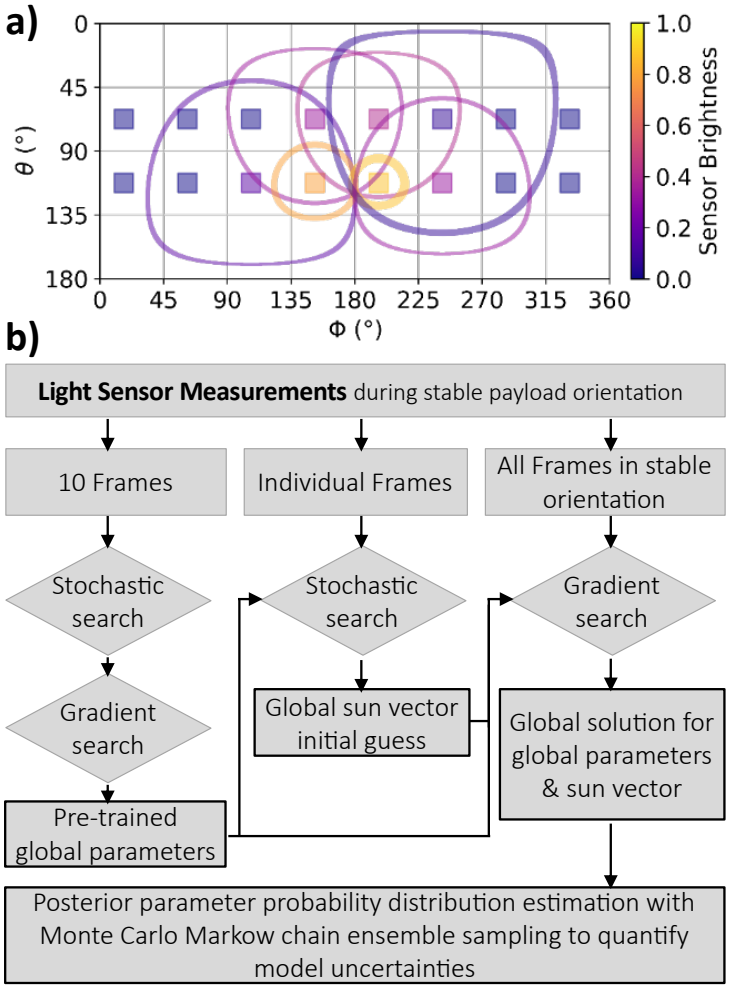

Figure 5.5: a) Simulation of a point source at and with the corresponding sensor responses. By selecting an interval in the contour map in Fig. 5.2d, each sensor response ring represents possible positions of the point source to create this individual response. At the intersection of sensor response rings, we can allocate the solar position. b) Model optimization flow diagram. The small selection of 10 frames from the entire dataset is used to derive pre-trained model parameters. These parameters are the basis for the stochastic search of the orientation parameters in all 256 individual frames. These results enter a gradient-based global optimization run to obtain a consistent solution for all parameters simultaneously. Starting from this maximum likelihood estimate, posterior probability distribution sampling is applied to get parameter uncertainties and correlation (details see text). Reproduced from Reb et al. with permission [220]. Copyright © 2022 Wiley.

Earth radiation model is, first, not sensible of its discretized nature during optimization, and second, where a change of Earth's normal direction changes Earth radiation influence of the sensors in a continuous way to enable gradient-based optimizations. Radiating Earth points are selected, limiting their angular distance to the normal direction to 90° by using the sigmoidal function introduced above to assign weights to the Earth points (see color in Fig. 5.6). This ensures a gradual change in horizon-point weighting. Second, rotating Earth points can lead to a non-monotonic sensor signal response and thus hinder the convergence of gradient-based

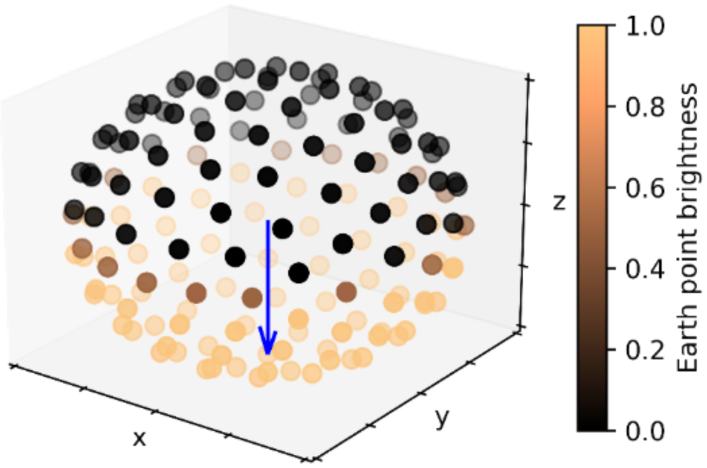

Figure 5.6: Earth model grid points after 2 Icosahedron segmentation iterations (162 points equally distributed over the spherical surface). For a given Earth-normal direction (direction indicated with the blue arrow), the individual point weight is calculated via the sigmoidal function and represented color-coded. Reproduced from Reb et al. with permission [220]. Copyright © 2022 Wiley.

optimizations. Thus the coordinates of Earth points are kept fixed relative to the light sensors, to avoid such discretization artifacts. In other words, all the point sources that are making up the Earth model are fixed in the coordinate system but their weight changes in a continuous way with $\mathbf{n}_e$. Earth's brightness is defined with a new parameter E that is normalized to the (weighted) sum of points. This way, the model is independent of the number of Earth points used, and Earth's brightness becomes a resilient estimate parameter.

The previously described coordinate system is used to extend the Sun-only model with the Earth component. For the rocket flight of a few minutes, a fixed effective angle of the solar position and Earth-normal direction is assumed. At apogee time, 4:25 a.m. on the 13th of June 2019 in Kiruna, Sweden, the geometric solar angle above the horizon was $10°$. Thus the effective angle between the direction of the Sun and the normal direction of Earth is $\alpha_e = \angle(\mathbf{n}_e, \mathbf{r}) \approx 100°$. Within the time passed during the dataset, the Sun moves by an angle that roughly equals its angular diameter. Thus, only a small error is introduced by fixing the angle. A rotation of the payload around the Sun direction $\mathbf{r}$ is equivalent to a rotation of the Earth's normal vector $\mathbf{n}_e$ around the Sun direction. Thus, all possible payload orientations are included when describing all possible Earth-normal orientations. They lie on a cone around the solar position with the fixed opening angle α_e and an Earth phase angle β. We define $\beta = 0°$ to be eastwards and $\beta = 90°$ to be northwards relative to the solar vector in the payload coordinate system. The advantage of defining Earth's position with this Earth phase angle is that only one more angular parameter is introduced for each frame in the later optimization to limit the model complexity. Later back transformation of the Earth's normal orientation to the payload coordinate system is straightforward and computationally fast.

Earth can be treated as a first-order perturbation of the Sun-only model. To clarify this

reasoning, consider the limiting case from basic radiative concepts: A perfectly white Lambertian disk covers the semisphere and is illuminated from a point source that is opposed to it (maximum Lambertian emission, Sun in disk surface zenith). Then the integrated flux that is reflected from this disk and passes through a unit surface (the sensor) cannot be larger than the flux passing the surface from the initial point source. For a lower Earth Albedo and for a Sun position that is far away from Earth's zenith, Earth reflection is reduced and, consequently Earth's contribution. We can estimate the magnitude of Earth brightness for a typical Earth Albedo of 0.3 and the projection effect for given geometry which scales as the sinus of solar angle above the Earth horizon, $E_{exp} \approx 0.3 \cdot \sin(10) L \approx 0.05 L$. In the next step, we estimate the effective Earth radiation contribution for a sensor measurement by comparing the maximum normalized sensor response from Sun (0.93) and Earth ($\sim$0.3) from our numerical model, including glass reflection effects. In other words, the maximum normalized single sensor response from an extended source of 2π cannot be more than 1/3 of the response from a point source. Considering these numbers, solar irradiation is significantly stronger than Earth irradiation for a single sensor and dominates orientation determination. However, in phases where solar illumination of the sensors is weak, the Earth model is expected to significantly improve the quality of orientation estimation, especially since Earth produces a smooth response curve for multiple light sensors simultaneously. Based on the above reasoning, the number of icosahedral splitting iterations used is two, resulting in 162 Earth points used to model Earth in a reasonable time. Fig. 5.6 shows a 3D visualization of the resulting Earth radiation model for Earth-normal direction pointing towards the nadir. With this, all the important model components are defined. The set of variable global model parameters are solar brightness L and cutoff angle α_c for the Sun-only model, plus Earth brightness E for the composite model. The noise parameter will be introduced below. Fixed parameters are the cutoff slope and relative angle between the Sun and Earth-normal directions. Each frame is characterized by the orientation parameters, i.e., the Sun position ϕ and θ for the Sun-only model, plus the Earth phase β for the composite model. The entire calculation of the model is done in a fully vectorized fashion, meaning that with all model parameters for all frames in time, the model predictions for each sensor are calculated simultaneously, which allows to performantly create a global residual and optimize the loss function.

5.3 Bayesian Optimization

The entire optimization routine is implemented in Python using packages like NumPy, SciPy, pandas, emcee, LMFit, and matplotlib extensively [223, 224, 225, 226, 227, 228, 229]. To optimize the model prediction for the best resemblance of the measurement dataset, maximum likelihood estimation (MLE) is used, assuming normally distributed residuals. This means an independent and symmetric distribution of measurement errors around their expectation value is assumed. This approach is equivalent to solving the ordinary least-squares minimization problem that also returns the MLE. In the first step, the most likely parameter solution for the employed

model for the given data is obtained. On top of that, Bayesian posterior sampling is the second step, using the affine invariant Monte Carlo Markov chain (MCMC) to estimate the posterior probability distributions of the model parameters [229, 230]. These distributions, in turn, allow us to consistently infer the uncertainty of the model parameters.

MCMC sampling is chosen to construct probability distributions for the parameters in a robust way. First, non-linearities in the mathematical model require a careful calculation of confidence intervals of the parameter estimates. MCMC sampling converges to the true underlying probability distribution of model parameters; thus, it directly imagines the desired objective. Second, the Monte-Carlo sampled high-dimensional parameter space contains all information required for subsequent analysis. The marginalization over certain parameters allows us to directly obtain the desired value distribution for a parameter of interest from which confidence intervals can be read-off. In addition, all model uncertainties, for example, uncertainties of the estimation of solar position, are propagated automatically, i.e., they consistently enter the derivation of solar irradiance uncertainty. This routine is done twice, once for the Sun-only model and once for the Sun+Earth model, as described below.

Maximizing the likelihood function is equivalent to maximizing the log-likelihood function

$$LL = \ln\left[L_{\mathbf{X}}(\mathbf{\Lambda}, \sigma^2)\right] = -\frac{n\ln(2\pi)}{2} - n\ln(\sigma) - \frac{1}{2\sigma^2}\sum_{i}^{n}\left(\mathbf{x}_i - \lambda_i\right)^2 \tag{5.12}$$

where n is the number of measurement frames, σ is the width of the presumed normal distribution of the residuals, $\mathbf{x}_i$ is the light sensor measurement vector consisting of the 16 measurements of the ith frame, and λ_i is the model prediction for the ith frame. $\mathbf{X}$ and $\mathbf{\Lambda}$ contain all the observations and predictions, respectively, and can be considered as matrices. The sum of the squared residuals in the last term corresponds to the objective function in least-square minimization. In the present case, the log-likelihood is the objective function that is to be maximized during the optimization routine. In practice, minimization of the negative log-likelihood function is used, the pedant to a cost function or internal energy for simulated annealing methods. $\mathbf{\Lambda}$ contains the entire model, and here enter all parameters of the optimization. This direct definition of the model for all frames and all sensors allows simultaneous training of all global model parameters. The single-frame model prediction for the orientation, given by ϕ_i, θ_i, and β_i for the solar and Earth position, are independent estimations for each frame. In other words, the optimizations of the solar position of two different frames are independent of each other. However, all frames influence the global parameters with equal weighting and hence influence each other indirectly.

The parameter σ is a weighting parameter that describes the uncertainty of the measurements in the dataset. Into such uncertainties, all deviations from the ideal model are subsumed, i.e., systematic and stochastic measurement noise of individual light sensors, absolute sensitivity scaling differences of the sensors, misalignment of the sensor orientation, timing differences between the measurement times within a single frame, model imperfections such as sensor sensitivity curve deviations. Since σ enters the optimization as an unconstrained parameter, its final value

can be considered as an independent measure of the amount of model-to-measurement deviation that is left over after optimization, where a lower value signifies better matching.

The first step of optimization aims to find the global minimum of the negative log-likelihood function to derive the MLE for all parameters. To do so, an optimization routine that comes in three parts is adopted (see Fig. 5.5b). In the first part (pre-training), the first 10 frames of the dataset are selected for a basin hopping algorithm that explores the high-dimensional parameter space by executing random walks [231]. Such a hopping algorithm is required for the given problem since the loss function is not globally convex, and gradient methods become stuck in local minima. The hopping algorithm overcomes barriers in the loss function that hinder gradient-based optimization methods to find global convergence. After a configuration close to the global minimum of this small pre-training dataset is found in solid estimates of the model and orientation parameters, a gradient-based minimization method optimizes the parameter values for the pre-training set. In the second part of optimization, the pre-trained model parameters are fixed. The basin hopping algorithm is then applied to each frame to obtain orientation parameter estimates that again are in the vicinity of the global solution of the entire dataset. Thus, good start values for the orientation parameter are obtained for each frame. In the third part, the pre-trained model parameters are fed together with the orientation parameters from the single frame estimates into a global gradient-based optimization, where all parameters are released to settle down at their optimum. Thus, simultaneous optimization of model and orientation parameters takes place to find the MLE for the given measurement dataset. For this large set of parameters and iterations, the linearity of the LL function allows computing the global residual in a vectorized hence performant fashion. Fig. 5.5b) shows only one possible solution to achieve global convergence of the optimization routine. Due to the non-linearity of the model, in particular, due to the vanishing gradient for the sun being more than 90° apart from a single sensor viewing direction, gradient-based methods are prone to failure for most initial conditions. This is the reason why a stochastic search is used first to identify good initial conditions where gradient-based methods likely converge. Acting with such a stochastic search onto the entire dataset would give rise to hundreds of parameters which increase computational time exponentially up to unfeasible times until proper initial conditions would be found. This is the reason why the model training on a small part of the data is performed first and stochastic searches are carried out subsequently for roughly correct model parameters. Other optimization routines that include both, stochastic and gradient components and that have an intrinsic memory for good parameter configurations could potentially do all these steps at once. In this context, the interested reader is referred to the methods of Simulated Annealing or Adaptive Memory Programming for Global Optimization that are suited to solve complex optimization without well-defined gradients[226]. However, fine-tuning iteration parameters such as stochastic jump width, temperature decay, or convergence criteria and their interaction during optimization are hard to control in such a non-trivial optimization problem. The scheme in Fig. 5.5b allows keeping control and test possibilities along the way to the globally optimized solution.

In the second step, the posterior probability distribution using the affine invariant MCMC ensemble sampling starting from the gradient-optimized result is used. This method samples the true posterior probability distribution and asymptotically becomes the distribution for an infinite number of samples. Parameter value distributions and correlations are obtained for the ϕ, θ, and β values of the single frames i.e. marginalized over the distributions of the global parameters and independent for every single frame.

As a final remark, the inclusion of additional prior knowledge, e.g. about the limited pitch and roll rate of the payload during the µ-gravity time in the form of Bayesian or Kalman filtering could stabilize the predictions and hence improve the obtained prediction accuracy[232]. However, the focus here is to investigate the solar position determination method and its accuracy without the use of other refinement techniques.

5.4 Results and Discussion

According to the Bayesian optimization method described above, a full and consistent model and orientation parameter estimates for both, the Sun-only and Sun+Earth model are obtained for the entire data set as a result of the gradient-based global optimization. For the Sun-only model, α_c stabilized at around 65° for the pre-training, while it drifted to 90° during the global optimization. Consequently, it is excluded from the global optimization, thus the only varied model parameters are the L, σ, and solar position ϕ_i and θ_i in each frame i. For the Sun-only model, the drift of α_c towards high values is attributed to the incompleteness of the model. The pre-training data contains measurements of the phase of solar positions close to the equator, while the complete dataset also includes measurements during solar positions at high polar angles. In the latter case, the model sensor estimates underestimate the measured sensor response, since any additional radiation from Earth is not covered by the model. This naturally pushes the cutoff angle towards higher values to minimize residuals and prevent convergence. Fig. 5.7 shows the results of the MLE estimation of the Sun-only model (dark-green and red lines) of the complete dataset. In addition, it shows the solar trajectories, which are once directly derived from the Sun detected on the images of camera 1 and camera 2 (light green and cyan lines), and once computed from the integrated orientation solution, which is estimated by fusing the Earth's horizon and Sun detected on the camera images and the IMU measurements, and will be referred to as the fused DLR trajectory in the following (dashed-grey lines). Camera 1 sees the Sun in the central area of the image only between T+240 s and T+370 s, and camera 2 between T+170 s and T+255 s.

To summarize the solar trajectory during the flight of MAPHEUS-8, at the beginning of the dataset the solar position was located close to the equator and then wandered gradually to a polar position. It crossed the payload nadir and then wandered back to an equatorial position of a different azimuth. According to Braun et al., the error of the estimated orientation of the payload is assumed to be below 1.5° (3σ) in the period between T+170 s and T+370 s when at

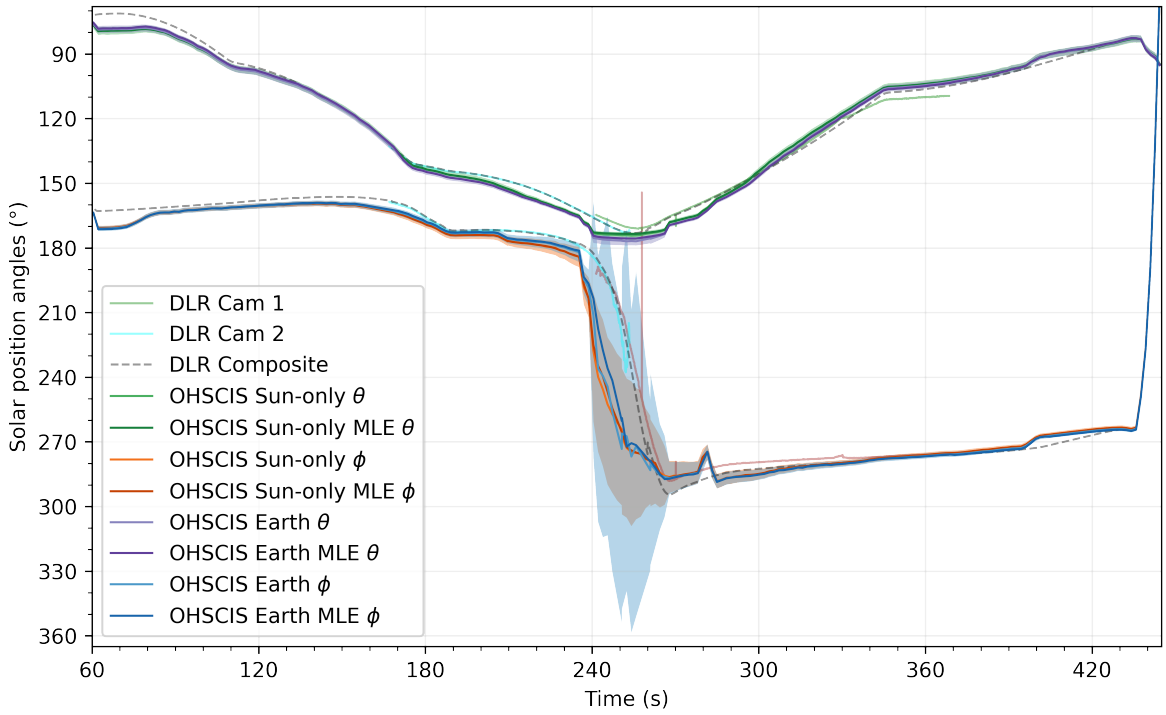

Figure 5.7: Solar position evolution for different models and techniques in the MORABA coordinate system. The solar position as derived from the Sun detected on the camera images is shown in light green and cyan, and the solar position as derived from the integrated orientation solution is shown as dashed-grey lines.[222] In the green and orange colors, the Sun-only estimates and in the purple and blue colors, the Sun+Earth estimates of Θ and ϕ are shown. The darker color depicts the MLE solution and the lighter color the median of the MCMC sampling distribution. In the lightly shadowed areas, 1-σ errors in the positioning estimation obtained from MCMC sampling are shown. Note that at angles θ approaching 180°, small changes in solar positions convert into large uncertainties in ϕ estimations due to the nature of coordinate representation. Reproduced from Reb et al. with permission [220]. Copyright © 2022 Wiley.

least one of the cameras sees the Sun and the estimated Sun direction vectors are directly used for aiding. In the initial period between T+60 s and T+170 s, neither camera sees the Sun, and the orientation is estimated by backpropagating the orientation solution of T+170 s using the IMU measurements, with the orientation error increasing due to the integration of IMU measurement errors over time. In the period between T+370 s and T+445 s, the orientation is estimated by forward propagating the orientation solution at T+370 s using IMU measurements. Interestingly, the OHSCIS result at T+360 s strongly supports the fused DLR trajectory with low deviation while it does not support the trajectory as derived from camera 1 only.

On top of the DLR trajectories, the OHSCIS solar positioning determination results from this work are presented. The Sun-only model MLE trajectory and the MCMC sampling median and the central 1 σ sampling distribution in green and orange for ϕ and θ are shown, respectively. For the MCMC sampling for the Sun-only model, 5 walkers and 10000 steps are used and

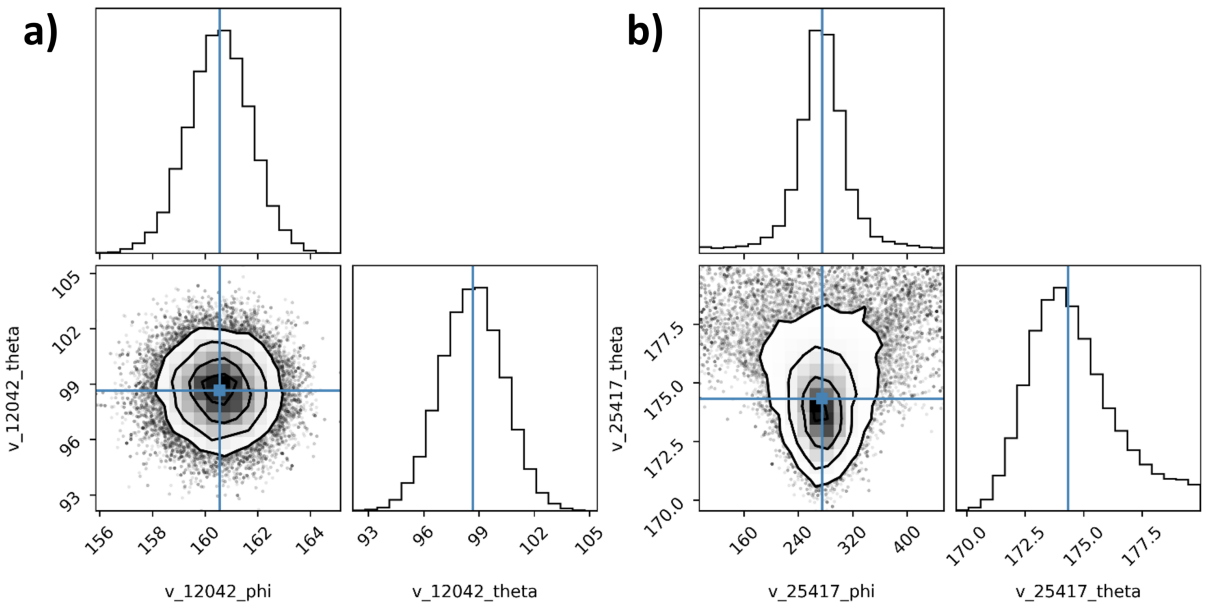

Figure 5.8: Corner plots of MCMC ensemble sampling results for the Sun-only model for an equatorial solar position a) and the Sun in nadir position b). Frame b) is the darkest frame during the entire dataset. The MLE solution is shown in blue. For plots of more frames and plots of the Sun+Earth model, see Fig. 5.9. Note the automatic axes range adaption. Reproduced from Reb et al. with permission [220]. Copyright © 2022 Wiley.

for the Sun+Earth model, 20 walkers and 20000 steps to better capture the richer probability landscape. To determine 1σ or 2σ from the sampling, the samples are sorted along the axis (parameter) of interest. Then the lower and upper bound of the corresponding central 68 % or 95 % of the samples are selected. Interestingly, the frame-to-frame differences for the OHSCIS determination method are very small for the majority of the data. This is a very encouraging result since the parameter solutions are independently estimated for each frame and this underlines that measurement signal-to-noise is high and the triangulation method reliable. The trajectory follows the fused DLR trajectory closely over very large portions of the entire flight with only small deviations.

Focusing first on the phase with camera aiding between T+170 s and T+370 s including the solar movement crossing nadir, the maximum measurement deviations of the fused DLR trajectory and the Sun-only model are $\Delta\theta \approx 5°$. For $\Delta\phi$ deviations reach 30° at T+240-250 s, however, this is during times where θ approaches 180°, and thus small angular distances on the unit-sphere surface translate into large ϕ differences. The large ϕ deviations and also the ϕ uncertainty as derived from MCMC sampling are thus a direct consequence of the choice of the coordinate system and no intrinsic model weakness to determine the solar position. To underline this, Fig. 5.8 shows the results of MCMC sampling for a phase of equatorial and polar solar position. During equatorial phases, the distribution width of θ and ϕ are small, covering around 3° for the 1σ range each. During polar phases, the θ sampling precision is still high (see also Fig. 5.9) but the ϕ angle distributions blow up towards the polar region, losing significance.

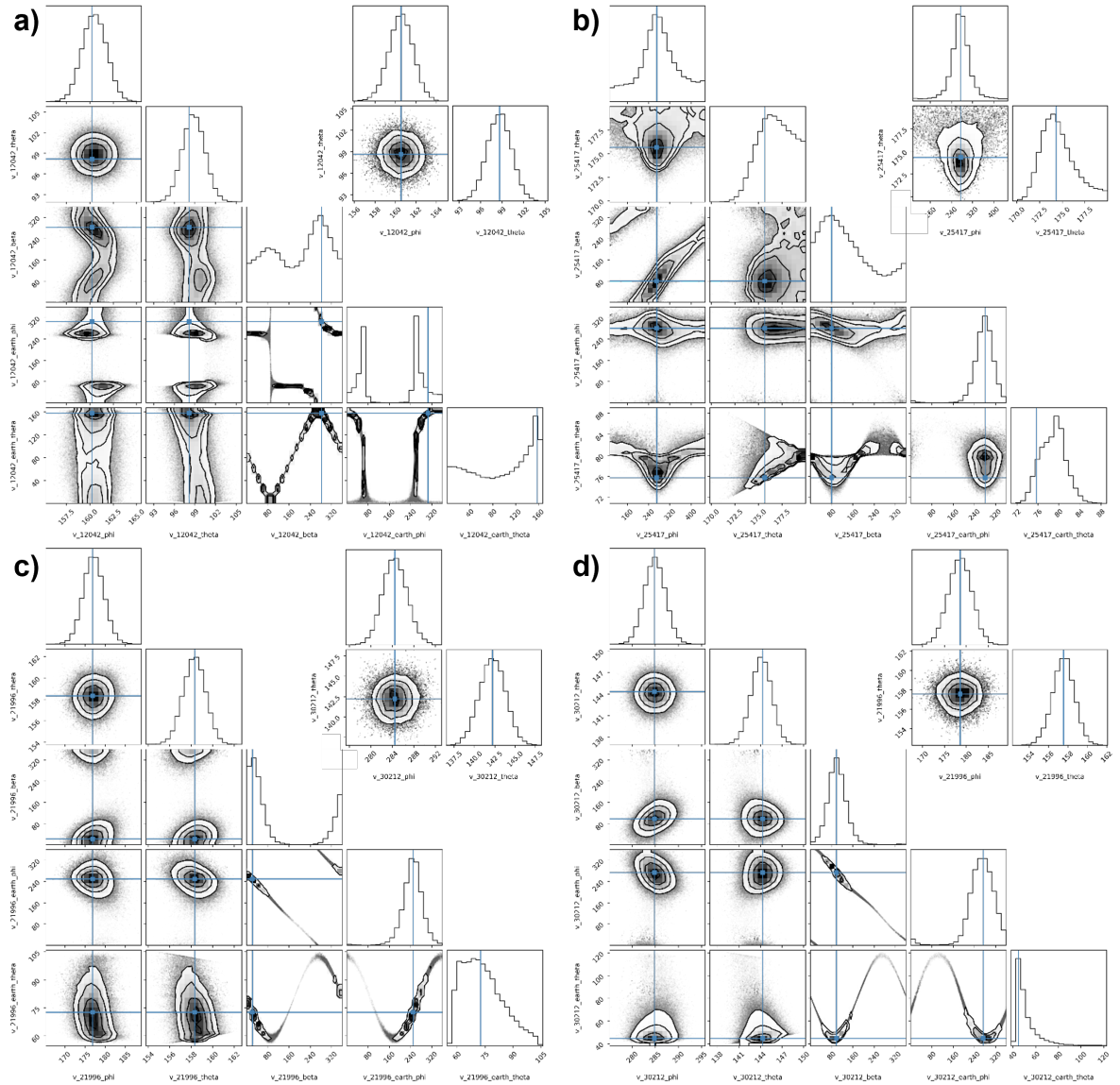

Figure 5.9: Corner plots of the Sun+Earth model for different times from a)-d). On the upper right of each Sun+Earth corner plot, the corresponding Sun-only corner plot is added to show differences. Reproduced from Reb et al. with permission [220]. Copyright © 2022 Wiley.

Fig. 5.10 shows the DLR and OHSCIS solar trajectories on an orientation sphere surface in Hammer-projection, which is an equal-area map projection with low distortions in the polar regions. This representation illustrates the magnitude of effective positioning deviations between the trajectories in a way that reduces misleading coordinate representation effects, especially for ϕ.

θ shows exceptional agreement of the solar position estimates of the fused DLR trajectory and the OHSCIS model for measurements at times around T+170 s and T+370 s, i.e. during phases of rather equatorial Sun positions where the fused DLR trajectory is aided by camera

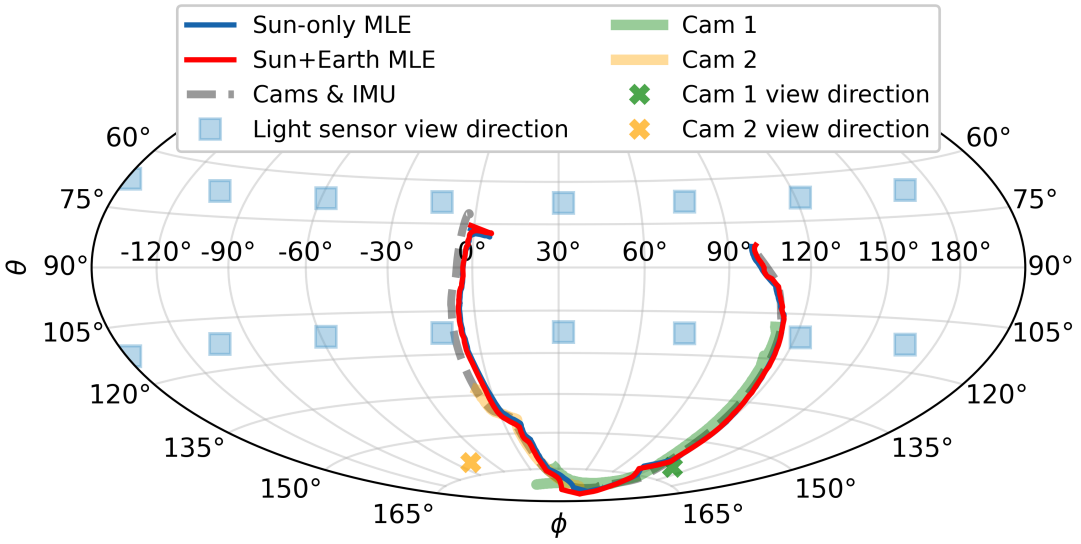

Figure 5.10: Hammer projection of the solar trajectories in the MORABA coordinate system. The movement of the solar position is counterclockwise. For additional orientation of the reader, the view direction of the two opposite cameras and the light sensors is shown. The dashed line shows the fused trajectory of Braun et al., in yellow and green their standalone camera-based solar position estimates are shown. On top, the OHSCIS Sun-only MLE (blue) and the Sun+Earth MLE (red) are shown. In this representation, absolute trajectory deviations become better visible. Reproduced from Reb et al. with permission [220]. Copyright © 2022 Wiley.

measurements. In other words, when θ is not more than $\tilde{1}50°$, the orientation estimates of both methods are in excellent agreement. At higher polar angles, the corner plot contours become spread out towards higher polar angles, and the θ-angle distribution becomes skewed and generally less peaked. Still, the MCMC sampling appears to slightly underestimate the model uncertainty at such high polar angles. Likely, due to the rather weak sensor response, not-included noise effects or model imperfections become stronger during these times and cannot be fully captured by the model. This can be also seen with the noisy solar position estimates at very high polar angles. However, in this regard, MAPHEUS-8 produced an untypical dataset, because it is statistically unlikely that the Sun directly crosses the nadir.

The deviations outside the camera-aided periods between the two methods, i.e. in the beginning and end of the selected dataset appear to grow. For example, between T+60 s and T+120 s, the OHSCIS model experiences strong solar irradiance and thus the obtained solar positioning estimates show a 1σ uncertainty of 2° and 3° for ϕ and θ, respectively in Fig. 5.7 (see also Fig. 5.8 and Fig. 5.9 for parameter distributions from sampling results). Note that the angle ϕ can be determined more precisely than θ at equatorial positions by the OHSCIS module since the light sensors react more strongly to a change in azimuthal solar position. The orientation accuracy of the fused DLR trajectory is expected to decrease with increasing period of time without camera image aiding due to the IMU-based backward and forward propagation, respectively. Thus, it is likely that deviations between the two models at such phases, especially for ϕ are dominantly

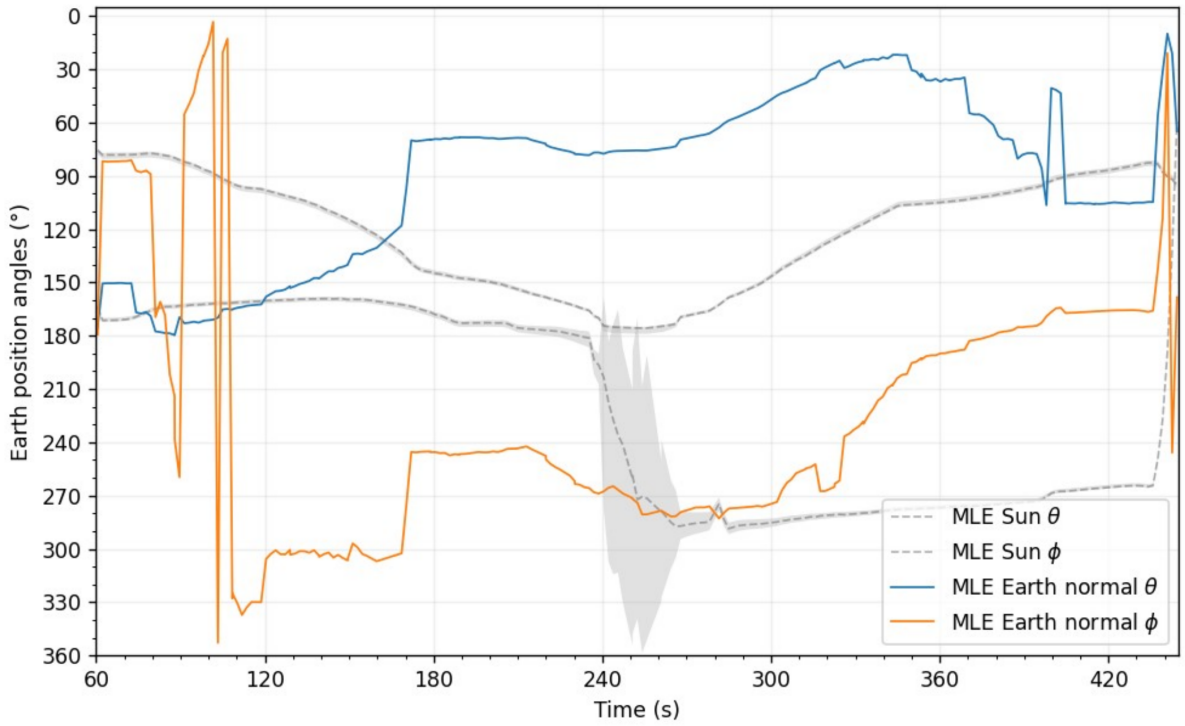

Figure 5.11: Earth position angle evolution. In grey, the MLE for the Sun position from the Sun+Earth model for visual guidance (from Fig. 5.7) is shown. For the MLE for Earth's normal position, θ and ϕ are shown in blue and in orange. Reproduced from Reb et al. with permission [220]. Copyright © 2022 Wiley.

attributed to the deviations of the fused DLR trajectory rather than deviations of the OHSCIS trajectory from the real solar trajectory.

To sum up the Sun-only model, the strong deviations in the orientation estimation of both methods at the beginning and end of the dataset are likely attributed to cumulative deviations in the propagation of the fused DLR trajectory. During and in the vicinity of phases that benefit from camera aiding (i.e. during times from T+100 s until the end of the dataset, where propagation time is not exceeding around a minute), the maximum deviation of both methods is less than $\Delta\theta \approx 5°$ for $\theta \lessapprox 150°$. Deviations of ϕ lie within a similar range, but strongly increase at high polar angles due to the coordinate system used. In the refined model, a second, extended radiation source is incorporated as described in the Radiation Model section to add the Earth as another component. In Fig. 5.7, the Sun+Earth model MLE trajectory and the MCMC sampling median and 1 σ sampling distribution are added in purple and blue for ϕ and θ respectively.

Fig. 5.11 shows Earth's normal direction evolution over time as obtained from the MLE solution. At first sight, the estimated solar position trajectory from the composite model does not deviate significantly from the Sun-only model. Thus, the inclusion of Earth does not distort

the solution for the solar position substantially. The global model parameter changed slightly (see Table 1).

Table 5.1: Values of global model parameters and log likelihood function.

	Sun Brightness	Earth	σ	LL
Sun only	33333	-	1110	32692
Sun+Earth	32703	3251	934	32170

The solar brightness L is lowered by around 2 %. The Earth's brightness reaches around 10 % of the solar brightness, hence the maximum Earth contribution is approximately 3 % of the maximum solar contribution for a single sensor. Absolute brightness values are not analyzed more closely, since this general scaling value only has a minor influence on the orientation estimation in single frames. Comparing the Sun+Earth model with the Sun-only model, the most pronounced changes are that differences in ϕ and θ estimations are largest during polar solar positions, well visible for θ in Fig. 5.7. This is in agreement with our expectations since during this phase the solar irradiation onto the light sensors is weak, and the Earth component gains relative strength. Thus, the model is expected to be more strongly influenced by the Earth component. Second, it appears that corrective changes of the Sun+Earth model tend to be more pronounced in moments where the Sun-only model deviation from the fused DLR trajectory is larger. Interestingly, the Earth component shifts the estimated solar position systematically towards the fused DLR trajectory, effectively reducing deviations. The only exception is the θ estimation while the Sun crosses the nadir, where the inclusion of Earth systematically increases θ to larger values. This effect is natural since, upon inclusion of the Earth, the Sun does not need to account for equatorial light scattered light from the Earth anymore and thus moves freely to higher θ values. The apparent larger uncertainty of ϕ from MCMC sampling stems from the larger θ values. Apart from that, there is no significant reduction of the 1-σ band visible. The σ parameter is reduced by 15 %, showing that the inclusion of Earth, although a weak component, effectively reduces data–prediction discrepancies.

A stable cutoff angle after including the Earth radiation model is expected. However, this does not turn out to be true: It still drifts towards higher values, consequently, the sensor cutoff is excluded also for the Sun+Earth model. Possible explanations for the lack of stability for the refined model are, first of all, that the geometrical shadowing angle is not a constant value but rather has a directional dependency. To assess this effect more closely, Fig. 5.12 shows the geometrical shadowing angles in polar and azimuthal directions using the computer-aided design of the OHSCIS module. The geometrical shadowing angles in the four directions range from 55-90° for the sensor and the incidence angle to the glass normal direction range from 67.5-79°. Interestingly, the lower sensor cutoff angles coincide with higher glass incidence

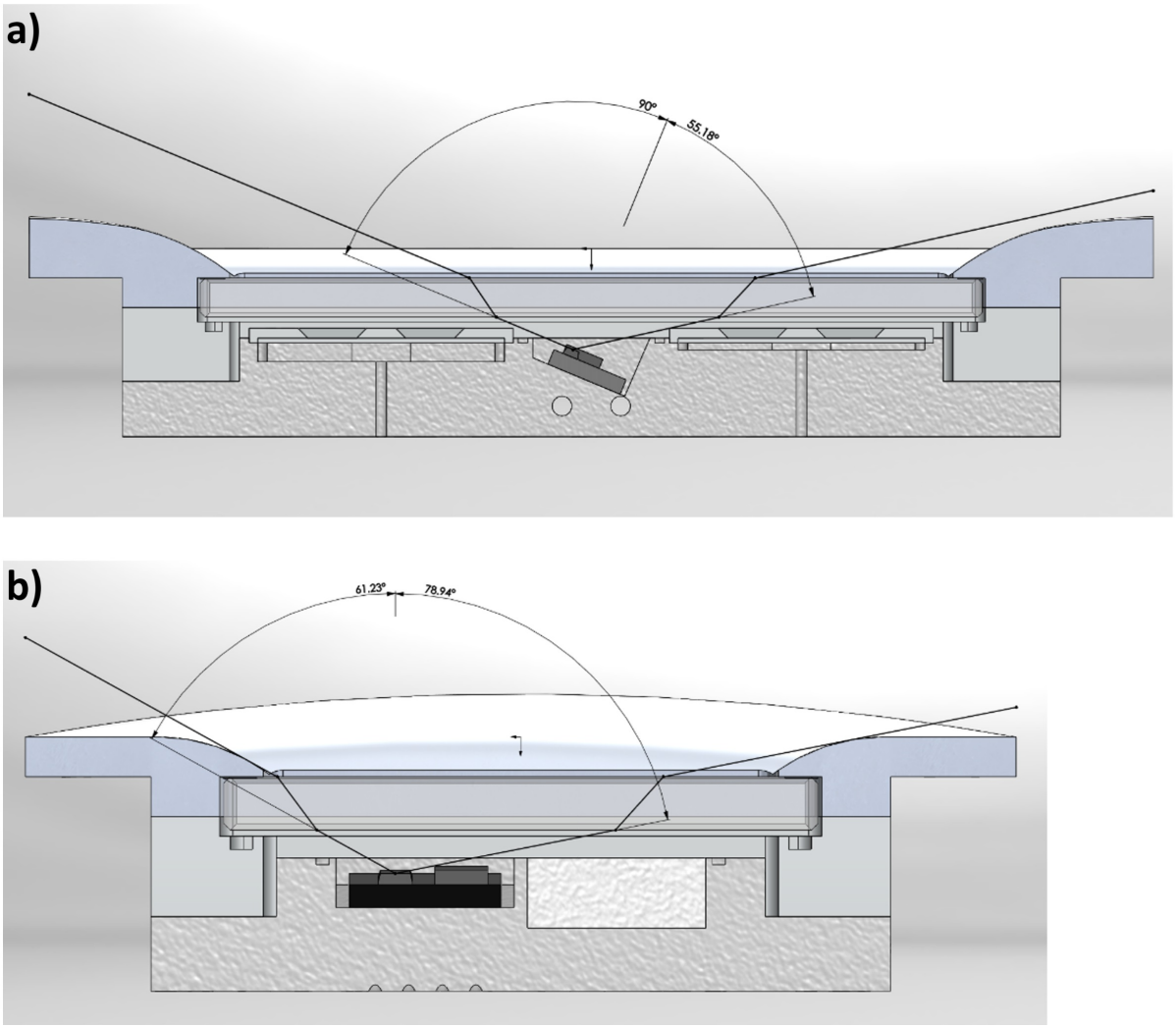

Figure 5.12: Computer-assisted design visualizations of the geometrical shadowing of the light sensors for a downwards-facing sensor a) in polar and b) in the azimuthal direction. In the polar direction, the cutoff angles measured from the sensor's normal directions are 90° (no geometrical shadowing) and 55°. In the azimuthal direction, the shadowing angles are 61° and 79°, respectively. The angles are determined for the light-sensor surface area center. Note that for a solar position that includes a polar and azimuthal inclination at the same time, the effective shadowing angle is strictly increased to higher angles since geometrical shadowing occurs later. Reproduced from Reb et al. with permission [220]. Copyright © 2022 Wiley.

angles, effectively creating a smooth response leveling-off that renders the geometrical cutoff angle weakly constrained intrinsically. Second, the cutoff angle shows degeneration to a certain extent. It cuts off the sensor response at high angles where the effective response including glass transmission is already strongly reduced, limiting its total influence. Third, the radiation model does not account for any stray light reaching the sensors, e.g. reflected from the hatch. Note that such stray light does not influence the solar cell measurements since they are placed close to the window and their aperture masks efficiently shield possible stray light from entering. Lastly,

the basic assumption of normally distributed measurement noise is not questioned. Especially for processes like photon counting measurements of limited exposure usually follow Poisson count statistics. However, for sufficient exposure and count statistics, optimizations based on Poisson or Gaussian weighting deliver usually similar results. Poisson weighting would favor low-brightness measurements and thus improve e.g. the accuracy of Earth position determination. However, in this work, the priority is to achieve precise Sun position estimation, i.e. to get reliable estimates for the strong radiation component that dominates the incident light on the light sensors for reliable irradiance determination for the solar cells.

From the solar position, the irradiance onto each solar cell module is derived for each time by executing the following steps: For a given solar position, the fused silica glass transmission is calculated for each window. For relative solar angles of less than 90°, the area projection effect is included as $\cos\alpha$. This work uses the AM0 irradiation strength of the solar constant of 1366.1 $\mathrm{W\,m^{-2}}$ according to the ASTM E-490 standard extraterrestrial spectrum [38, 39]. It scales with fused silica glass transmission and angular projections, resulting in the effective irradiation of each of the eight viewing directions of the different solar cell types. Note that

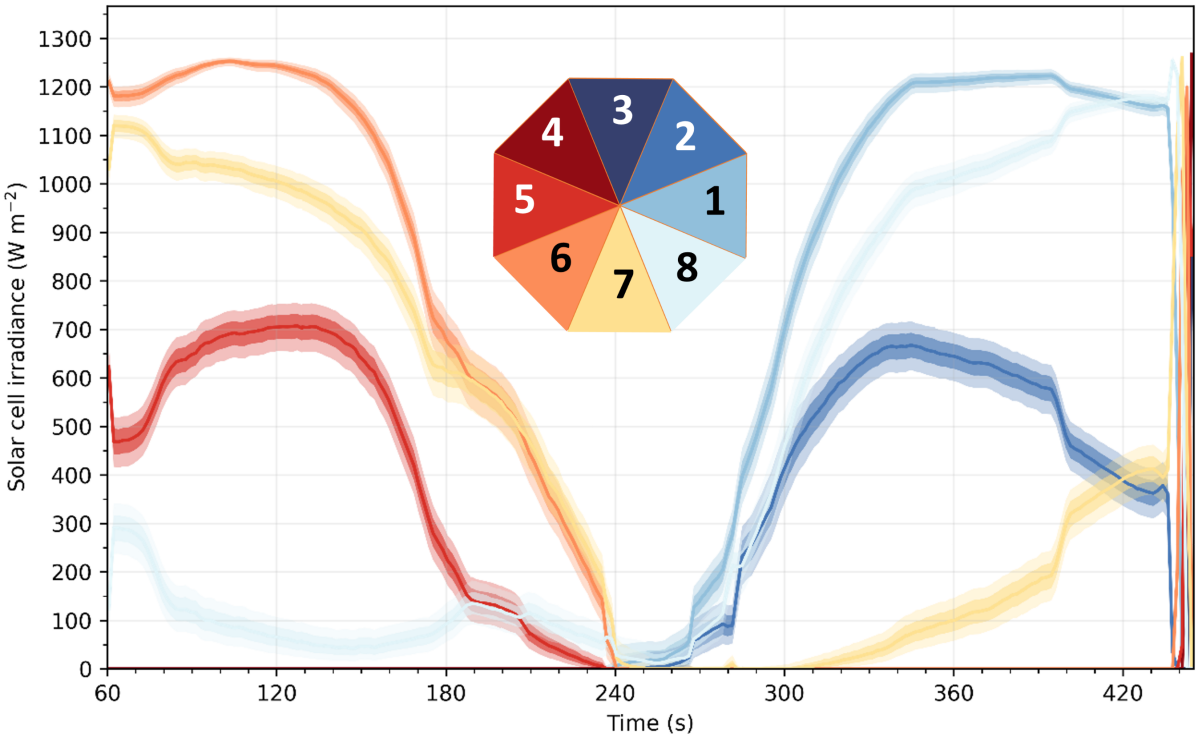

Figure 5.13: Irradiance evolution onto the solar cells during the flight for the eight different segments. The MCMC solar position sampling results are further processed to obtain the irradiance distributions similarly as in Fig. 5.7. The colored lines represent the median of the irradiance distributions for each solar cell orientation, color-coded according to the octagonal inset. 1 and 2 bands are shown in addition. No geometrical shadowing effect is considered. Reproduced from Reb et al. with permission [220]. Copyright © 2022 Wiley.

here no geometrical shadowing effects are included. They are expected to occur at high relative angles α or low irradiances (similar reasoning as for the light sensors, cf. Fig. 5.12). Fig. 5.13 shows the resulting reconstructed irradiance evolution during flight. The irradiance evolution can be considered as the final result to be used for further analysis of the solar cell performance parameters.

As expected from geometrical reasons, significant solar irradiance is present usually only for three segments at the same time. At the beginning of the µ-gravity phase, segment 6 receives solar irradiance close to AM0, i.e. 1200 $\mathrm{W\,m^{-2}}$ and above, and for segment 7 the solar irradiances are comparable to one sun. During payload alignment with the sun at around T+250 s, no direct sunlight irradiates the segments. At the end of the µ-gravity phase, segment 1 receives strong solar exposure. The equatorial crossing of the sun at T+420 s shows a special configuration of symmetry. At this crossing, segments 1 and 8, as well as segments 2 and 7 show the same irradiance values, respectively, where the latter values of 400 $\mathrm{W\,m^{-2}}$ correspond to a relative angle of around 67.5°.

Focusing on the 1 and 2 σ distribution bands, it becomes apparent that typically for high irradiance values, their uncertainties decrease and the estimates become more robust. This effect can be understood by having a closer look at Fig. 5.2d, which shows the effective angular sensor response map including the fused silica glass transmission. The response map is relatively flat for small relative light source position angles to the fused silica glass normal, i.e. the sensor response is weakly sensitive to shifts of the solar position angle. The other way round, shifts of the solar position angle at equatorial solar positions do not translate into substantial shifts of derived irradiance, rendering this solar position estimation method robust for precise solar irradiance determination, especially for solar cells oriented in similar directions as the light sensors.

5.5 Conclusion

By using measurement data of 16 $\mathrm{I^2C}$ ambient light sensors facing in different directions and refining a point source model to the data a precise solar positioning estimate is achieved for the entire µ-gravity time of the MAPHEUS-8 mission. Using Monte-Carlo Markow chain methods, the posterior likelihood distribution of the model parameters is sampled to derive estimates for orientation determination uncertainties. For equatorial solar positions, the method provides high accuracy of within 3° uncertainty (1σ) that is comparable to or in phases more accurate than the camera-based estimates of Braun et al. Interestingly, our solution is closer to the fused trajectory of Braun et al. than to the standalone camera-based trajectories, validating their model that includes IMU measurements and propagation methods. Also for high solar inclinations, the optimized models give reasonable results with effective angular deviations that are largely below 10°. With our light sensor geometry, the effective field of view to determine the solar position encompasses practically the entire sky, even solar nadir (as well as zenith) crossings

are registered by the model. The inclusion of Earth as a second radiation component improves the model likelihood and estimates, bringing the trajectory closer to the fused trajectory of Braun et al. Our results show that first, our method is capable of improving the payload orientation estimation for sounding rocket flights, and second, that our method gives stable estimates for a broad range of solar positions with high accuracy for payload orientations where the cameras cannot capture the Sun, making this a powerful complementary method. During the flight, the payload covered many different orientations, making MAPHEUS-8 the ideal test case for this method. This will help to assess the quality of attitude determination in potential future flights with different orientation profiles. The presented approach of using ambient light sensors together with light source modeling in combination with machine learning results in powerful results for simplistic sensors that are commercially broadly available. The presented system of light sensor parallelization is capable of predicting the solar position with comparable accuracy to advanced optical components and with very low power consumption and data storage requirements. It is not limited to space applications, instead, the concept can be transferred to terrestrial applications, more general to applications where attitude determination with respect to point-like and extended light sources is required. Using the trained model global parameters, together with a customized optimization routine, a handful of iteration steps for every single frame can determine the solar position, rendering these calculations computationally cheap. Hence, this method promises real-time solar triangulation with an accuracy of a few degrees, also with a limited computational effort, and for arbitrary sensor orientation configurations. Using this technique and the chosen ambient light sensor geometry, highly precise solar irradiance estimates are obtained that allow reconstructing the incident solar power onto the differently oriented solar cells at each time during the flight. Especially for strong solar illumination, such precise measurements are the basis for quantitative performance analysis for testing and qualifying novel thin film solar cell technologies for application in space and beyond.

6 Flight Solar Cell Results

Most of the results shown in this chapter have been published in the article *Perovskite and organic solar cells on a rocket flight* [189] (L. K. Reb et al., *Joule*, 4 (9):1880–1892, 2020, doi:10.1016/j.joule.2020.07.004) and in the article *Space- and post-flight characterizations of perovskite and organic solar cells* [233] (L. K. Reb et al., *Solar RRL*, 7 (9):2300043, 2023, doi:10.1002/solr.202300043).

In this chapter, the results of the photovoltaic characterization of the thin-film space solar cells are presented. Fig. 6.1 illustrates the general experiment concept of the sounding rocket flight, reaching orbital altitudes while exposing different perovskite and organic solar cell types as indicated by the colored areas facing radially outwards of the rocket payload. In the first Section 6.1, the results of the photovoltaic pre-characterization in the laboratory of the different solar cell types are presented. Sections 6.2, 6.3, and 6.4 give an overview of the collected J-V

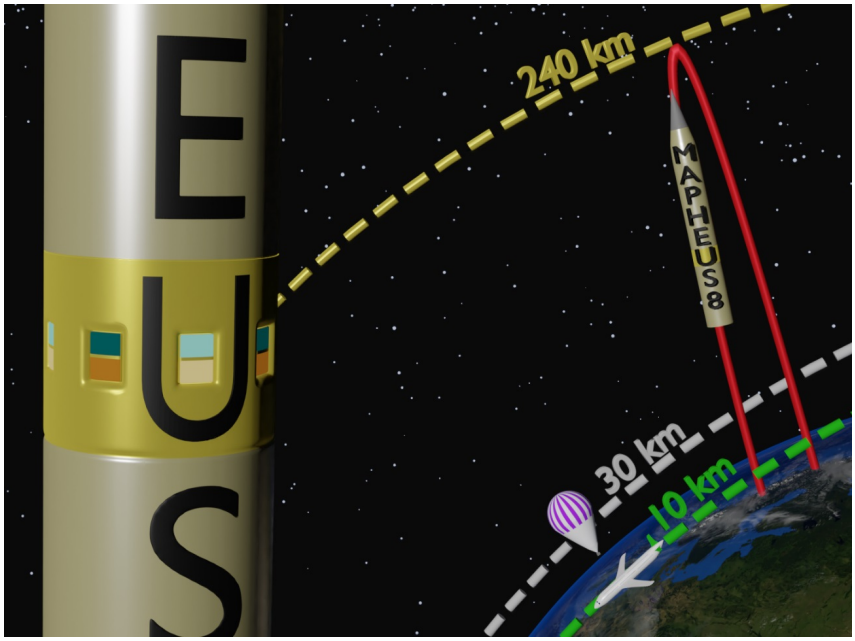

Figure 6.1: In the foreground on the left, the experimental setup OHSCIS, highlighted in gold, is part of the payload. Eight symmetrically arranged hatches contain one organic (green) and one perovskite (brown) solar cell module (details see text). Neighboring hatches contain different cell types indicated in different colors. The background shows the suborbital parabolic flight trajectory with the apogee reaching altitudes common for low-Earth-orbit satellites. Reproduced from Reb et al. with permission [189]. Copyright © 2020 Elsevier.

key parameters. They are used to separate the acquired performance parameters into different phases based on illumination states, solely derived from solar cell parameters, separating in high solar irradiance and low solar irradiance solar cell behavior. Then, by adding the solar irradiance to the solar cell measurements, performance parameters are reconstructed in Section 6.6, and correlations and trends of photovoltaic parameters with solar irradiance are established. Power conversion efficiencies are calculated and the champion space solar cell efficiency measurements are presented, followed by the conclusion.

6.1 Solar Cell Pre-Characterization

The four solar cell module types represented a simplified selection of state-of-the-art single-junction perovskite and organic architectures and absorber materials: The mixed organic lead mixed halide perovskite solar cells in planar (SnO_2) and mesoscopic (m-TiO_2) architectures can exceed power conversion efficiencies of 20% [85]. The inverted organic bulk-heterojunctions of non-fullerene PBDB-T:ITIC and of narrow bandgap polymer:fullerene PTB7-Th:$PC_{71}BM$ type used in the flight architecture are reported with 8.6% and 8.25%, respectively [199, 234]. The fabrication details can be found in section 3.1. Fig. 6.2 shows the champion solar cell

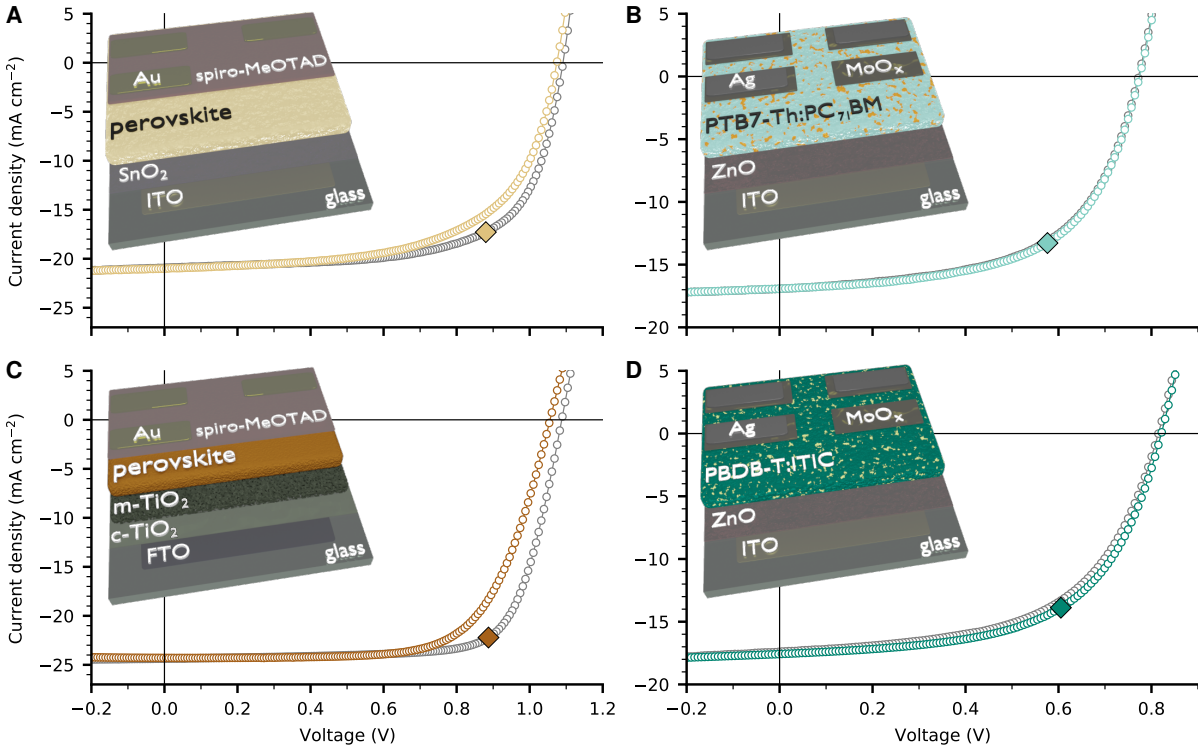

Figure 6.2: Precharacterization. (A) Planar perovskite with SnO_2 electron-transport layer. (B) Fullerene organic cell. (C) Mesoscopic perovskite with TiO_2 electron-transport layer. (D) Non-fullerene organic cell. The voltage sweep forward is colored and backward greyed out; the maximum power points are indicated by marks. Reproduced from Reb et al. with permission [189]. Copyright © 2020 Elsevier.

measurements in the pre-characterization measurements together with a schematic layer stacking of each solar cell type. An overview of the photovoltaic parameters including V_{oc}, J_{sc}, FF, V_{mpp}, J_{mpp}, p_{mpp} is given in the left part of Table 6.1.

Table 6.1: Overview of champion performance parameters of the pre-flight characterization (left) and the in-flight characterization (right) for all different solar cell types.

Solar cell type	V_{oc} (V)	J_{sc} ($\frac{mA}{cm^2}$)	FF (%)	V_{mpp} (V)	J_{mpp} ($\frac{mA}{cm^2}$)	p_{mpp}* ($\frac{mW}{cm^2}$)	V_{oc} (V)	J_{sc} ($\frac{mA}{cm^2}$)	FF (%)	V_{mpp} (V)	J_{mpp} ($\frac{mA}{cm^2}$)	p_{mpp} ($\frac{mW}{cm^2}$)
	Pre-flight characterization						Best in-flight performance					
Perovskite m-TiO_2, bw.	1.09	24.37	74.3	0.89	22.21	19.71	1.05	22.27	62.3	0.82	17.40	14.21
Perovskite m-TiO_2, fw.	1.06	24.29	68.1	0.81	21.42	17.45	1.05	22.35	60.6	0.84	17.51	14.70
Perovskite c-SnO_2, bw.	1.06	20.90	69.5	0.87	17.85	15.45	1.11	19.15	69.1	0.91	16.23	14.69
Perovskite c-SnO_2, fw.	1.03	21.16	64.1	0.81	17.27	13.95	1.12	19.11	67.9	0.91	15.94	14.49
PBDB-T:ITIC inv.	0.82	17.58	58.2	0.61	13.89	8.40	0.63	15.61	43.7	0.40	10.86	4.31
PTB7-th:$PC_{71}BM$ inv.	0.77	16.92	58.4	0.58	13.82	7.65	0.74	17.12	60.3	0.57	13.38	7.68

*For the pre-flight characterization under AM1.5G illumination (100 mW cm^{-2}) the unitless number of the power density p_{mpp} equals the PCE in percent.

Note: For the perovskite solar cells the values corresponding to the backward (bw.) and forward (fw.) sweep are given. Reproduced from Reb et al. with permission [189]. Copyright © 2020 Elsevier.

6.2 Payload Orientation During Phases of Flight

The OHSCIS main measurement time, i.e. the phase with pitch-, yaw-, and roll-rate control of less than 0.9° s^{-1}, began with rate-control system switch-on 61 s after lift-off (LO) at an altitude above 70 km. Please see table 4.2 for a detailed launch timeline with a focus on the important events before, during, and after launch. Fig. 6.3B presents the altitude as a function of time after LO as obtained from GPS data. The payload reached the apogee at 239 km altitude after 251 s; re-entry mode detection occurred after 428 s at an altitude of 100 km. This resulted in a main measurement time of around six minutes, in which current-voltage characteristics were continuously recorded.

A stable orientation of the payload is crucial for a constant irradiation intensity during single measurements. The rate control preserved a fairly constant incident angle of solar and Earth illumination onto the cells with only a small change during single sweeps. Especially for sunlight shining perpendicularly onto the cell surface, i.e. in phases of strongest intensity, only small changes of the irradiation intensity occur as a reason of the sinusoidal character of the projection effect. A detailed discussion about reasoning related to solar irradiation intensity can be found in the previous chapter 5.

Fig. 6.3B schematically visualizes the payload orientation during the main measurement time. During the ascent, the sun strongly illuminated one side of the payload denoted as phase I. A

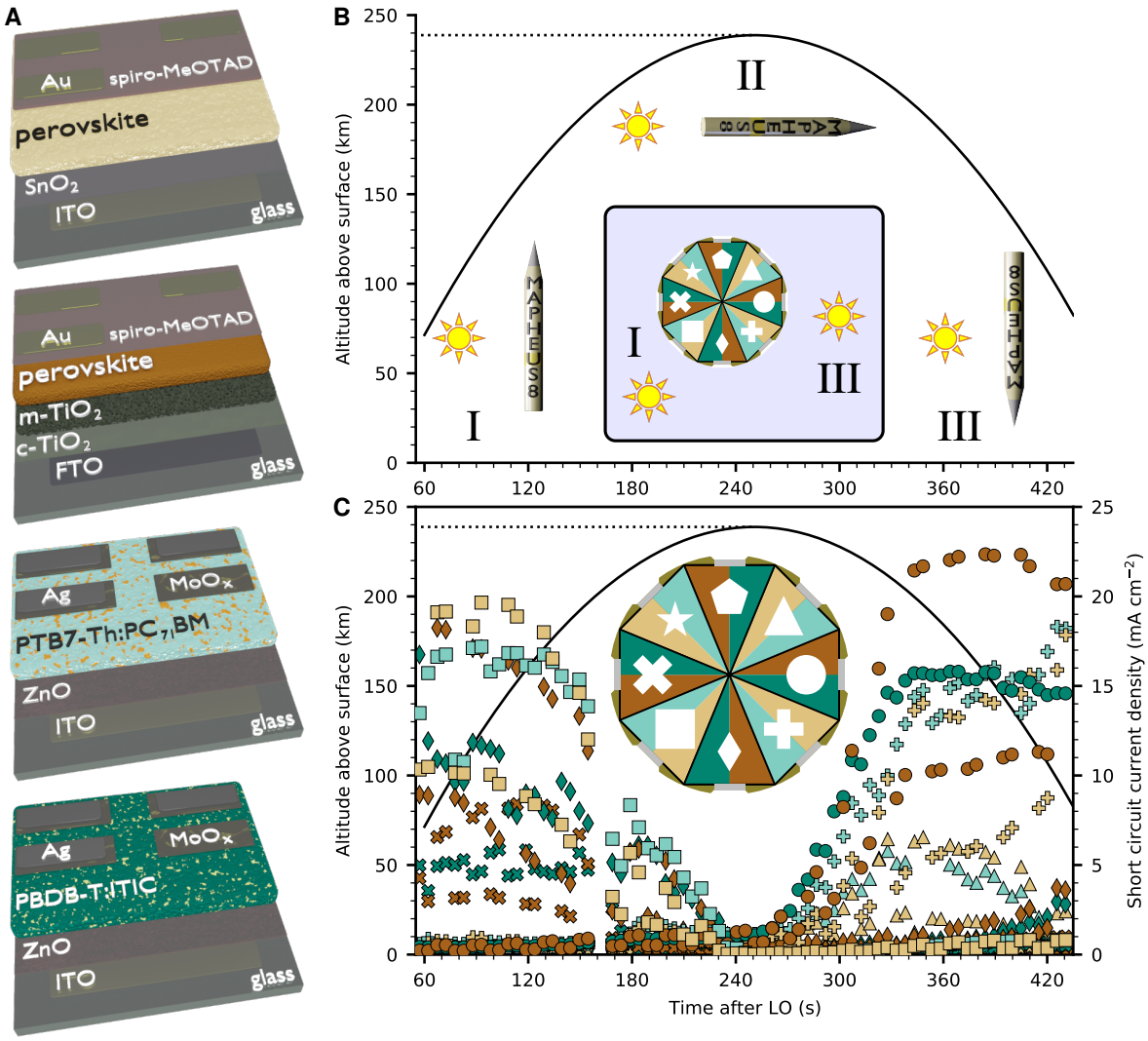

Figure 6.3: Solar Cells and Flight Phases Overview. (A) Schematic solar cell stacking of the four different types mounted in the experiment. The absorber layer is colored differently for each type: PTB7-Th:$PC_{71}BM$ in turquoise, PBDB-T:ITIC in dark green, mesoscopic perovskite in brown, and planar perovskite in beige. (B) Schematic payload orientations during flight and the blue-shaded inset with a cut through the cylindrically shaped payload to illustrate the payload orientation relative to the solar position. The illumination states are distinguishable into three different main phases of incident illumination onto the solar cells. I, intense solar illumination from one side; II, no direct solar illumination onto the solar cells, reflected solar radiation from Earth's surface; III, intense solar illumination from a side opposite to phase I. (C) Scatter plot showing the short-circuit current density (J_{sc}) evolution and flight-altitude (black line) during micro-gravity. Each solar cell sweep is depicted with a mark according to the segment labeling in the octahedral inlet and colored according to the respective cell type. The octahedral inlet illustrates the solar cell positioning in the cylindrical rocket body, where the radially outward-facing solar cells were mounted parallel to the gray-indicated windows. The solar cell orientation and type are defined by mark and color. Reproduced from Reb et al. with permission [189]. Copyright © 2020 Elsevier.

slow angular drift gradually aligned the payload with the direction of solar radiation to cross the parallel alignment in phase II. The slow angular drift continued, gradually increasing the solar illumination onto the opposite side of the payload with respect to phase I, resulting in a strong illumination in phase III again. This sequence can be deduced from the evolution of short circuit current densities (J_{sc}s) of the cells in Fig. 6.3C. The photo-generated current scales proportionally with the irradiation intensity and therefore can be considered as a measure for the illumination intensity, apart from possible performance deviations of individual cells. Directly at the beginning of micro-gravity, high J_{sc}s are measured in the segments labeled in Fig. 6.3C as 'square', 'diamond', and 'X', in descending order. For the first minute in the main measurement phase, the J_{sc}s of these segments form a plateau, indicating a stable orientation and therefore stable light intensity during several measurement cycles (phase I). Thereafter the J_{sc}s decline gradually and reach a minimum approximately in the apogee (phase II). This is the moment of lowest incident light of the entire flight. Then the J_{sc}s of segments labeled as 'circle', 'plus', and 'triangle', in descending order, gradually increase and reach a second plateau, beginning at around 340 s after LO and lasting around one minute (phase III).

A detailed overview of the photovoltaic performance parameters can be found in the boxplots in Fig. 6.4. Here the boxplots show V_{oc}, J_{sc}, p_{mpp}, and FF (in rows) for flight phases I, II, and III (in columns). In the top of Fig. 6.4, the direction of incident solar light onto the payload is indicated for the respective phases. In each phase, each solar cell type is shown in its respective color. For phase I, measurements of the illuminated segments 'square', 'diamond', and 'X' are presented, beginning 65 s after LO for one complete measurement cycle (80 s), i.e. showing data for each device for the segments during strong solar illumination. Similarly, for phase III, measurements of the illuminated segments 'circle', 'plus', and 'triangle' are extracted beginning after 330 s after LO for one complete measurement cycle (80 s). For phase II, the simultaneous measurements of the eight segments within two up and down sweeps (240 s – 260 s) are evaluated. Measurements are depicted as open circles, colored in the respective cell type color. Boxplot conventions are used as follows: the median is shown as a dashed line, the box limits are first to third quartile comprising the interquartile range (50%) of the measurements, and the box whisker lengths are the last measurement inside of 1.5 times the interquartile range distance to the box. Also, the mean value is depicted on top of the box as the colored symbol according to the segment for phases I and III, whereas as a solid horizontal line for phase II.

6.3 Highest Power Densities in Space Under Strong Solar Irradiation

During phase I, the highest J_{sc}s were measured in segment 'square'. Therefore, the focus is on this segment and the phase-I plateau to select solar cell measurements for SnO_2 perovskite and PTB7-Th:PC_{71}BM architectures under stable and strong illumination. As a measure of the performance, the maximum power point density p_{mpp} is introduced, defined as the maximum power per area which can be extracted during solar cell operation. Thus, measurements of the highest p_{mpp} for SnO_2 perovskite and PTB7-Th:PC_{71}BM architectures are selected during the

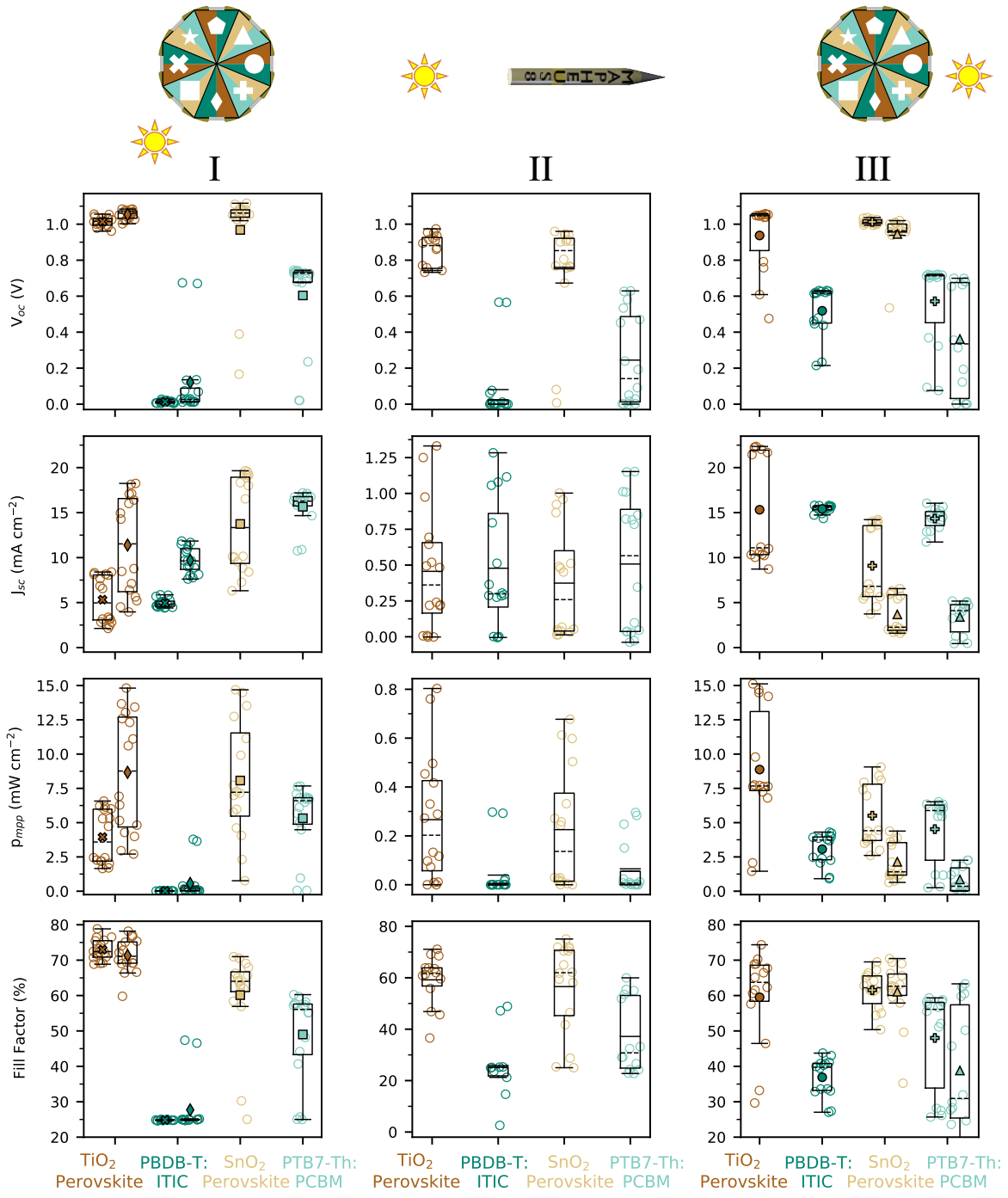

Figure 6.4: Boxplots of V_{oc}, J_{sc}, p_{mpp}, and FF (in rows) for flight phases I, II, and III (in columns). For a detailed description see text. Reproduced from Reb et al. with permission [189]. Copyright © 2020 Elsevier.

phase-I plateau (measurements start 67.4 s and 87.9 s after LO, respectively). During phase III, the highest J_{sc}s were measured in segment 'circle'. In the same manner, the measurements of the highest p_{mpp} for mesoscopic TiO_2 perovskite and PBDB-T:ITIC architectures are selected

(measurements start 384.3 s and 353.5 s after LO, respectively). Fig. 6.5 presents the resulting current-voltage measurements for each solar cell architecture.

To assess the solar cell performance during the different phases in more detail, Fig. 6.4 presents an overview of the key parameters V_{oc}s, J_{sc}s, p_{mpp}s, and fill factors of all devices measured during phases of solar illumination.

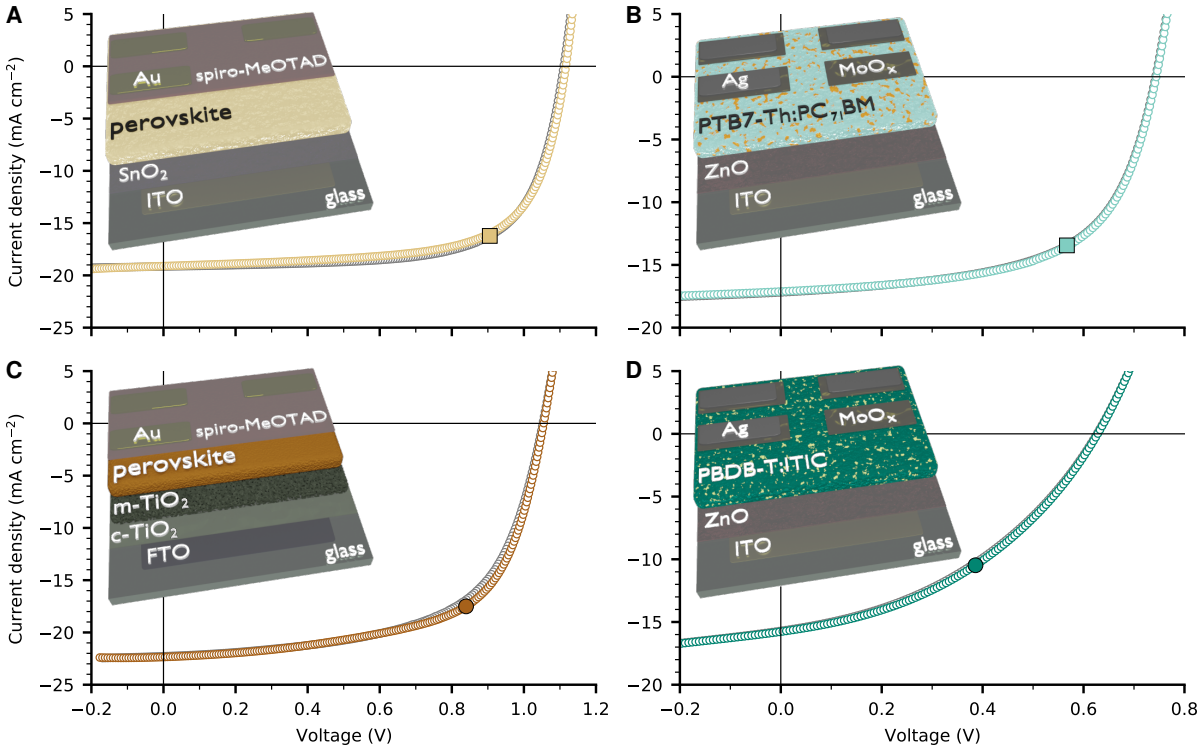

Figure 6.5: In-flight champion power-density measurement cycles of the perovskite with planar SnO_2 blocking layer (A), fullerene organic cell (B), perovskite with mesoscopic TiO_2 blocking layer (C) measurement from phase I. Non-fullerene organic cell (C) measurement from phase III. In accordance with Fig. 6.2, the voltage sweep forward is colored and backward greyed out; the maximum power points are indicated by marks that correspond to the respective segments. Reproduced from Reb et al. with permission [189]. Copyright © 2020 Elsevier.

In Fig. 6.5A the smoothness of the current-voltage curves and the similarity of forward and backward scans suggest a negligible change of irradiance during single-cell measurements. This validates our selection from the illumination plateaus in Fig. 6.3C. All four solar cell types show typical diode curves with a vertical offset due to the strong illumination. The highest measured J_{sc}s exceeded 20 mA cm^{-2} for the TiO_2 perovskite cells and thereby surpassed the SnO_2 perovskite cell's J_{sc}s. Since the same behavior during pre-characterization in the home laboratories was observed, it is not attributed to the flight. The SnO_2 compensated the lower currents with a higher fill factor (FF) of about 70% and a higher open-circuit voltage (V_{oc}) to reach a similar high p_{mpp} and hence flight performance. Thus, both perovskite types exceeded 14 mW cm^{-2}, which is in the same magnitude as the power densities measured in the pre-characterization. Un-

expectedly, these measurements show a lower hysteresis than during the pre-characterization. Hysteresis in perovskite solar cells is frequently attributed to the presence of both ion migration and interfacial recombination of charge carriers [235]. In our case, a lower photo-current during flight compared to pre-characterization could reduce the charge carrier accumulation and hence the interfacial recombination, effectively reducing the observed hysteresis. Moreover, since this effect is observed for both perovskite solar cell types, it could also be related to oxygen doping of the electron-blocking layer spiro-MeOTAD during the countdown. This material is known to show an enhanced conductivity after oxygen doping, which could also reduce the observed hysteresis [236]. The PTB7-Th:$PC_{71}BM$ organic solar cell surpassed 7.5 mW cm^{-2}, similarly high performance as during pre-characterization, whereas the PBDB-T:ITIC organic cell showed a significant decrease of V_{oc} and FF compared to pre-characterization, but still reached 4 mW cm^{-2}. With these performances, even our least performing solar cell type reached a similar power density as an organic solar cell deposited on an ultra-thin PET foil by Kaltenbrunner et al. some time ago [19]. That power density was sufficient to reach a specific power of 10 W g^{-1}. Assuming a similar weight per area for our solar cells, the power densities measured during space operation would give rise to remarkable specific powers. Based on this comparison, the organic solar cells would outperform inorganic solar cells (reaching 3 W g^{-1} in AM0) by a factor of three, whereas our perovskite solar cells with their higher power densities would exceed the inorganic solar cells by up to one order of magnitude in terms of specific powers. Therefore, there do not seem to be obstacles to reaching such high specific powers with HOPVs in orbital altitudes. Owing to all the aforementioned effects, the HOPVs impressively demonstrated their efficient operation in space under strong solar irradiation and reached their performance expectations.

6.4 Maintained Power Generation under Weak Terrestrial Irradiation

During phase II a unique possibility occurred to measure HOPVs under special illumination conditions. The payload aligned with the sun, hence a significant illumination source was diffuse reflection arising from the Earth's surface. At these high inclinations, geometrical parts of the experiment effectively shadowed the solar cells from the sun.

To substantiate this, Fig. 6.6 shows snapshots of all backward-sweep measurements of perovskite solar cells at the same time, one from phase II and one at phase III, corresponding to measurement starting times of 245.7 s and 327.9 s, respectively. All eight simultaneously measured cells distributed around the ring show diode behavior with different vertical offsets, due to different irradiances. In phase III, three perovskite cells are simultaneously and strongly illuminated as expected for sunlight, i.e. parallel light. However, in phase II five of the eight perovskite cells show significant illumination, which requires a different scenario where direct sunlight cannot be the only illumination source. The surface of the Earth, however, is a spatially extended diffuse-light source that can illuminate more than half-side of the rocket simultaneously. Therefore, at least two segments were illuminated by reflected sunlight arising from Earth's surface only. The power densities of the five simultaneously illuminated perovskite solar

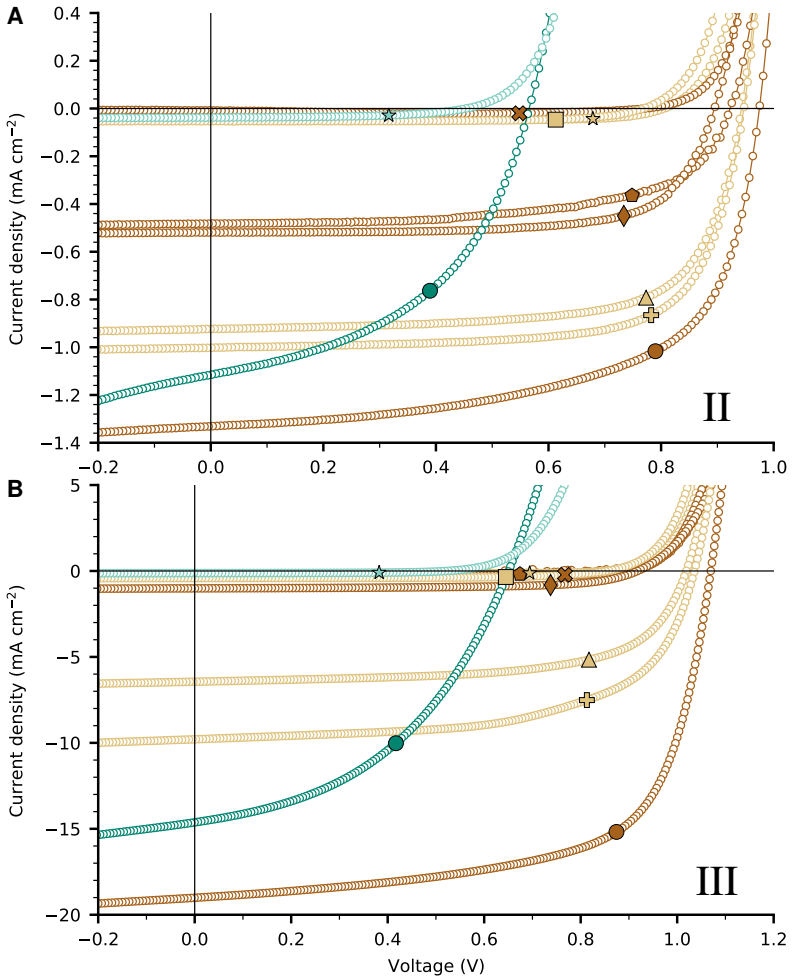

Figure 6.6: (A) Faint scattered light from Earth illuminating five segments (phase II, measurement begin 245.7 s after LO). (B) Strong solar irradiation illuminating three segments (phase III, measurement begin 327.9 s after LO). Also, two representative organic solar cell measurements are shown. Note the different current-density scales in both graphs. Reproduced from Reb et al. with permission [189]. Copyright © 2020 Elsevier.

cells are ranging from 0.3–0.8 mW cm^{-2}. During this phase of weak light exposure to the cells, the V_{oc}s and also the fill factors are largely preserved, as also shown in Fig. 6.4.

Inspecting the J_{sc}s more closely, they reach above 1.3 mA cm^{-2} for the 'circle' segment in Fig.6.4A, which is capable of reaching about 20 mA cm^{-2} as seen in B. There is approximately a factor of 15 between those two values, which is a consistent result with the values from Table 5.1 in Chapter 5. There, the Earth radiation component with a total irradiation of around 10 % of the solar constant is reduced when angularly integrating Earth irradiation due to the projection effect. Thus the reasoning introduced here with the diffuse illumination by Earth is consistent with the results obtained from the light sensors only, underlining the power of the approach in 5.

The average V_{oc}s of the perovskite solar cells drop slightly from around 1 V in phases I and III to around 0.85 V during phase II, also the fill factors drop slightly but remain above 60 %

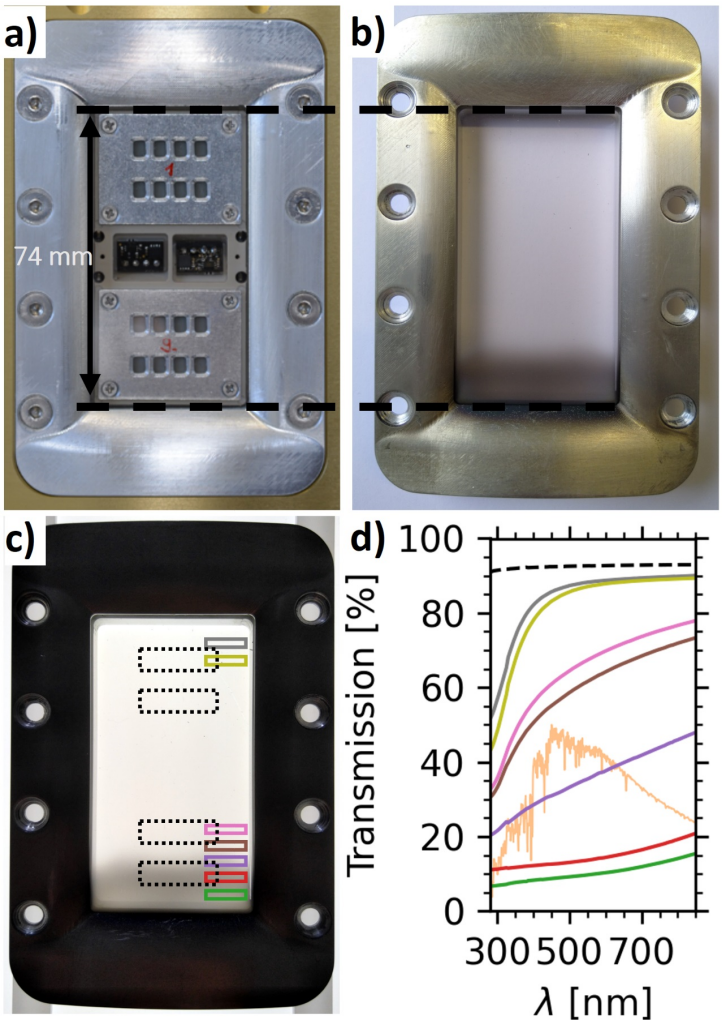

Figure 6.7: a)-c) Photographs of the insertion module window, including the fused silica glass: a) The insertion module including solar cell aperture masks to show the exact position of the solar cell apertures relative to the window frame. b) Photograph of the recovered and disassembled insertion module. One can see smut deposited on the glass window's lower part, presumably dominantly deposited during supersonic ascent. The upper part of the window appears clear. c) Backlight illumination photograph of the same window to see the smut with a uniform contrast response. The four black-dotted rectangles indicate the approximate position of the rows of solar cell apertures (cf. a). The smaller colored rectangles depict the UV-vis slit size at various positions along the glass. d) the graph on the lower right shows the corresponding measured transmissions, where the black dashed line is the reference measurement of a clean glass. In addition, the AM0 solar spectrum is shown in arbitrary scale in orange [38, 39]. Note the dominant decrease of glass transmission in UV, where the glass appears clear in the photographs. Reproduced from Reb et al. with permission [233]. Copyright © 2023 Wiley.

during the seconds of lowest incident light. The organic solar cells show a similar trend, i.e. the obtained power densities correlate strongly with the short circuit currents, and the power densities are reduced by a similar factor compared to phase III. These findings support that the power conversion efficiency of HOPVs can be maintained even under weak diffuse light known

from previous studies, while here these results are derived from measurements in real space [237]. Interestingly, the HOPVs hereby generate power as expected for illumination conditions of the outer solar system at Jupiter and Saturn [237]. Up to now, only probe Juno was powered by solar energy in Jupiter's distance from the sun [238]. Therefore, these measurements prove the ability of HOPVs situated in space to operate in diffuse and low irradiance light conditions – a promising result for their possible application in deep space missions.

6.5 Influence of Soot on the Windows

At the very beginning should be emphasized that both, solar irradiance values as well as solar cell performance parameters from previous sections and similarly in this section are derived without the consideration of soot on the windows and thus are upper limits to the in-reality received somewhat lower solar power, and photovoltaic performance potential, respectively. Consequently, PCE values are conservative estimates throughout this thesis. All irradiance values are calculated based on the assumption of a negligible absorption of the fused silica glass windows. However, during super-sonic ascent, soot originating from the cork ablative nose-cone heatshield is deposited on the fused silica windows, thus effectively lowering the transmission through the glass.

Fig. 6.7 shows photographs of one of the eight hatch windows after recovery. Fig. 6.7 shows the glass window transmission of spatially distributed UV-vis slit positions. Interestingly, even in the glass regions where no visual absorption takes place, the UV transmission is strongly reduced, while the transmission in the optical range is reduced from Fresnel-limited transmission by around 5%. Hence, the cork soot acts as UV protection for the solar cells behind the window as it preferentially reduces the transmission at lower wavelengths. The light attenuation becomes significant for the lower solar-cell modules, which in this flight are all perovskite solar cells. While the upper row of solar cells experiences around 20 % effective irradiance decrease, the lower row only receives 1/2 to 1/3 of the possible solar irradiance. Note that all high-performance solar-cell data of the perovskite solar cells are strictly derived from the upper row. It is not attempted to recalibrate for this soot effect since it is small for the organic solar cells and the perovskite solar cells. The pronounced edge of soot and the transmission gradient along the glass would make irradiance reconstruction more complex and error-prone for inclined solar directions.

6.6 In-Depth Photovoltaic Characterization During Flight

The photovoltaic parameters presented and discussed in this section are extracted from the main measurement time, i.e. the $\sim$6 minutes while the rocket payload is on its parabolic trajectory outside Earth's atmosphere with stabilized orientation. For each sweep, the open circuit voltage (V_{oc}), the short-circuit current density (J_{sc}), and the fill factor (FF) are ad-hoc determined as studied in the previous section. To relate these values with the power conversion efficiency

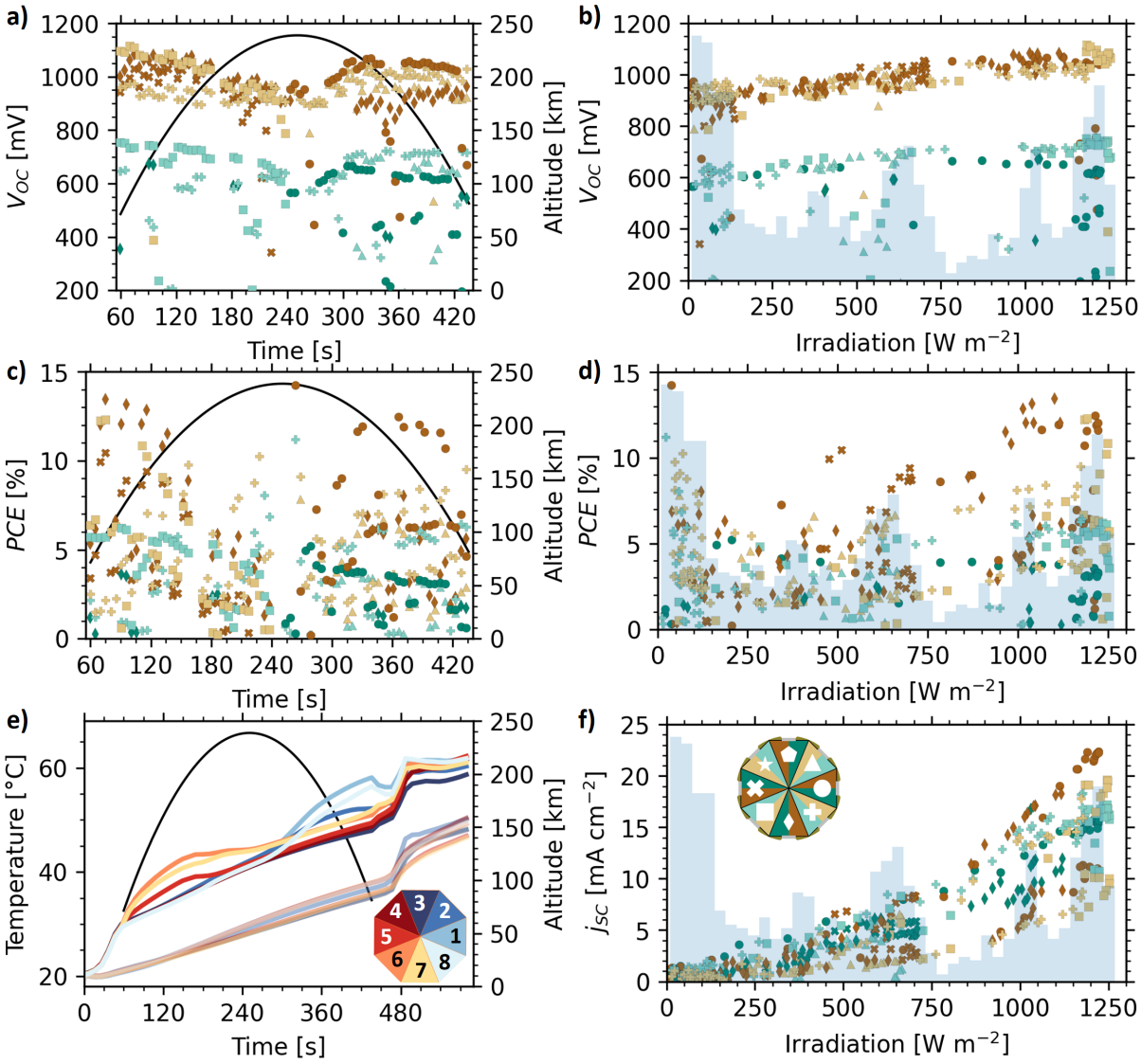

Figure 6.8: Overview of the solar cell parameter evolution during the space flight for perovskite (brown symbols) and organic (green symbols) solar cells: a) V_{oc} as a function of time after LO (lift-off time of the rocket) shown together with the altitude above ground. b) V_{oc} as a function of irradiance. The blue background histogram indicates the relative number of measurements that could be performed at the respective irradiance, irradiances below 0.01 sun are excluded. c) PCE as a function of time after LO shown together with the altitude above ground. d) PCE as a function of irradiance. e) Temperature measurements during flight shown together with the altitude above ground. The upper group of thicker lines is the average temperature from both sensors placed next to the solar cells. The lower group of thinner lines are the average temperatures from inside the rocket of the bottom plate. f) J_{sc} as a function of irradiance. The insets in e) and f) assign the different solar cell types to the respective segment by color and symbol and allow for relating the segment symbol with the segment colors used in previous sections. Reproduced from Reb et al. with permission [233]. Copyright © 2023 Wiley.

(PCE), the irradiance maximum-likelihood-estimate that is most time-synchronous with the half-time sweep is selected for each segment as shown in section 5.4. For readability, the wording of

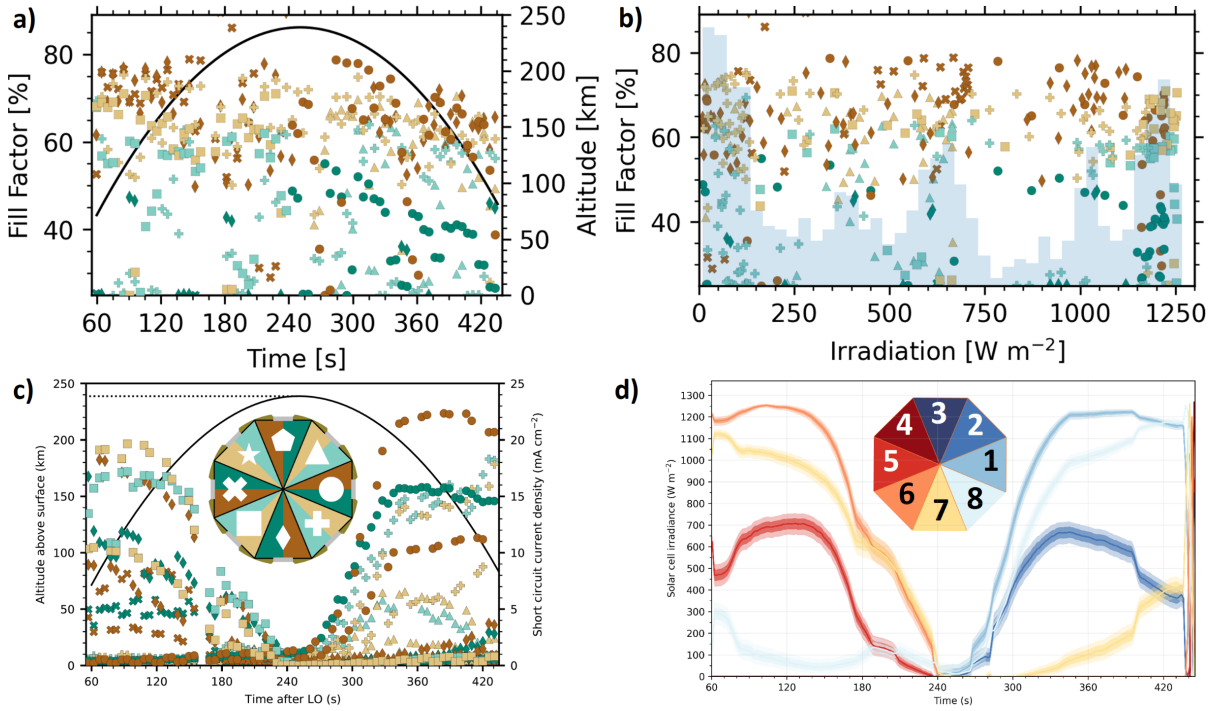

Figure 6.9: a) FF as a function of time after LO (lift-off time of the rocket) shown together with the altitude above ground. b) FF as a function of irradiance. The blue background histogram indicates the relative number of measurements that could be performed at the respective irradiance, irradiances below 0.01 sun are excluded. Reproduced from Reb et al. with permission [233]. Copyright © 2023 Wiley. For allowing direct comparison, c) shows the short-circuit current density evolution from Fig. 6.3c), d) the solar irradiation evolution from Fig. 5.13.

"1 sun" is used in the following text, defined in accordance with terrestrial tests to be 1000 W m^{-2}.

A detailed solar-cell parameter overview during the rocket flight can be found in Fig. 6.8. A detailed table with computed Pearson correlation for solar-cell parameter and irradiance is shown in Table 6.2. The perovskite open-circuit voltage V_{oc} values lie around 1 V, reaching up to 1.1 V in phases of strongest solar illuminations, while the organic solar cells show lower V_{oc} values with maximum values exceeding 0.7 V (Fig. 6.8a). In phases of weak solar irradiance at around 250 s after lift-off, there is a notable decline of the V_{oc} values. Since the solar irradiance varies over the rocket flight, the V_{oc} values are sorted as a function of the solar irradiance (Fig. 6.8b). The histograms in the background of Fig. 6.8b show the relative number of measurements performed at the respective irradiance values. There is a lack of data of measurements at around 0.8 sun. 0.7 sun is chosen as a threshold for the tabulated Pearson correlation coefficients, which is below the sparsely sampled region at around 0.8 sun and above the threshold of any shadowing effects. Therefore, the Pearson correlation values in the higher irradiance range in Table 6.2 are not biased by shadowing influences. While the perovskite V_{oc} values increase steadily towards higher irradiances within the measurement range ($P_{<0.7}$=0.62, $P_{>0.7}$=0.16), the correlation for

Table 6.2: Pearson correlation values.

	Perovskite Solar Cells			Organic Solar Cells		
Solar irradiance [$\mathrm{W\,m^{-2}}$]	$150<x$	$150<x<700$	$700<x$	$150<x$	$150<x<700$	$700<x$
P(PCE)	0.51	0.23	0.23	0.36	0.01	0.01
P(V_{oc})	0.66	0.62	0.16	0.43	0.42	−0.05
P(J_{sc})	0.78	0.52	0.57	0.94	0.70	0.86
P(FF)	−0.05	0.05	−0.31	−0.02	0.05	0.01

Pearson correlation values of solar cell parameters with solar irradiance, separated in three irradiance regimes, full range, low irradiance, and high irradiance. Measurements included for the respective parameter above the following thresholds: PCE = 1 %, V_{oc}(Perovskite) = 750 mV, V_{oc}(Organic) = 500 mV, FF = 25 %, J_{sc} = 1 mA cm^{-2}. Reproduced from Reb et al. with permission [233]. Copyright © 2023 Wiley.

organic solar cells holds only up to a threshold of around 0.6 suns ($P_{<0.7}$=0.42). Consecutively the V_{oc} values appear to level off and stay constant for the organic solar cells ($P_{>0.7}$=-0.05).

The evolution of FFs over time and the FFs as a function of irradiance can be found in 6.9a,b. The FFs of perovskite solar cells lie in the range of 60-75 %, where the m-TiO_2 architecture solar cells show a higher average than the ones with SnO_2, which follows the systematic trend that was already seen during pre-characterization, where the former system showed higher PCE and larger FF values. The FFs, in particular of the perovskite solar cells, seem to decrease over time, which could be correlated to the steadily increasing temperatures measured at the solar-cell positions during flight.

During the measurement time in vacuum, the outside-facing sensors measure temperatures that increase from initially 30 °C to 50-55 °C at the end of the micro-gravity phase (Fig. 6.9d). Since the temperature sensors are placed directly next to the solar cells, they are considered to give reasonable indications of the actual temperature present for the solar cells. The effect of solar irradiation warming up the outside temperature sensor when shining onto them is visible as additional bumps for some segments of the outside temperature evolutions (Fig. 6.9d). The main temperature increase is likely due to thermal conduction or radiation from the hot mantle surface to the solar-cell holders. The reentry shock heats the temperature sensors at the windows to around 60 °C. The last measurements before experiment shut off imply a stabilization of the temperatures with no further substantial warming.

To quantify a possible temperature effect, decoupling the strong correlation of temperature with irradiance is required (cf. Fig. 6.8b). To do so, Fig. 6.10 shows selected photovoltaic parameters from Fig. 6.8 and Fig. 6.9 in scatter plots, including the temperature information as color code. For the perovskite measurements, the highest FFs (Fig. 6.10a) and V_{oc}s (Fig. 6.10c) are measured for the cold subset below 44 °C (mean measurement temperature used as threshold). This shows that the reduction of V_{oc} is correlated with a temperature increase. The J_{sc}s,

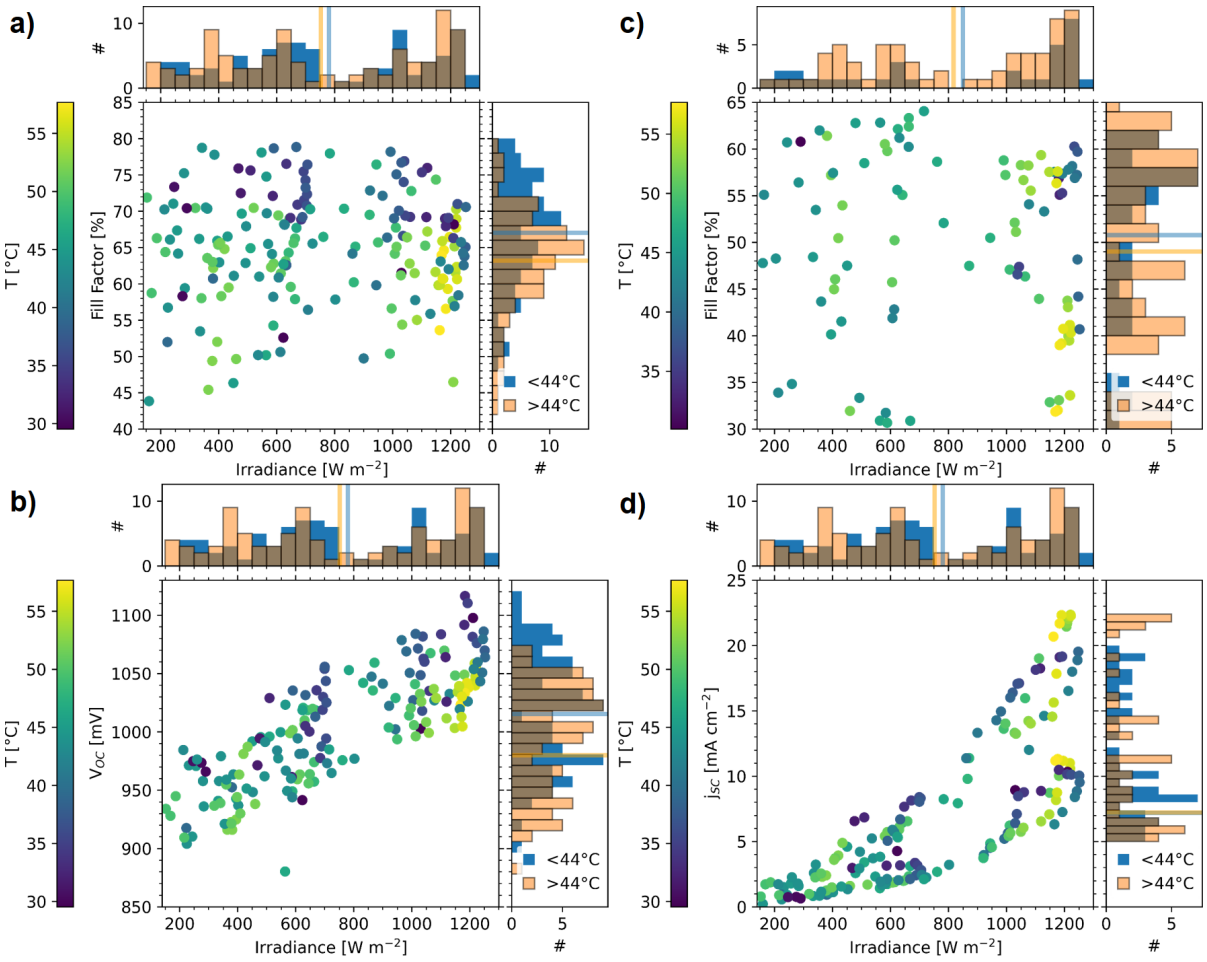

Figure 6.10: Scatterplots showing the temperature during the measurement as a function of irradiance and the photovoltaic parameter: a) FF of perovskite solar cells, b) FF of organic solar cells, c) V_{oc} of perovskite solar cells, d) J_{sc} of perovskite solar cells. Each measurement's temperature (measured by the adjacent sensors) codes the data point color according to the color bar on the left. The histograms on the right side and the top of the scatterplots show the marginalized data on the respective axes. Here, the data is separated into two subsets, the cold set with temperatures below the mean temperature (44 °C) shown in blue, and the warm set with temperatures above 44 °C shown in orange, to make the temperature trend quantitatively accessible. In addition, the mean histogram values of the cold and warm subsets are indicated with the straight line in the subplots in blue and orange, respectively. The top histogram of the irradiance distributions of the cold and warm subset allows for assessing possible bias due to selection effects.

however, are not reduced for the warm measurements (Fig. 6.10c). The average photovoltaic parameters of the subsets are given in Table 6.3. The biggest perovskite photovoltaic parameter change on temperature seems to be present for the FFs, which are reduced by about 6 % relatively on average, and the V_{oc}s decline by more than 3 %. The reduction of average PCEs of 11 % (relative) is hence attributable to the reduction of FFs and V_{oc}s for the perovskite solar cells. Regarding the voltage reduction, the perovskite solar cells behave as expected from the

Table 6.3: Irradiance marginalized photovoltaic parameters for the cold and warm subsets.

	V_{oc} [mV]	J_{sc} [mA cm^{-2}]	FF [%]	PCE
Perovskite Cold Set (< 44 °C)	1015	7.18	67.0	5.78
Perovskite Warm Set (> 44 °C)	980	7.23	63.2	5.16
Organic Cold Set (< 44 °C)	664	10.8	50.8	4.29
Organic Warm Set (> 44 °C)	626	9.7	49.0	3.46

Measurements are included for the respective parameter for the following thresholds: Solar irradiance > 150 W m^{-2}, 40% < FF(Perovskite)<80 %, 30 % < FF(Organic)<65 %. Note that the selection here also includes the perovskite solar cells heavily affected by soot, biasing the current and efficiency estimates consistently to lower values. The perovskite average irradiance is 780 W m^{-2} (cold set) and 752 W m^{-2} (warm set). The organic average irradiance is 849 W m^{-2} (cold set) and 817 W m^{-2} (warm set).

temperature-dependent detailed balance limit found for terrestrial test solar cells, where the V_{oc}-decrease is most pronounced upon temperature increase [107]. The relative FF reduction of 6 % is in good agreement with field studies, where a similar margin of relative reduction occurred [239].

For the organic solar cells, the FFs do not exhibit the largest change (Fig. 6.10b). Their relative FF-decrease is smaller (< 4%) than the decrease of J_{sc}s (> 10%) and V_{oc}s (> 6%) as given in Table 6.3, amounting to a reduction of 20 % relative PCE. Here, parts of the decrease of the J_{sc}s can be attributed partially to a data selection effect, where the warm subset experiences, on average, a slightly lower irradiance (see Table 6.3). The pronounced drop in V_{oc}s agrees with expectations from terrestrial tests with polymer solar cells, which found a linear decrease of open-circuit voltage with temperature [240, 241, 242].

It is important to note that within the presented reasoning, photovoltaic parameter changes cannot be unambiguously attributed to sole changes in temperature because the temperature increases steadily over the entire measurement time. Without measuring the parameter recovery for decreasing temperatures, photovoltaic changes could also be related to effects triggered during the exposure time of the solar cells to space conditions. In other words, the observed correlation does not necessarily imply causation. It is worth mentioning that, due to the trajectory of the payload orientation in Fig. 5.10, some segments are in the shadow most of the experiment time (cf. Fig. 5.13) before being strongly illuminated at later stages of the flight-time. Therefore, most warm subset measurements come from solar cells warmed by the payload mantle without direct solar exposure before receiving strong sunlight for longer periods. Thus, the observed decline of photovoltaic parameters (e.g. the V_{oc}s) during flight is unlikely attributed to effects caused by continuous solar exposure. Instead, the decrease of FF and V_{oc}s of the perovskite solar cells and the significant reduction of V_{oc}s matches the expectation upon temperature increase [107, 239, 240, 241, 242].

The PCE analysis is done by relating the power density measurements at the MPP to the

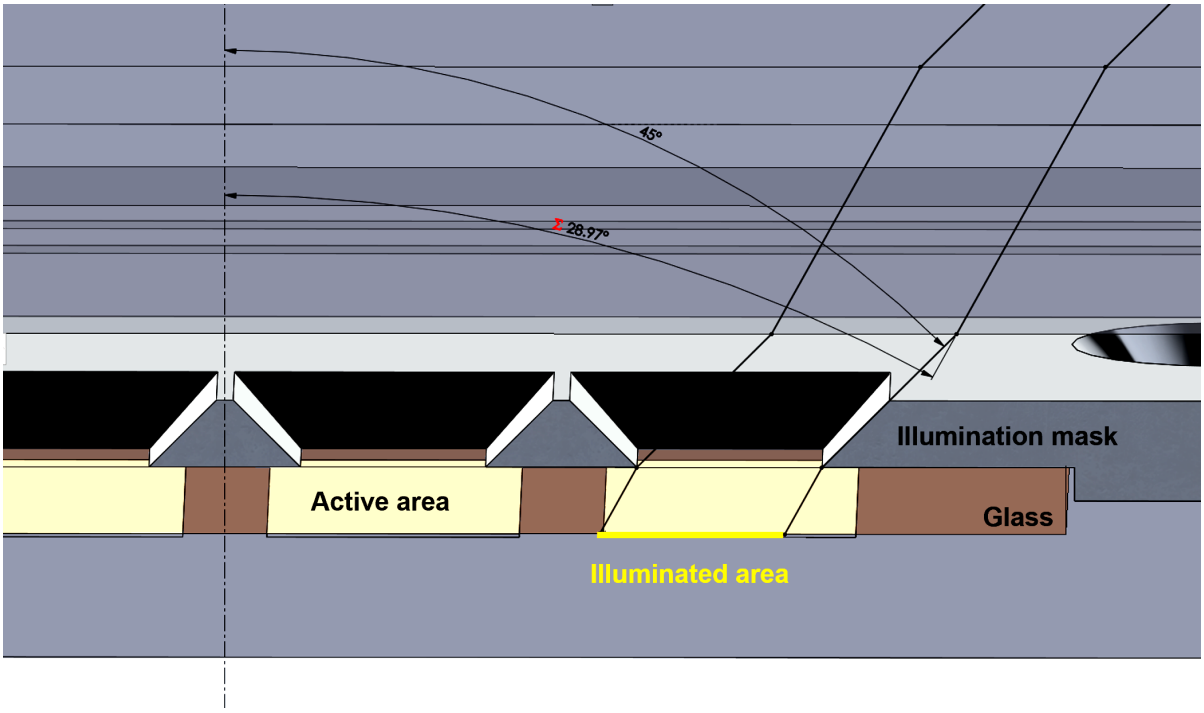

Figure 6.11: Geometrical shadowing and illumination offset effects. Above about 45° solar inclination, shadowing and illumination offsets (between active and illuminated areas) effectively reduce the illuminated area of the solar cell. Reproduced from Reb et al. with permission [233]. Copyright © 2023 Wiley.

irradiance at that time and for that particular segment (Fig. 6.8c). Here, the irradiance values from previous work are used, which do not account for soot and thus should be considered as upper limits to the effectively received solar power (see Chapter 5). The interpretation of the PCE values should thus consider the soot discussion above. The PCE evolution shows values from typically 6-13 % for the perovskite solar cells and 2-6 % for organic solar cells. There are outliers of higher efficiency in the phase of very low solar irradiance (below ∼0.1 sun) since a small absolute underestimation of solar irradiance at faint conditions is converted into a large relative underestimation that in turn biases the PCE to high values. This effect can be seen in detail in Fig. 6.8d, where especially in the region below 0.1 sun, high efficiencies occur that should not be considered for further interpretation. Hence only measurements above 0.15 sun are included in the Pearson statistics. In the range between 0.1-0.4 sun, there is an underpopulation of well-performing solar cells in terms of their PCE. This underrepresentation cannot be seen in the V_{oc} values in Fig. 6.8b, nor in the FF values in Fig. 6.9, but instead in the J_{sc} values in Fig. 6.8f At these moderate irradiances, the solar inclination is still high and leads to a relative shift of the illuminated area with respect to the active area of the solar cells, as well as to geometrical shadowing effects due to the aperture mask, effectively reducing the current-generating area below the aperture size (see Fig. 6.11).

Interestingly, this effect is strong enough to occur in the Pearson correlation coefficients, where for both perovskite and organic solar cells the correlation is stronger above 0.7 sun. Apart from

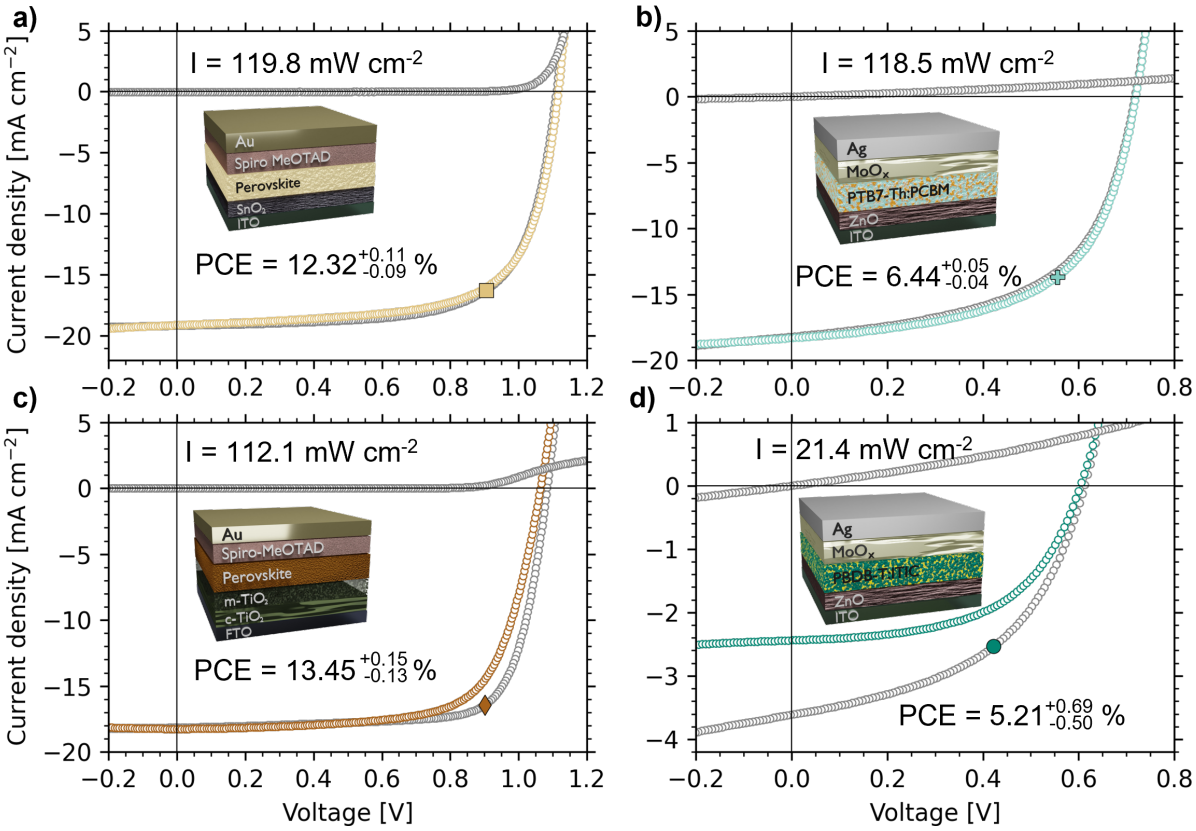

Figure 6.12: J-V curves in forward (open symbol) and backward (filled symbol) directions used for calculating the champion power-conversion efficiencies measured during the space flight. The error bars are derived from the standard deviation of the solar irradiance determination. The simultaneous irradiance measurement during the sweep used for PCE calculation is stated inside the respective graph. The MPP is indicated with the largely filled symbol. Crossing the origin, the dark-current measurements before launch can be seen (gray curve). The insets show the respective device architectures. Reproduced from Reb et al. with permission [233]. Copyright © 2023 Wiley.

these moderate irradiance effects, there appears to be a slight non-linearity in the J_{sc}s as a function of irradiance – for increasing irradiances, the J_{sc} values grow over-proportionally also at higher irradiances (Fig. 6.8f). Such a non-linear dependency was not found for terrestrial tests for perovskite and organic solar cells, where the current density was a linear function of irradiance [239, 242]. However, this visual trend should not be over-interpreted here since due to the unequal distribution of measurements as a function of irradiance and due to individual scattering of the J_{sc} values, errors could enter in and further tests will be required.

The effect of soot is best accessible in the sorted J_{sc} values as a function of irradiances (Fig. 6.8f) for the perovskite solar cells. There appear to be one upper and one lower branch of J_{sc} values, where the lower branch shows approximately half the current as compared to the upper branch, with not much scatter in between, underlining the high reproducibility of the perovskite solar cells selected for the space flight. A trend for the perovskite solar cells can be identified that PCE increases with increasing irradiances ($P_{<0.15}$=0.51), while this effect is not as

pronounced for the organic solar cells ($P_{<0.15}$=0.36). An apparent increase in fluctuations of the PCE values compared to V_{oc}, J_{sc}, and FF can be explained by the attenuation influence of soot on the fused-silica windows. The presence of soot and the soot gradient in Fig. 6.7 introduce a variable bias toward overestimating the received solar irradiance and hence an underestimation of the PCE values for all solar cells. For example, the lower branch of the beforementioned J_{sc} measurements of perovskite solar cells reaches only around 6 % PCE, while these solar cells are supposed to be equal to their conservative 12 % PCE estimate counterparts with lower soot bias.

As a final result, the resulting champion performances for each solar-cell type on the rocket are shown measured during the space flight in Fig. 6.12. In addition to the forward and backward voltage sweep, the dark measurements of the very same cells prior to launch are shown. The highest PCEs for the different solar-cell types in descending order are for the m-TiO_2 perovskite solar cells 13.45 % (Fig. 6.12c), for the SnO_2 perovskite solar cells 12.32 % (Fig. 6.12a), for the fullerene system 6.44 % (Fig. 6.12b), and the small-acceptor molecule 5.21 % (Fig. 6.12d). The irradiance value is stated in the figure together with errors given in the PCE determination corresponding to 1-σ standard error from the uncertainty of the irradiance value. In accordance with the trends observed with irradiance, most champion performance measurements occur at strong irradiances of more than 1 sun.

6.7 Conclusion

The voltage-current characteristics of different perovskite and organic solar cells were measured during a suborbital rocket flight. All four types generate power in orbital altitudes under stable irradiance conditions in space conditions. Moreover, in phases of strong solar irradiation, the perovskite and organic solar cells showed considerably efficient performance and exceeded power densities of 14 mW cm^{-2} and 7 mW cm^{-2}, respectively. A detailed photovoltaic characterization overview of the space flight of perovskite and organic solar cells on a sounding rocket is presented, including a detailed irradiance-based performance analysis by relating solar-cell performance to reconstructed solar irradiance. All four solar-cell types show reasonable PCE values ranging from 5-14 %. These encouraging results are based on a conservative estimate and are reached despite all measurements carried out in exotic experimental circumstances in space conditions. In a phase of payload alignment with solar irradiation, the solar cell performance under diffuse terrestrial irradiation is investigated. This confirms that all perovskite and organic solar cell types produce power under low irradiances in space environments. Interestingly, the perovskite solar cells show current densities as associated with solar irradiation conditions as present for deep space missions, underlining their potential for such applications. There is a positive correlation between solar-cell performance with irradiance, especially for perovskite solar cells. This difference is mainly attributed to the increasing V_{oc} values for increasing irradiances for perovskite solar cells within the irradiance range of up to approximately 1.1 sun, while V_{oc} values of organic solar cells tend to level off above 0.6 suns. The short-current density seems

to increase more than linearly for increasing irradiances, which cannot be solely attributed to geometrical or shadowing effects. With the time of the rocket flight in space, the V_{oc} values decline significantly for organic solar cells and slightly for perovskite solar cells, while FF values decline moderately for perovskite solar cells and slightly for organic solar cells. This is correlated to increasing solar-cell temperatures due to thermal conduction or radiation from the hot mantle surface to the inside, and the observed behavior is in line with previous terrestrial experiments investigating the temperature influence on photovoltaic parameters. All solar cell types reached performances that underline their potential to significantly outperform state-of-the-art inorganic space solar cells in terms of specific power. Our findings highlight that the technologies of perovskite and organic solar cells can be brought to space without mitigations and operate efficiently under various illumination conditions in space environment. The large potential for material optimizations to enhance the stability will help to resolve possible concerns related to the lifetime. Proving the long-term operation in space environment in another experiment could be the next step toward space applications for these revolutionary technologies.

7 Post-Flight Analysis Using Grazing-Incidence X-Ray Scattering

The results shown in this chapter have been published in the article *Space- and post-flight characterizations of perovskite and organic solar cells* [233] (L. K. Reb et al., *Solar RRL*, 7 (9):2300043, 2023, doi:10.1002/solr.202300043).

This chapter details the X-ray analysis of the space solar cells after retrieval. In Section 7.1 the general framework is described including sample storage, in Section 7.2 and Section 7.3 the GISAXS and GIWAXS measurement results are detailed, Section 7.4 these results are interpreted and possible environmental influences on the solar cells are discussed, followed by the conclusion in Section 7.5.

7.1 Experiment Description and Sample Storage

The sounding rocket experiment enables a post-flight characterization in addition to the in-flight SC studies. To assess potential changes in the SCs due to the exposure to space during the rocket flight, including the harsh rocket launch with extreme accelerations and vibrations and rocket reentry with more than 20 g peak acceleration, studies of the morphology and crystal structure of the SCs are ideal. To investigate buried structures in thin film devices and to probe a statistically large sample volume, GISAXS and GIWAXS measurements were demonstrated to be extremely powerful [168, 169, 183]. Accordingly, GISAXS and GIWAXS measurements were performed on the SCs that went to space and present the first post-spaceflight characterization of organic and perovskite SCs. In this work, the focus is on the active layer bulk morphology and structure by impinging above the material's critical angle as described in detail in Section 3.3.2. For reference, GISAXS and GIWAXS measurements were also done on identical SCs that stayed in Munich inside the nitrogen-filled glovebox and SCs that traveled to Sweden in nitrogen-filled packages but were not exposed to space conditions or ambient air. Fig. 7.1a shows schematically the travel of the different SC groups. In Fig. 7.1b, exemplary GISAXS and GIWAXS measurements of an organic and a perovskite SC returned from space are shown, respectively.

The sample storage procedure and environmental conditions apart from the rocket flight are detailed below. After sample fabrication in N_2-filled gloveboxes (details see in Section 3.1), some reference SCs were left in Munich inside the glovebox (denoted the Munich SCs) while several packages of sealed SC mounting batches were carried by airplane flight in the hand

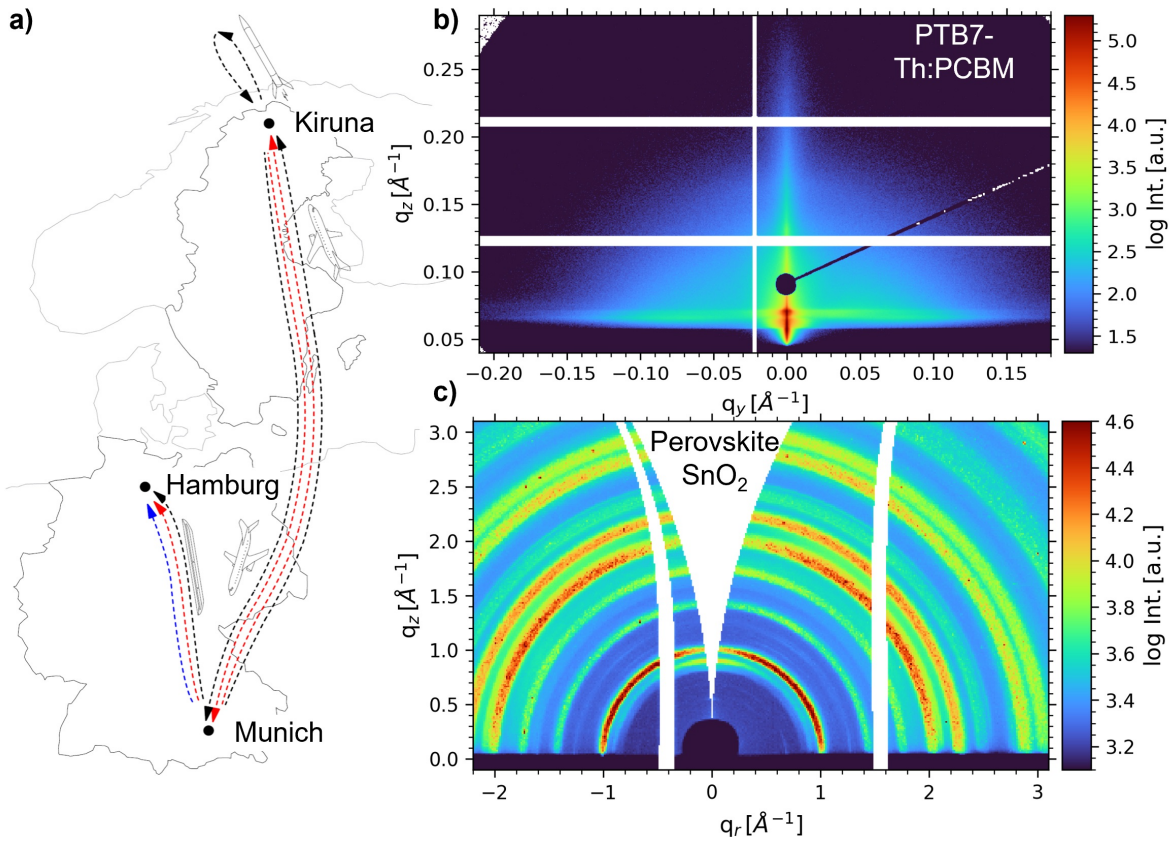

Figure 7.1: a) The travel paths of the three different SC groups: Munich reference SCs (blue), the Sweden reference SCs (red), and the SCs on the rocket flight (black). Exemplary b) GISAXS measurement of an organic rocket SC and c) GIWAXS measurement of a perovskite rocket SC, respectively. An overview of all the preprocessed 2D GISAXS and 2D GIWAXS data can be found below in Fig. 7.2 and Fig. 7.5, respectively. Reproduced from Reb et al. with permission [233]. Copyright © 2023 Wiley.

luggage to the rocket launch site in Kiruna, northern Sweden. There, the SC packages were stored at room temperature for around ten days. Note that the different SC types were stored in common bags, i.e. they were not separated according to their type. Several hours before launch (see table 4.2 for a detailed launch timeline), the space SCs were unpacked from their protective nitrogen atmosphere light-proof packaging to mount them in the experiment, while avoiding light exposure (cf. Fig. 4.13e). During mounting, tiny drops of silver conductive paste were added with a fine brush to the contact pin area to ensure a stable electrical connection several millimeters away from the aperture area. The reference SCs in Sweden remained in their protective nitrogen atmosphere (denoted the Sweden SCs). After flight and reentry, the payload landed safely on dry solid ground in a parachute descent and was recovered by helicopter within a few hours. The space SCs experienced, including the time before launch, around 8 hours of ambient conditions of 15-20 °C with < 30 % relative humidity. Then the SCs were recovered, with no sign of any visual degradation. After recovering the SCs, they were packed together

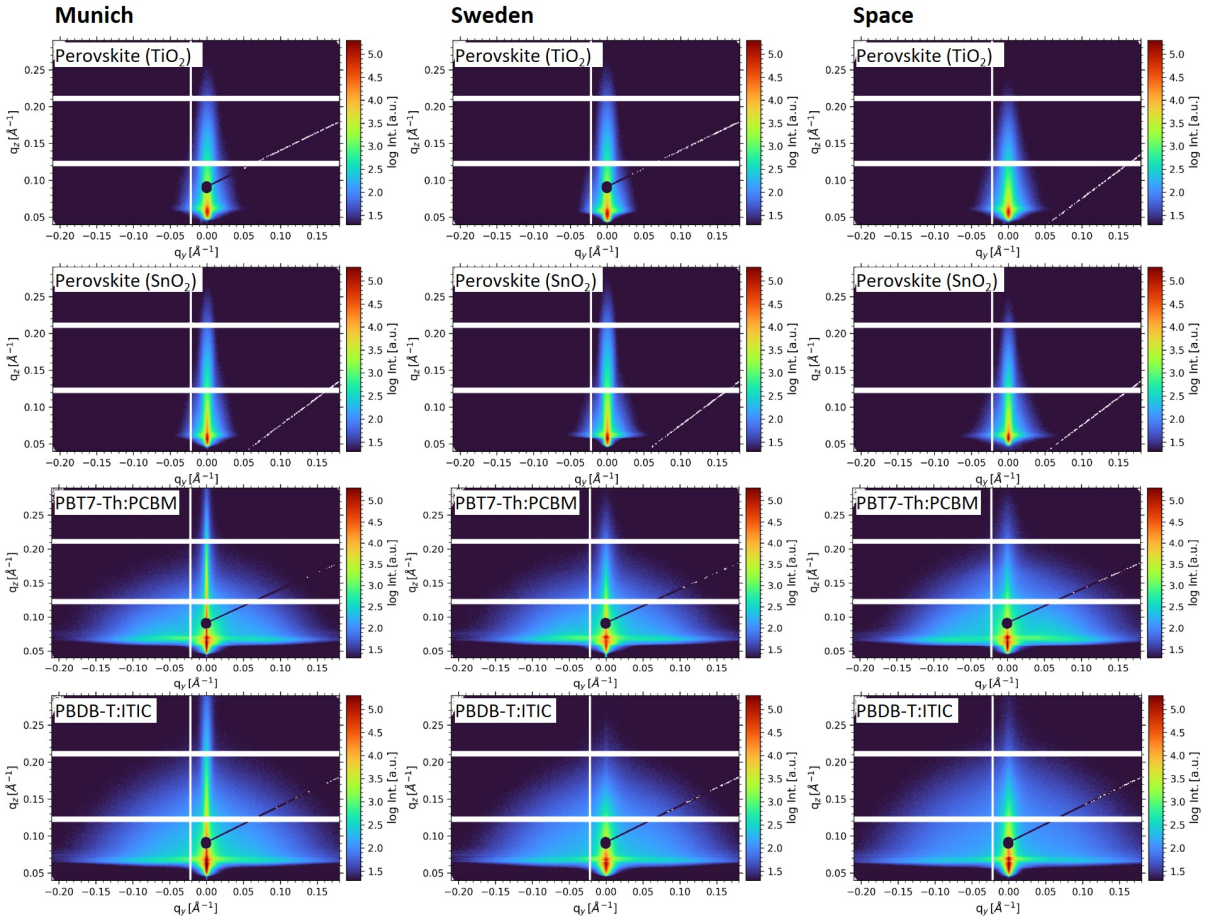

Figure 7.2: 2D GISAXS data measured with an incident angle of 0.4° for solar cells stayed in Munich (left), solar cells traveled to Sweden (middle) and solar cells traveled to space (right row). Solar cells were mixed organic lead mixed halide perovskite with mesoporous TiO_2 (denoted TiO_2) and planar SnO_2 (denoted SnO_2) architectures as well as organic solar modules with bulk-heterojunction active layers of narrow bandgap PTB7-Th:$PC_{71}BM$ and non-fullerene PBDB-T:ITIC small molecule acceptor. Reproduced from Reb et al. with permission [233]. Copyright © 2023 Wiley.

and due to the lack of nitrogen, partly evacuated with a vacuum sealer machine. After traveling back to Munich by airplane in hand luggage, the space SCs and the Sweden reference cells were brought back into the laboratory gloveboxes. After repacking the Munich reference, Sweden reference, and space SCs in nitrogen-filled bags they were carried by train to DESY, Hamburg, for the X-ray measurements.

7.2 Grazing-Incidence Small-Angle X-Ray Scattering

To analyze the morphology of the SCs exposed to the rocket flight and compare it to the reference SCs, which traveled to Sweden or stayed in Munich instead of the Sweden travel, GISAXS measurements are performed on all four SC types (see Fig. 7.2). The resulting horizontal line cuts of the 2D GISAXS data performed at the critical angle of the respective active layer materials

contain the lateral morphology information. When comparing the line cuts for one type of SC, which was exposed to different experimental conditions, moderate changes in scattering data can be found. To quantify these changes, the data sets are analyzed with fits (Fig. 7.3) based on models as described in the Sections 2.4.14, and 3.3.2. Since modeling with only two distinct object sizes (form factors) and distances (structure factors) did not result in good representations, three distinct object sizes and distances in the GISAXS data analysis are used. Moreover, the small, medium, and large-sized objects have a size distribution to account for their polydispersity. This way, the modeling results in data representations of acceptable quality. Note that the complex physics of GISAXS are described with a model that includes simplifications and hence, the model is not expected to provide a perfect fit to the data. However, the modeling with three form and structure factors gives us the possibility to quantitatively assess the changes in the thin-film morphology of the active layers.

Due to the polydispersity taken into account in the data analysis, obtained fit results are best shown with the form factor size distributions and structure distances (Fig. 7.4). Here the

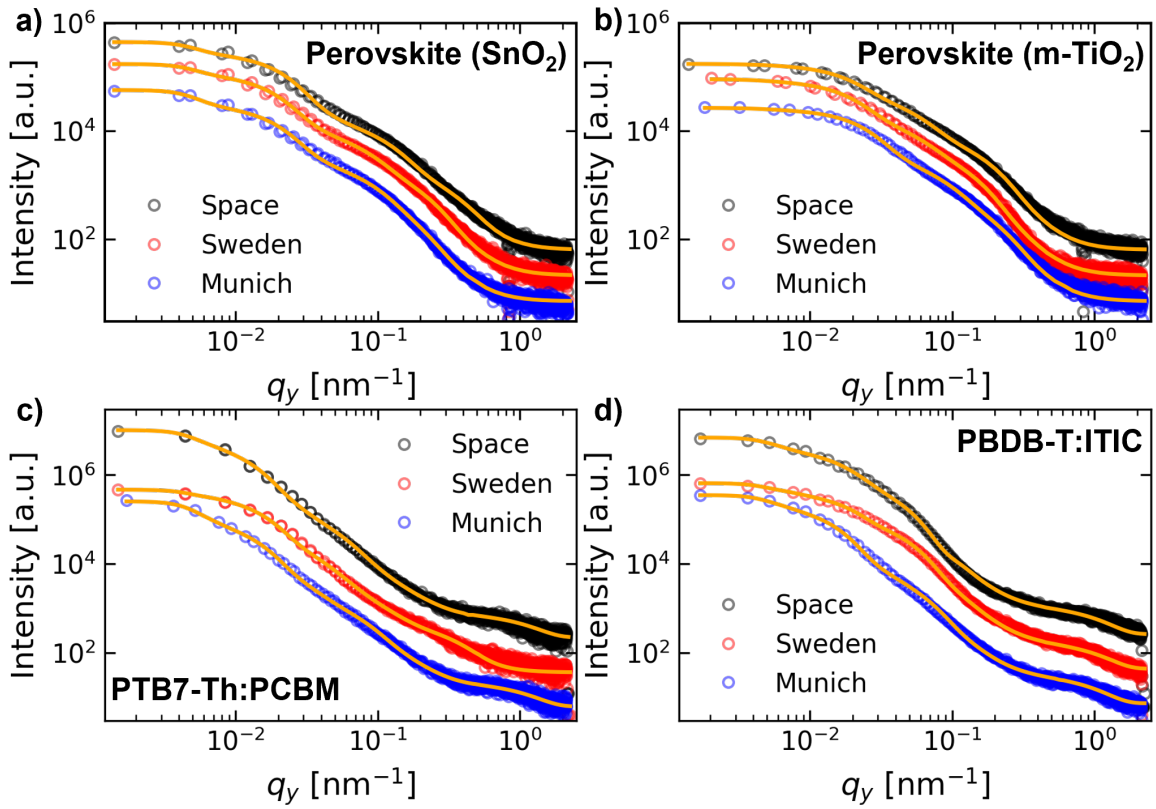

Figure 7.3: Horizontal line cuts of the 2D GISAXS data of SCs exposed to the space flight (black), SCs that traveled to Sweden (red), and SCs that stayed in Munich (blue) are shown together with the best model fits (solid lines): a) Planar SnO_2 perovskite SC, b) mesoporous TiO_2 perovskite SC, c) fullerene organic SC and d) small-molecule acceptor organic SC. Reproduced from Reb et al. with permission [233].

counts represent the number of scattering objects for the given size. Note that the curves are not normalized. On the first view, the morphology of the SCs that stayed in Munich differs from those that traveled to Sweden and those that experienced the space flight. Thus, the transport as well as the rocket flight cause changes in the morphology of the active layers in the nanoscale.

In more detail, for the planar SnO_2 perovskite SCs (Fig. 7.4a), the small domains become smaller and increase in number from the Munich to the Sweden samples and the trend continues from the Sweden to the space samples. For the mesoporous TiO_2 perovskite SCs (Fig. 7.4b) an effectively similar trend occurs, however, the explanation approaches from the opposite direction. The large domains become less when going from the Munich samples to the Sweden samples and the trend continues for the space samples. In essence, both trends indicate a drive towards smaller domains of the domain size distribution. Interestingly, the space flight does not show a particularly strong influence. Instead, the change is comparable to the shift of the Sweden samples experienced without being exposed outside their protective nitrogen atmosphere.

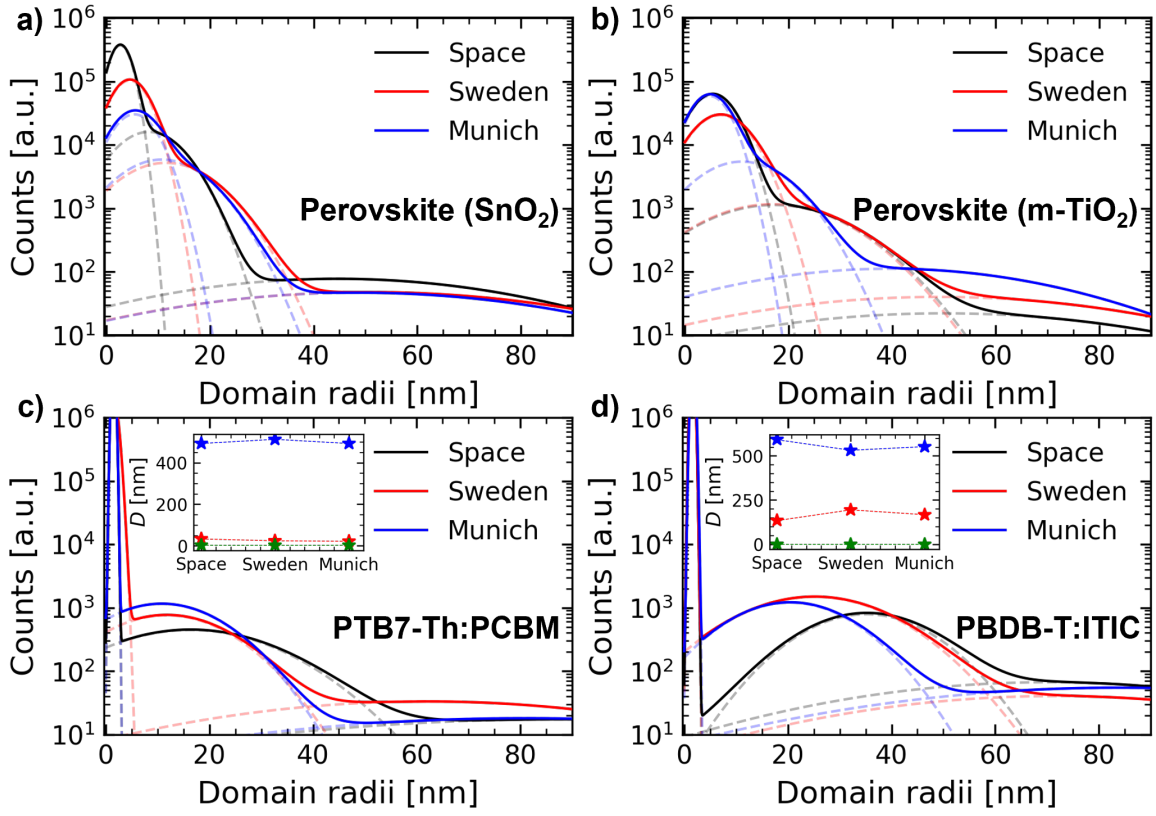

Figure 7.4: Domain size distributions of SCs exposed to the space flight (black), SCs that traveled to Sweden (red), and SCs that stayed in Munich (blue): a) Planar SnO_2 perovskite SC, b) mesoporous TiO_2 perovskite SC, c) fullerene organic SC and d) small-molecule acceptor organic SC. The insets show the characteristic nearest neighbor distances of the large (D1), medium (D2), and small (D3) domains. Reproduced from Reb et al. with permission [233]. Copyright © 2023 Wiley.

For the organic SCs, the scenario is somewhat more complex. Table 7.1 lists the resulting

Table 7.1: Organic SC domain radii obtained from the GISAXS models.

Active Layer	PBDB-T:ITIC			PBT7-Th:PCBM		
[nm]	Munich	Sweden	Space	Munich	Sweden	Space
Large domain	89±4	61^{+14}_{-11}	92^{+4}_{-23}	84^{+7}_{-5}	62^{+5}_{-7}	$90\ ^{+10}_{-1}$
Middle domain	32^{+3}_{-5}	23-3	30^{+4}_{-1}	16-2	22^{+2}_{-3}	30^{+8}_{-3}
Small domain	1.8	1.9	1.3+0.4	$1.0^{+0.3}_{-0.0}$	$2.0^{+0.2}_{-0.1}$	1.0+0.4

Uncertainties stated are derived from a 1σ confidence interval search. If no confidence bounds could be determined no value is given. Reproduced from Reb et al. with permission [233]. Copyright © 2023 Wiley.

sizes from the modeling as an additional overview. The PBT7-Th:PCBM active layer system (Fig. 7.4c) experiences a moderate size growth but a relative number reduction of the medium-sized domains due to the travel to Sweden. The space flight does not alter the domain radii distribution in a broad range from 10 to 90 nm, while there is an increase in the typical distance of the large domains from Munich over Sweden to space. For the PBDB-T:ITIC active layer system (Fig. 7.4d), large domains become smaller from Munich to Sweden but become larger from Sweden to space, the middle-size domains showing the same trend. However, these changes are mostly covered within the 1σ confidence interval and the relative number of large domains is much lower for the space sample compared to the Munich sample. In the horizontal line cuts, one can accordingly see in Fig. 7.3d how a broad region of a single power law for intermediate q_y values forms a buckled curve for the Sweden sample, where after the rocket flight and oxygen exposure the buckle spreads out, i.e. towards a broader domain size distribution. The evolution from Munich over Sweden to space does not follow a directed trend, in particular, the middle-sized domains appear to increase first in relative number for Sweden and grow and flatten out for the space sample. There seem to be concurring mechanisms present that would need further investigation to disentangle transport and flight influence for the space SCs.

7.3 Grazing-Incidence Wide-Angle X-Ray Scattering

Since the morphology undergoes changes during transport to Sweden or during the rocket flight to space, it is of interest if there are also changes to the structure on a smaller scale, i.e., to the crystalline regions of the active layers. Therefore, the crystalline structure is probed with GIWAXS. GIWAXS data are shown in Fig. 7.5 for the four different SC types in the different sample groups. No crystal structure changes are visible for the perovskite SCs. The Pseudo X-ray diffractogram reveals a phase-pure perovskite with only a minor PbI_2 side phase (Fig. 7.6). Neither do Bragg peak intensities change from reference samples to space samples nor are significant changes in the peak FWHM maxima observed for the Bragg peaks. Also, the

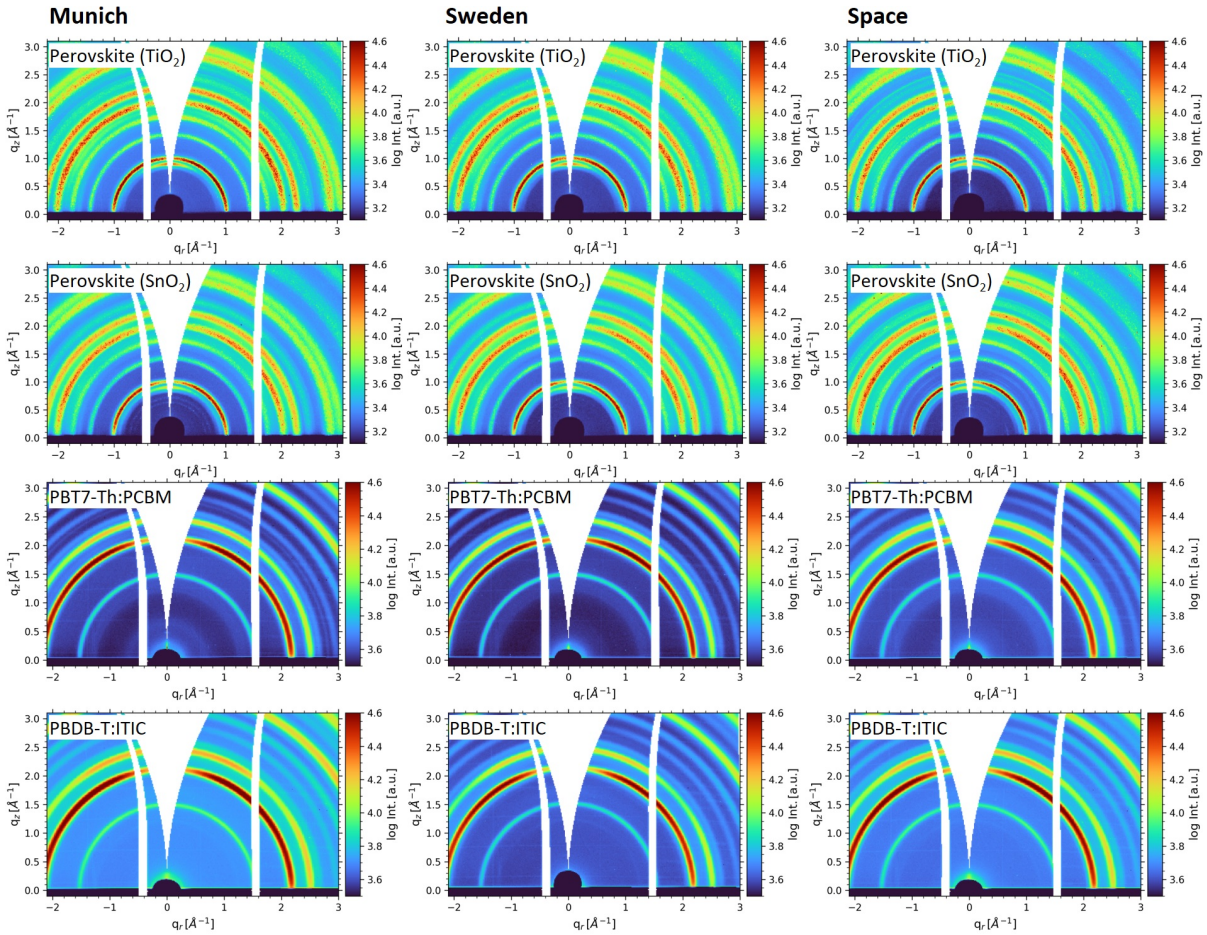

Figure 7.5: 2D GIWAXS data measured with an incident angle of 0.4° for solar cells stayed in Munich (left), solar cells traveled to Sweden (middle) and solar cells traveled to space (right row). Solar cells were mixed organic lead mixed halide perovskite with mesoporous TiO_2 (denoted TiO_2) and planar SnO_2 (denoted SnO_2) architectures as well as organic solar modules with bulk-heterojunction active layers of narrow bandgap PTB7-Th:$PC_{71}BM$ and non-fullerene PBDB-T:ITIC small molecule acceptor. Reproduced from Reb et al. with permission [233]. Copyright © 2023 Wiley.

crystal orientation of the perovskite phase and PbI_2 phase with respect to the electrodes exhibits no noticeable differences (Fig. 7.6b, c). For mixed halide mixed cation perovskite SCs, related to Guo et al., the breaking of small crystals was attributed to a strain release and linked with the demixing of the perovskite phase [243]. However, in the present study, phase segregation can be ruled out because this would become visible in the 2D GIWAXS data (Fig. 7.5) and the Pseudo X-ray diffractograms. As suggested by GISAXS, the relative reduction of large domain numbers and increase of small domain numbers in the perovskite did not result in measurable changes in the crystal phase as accessed in GIWAXS. The silver conductive paste used to aid electrode contacting is known to be detrimental to the long-term stability of perovskite SCs, since silver diffuses inside the perovskite, triggering chemical degradation of the perovskite [244]. However, no degradation was observed, possibly due to vacuum exposure where solvent removal

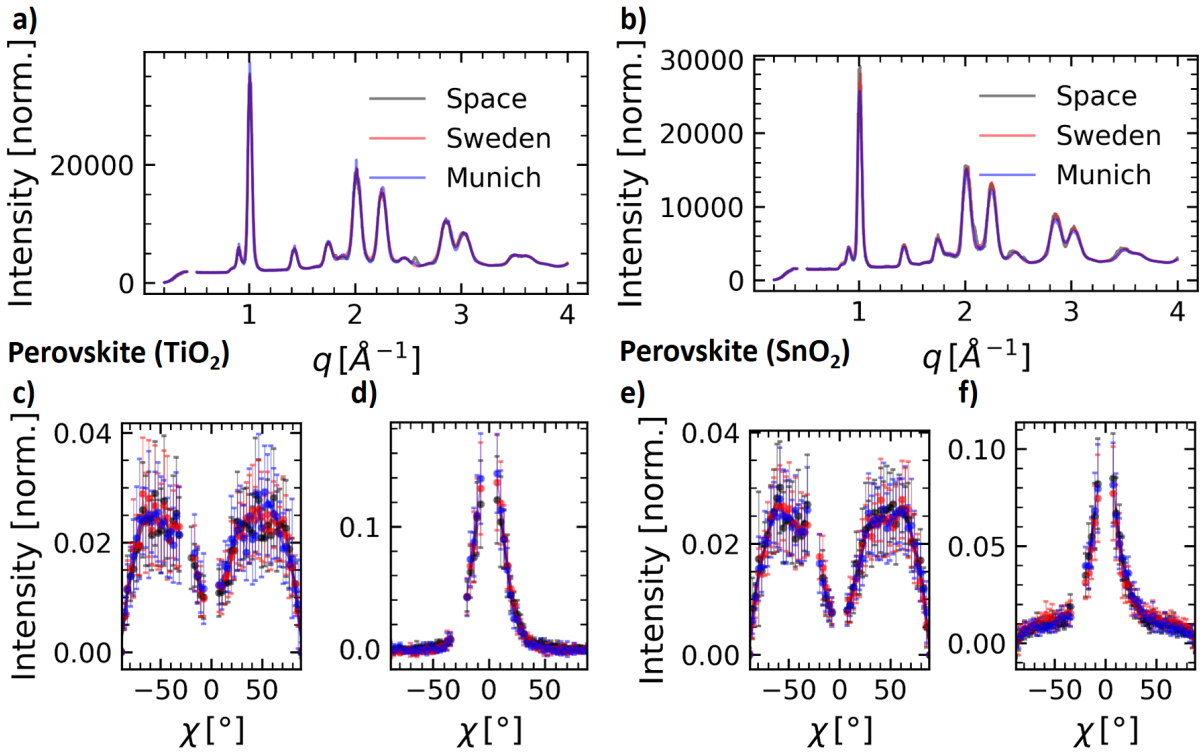

Figure 7.6: Analysis of the crystalline part of the TiO_2 perovskite SCs: a) Pseudo X-ray diffractogram of all three samples, intensity-normalized to the low-q range. b) Radially integrated azimuthal tube cut of the (001) perovskite Bragg peak, which is the strongest peak in the diffractogram, including local background subtraction with area normalization. c) Radially integrated azimuthal tube cut of the PbI_2 reflex with the same treatment. Reproduced from Reb et al. with permission [233]. Copyright © 2023 Wiley.

could constrain the mobility of silver atoms, the small amount used, or simply the too short time for significant silver diffusion.

For the organic SCs, the overview of resulting q-maps measured in GIWAXS to probe their crystallinity can be seen in Fig. 7.5 for the PTB7-Th:PCBM and PBDB-T:ITIC active layers at an incident angle of 0.4°. The extracted line cuts are presented in Fig. 7.7, respectively. From the graphs, similarly, as for the perovskite SCs, no obvious changes in the crystalline structure can be identified. Note that the measurements presented here with the incident angle of 0.4° are not particularly sensitive to organic crystallinity but rather probe the inorganic part of high crystallinity. Thus, the measurements in this geometry indicate no significant changes in crystallinity in the SC inorganic layers. Therefore, measurements were also performed around the critical angle of the active layer at 0.12° incident angle to probe the crystallinity of the bulk-heterojunction with a stronger scattering signal from the polymer:small molecule layer. The resulting q-maps can be found in Fig. 7.9 with a focus on the region within q $\sim$ 2 Å^{-1}. Apparently, from closer inspection of the inner q-region at around 0.3-0.5 Å^{-1}, and 1.3-1.7 Å^{-1} crystalline signal of the polymer bulk-heterojunctions can be found [245]. To assess the

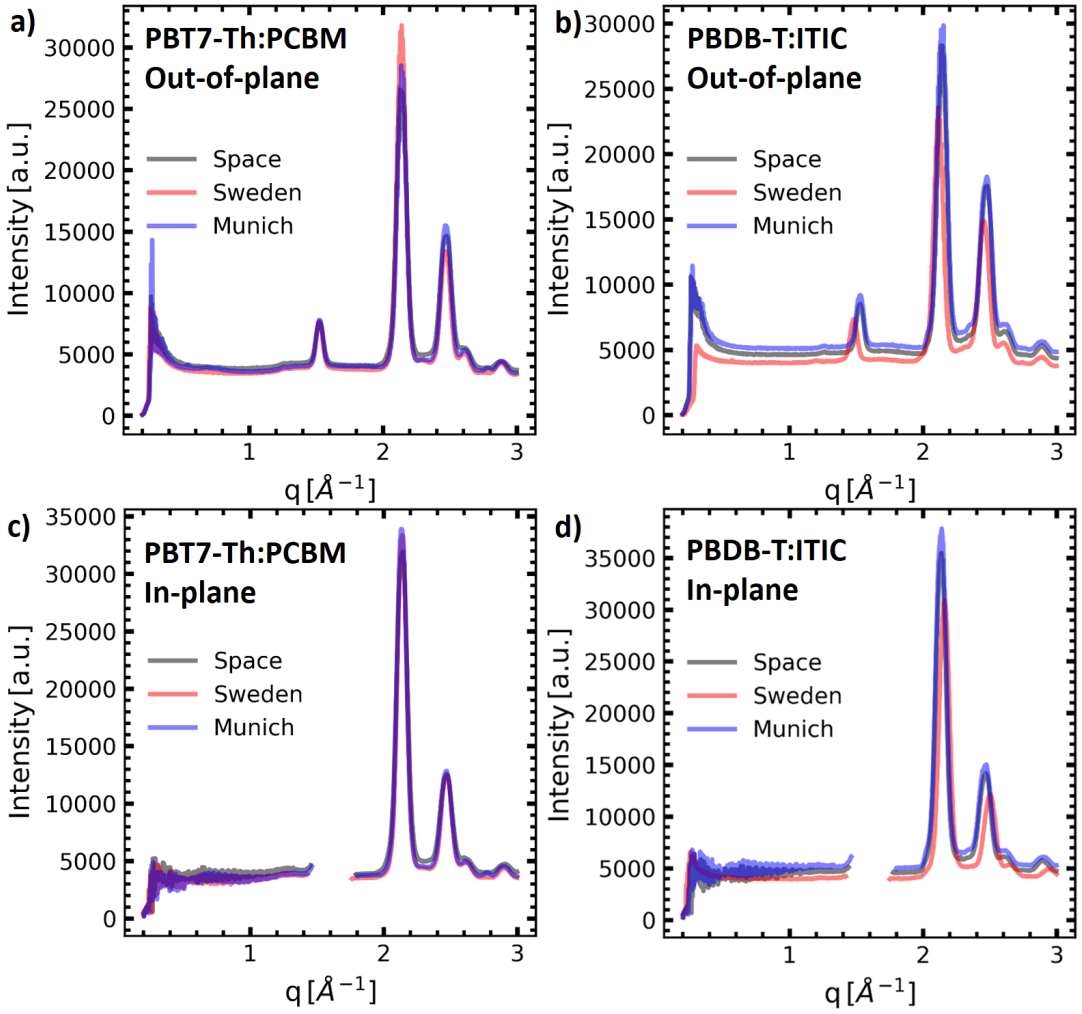

Figure 7.7: Azimuthally integrated radial sector cuts of the 2D GIWAXS data measured at an incident angle of 0.4° for PBT7-Th:PCBM (left) and PBDB-T:ITIC (right) solar cells. The upper row shows the out-of-plane (sample plane) sector cuts and the lower row the in-plane sector cuts. Reproduced from Reb et al. with permission [233]. Copyright © 2023 Wiley.

differences between the Munich, Sweden, and space samples in more detail, out-of-plane and in-plane sector cuts are shown in Fig. 7.8 for PTB7-Th:PCBM and accordingly for PBDB-T:ITIC.

Focusing on the in-plane azimuthally integrated radial sector cuts for PTB7-Th:PCBM organic SCs, no polymer signal is observed at around 0.3 Å^{-1}. The Munich, Sweden, and space measurement intensity trends do not show any pronounced differences in the range of interest up to 1.5 Å^{-1}. For the space sample, the crystalline polymer signal of the (100) Bragg peak of PTB7-Th including higher orders appears, while this cannot be found for the reference samples. The broad amorphous peak of PCBM is located at around 1.3 Å^{-1} and seems to be increasing in intensity from Munich over Sweden to the space sample [88]. The increased Bragg signal of PTB7-Th is a result of the ordering of the PTB7-Th by a face-on sheet stacking, which is accompanied by an increased amorphous scattering signal arising from the PCBM-phases. These

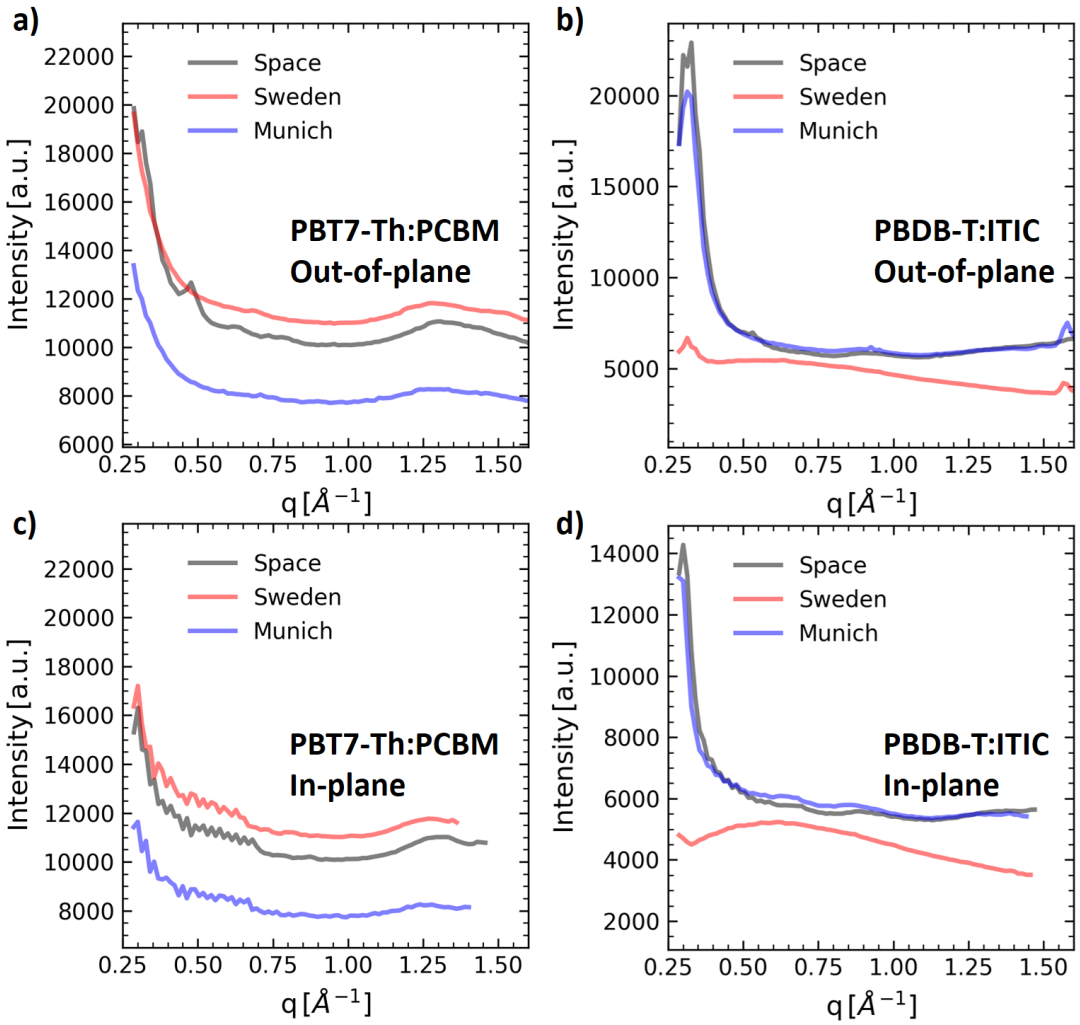

Figure 7.8: Analysis of the crystalline part of the PTB7-Th:PCBM organic SCs from GIWAXS measurements at 0.12° incident angle: a) Out-of-plane azimuthally integrated radial sector cut and b) in-plane azimuthally integrated radial sector cut. Reproduced from Reb et al. with permission [233]. Copyright © 2023 Wiley.

findings show a demixing of the polymer blend, while for the Sweden sample, minor stacking changes occur, only indicating a mild PCBM-signal increase. For the space sample, polymer sheet stacking pronounces the signal more strongly, leading to the appearance of higher Bragg-reflex orders. The PCBM scattering signal is increased simultaneously, showing aggregation and demixing of the bulk-heterojunction blend, which is undesired for organic photovoltaics using such a blend system[246].

The 2D GIWAXS data of the PBDB-T:ITIC organic SCs measured at 0.12° show PBDB-T (100) Bragg reflexes at 0.3 Å^{-1} for all three samples, the Munich reference, the Sweden reference, and the space SCs (Fig. 7.9) [245]. This intrinsic polymer crystallinity is present for all the samples in the form of a primarily isotropic ring, apart from the out-of-plane direction where the SAXS region overlays. The space sample is in this regard the only sample that shows a

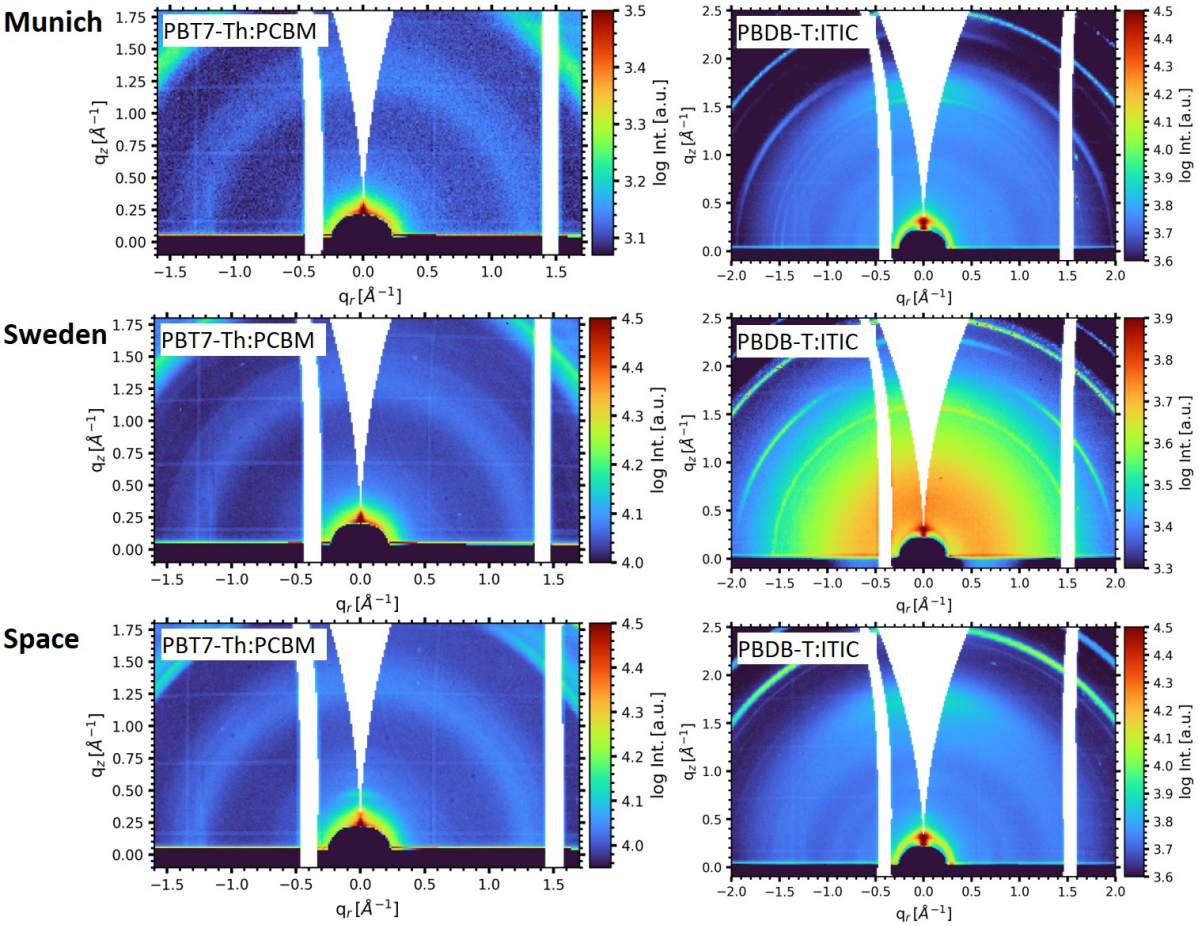

Figure 7.9: 2D GIWAXS data measured with an incident angle of 0.12° for PBT7-Th:PCBM (left) and PBDB-T:ITIC (right) solar cells to enhance the polymer scattering signal. Reproduced from Reb et al. with permission [233]. Copyright © 2023 Wiley.

weak second-order peak in the out-of-plane direction at 0.55 Å^{-1}, which cannot be found for the Munich and Sweden reference samples. Note that the intensity of the polymer peaks for the Sweden reference sample is not comparable to the Munich or space sample due to enhanced air scattering. However, the features follow the trend as best visible in Fig. 7.7. Comparing the Munich and space SCs in the out-of-plane sector cuts, the ITIC amorphous peak found at around 1.7 Å^{-1} shows similar intensities; Nevertheless, for the space SC, the q position of the peak increases, indicative of a smaller ITIC crystal lattice spacing. This finding indicates slight phase segregation where ITIC pure phases assemble in denser packing, while the PBDB-T second-order reflex indicates slightly increased phase separation in the blend.

7.4 Spaceflight Influences on the Solar Cells

Combining the findings from the X-ray characterization with GISAXS and GIWAXS, a complex scenario is found for the processes that influence the active layer of the perovskite and organic

SCs during travel and space flight. Interestingly, the travel from Munich to Sweden and back alone slightly changed the SCs' morphology. Especially the organic materials respond with minor changes in their domain size distribution. In the non-fullerene PBDB-T:ITIC system, the travel appears to reduce the size of the intermediate structures but to increase their relative number, while larger structures remain unaltered. In the fullerene PBT7-Th:PCBM system, there appears to be a subtle increase in amorphous PCBM content as seen in GIWAXS upon travel. GISAXS shows a number reduction of intermediate structures and a number increase of large structures. Typically, such agglomeration effects are not desirable since domains grow too large to sustain efficient exciton transfer and separation anymore. In contrast, the perovskite SCs show more subtle changes in their morphology, where the number of small domains increases compared to the number of large domains. However, the crystal phases of all SC types are stable without measurable changes in GIWAXS for the stationary and travel SCs.

Focusing now on the space SCs, the perovskite space samples continue the trend of domain polydispersity being shifted towards a higher number of smaller domains while the crystal phase remains stable without observed changes. The organic space samples, however, show a slight increase in polymer crystallinity in GIWAXS, which suggests a mild demixing and aggregation of the blend after exposure to space conditions and environmental conditions. The morphological changes of the PBDB-T:ITIC active layer support this finding with the growth of intermediate-size domains, while large, probably well-mixed domains decrease in their number. In contrast to this, there is no significant change of morphology from travel to spaceflight of the PBT7-Th:PCBM active layer. Slight PCBM demixing first reduces the domain size of the blend where thereafter space and environmental exposure, e.g. the abundance of oxygen, accelerate PBT7-Th stacking, which slightly increases the observed domain sizes in GISAXS. However, the latter effect is not strong and further studies will be required to disentangle the different processes occurring in different environments more precisely.

To assess the reason for changes during travel to Sweden, several possibilities that could influence the SC morphology and crystal structure are speculated. Influences due to cosmic radiation during airplane travel are possible but unlikely to cause such significant changes. Also, in such a case, the expectation would be to identify radiation effects in GIWAXS more than in GISAXS, because the former is sensitive to the crystal phase on the nanometer scale. Alternatively, tiny amounts of oxygen in the sealed bags or not being perfectly diffusion-proof in combination with pressure differences during take-off and landing of the airplane could play a role for the Sweden reference SCs. However, the bag protection seems sufficient to maintain stable crystal phases for all SC systems, and the nitrogen-filled glovebox is not completely oxygen-free. Also, there could be some solvent traces or other volatile species present that act in the sealed bags and lead to a kind of solvent post-treatment, especially since the perovskite and organic SCs have been packaged inside one single bag, enabling some cross-effects to take place. Traces of residual solvent were reported in the literature for perovskite and organic SCs and could promote mobility inside the active layer to introduce morphology changes [247, 248].

Future studies would be necessary to separate the influence of such different effects, which would affect every transport of perovskite and organic SCs.

7.5 Conclusion

During the rocket flight, the SCs were exposed to ultra-high vacuum, temperatures ranging from 20-65 °C, and strong solar irradiation of more than 1 sun. The retrieved space SCs have been brought back for a post-spaceflight characterization using GISAXS/GIWAXS to study potential changes in their morphology and crystal structure. Importantly, the travel from Munich to Sweden and back alone changed somewhat the morphology of the active layers. Regarding the SCs exposed to environmental conditions during the rocket flight, the fullerene system shows no significant changes, while the small-acceptor system experiences a slight coarse-graining of intermediate structures and a reduction of large structures. The perovskite SCs show clear but small changes of reduction of the relative number of large domains and a number increase of small domains. In contrast to these changes in the active layer morphology on the nanoscale, the crystalline structure does not show significant differences for any of the studied SC types. In this regard, the perovskite SCs do not show any sign of changes, and the organic SCs remain unaltered during space travel. Notably, the observed changes in the morphology of the travel SCs, which presumably are experienced similarly for the space SCs, do not cause a failure of the latter. Slight increases in organic crystallinity are likely attributed to gentle demixing of the bulk-heterojunction blends, which can be attributed to environmental effects during and after the space flight. Thus, neither the travel to the rocket launching side in Sweden nor the harsh rocket launch or the short stay in space as well as the Earth's atmosphere reentry, prevent the organic and perovskite SCs from functioning with satisfactory quality. These findings are highly promising for moving forward and studying these next-generation SCs in future flights to space with a more detailed post-characterization study and for longer time durations in space to investigate long-term aging under real space conditions.

8 Conclusion and Outlook

Ever since, space has been driving the curiosity of humankind. When scientific and technical developments opened up the opportunity to explore space, the multitude of extreme environmental conditions and difficulties in reaching space acted as a cradle for new technologies – as a driving force for innovations.

One of the first applications of silicon photovoltaics has been on satellites. Sixty years later, established silicon-based photovoltaics is facing the advent of new competitors: The raising perovskite and organic photovoltaic technologies support genuine flexibility and lightweight panel architectures and provide new application possibilities for photovoltaics on Earth and in space. There is a striking contrast in the technological setting for space applications when comparing novel photovoltaic materials with mature silicon. The first satellites used silicon photovoltaics as a power source because of very limited alternatives. Today, there are established competitors for the next-generation photovoltaics. Instead of rushing to incorporate the new technologies directly into orbital missions, incremental steps need to answer pending questions: Are they stable enough to survive conditions pre- and during launch? Do they function in the space environment? Their way toward orbital missions can be subsumed in three steps.

The first step is to perform terrestrial tests with perovskite and organic solar cells, simulating various environmental space conditions to study and understand their behavior regarding performance, stability, and degradation pathways. The tests add knowledge about the behavior of these solar cells under vacuum conditions with extraterrestrial solar irradiation, particle irradiation, heat-cycling experiments, combined tests, and many more.

The second step has been entered by real-world testing on high-altitude stratospheric balloons. This near-space environment testing gives an exciting insight into the behavior of the technologies in conditions of low atmospheric pressure close to vacuum and solar irradiation that is space-like. Also, different temperature ranges can be explored by covering different altitudes in Earth's atmosphere or by diurnal transitions during an experiment of several hours. These intermediate-duration tests permit the study of short-time aging effects.

This thesis performs the third step: exploring the new-generation solar cells for their use in space. Building upon successful previous space simulations and near-space experiments with encouraging results, the first space experiment of the novel solar cell technologies is reported here. Aboard a sounding rocket, perovskite and organic solar cells witnessed the procedure of a rocket launch, including exposure to the space environment for several minutes with simultaneous *in-situ* characterization. Sounding rockets are ideal platforms for such an experiment because

they exert similar stressors as orbital missions on the solar cells. Therefore, a successful sounding rocket experiment, including solar cell characterization, is a powerful positive result for the new technologies on the way to a full orbital test.

This thesis presents details of the planning, construction, and testing of the reusable OHSCIS experiment module in Chapter 4. The experiment with all the electronics and mechanics is designed and constructed within less than half a year. Subsequently, rigorous and detailed testing is performed to validate the mechanical integrity for the requirements posed by the rocket flight. This includes shaking and environmental stress tests to assess components' stability, validate the electronics' measurement principle and functionality, and optimize the mounting and electrical contacting of the solar cells. The experiment has successfully undergone its maiden flight during the MAPHEUS-8 campaign within one year of project initiation. Data extraction and parallelization demonstrate mechanical integrity and nominal data acquisition of every part of the experiment, including the successful electrical contacting and measurement of perovskite and an organic solar cell in space.

The second result's Chapter 5 establishes a novel method for determining the solar position during the primary measurement time of the solar cells in space. Using the measurements of multiple ambient light sensors and a Bayesian approach, a light-sensor model is optimized for the data acquired during the flight. The versatility of using multiple off-the-shelf small light sensors in combination with advanced mathematical modeling allows the adaption to arbitrary light sensor geometrical positions and consistent uncertainty propagation utilizing Monte Carlo Markow chains. The resulting solar trajectory is compared with the trajectory of a camera and inertia-unit-based model with effective deviations of a few degrees. From this, the solar irradiance is reconstructed for every solar cell during the entire space measurement time.

The third result's Chapter 6 performs a detailed analysis of the measurements of perovskite and organic solar cells during the flight. The solar cells have survived the transport and ascent with an acceleration of more than 10 g and have proved functional during microgravity. Investing a significant amount of time, the perovskite solar cells have been optimized in terms of their manufacturing to achieve high, reproducible performance for a mesoscopic and a planar n-i-p architecture using a mixed organic mixed halide lead perovskite $(FAPbI_3)_{0.87}(MAPbBr_3)_{0.17}$ with maximum efficiencies of more than 19% and 15% in pre-tests, respectively.

Solely using the measured short-circuit current densities of the solar cells, a qualitative orientation evolution respective to the sun can be established. This results from the measurements' high consistency and accuracy and highlights the solar cells' quality, proving the experiment's success. Phases of strong solar irradiance on the solar cell and a phase without direct solar irradiance are identified. At one moment, when no direct sunlight reaches the solar cells, multiple solar cells generate a current by collecting stray light coming from the Earth's surface. This moment demonstrates the general ability of solar cells to efficiently use diffuse, weak light in space that has only been confirmed in terrestrial tests so far.

Furthermore, quantitative power-conversion efficiency calculations are consistently performed

by combining the information on the solar irradiance from Chapter 5 with the photovoltaic measurements. In a conservative estimate, the best perovskite solar cell measurement exceeds 13 % efficiency, whereas the best organic solar cell measurement 6 %, respectively. The highest efficiencies are reached during phases of strong solar irradiance onto the solar cells. Significant correlations are identified by combining the solar cell performance parameters with solar irradiance. Perovskite solar cells' power conversion efficiency increases with irradiance, primarily due to increased open-circuit voltage. In contrast, the open-circuit voltage of organic solar cells stabilizes above 0.6 suns and hence also their power conversion efficiency is reached for weaker solar irradiance. With the warming of the solar cells due to thermal conduction or radiation from the mantle, the open-circuit voltages and fill factors decline moderately, as known from terrestrial tests.

Retrieval of the space solar cells enables postflight characterization using GISAXS and GIWAXS to identify changes in morphology or crystal structure upon exposure to space detailed in Chapter 7. GISAXS shows that the non-fullerene organic solar cells experience slight coarse-graining but a reduction of large structures. The domain size distributions tend to have smaller values in the perovskite solar cells. GIWAXS shows no significant changes regarding the crystal structure. In organic solar cells, a slight increase in crystallinity is likely caused by demixing during terrestrial exposure before and after the flight. A close inspection of the perovskite solar cells shows no differences for the space samples compared to the reference samples.

This thesis extensively overviews the first space experiment for novel material solar cells. Perovskite and organic solar cells have reached 240 km altitude aboard a sounding rocket. The thesis embraces the rocket flight experiment from concepts to realization with detailed insights into the mechanical and electrical properties. The sounding rocket experiment simulates stresses on the perovskite and organic solar cells present during a rocket launch, enables experiments in orbital altitudes for several minutes, and retrieves the scientific payload. The solar cells are characterized in space *in situ* by measuring their current-voltage characteristics and monitoring the surrounding space conditions. Findings prove that perovskite and organic solar cells operate in space conditions. They withstand the harsh launch of a sounding rocket, including extreme accelerations and vibrations, and still function well. When the sun shines, they reach their performance expectations, and while being in the shadow, they create power using diffuse and weak terrestrial stray light. The photovoltaic parameters are determined under solar irradiance and solar cell temperature variations and show behavior as anticipated from terrestrial tests. Perovskite solar cells' efficiency increases with stronger light, while organic solar cells reach reasonable efficiency at moderate irradiance. Postflight measurements using GISAXS and GIWAXS show structural stability without significant degradation.

After previous laboratory simulations and near-space high-altitude tests, this thesis shows the general suitability of perovskite and organic solar cells for space applications. The space experiment is a starting point for closing the gap to the next step: orbital missions. Providing sufficient long-term stability of a few years, long-term orbital tests of perovskite and organic solar cells are within reach. Space tests are essential because there can be differences between

laboratory test results and real space behavior. For particle irradiation tests, the established test protocols developed for conventional technologies give misleading results due to unexplored effects and require adaption for perovskite solar cells. Similar pitfalls could be present for any isolated environmental tests. Therefore, the new solar cell technologies shall advance simultaneously in all directions, including more terrestrial tests, near-space experiments, and space experiments. Future space experiments could test intrinsically stable quantum dot solar cells or solar cells on flexible polymer foils, favorably deposited via scalable deposition methods. Systematic post-characterization of the samples opens up new prospects for comparative studies to test assumptions and establish correlations between environment-induced degradation pathways in terrestrial tests and space conditions.

Space testing of thin-film solar cell encapsulation will be crucial to increasing their lifetimes. Recently, new approaches allow sealing the solar cells without sacrificing initial performance or causing chemical degradation by the resins, which is also highly promising for terrestrial applications. Such advances will help improve long-term stability to reduce the gap to the high technological standards established for conventional space solar cells in the last decades. Still, perovskite and organic solar cells would likely take a long time to reach this readiness in terrestrial qualification tests. However, requesting the same standards might be too ambitious for the moment. In contrast to geostationary telecommunication satellites, cube sats in low-Earth orbit are not designed for lifetimes of decades and could be powered by solar cells that only survive a few years.

As a final word, repeated thermal cycling in Earth's orbits seems to exert stress on the novel material solar cells due to a mismatch in the thermal expansion coefficients between them and the glass supports. This can damage the perovskite layer and requires substrates with matching coefficients; interestingly, polymer foils are a promising candidate. Perhaps, this could become another challenge that emerges in space research and is addressed in space research. But might this solution also improve the general long-term stability of these technologies? It could become one of the many solutions transferred to terrestrial use one day.

Bibliography

[1] Martin A. Green, Ewan D. Dunlop, Masahiro Yoshita, Nikos Kopidakis, Karsten Bothe, Gerald Siefer, and Xiaojing Hao. Solar cell efficiency tables (version 62). *Progress in Photovoltaics: Research and Applications*, 2023. ISSN 10627995. doi:10.1002/pip.3726.

[2] Lei Zhu, Ming Zhang, Jinqiu Xu, Chao Li, Jun Yan, Guanqing Zhou, Wenkai Zhong, Tianyu Hao, Jiali Song, Xiaonan Xue, Zichun Zhou, Rui Zeng, Haiming Zhu, Chun-Chao Chen, Roderick C. I. MacKenzie, Yecheng Zou, Jenny Nelson, Yongming Zhang, Yanming Sun, and Feng Liu. Single-junction organic solar cells with over 19% efficiency enabled by a refined double-fibril network morphology. *Nature Materials*, 21(6):656–663, 2022. ISSN 1476-4660. doi:10.1038/s41563-022-01244-y.

[3] Boudia Mohamed El Amine, Yi Zhou, Hongying Li, Qiuwang Wang, Jun Xi, and Cunlu Zhao. Latest updates of single-junction organic solar cells up to 20% efficiency. *Energies*, 16(9):3895, 2023. doi:10.3390/en16093895.

[4] Peter Müller-Buschbaum, Mukundan Thelakkat, Thomas F. Fässler, and Martin Stutzmann. Hybrid photovoltaics - from fundamentals towards application. *Advanced Energy Materials*, 7(16):1700248, 2017. ISSN 16146832. doi:10.1002/aenm.201700248.

[5] Rui Sun, Wei Wang, Han Yu, Zeng Chen, XinXin Xia, Hao Shen, Jing Guo, Mumin Shi, Yina Zheng, Yao Wu, Wenyan Yang, Tao Wang, Qiang Wu, Yang Yang, Xinhui Lu, Jianlong Xia, Christoph J. Brabec, He Yan, Yongfang Li, and Jie Min. Achieving over 17% efficiency of ternary all-polymer solar cells with two well-compatible polymer acceptors. *Joule*, 5(6):1548–1565, 2021. ISSN 25424351. doi:10.1016/j.joule.2021.04.007.

[6] Akihiro Kojima, Kenjiro Teshima, Yasuo Shirai, and Tsutomu Miyasaka. Organometal halide perovskites as visible-light sensitizers for photovoltaic cells. *Journal of the American Chemical Society*, 131(17):6050–6051, 2009. doi:10.1021/ja809598r.

[7] Yuanyuan Zhou, Laura M. Herz, Alex K-Y. Jen, and Michael Saliba. Advances and challenges in understanding the microscopic structure–property–performance relationship in perovskite solar cells. *Nature Energy*, 7(9):794–807, 2022. ISSN 2058-7546. doi:10.1038/s41560-022-01096-5.

[8] NREL. Best research-cell efficiencies, 2023. URL `https://www.nrel.gov/pv/cell-efficiency.html`.

[9] Lingling Zhan, Shuixing Li, Yaokai Li, Rui Sun, Jie Min, Yiyao Chen, Jin Fang, Chang-Qi Ma, Guanqing Zhou, Haiming Zhu, Lijian Zuo, Huayu Qiu, Shouchun Yin, and Hongzheng Chen. Manipulating charge transfer and transport via intermediary electron acceptor channels enables 19.3% efficiency organic photovoltaics. *Advanced Energy Materials*, 12 (39):2201076, 2022. ISSN 16146832. doi:10.1002/aenm.202201076.

[10] Jin Young Kim, Jin-Wook Lee, Hyun Suk Jung, Hyunjung Shin, and Nam-Gyu Park. High-efficiency perovskite solar cells. *Chemical Reviews*, 120(15):7867–7918, 2020. ISSN 1520-6890. doi:10.1021/acs.chemrev.0c00107.

[11] Jaewang Park, Jongbeom Kim, Hyun-Sung Yun, Min Jae Paik, Eunseo Noh, Hyun Jung Mun, Min Gyu Kim, Tae Joo Shin, and Sang Il Seok. Controlled growth of perovskite layers with volatile alkylammonium chlorides. *Nature*, 616(7958):724–730, 2023. doi:10.1038/s41586-023-05825-y.

[12] Sara Pescetelli, Antonio Agresti, George Viskadouros, Stefano Razza, Konstantinos Rogdakis, Ioannis Kalogerakis, Emmanuel Spiliarotis, Enrico Leonardi, Paolo Mariani, Luca Sorbello, Marco Pierro, Cristina Cornaro, Sebastiano Bellani, Leyla Najafi, Beatriz Martín-García, Antonio Esaú Del Rio Castillo, Reinier Oropesa-Nuñez, Mirko Prato, Simone Maranghi, Maria Laura Parisi, Adalgisa Sinicropi, Riccardo Basosi, Francesco Bonaccorso, Emmanuel Kymakis, and Aldo Di Carlo. Integration of two-dimensional materials-based perovskite solar panels into a stand-alone solar farm. *Nature Energy*, 7(7):597–607, 2022. ISSN 2058-7546. doi:10.1038/s41560-022-01035-4.

[13] J. Li, A. Aierken, Y. Liu, Y. Zhuang, X. Yang, J. H. Mo, R. K. Fan, Q. Y. Chen, S. Y. Zhang, Y. M. Huang, and Q. Zhang. A brief review of high efficiency iii-v solar cells for space application. *Frontiers in Physics*, 8, 2021. ISSN 2296-424X. doi:10.3389/fphy.2020.631925.

[14] Yulia Galagan, Francesco Di Giacomo, Harrie Gorter, Gerwin Kirchner, Ike de Vries, Ronn Andriessen, and Pim Groen. Roll-to-roll slot die coated perovskite for efficient flexible solar cells. *Advanced Energy Materials*, 8(32):1801935, 2018. ISSN 16146832. doi:10.1002/aenm.201801935.

[15] Zhen Li, Talysa R. Klein, Dong Hoe Kim, Mengjin Yang, Joseph J. Berry, Maikel F. A. M. van Hest, and Kai Zhu. Scalable fabrication of perovskite solar cells. *Nature Reviews Materials*, 3(4), 2018. doi:10.1038/natrevmats.2018.17.

[16] N. Yaghoobi Nia, M. Zendehdel, L. Cinà, F. Matteocci, and A. Di Carlo. A crystal engineering approach for scalable perovskite solar cells and module fabrication: a full out of glove box procedure. *Journal of Materials Chemistry A*, 6(2):659–671, 2018. ISSN 2050-7488. doi:10.1039/C7TA08038G.

[17] Benjia Dou, James B. Whitaker, Karsten Bruening, David T. Moore, Lance M. Wheeler, John Ryter, Nicholas J. Breslin, Joseph J. Berry, Sean M. Garner, Frank S. Barnes, Sean E. Shaheen, Christopher J. Tassone, Kai Zhu, and Maikel F. A. M. van Hest. Roll-to-roll printing of perovskite solar cells. *ACS Energy Letters*, 3(10):2558–2565, 2018. ISSN 2380-8195. doi:10.1021/acsenergylett.8b01556.

[18] David Beynon, Ershad Parvazian, Katherine Hooper, James McGettrick, Rahul Patidar, Tom Dunlop, Zhengfei Wei, Peter Davies, Rodrigo Garcia-Rodriguez, Matt Carnie, Matthew Davies, and Trystan Watson. All-printed roll-to-roll perovskite photovoltaics enabled by solution-processed carbon electrode. *Advanced materials (Deerfield Beach, Fla.)*, 35(16):e2208561, 2023. doi:10.1002/adma.202208561.

[19] Martin Kaltenbrunner, Matthew S. White, Eric D. Głowacki, Tsuyoshi Sekitani, Takao Someya, Niyazi Serdar Sariciftci, and Siegfried Bauer. Ultrathin and lightweight organic solar cells with high flexibility. *Nature Communications*, 3(1):770, 2012. ISSN 2041-1723. doi:10.1038/ncomms1772.

[20] Martin Kaltenbrunner, Getachew Adam, Eric Daniel Głowacki, Michael Drack, Reinhard Schwödiauer, Lucia Leonat, Dogukan Hazar Apaydin, Heiko Groiss, Markus Clark Scharber, Matthew Schuette White, Niyazi Serdar Sariciftci, and Siegfried Bauer. Flexible high power-per-weight perovskite solar cells with chromium oxide-metal contacts for improved stability in air. *Nature Materials*, 14(10):1032–1039, 2015. ISSN 1476-4660. doi:10.1038/nmat4388.

[21] Jiang Wu, Peng Chen, Han Xu, Maotao Yu, Lei Li, Haoming Yan, Yiming Huangfu, Yun Xiao, Xiaoyu Yang, Lichen Zhao, Wei Wang, Qihuang Gong, and Rui Zhu. Ultralight flexible perovskite solar cells. *Science China Materials*, 65(9):2319–2324, 2022. ISSN 2095-8226. doi:10.1007/s40843-022-2075-7.

[22] Valentino Romano, Antonio Agresti, Rosaria Verduci, and Giovanna D'Angelo. Advances in perovskites for photovoltaic applications in space. *ACS Energy Letters*, 7(8):2490–2514, 2022. ISSN 2380-8195. doi:10.1021/acsenergylett.2c01099.

[23] N. S. Fatemi, H. E. Pollard, H. Q. Hou, and P. R. Sharps. Solar array trades between very high-efficiency multi-junction and si space solar cells: Cat. no.0°ch37036: Piscataway nj september 2000. In *IEEE Photovoltaic Specialists Conference Record of the Twenty-Eighth 15-22 Sept. 2000*, pages 1083–1086. doi:10.1109/PVSC.2000.916075.

[24] D. Cardwell, A. Kirk, C. Stender, A. Wibowo, F. Tuminello, M. Drees, R. Chan, M. Osowski, and N. Pan. Very high specific power elo solar cells (>3 kw/kg) for uav, space, and portable power applications. In *2017 IEEE 44th Photovoltaic Specialists Conference (PVSC)*. IEEE, 25.06.2017 - 30.06.2017. ISBN 978-1-5090-5605-7. doi:10.1109/PVSC.2017.8366552.

[25] Jianming Yang, Qinye Bao, Liang Shen, and Liming Ding. Potential applications for perovskite solar cells in space. *Nano Energy*, 76:105019, 2020. ISSN 22112855. doi:10.1016/j.nanoen.2020.105019.

[26] Yaowen Li, Lei Meng, Yang Michael Yang, Guiying Xu, Ziruo Hong, Qi Chen, Jingbi You, Gang Li, Yang Yang, and Yongfang Li. High-efficiency robust perovskite solar cells on ultrathin flexible substrates. *Nature Communications*, 7(1):10214, 2016. ISSN 2041-1723. doi:10.1038/ncomms10214.

[27] Taesu Kim, Jae-Han Kim, Tae Eui Kang, Changyeon Lee, Hyunbum Kang, Minkwan Shin, Cheng Wang, Biwu Ma, Unyong Jeong, Taek-Soo Kim, and Bumjoon J. Kim. Flexible, highly efficient all-polymer solar cells. *Nature Communications*, 6(1):8547, 2015. ISSN 2041-1723. doi:10.1038/ncomms9547.

[28] Saewon Kang, Jaeki Jeong, Seungse Cho, Yung Jin Yoon, Seungyoung Park, Seongdong Lim, Jin Young Kim, and Hyunhyub Ko. Ultrathin, lightweight and flexible perovskite solar cells with an excellent power-per-weight performance. *Journal of Materials Chemistry A*, 7(3):1107–1114, 2019. ISSN 2050-7488. doi:10.1039/c8ta10585e.

[29] Wenchao Huang, Zhi Jiang, Kenjiro Fukuda, Xuechen Jiao, Christopher R. McNeill, Tomoyuki Yokota, and Takao Someya. Efficient and mechanically robust ultraflexible organic solar cells based on mixed acceptors. *Joule*, 4(1):128–141, 2020. ISSN 25424351. doi:10.1016/j.joule.2019.10.007.

[30] Felix Lang, Giles E. Eperon, Kyle Frohna, Elizabeth M. Tennyson, Amran Al-Ashouri, Georgios Kourkafas, Jürgen Bundesmann, Andrea Denker, Kevin G. West, Louise C. Hirst, Heinz-Christoph Neitzert, and Samuel D. Stranks. Proton–radiation tolerant all–perovskite multijunction solar cells. *Advanced Energy Materials*, 11(41):2102246, 2021. ISSN 16146832. doi:10.1002/aenm.202102246.

[31] Axel F. Palmstrom, Giles E. Eperon, Tomas Leijtens, Rohit Prasanna, Severin N. Habisreutinger, William Nemeth, E. Ashley Gaulding, Sean P. Dunfield, Matthew Reese, Sanjini Nanayakkara, Taylor Moot, Jérémie Werner, Jun Liu, Bobby To, Steven T. Christensen, Michael D. McGehee, Maikel F.A.M. van Hest, Joseph M. Luther, Joseph J. Berry, and David T. Moore. Enabling flexible all-perovskite tandem solar cells. *Joule*, 3(9):2193–2204, 2019. ISSN 25424351. doi:10.1016/j.joule.2019.05.009.

[32] Renxing Lin, Jian Xu, Mingyang Wei, Yurui Wang, Zhengyuan Qin, Zhou Liu, Jinlong Wu, Ke Xiao, Bin Chen, So Min Park, Gang Chen, Harindi R. Atapattu, Kenneth R. Graham, Jun Xu, Jia Zhu, Ludong Li, Chunfeng Zhang, Edward H. Sargent, and Hairen Tan. All-perovskite tandem solar cells with improved grain surface passivation. *Nature*, 603(7899):73–78, 2022. doi:10.1038/s41586-021-04372-8.

[33] Rui He, Wanhai Wang, Zongjin Yi, Felix Lang, Cong Chen, Jincheng Luo, Jingwei Zhu, Jarla Thiesbrummel, Sahil Shah, Kun Wei, Yi Luo, Changlei Wang, Huagui Lai, Hao Huang, Jie Zhou, Bingsuo Zou, Xinxing Yin, Shengqiang Ren, Xia Hao, Lili Wu, Jingquan Zhang, Jinbao Zhang, Martin Stolterfoht, Fan Fu, Weihua Tang, and Dewei Zhao. Improving interface quality for 1-cm2 all-perovskite tandem solar cells. *Nature*, 618(7963): 80–86, 2023. doi:10.1038/s41586-023-05992-y.

[34] Bahram Abdollahi Nejand, David B. Ritzer, Hang Hu, Fabian Schackmar, Somayeh Moghadamzadeh, Thomas Feeney, Roja Singh, Felix Laufer, Raphael Schmager, Raheleh Azmi, Milian Kaiser, Tobias Abzieher, Saba Gharibzadeh, Erik Ahlswede, Uli Lemmer, Bryce S. Richards, and Ulrich W. Paetzold. Scalable two-terminal all-perovskite tandem solar modules with a 19.1% efficiency. *Nature Energy*, 7(7):620–630, 2022. ISSN 2058-7546. doi:10.1038/s41560-022-01059-w.

[35] Ezgi Nur Güler, Andreas Distler, Robin Basu, Christoph J. Brabec, and Hans-Joachim Egelhaaf. Fully solution-processed, light-weight, and ultraflexible organic solar cells. *Flexible and Printed Electronics*, 7(2):025003, 2022. doi:10.1088/2058-8585/ac66ae.

[36] Lyndsey McMillon-Brown, Joseph M. Luther, and Timothy J. Peshek. What would it take to manufacture perovskite solar cells in space? *ACS Energy Letters*, 7(3):1040–1042, 2022. ISSN 2380-8195. doi:10.1021/acsenergylett.2c00276.

[37] Robert Thirsk, Andre Kuipers, Chiaki Mukai, and David Williams. The space-flight environment: the international space station and beyond. *Canadian Medical Association Journal*, 180(12):1216–1220, 2009. ISSN 1488-2329. doi:10.1503/cmaj.081125.

[38] Martin A. Green. Limiting photovoltaic efficiency under new astm international g173-based reference spectra. *Progress in Photovoltaics: Research and Applications*, 20(8):954–959, 2012. ISSN 1062-7995. doi:10.1002/pip.1156.

[39] NREL. Reference air mass 1.5 spectra: The american society for testing and materials (astm) g-173 spectra represent terrestrial solar spectral irradiance on a surface of specified orientation under one and only one set of specified atmospheric conditions. URL `https://www.nrel.gov/grid/solar-resource/spectra-am1.5.html#`.

[40] Shuai Guo, Christian Brandt, Thomas Andreev, Ezzeldin Metwalli, Weijia Wang, Jan Perlich, and Peter Müller-Buschbaum. First step into space: performance and morphological evolution of p3ht:pcbm bulk heterojunction solar cells corrected under am0 illumination. *ACS applied materials & interfaces*, 6(20):17902–17910, 2014. doi:10.1021/am504608p.

[41] Cong Chen, Hao Li, Junjie Jin, Xu Chen, Yu Cheng, Yan Zheng, Dali Liu, Lin Xu, Hongwei Song, and Qilin Dai. Long-lasting nanophosphors applied to uv-resistant and energy storage perovskite solar cells. *Advanced Energy Materials*, 7(20):1700758, 2017. ISSN 16146832. doi:10.1002/aenm.201700758.

[42] Martin A. Green, Anita Ho-Baillie, and Henry J. Snaith. The emergence of perovskite solar cells. *Nature Photonics*, 8(7):506–514, 2014. ISSN 1749-4885. doi:10.1038/nphoton.2014.134.

[43] Renjun Guo, Dan Han, Wei Chen, Linjie Dai, Kangyu Ji, Qiu Xiong, Saisai Li, Lennart K. Reb, Manuel A. Scheel, Shambhavi Pratap, Nian Li, Shanshan Yin, Tianxiao Xiao, Suzhe Liang, Anna Lena Oechsle, Christian L. Weindl, Matthias Schwartzkopf, Hubert Ebert, Peng Gao, Kai Wang, Mingjian Yuan, Neil C. Greenham, Samuel D. Stranks, Stephan V. Roth, Richard H. Friend, and Peter Müller-Buschbaum. Degradation mechanisms of perovskite solar cells under vacuum and one atmosphere of nitrogen. *Nature Energy*, 6(10): 977–986, 2021. ISSN 2058-7546. doi:10.1038/s41560-021-00912-8.

[44] Yang Bai, Zijian Huang, Xiao Zhang, Jiuzhou Lu, Xiuxiu Niu, Ziwen He, Cheng Zhu, Mengqi Xiao, Qizhen Song, Xueyuan Wei, Chenyue Wang, Zhenhua Cui, Jing Dou, Yihua Chen, Fengtao Pei, Huachao Zai, Wei Wang, Tinglu Song, Pengfei An, Jing Zhang, Juncai Dong, Yiming Li, Jiangjian Shi, Haibo Jin, Pengwan Chen, Yuchao Sun, Yujing Li, Haining Chen, Zhongming Wei, Huanping Zhou, and Qi Chen. Initializing film homogeneity to retard phase segregation for stable perovskite solar cells. *Science (New York, N.Y.)*, 378 (6621):747–754, 2022. doi:10.1126/science.abn3148.

[45] Yan Jiang, Shih-Chi Yang, Quentin Jeangros, Stefano Pisoni, Thierry Moser, Stephan Buecheler, Ayodhya N. Tiwari, and Fan Fu. Mitigation of vacuum and illumination-induced degradation in perovskite solar cells by structure engineering. *Joule*, 4(5):1087–1103, 2020. ISSN 25424351. doi:10.1016/j.joule.2020.03.017.

[46] Ilaria Cardinaletti, Tim Vangerven, Steven Nagels, Rob Cornelissen, Dieter Schreurs, Jaroslav Hruby, Jelle Vodnik, Dries Devisscher, Jurgen Kesters, Jan D'Haen, Alexis Franquet, Valentina Spampinato, Thierry Conard, Wouter Maes, Wim Deferme, and Jean V. Manca. Organic and perovskite solar cells for space applications. *Solar Energy Materials and Solar Cells*, 182:121–127, 2018. ISSN 0927-0248. doi:10.1016/j.solmat.2018.03.024.

[47] Ahmad R. Kirmani, David P. Ostrowski, Kaitlyn T. VanSant, Todd A. Byers, Rosemary C. Bramante, Karen N. Heinselman, Jinhui Tong, Bart Stevens, William Nemeth, Kai Zhu, Ian R. Sellers, Bibhudutta Rout, and Joseph M. Luther. Metal oxide barrier layers for terrestrial and space perovskite photovoltaics. *Nature Energy*, 8(2):191–202, 2023. ISSN 2058-7546. doi:10.1038/s41560-022-01189-1.

[48] Narges Yaghoobi Nia. Barrier layer for space. *Nature Energy*, 8(2):117–118, 2023. ISSN 2058-7546. doi:10.1038/s41560-023-01197-9.

[49] Kaitlyn T. VanSant, Ahmad R. Kirmani, Jay B. Patel, Laura E. Crowe, David P. Ostrowski, Brian M. Wieliczka, Michael D. McGehee, Laura T. Schelhas, Joseph M. Luther, Timothy J. Peshek, and Lyndsey McMillon-Brown. Combined stress testing of perovskite

solar cells for stable operation in space. *ACS Applied Energy Materials*, 2023. ISSN 2574-0962. doi:10.1021/acsaem.2c03972.

[50] Minh Tam Hoang, Yang Yang, Bryan Tuten, and Hongxia Wang. Are metal halide perovskite solar cells ready for space applications? *The journal of physical chemistry letters*, 13(13):2908–2920, 2022. doi:10.1021/acs.jpclett.2c00386.

[51] T. Jesper Jacobsson, Wolfgang Tress, Juan-Pablo Correa-Baena, Tomas Edvinsson, and Anders Hagfeldt. Room temperature as a goldilocks environment for ch 3 nh 3 pbi 3 perovskite solar cells: The importance of temperature on device performance. *The Journal of Physical Chemistry C*, 120(21):11382–11393, 2016. ISSN 1932-7447. doi:10.1021/acs.jpcc.6b02858.

[52] Nicholas Rolston, Kevin A. Bush, Adam D. Printz, Aryeh Gold-Parker, Yichuan Ding, Michael F. Toney, Michael D. McGehee, and Reinhold H. Dauskardt. Engineering stress in perovskite solar cells to improve stability. *Advanced Energy Materials*, 8(29), 2018. ISSN 16146832. doi:10.1002/aenm.201802139.

[53] Huimin Mu, Yilin Zhang, Hongshuai Zou, Fuyu Tian, Yuhao Fu, and Lijun Zhang. Physical mechanism and chemical trends in the thermal expansion of inorganic halide perovskites. *The journal of physical chemistry letters*, 14(1):190–198, 2023. doi:10.1021/acs.jpclett.2c03452.

[54] Rongrong Cheacharoen, Nicholas Rolston, Duncan Harwood, Kevin A. Bush, Reinhold H. Dauskardt, and Michael D. McGehee. Design and understanding of encapsulated perovskite solar cells to withstand temperature cycling. *Energy & Environmental Science*, 11 (1):144–150, 2018. ISSN 1754-5692. doi:10.1039/C7EE02564E.

[55] Jérémy Barbé, Declan Hughes, Zhengfei Wei, Adam Pockett, Harrison K. H. Lee, Keith C. Heasman, Matthew J. Carnie, Trystan M. Watson, and Wing C. Tsoi. Radiation hardness of perovskite solar cells based on aluminum–doped zinc oxide electrode under proton irradiation. *Solar RRL*, 3(12):1900219, 2019. ISSN 2367-198X. doi:10.1002/solr.201900219.

[56] G. M. Paternò, V. Robbiano, K. J. Fraser, C. Frost, V. García Sakai, and F. Cacialli. Neutron radiation tolerance of two benchmark thiophene-based conjugated polymers: the importance of crystallinity for organic avionics. *Scientific Reports*, 7(1):41013, 2017. ISSN 2045-2322. doi:10.1038/srep41013.

[57] Gang Li, Yang Yang, R. A. B. Devine, and Clay Mayberry. Radiation induced damage and recovery in poly(3-hexyl thiophene) based polymer solar cells. *Nanotechnology*, 19 (42):424014, 2008. ISSN 1361-6528. doi:10.1088/0957-4484/19/42/424014.

[58] Felix Lang, Norbert H. Nickel, Jürgen Bundesmann, Sophie Seidel, Andrea Denker, Steve Albrecht, Victor V. Brus, Jörg Rappich, Bernd Rech, Giovanni Landi, and Heinrich C. Neitzert. Radiation hardness and self-healing of perovskite solar cells. *Advanced materials (Deerfield Beach, Fla.)*, 28(39):8726–8731, 2016. doi:10.1002/adma.201603326.

[59] Yu Miyazawa, Masashi Ikegami, Hsin-Wei Chen, Takeshi Ohshima, Mitsuru Imaizumi, Kazuyuki Hirose, and Tsutomu Miyasaka. Tolerance of perovskite solar cell to high-energy particle irradiations in space environment. *iScience*, 2:148–155, 2018. doi:10.1016/j.isci.2018.03.020.

[60] Ahmad R. Kirmani, Brandon K. Durant, Jonathan Grandidier, Nancy M. Haegel, Michael D. Kelzenberg, Yao M. Lao, Michael D. McGehee, Lyndsey McMillon-Brown, David P. Ostrowski, Timothy J. Peshek, Bibhudutta Rout, Ian R. Sellers, Mark Steger, Don Walker, David M. Wilt, Kaitlyn T. VanSant, and Joseph M. Luther. Countdown to perovskite space launch: Guidelines to performing relevant radiation-hardness experiments. *Joule*, 6(5):1015–1031, 2022. ISSN 25424351. doi:10.1016/j.joule.2022.03.004.

[61] Peter Müller-Buschbaum. Testing flexible polymer solar cells in near-space. *National science review*, 10(5):nwad071, 2023. doi:10.1093/nsr/nwad071.

[62] Yongguang Tu, Guoning Xu, Xiaoyu Yang, YiFei Zhang, ZhaoJie Li, Rui Su, DeYing Luo, WenQiang Yang, Ying Miao, Rong Cai, LuHua Jiang, XiaoWei Du, YanChu Yang, QianShi Liu, Yang Gao, Shuai Zhao, Wei Huang, Qihuang Gong, and Rui Zhu. Mixed-cation perovskite solar cells in space. *Science China Physics, Mechanics & Astronomy*, 62 (7), 2019. ISSN 1869-1927. doi:10.1007/s11433-019-9356-1.

[63] Zihan Xu, Guoning Xu, Qun Luo, Yunfei Han, Yu Tang, Ying Miao, Yongxiang Li, Jian Qin, Jingbo Guo, Wusong Zha, Chao Gong, Kun Lu, Jianqi Zhang, Zhixiang Wei, Rong Cai, YanChu Yang, ZhaoJie Li, and Chang-Qi Ma. In situ performance and stability tests of large-area flexible polymer solar cells in the 35-km stratospheric environment. *National science review*, 10(4):nwac285, 2023. doi:10.1093/nsr/nwac285.

[64] William Delmas, Samuel Erickson, Jorge Arteaga, Mark Woodall, Michael Scheibner, Timothy S. Krause, Kyle Crowley, Kaitlyn T. VanSant, Joseph M. Luther, Jennifer N. Williams, Jeremiah McNatt, Timothy J. Peshek, Lyndsey McMillon-Brown, and Sayantani Ghosh. Evaluation of hybrid perovskite prototypes after 10–month space flight on the international space station. *Advanced Energy Materials*, 13(19), 2023. ISSN 16146832. doi:10.1002/aenm.202203920.

[65] Gabriele Ghisellini. Radiative processes in high energy astrophysics. 873, 2013. doi:10.1007/978-3-319-00612-3. URL `http://arxiv.org/pdf/1202.5949v1`.

[66] Ajay Kumar Jena, Ashish Kulkarni, and Tsutomu Miyasaka. Halide perovskite photovoltaics: Background, status, and future prospects. *Chemical Reviews*, 119(5):3036–3103, 2019. ISSN 1520-6890. doi:10.1021/acs.chemrev.8b00539.

[67] Lukas Bauer. *Investigation of the Drying Kinetics via In-Situ Photoluminescence Measurements for Printed Perovskite Solar Cells*. B.Sc. thesis, Technical University of Munich, 2022.

[68] V. M. Goldschmidt. Die gesetze der krystallochemie. *Die Naturwissenschaften*, 14(21): 477–485, 1926. ISSN 0028-1042. doi:10.1007/BF01507527.

[69] Zijun Yi, Najib Haji Ladi, Xuxia Shai, Hao Li, Yan Shen, and Mingkui Wang. Will organic-inorganic hybrid halide lead perovskites be eliminated from optoelectronic applications? *Nanoscale advances*, 1(4):1276–1289, 2019. doi:10.1039/c8na00416a.

[70] Michael Grätzel. The light and shade of perovskite solar cells. *Nature Materials*, 13(9): 838–842, 2014. ISSN 1476-4660. doi:10.1038/nmat4065.

[71] Nam-Gyu Park. Perovskite solar cells: an emerging photovoltaic technology. *Materials Today*, 18(2):65–72, 2015. ISSN 13697021. doi:10.1016/j.mattod.2014.07.007.

[72] Dieter Weber. Ch 3 nh 3 pbx 3 , ein pb(ii)-system mit kubischer perowskitstruktur / ch 3 nh 3 pbx 3 , a pb(ii)-system with cubic perovskite structure. *Zeitschrift für Naturforschung B*, 33(12):1443–1445, 1978. ISSN 0932-0776. doi:10.1515/znb-1978-1214.

[73] Brian O'Regan and Michael Grätzel. A low-cost, high-efficiency solar cell based on dye-sensitized colloidal tio2 films. *Nature*, 353(6346):737–740, 1991. doi:10.1038/353737a0.

[74] Michael M. Lee, Joël Teuscher, Tsutomu Miyasaka, Takurou N. Murakami, and Henry J. Snaith. Efficient hybrid solar cells based on meso-superstructured organometal halide perovskites. *Science (New York, N.Y.)*, 338(6107):643–647, 2012. doi:10.1126/science.1228604.

[75] Hui-Seon Kim, Chang-Ryul Lee, Jeong-Hyeok Im, Ki-Beom Lee, Thomas Moehl, Arianna Marchioro, Soo-Jin Moon, Robin Humphry-Baker, Jun-Ho Yum, Jacques E. Moser, Michael Grätzel, and Nam-Gyu Park. Lead iodide perovskite sensitized all-solid-state submicron thin film mesoscopic solar cell with efficiency exceeding 9%. *Scientific Reports*, 2: 591, 2012. ISSN 2045-2322. doi:10.1038/srep00591.

[76] Julian Burschka, Norman Pellet, Soo-Jin Moon, Robin Humphry-Baker, Peng Gao, Mohammad K. Nazeeruddin, and Michael Grätzel. Sequential deposition as a route to high-performance perovskite-sensitized solar cells. *Nature*, 499(7458):316–319, 2013. doi:10.1038/nature12340.

[77] Samuel D. Stranks, Giles E. Eperon, Giulia Grancini, Christopher Menelaou, Marcelo J. P. Alcocer, Tomas Leijtens, Laura M. Herz, Annamaria Petrozza, and Henry J. Snaith. Electron-hole diffusion lengths exceeding 1 micrometer in an organometal trihalide perovskite absorber. *Science (New York, N.Y.)*, 342(6156):341–344, 2013. doi:10.1126/science.1243982.

[78] Victoria Gonzalez-Pedro, Emilio J. Juarez-Perez, Waode-Sukmawati Arsyad, Eva M. Barea, Francisco Fabregat-Santiago, Ivan Mora-Sero, and Juan Bisquert. General working principles of ch3nh3pbx3 perovskite solar cells. *Nano letters*, 14(2):888–893, 2014. doi:10.1021/nl404252e.

[79] Fusheng Ma, Jiangwei Li, Wenzhe Li, Na Lin, Liduo Wang, and Juan Qiao. Stable a/d phase junction of formamidinium lead iodide perovskites for enhanced near-infrared emission. *Chemical science*, 8(1):800–805, 2017. ISSN 2041-6520. doi:10.1039/C6SC03542F.

[80] Thomas Burwig, Wolfgang Fränzel, and Paul Pistor. Crystal phases and thermal stability of co-evaporated cspbx3 (x = i, br) thin films. *The journal of physical chemistry letters*, 9(16):4808–4813, 2018. doi:10.1021/acs.jpclett.8b02059.

[81] Yuhang Liu, Seckin Akin, Alexander Hinderhofer, Felix T. Eickemeyer, Hongwei Zhu, Ji-Youn Seo, Jiahuan Zhang, Frank Schreiber, Hong Zhang, Shaik M. Zakeeruddin, Anders Hagfeldt, M. Ibrahim Dar, and Michael Grätzel. Stabilization of highly efficient and stable phase-pure fapbi3 perovskite solar cells by molecularly tailored 2d-overlayers. *Angewandte Chemie (International ed. in English)*, 59(36):15688–15694, 2020. doi:10.1002/anie.202005211.

[82] Ziqi Xu, Zonghao Liu, Nengxu Li, Gang Tang, Guanhaojie Zheng, Cheng Zhu, Yihua Chen, Ligang Wang, Yuan Huang, Liang Li, Ning Zhou, Jiawang Hong, Qi Chen, and Huanping Zhou. A thermodynamically favored crystal orientation in mixed formamidinium/methylammonium perovskite for efficient solar cells. *Advanced materials (Deerfield Beach, Fla.)*, 31(24):e1900390, 2019. doi:10.1002/adma.201900390.

[83] Nam Joong Jeon, Jun Hong Noh, Woon Seok Yang, Young Chan Kim, Seungchan Ryu, Jangwon Seo, and Sang Il Seok. Compositional engineering of perovskite materials for high-performance solar cells. *Nature*, 517(7535):476–480, 2015. doi:10.1038/nature14133.

[84] Juan Pablo Correa Baena, Ludmilla Steier, Wolfgang Tress, Michael Saliba, Stefanie Neutzner, Taisuke Matsui, Fabrizio Giordano, T. Jesper Jacobsson, Ajay Ram Srimath Kandada, Shaik M. Zakeeruddin, Annamaria Petrozza, Antonio Abate, Mohammad Khaja Nazeeruddin, Michael Grätzel, and Anders Hagfeldt. Highly efficient planar perovskite solar cells through band alignment engineering. *Energy Environ. Sci.*, 8(10):2928–2934, 2015. ISSN 1754-5706. doi:10.1039/C5EE02608C.

[85] Michael Saliba, Juan-Pablo Correa-Baena, Christian M. Wolff, Martin Stolterfoht, Nga Phung, Steve Albrecht, Dieter Neher, and Antonio Abate. How to make over 20% efficient perovskite solar cells in regular (n–i–p) and inverted (p–i–n) architectures. *Chemistry of Materials*, 30(13):4193–4201, 2018. ISSN 0897-4756. doi:10.1021/acs.chemmater.8b00136.

[86] Qi Jiang, Zema Chu, Pengyang Wang, Xiaolei Yang, Heng Liu, Ye Wang, Zhigang Yin, Jinliang Wu, Xingwang Zhang, and Jingbi You. Planar-structure perovskite solar cells with efficiency beyond 21. *Advanced materials (Deerfield Beach, Fla.)*, 29(46), 2017. doi:10.1002/adma.201703852.

[87] Laura M. Herz. Charge-carrier mobilities in metal halide perovskites: Fundamental mechanisms and limits. *ACS Energy Letters*, 2(7):1539–1548, 2017. ISSN 2380-8195. doi:10.1021/acsenergylett.7b00276.

[88] Michael B. Johnston and Laura M. Herz. Hybrid perovskites for photovoltaics: Charge-carrier recombination, diffusion, and radiative efficiencies. *Accounts of chemical research*, 49(1):146–154, 2016. doi:10.1021/acs.accounts.5b00411.

[89] Daming Zhao, Hongwei Hu, Reinhard Haselsberger, Rudolph A. Marcus, Maria-Elisabeth Michel-Beyerle, Yeng Ming Lam, Jian-Xin Zhu, Chan La-O-Vorakiat, Matthew C. Beard, and Elbert E. M. Chia. Monitoring electron-phonon interactions in lead halide perovskites using time-resolved thz spectroscopy. *ACS nano*, 13(8):8826–8835, 2019. doi:10.1021/acsnano.9b02049.

[90] Michael C. Brennan, Sergiu Draguta, Prashant V. Kamat, and Masaru Kuno. Light-induced anion phase segregation in mixed halide perovskites. *ACS Energy Letters*, 3(1): 204–213, 2018. ISSN 2380-8195. doi:10.1021/acsenergylett.7b01151.

[91] Carolin M. Sutter-Fella, Quynh P. Ngo, Nicola Cefarin, Kira L. Gardner, Nobumichi Tamura, Camelia V. Stan, Walter S. Drisdell, Ali Javey, Francesca M. Toma, and Ian D. Sharp. Cation-dependent light-induced halide demixing in hybrid organic-inorganic perovskites. *Nano letters*, 18(6):3473–3480, 2018. doi:10.1021/acs.nanolett.8b00541.

[92] Alex J. Barker, Aditya Sadhanala, Felix Deschler, Marina Gandini, Satyaprasad P. Senanayak, Phoebe M. Pearce, Edoardo Mosconi, Andrew J. Pearson, Yue Wu, Ajay Ram Srimath Kandada, Tomas Leijtens, Filippo de Angelis, Siân E. Dutton, Annamaria Petrozza, and Richard H. Friend. Defect-assisted photoinduced halide segregation in mixed-halide perovskite thin films. *ACS Energy Letters*, 2(6):1416–1424, 2017. ISSN 2380-8195. doi:10.1021/acsenergylett.7b00282.

[93] Rachel E. Beal, Nanna Zhou Hagström, Julien Barrier, Aryeh Gold-Parker, Rohit Prasanna, Kevin A. Bush, Donata Passarello, Laura T. Schelhas, Karsten Brüning, Christopher J. Tassone, Hans-Georg Steinrück, Michael D. McGehee, Michael F. Toney,

and Ana Flávia Nogueira. Structural origins of light-induced phase segregation in organic-inorganic halide perovskite photovoltaic materials. *Matter*, 2(1):207–219, 2020. ISSN 25902385. doi:10.1016/j.matt.2019.11.001.

[94] Anoop K. M., Mark V. Khenkin, Francesco Di Giacomo, Yulia Galagan, Stav Rahmany, Lioz Etgar, Eugene A. Katz, and Iris Visoly-Fisher. Bias–dependent stability of perovskite solar cells studied using natural and concentrated sunlight. *Solar RRL*, 4(2):1900335, 2020. ISSN 2367-198X. doi:10.1002/solr.201900335.

[95] M. Kot, L. Kegelmann, H. Köbler, M. Vorokhta, C. Escudero, P. Kúš, B. Šmíd, M. Tallarida, S. Albrecht, A. Abate, I. Matolínová, D. Schmeißer, and J. I. Flege. In situ near-ambient pressure x-ray photoelectron spectroscopy reveals the influence of photon flux and water on the stability of halide perovskite. *ChemSusChem*, 13(21):5722–5730, 2020. doi:10.1002/cssc.202001527.

[96] Minjin Kim, Jaeki Jeong, Haizhou Lu, Tae Kyung Lee, Felix T. Eickemeyer, Yuhang Liu, In Woo Choi, Seung Ju Choi, Yimhyun Jo, Hak-Beom Kim, Sung-In Mo, Young-Ki Kim, Heunjeong Lee, Na Gyeong An, Shinuk Cho, Wolfgang R. Tress, Shaik M. Zakeeruddin, Anders Hagfeldt, Jin Young Kim, Michael Grätzel, and Dong Suk Kim. Conformal quantum dot-sno2 layers as electron transporters for efficient perovskite solar cells. *Science (New York, N.Y.)*, 375(6578):302–306, 2022. doi:10.1126/science.abh1885.

[97] Isaac Zarazua, Guifang Han, Pablo P. Boix, Subodh Mhaisalkar, Francisco Fabregat-Santiago, Ivan Mora-Seró, Juan Bisquert, and Germà Garcia-Belmonte. Surface recombination and collection efficiency in perovskite solar cells from impedance analysis. *The journal of physical chemistry letters*, 7(24):5105–5113, 2016. doi:10.1021/acs.jpclett.6b02193.

[98] Mojtaba Abdi-Jalebi, Zahra Andaji-Garmaroudi, Stefania Cacovich, Camille Stavrakas, Bertrand Philippe, Johannes M. Richter, Mejd Alsari, Edward P. Booker, Eline M. Hutter, Andrew J. Pearson, Samuele Lilliu, Tom J. Savenije, Håkan Rensmo, Giorgio Divitini, Caterina Ducati, Richard H. Friend, and Samuel D. Stranks. Maximizing and stabilizing luminescence from halide perovskites with potassium passivation. *Nature*, 555(7697):497–501, 2018. doi:10.1038/nature25989.

[99] SeongYeon Kim, Fei Zhang, Jinhui Tong, Xihan Chen, Enkhjargal Enkhbayar, Kai Zhu, and JunHo Kim. Effects of potassium treatment on sno2 electron transport layers for improvements of perovskite solar cells. *Solar Energy*, 233:353–362, 2022. ISSN 0038092X. doi:10.1016/j.solener.2022.01.053.

[100] A. Einstein. Über einen die erzeugung und verwandlung des lichtes betreffenden heuristischen gesichtspunkt. *Annalen der Physik*, 322(6):132–148, 1905. ISSN 00033804. doi:10.1002/andp.19053220607.

[101] Laura M. Herz. How lattice dynamics moderate the electronic properties of metal-halide perovskites. *The journal of physical chemistry letters*, 9(23):6853–6863, 2018. doi:10.1021/acs.jpclett.8b02811.

[102] Oleksandr V. Mikhnenko, Paul W. M. Blom, and Thuc-Quyen Nguyen. Exciton diffusion in organic semiconductors. *Energy Environ. Sci.*, 8(7):1867–1888, 2015. ISSN 1754-5706. doi:10.1039/C5EE00925A.

[103] Kai Müller, Karl S. Schellhammer, Nico Gräßler, Bipasha Debnath, Fupin Liu, Yulia Krupskaya, Karl Leo, Martin Knupfer, and Frank Ortmann. Directed exciton transport highways in organic semiconductors. *Nature Communications*, 14(1):5599, 2023. ISSN 2041-1723. doi:10.1038/s41467-023-41044-9.

[104] Johannes Schlipf. *The Morphology of Hybrid Perovskite Thin Films for Photovoltaic Application: Formation & Disintegration*. Universitätsbibliothek der TU München, München, 2018.

[105] Peter Würfel. *Physics of Solar Cells*. Wiley, 2005. ISBN 9783527404285. doi:10.1002/9783527618545.

[106] M. Burgelman, P. Nollet, and S. Degrave. Modelling polycrystalline semiconductor solar cells. *Thin Solid Films*, 361-362:527–532, 2000. ISSN 00406090. doi:10.1016/S0040-6090(99)00825-1.

[107] William Shockley and Hans J. Queisser. Detailed balance limit of efficiency of p-n junction solar cells. *Journal of Applied Physics*, 32(3):510–519, 1961. ISSN 0021-8979. doi:10.1063/1.1736034.

[108] Tomas Leijtens, Kevin A. Bush, Rohit Prasanna, and Michael D. McGehee. Opportunities and challenges for tandem solar cells using metal halide perovskite semiconductors. *Nature Energy*, 3(10):828–838, 2018. ISSN 2058-7546. doi:10.1038/s41560-018-0190-4.

[109] Ido Frenkel and Avi Niv. Effect of maintaining a fixed ambient temperature on the evaluation of photovoltaic device performance. *Physical Review Applied*, 19(6), 2023. doi:10.1103/PhysRevApplied.19.064023.

[110] Yuanyuan Zhou, Onkar S. Game, Shuping Pang, and Nitin P. Padture. Microstructures of organometal trihalide perovskites for solar cells: Their evolution from solutions and characterization. *The journal of physical chemistry letters*, 6(23):4827–4839, 2015. doi:10.1021/acs.jpclett.5b01843.

[111] Simon Ternes, Tobias Börnhorst, Jonas A. Schwenzer, Ihteaz M. Hossain, Tobias Abzieher, Waldemar Mehlmann, Uli Lemmer, Philip Scharfer, Wilhelm Schabel, Bryce S. Richards, and Ulrich W. Paetzold. Drying dynamics of solution–processed perovskite thin–film photovoltaics: In situ characterization, modeling, and process control. *Advanced Energy Materials*, 9(39):1901581, 2019. ISSN 16146832. doi:10.1002/aenm.201901581.

[112] Nam-Gyu Park. Perovskite solar cell: Research direction for next 10 years. *ACS Energy Letters*, 4(12):2983–2985, 2019. ISSN 2380-8195. doi:10.1021/acsenergylett.9b02442.

[113] Jun Yin, Daniele Cortecchia, Anurag Krishna, Shi Chen, Nripan Mathews, Andrew C. Grimsdale, and Cesare Soci. Interfacial charge transfer anisotropy in polycrystalline lead iodide perovskite films. *The journal of physical chemistry letters*, 6(8):1396–1402, 2015. doi:10.1021/acs.jpclett.5b00431.

[114] Andrea Vitaloni. *Compositional Improvement of Morphology and Opto-Electronics for Slot-Die Coated Perovskite Solar Cells*. M.Sc. thesis, Technical University of Munich, 2022.

[115] C. Jeffrey Brinker and George W. Scherer. *Sol-gel science: The physics and chemistry of sol-gel processing / C. Jeffrey Brinker, George W. Scherer*. Academic Press, Boston, 1990. ISBN 9780080571034.

[116] Dimo Kashchiev. *Nucleation: Basic theory with applications / Dimo Kashchiev*. Butterworth Heinemann, Boston, Mass., 1999. ISBN 0750646829.

[117] Jens Lothe and G. M. Pound. Reconsiderations of nucleation theory. *The Journal of Chemical Physics*, 36(8):2080–2085, 1962. ISSN 0021-9606. doi:10.1063/1.1732832.

[118] Victor K. LaMer and Robert H. Dinegar. Theory, production and mechanism of formation of monodispersed hydrosols. *Journal of the American Chemical Society*, 72(11):4847–4854, 1950. ISSN 0002-7863. doi:10.1021/ja01167a001.

[119] Manda Xiao, Fuzhi Huang, Wenchao Huang, Yasmina Dkhissi, Ye Zhu, Joanne Etheridge, Angus Gray-Weale, Udo Bach, Yi-Bing Cheng, and Leone Spiccia. A fast deposition-crystallization procedure for highly efficient lead iodide perovskite thin-film solar cells. *Angewandte Chemie (International ed. in English)*, 53(37):9898–9903, 2014. doi:10.1002/anie.201405334.

[120] Nam Joong Jeon, Jun Hong Noh, Young Chan Kim, Woon Seok Yang, Seungchan Ryu, and Sang Il Seok. Solvent engineering for high-performance inorganic-organic hybrid perovskite solar cells. *Nature Materials*, 13(9):897–903, 2014. ISSN 1476-4660. doi:10.1038/nmat4014.

[121] Maria Konstantakou, Dorothea Perganti, Polycarpos Falaras, and Thomas Stergiopoulos. Anti-solvent crystallization strategies for highly efficient perovskite solar cells. *Crystals*, 7 (10):291, 2017. doi:10.3390/cryst7100291.

[122] Shambhavi Pratap, Finn Babbe, Nicola S. Barchi, Zhenghao Yuan, Tina Luong, Zach Haber, Tze-Bin Song, Jonathan L. Slack, Camelia V. Stan, Nobumichi Tamura, Carolin M. Sutter-Fella, and Peter Müller-Buschbaum. Out-of-equilibrium processes in crystallization of organic-inorganic perovskites during spin coating. *Nature Communications*, 12(1):5624, 2021. ISSN 2041-1723. doi:10.1038/s41467-021-25898-5.

[123] Manuel A. Reus, Lennart K. Reb, Alexander F. Weinzierl, Christian L. Weindl, Renjun Guo, Tianxiao Xiao, Matthias Schwartzkopf, Andrei Chumakov, Stephan V. Roth, and Peter Müller-Buschbaum. Time–resolved orientation and phase analysis of lead halide perovskite film annealing probed by in situ giwaxs. *Advanced Optical Materials*, 10(14): 2102722, 2022. ISSN 2195-1071. doi:10.1002/adom.202102722.

[124] Congcong Wu, Kai Wang, Jing Li, Zihui Liang, Jin Li, Wenlu Li, Li Zhao, Bo Chi, and Shimin Wang. Volatile solution: the way toward scalable fabrication of perovskite solar cells? *Matter*, 4(3):775–793, 2021. ISSN 25902385. doi:10.1016/j.matt.2020.12.025.

[125] Yehao Deng, Charles H. van Brackle, Xuezeng Dai, Jingjing Zhao, Bo Chen, and Jinsong Huang. Tailoring solvent coordination for high-speed, room-temperature blading of perovskite photovoltaic films. *Science advances*, 5(12):eaax7537, 2019. doi:10.1126/sciadv.aax7537.

[126] Yuanhang Yang, Zexu Xue, Long Chen, Cho Fai Jonathan Lau, and Zhiping Wang. Large-area perovskite films for pv applications: A perspective from nucleation and crystallization. *Journal of Energy Chemistry*, 59:626–641, 2021. ISSN 20954956. doi:10.1016/j.jechem.2020.12.001.

[127] Jin Hyuck Heo, Sang Hyuk Im, Jun Hong Noh, Tarak N. Mandal, Choong-Sun Lim, Jeong Ah Chang, Yong Hui Lee, Hi-jung Kim, Arpita Sarkar, Md. K. Nazeeruddin, Michael Grätzel, and Sang Il Seok. Efficient inorganic–organic hybrid heterojunction solar cells containing perovskite compound and polymeric hole conductors. *Nature Photonics*, 7(6): 486–491, 2013. ISSN 1749-4893. doi:10.1038/nphoton.2013.80.

[128] Jeong-Hyeok Im, Hui-Seon Kim, and Nam-Gyu Park. Morphology-photovoltaic property correlation in perovskite solar cells: One-step versus two-step deposition of ch3nh3pbi3. *APL MATERIALS*, 2(8), 2014. doi:10.1063/1.4891275.

[129] Yunlong Guo, Kazutaka Shoyama, Wataru Sato, Yutaka Matsuo, Kento Inoue, Koji Harano, Chao Liu, Hideyuki Tanaka, and Eiichi Nakamura. Chemical pathways connecting lead(ii) iodide and perovskite via polymeric plumbate(ii) fiber. *Journal of the American Chemical Society*, 137(50):15907–15914, 2015. ISSN 0002-7863. doi:10.1021/jacs.5b10599.

[130] Simon Ternes, Jonas Mohacsi, Nico Lüdtke, H. Minh Pham, Meriç Arslan, Philip Scharfer, Wilhelm Schabel, Bryce S. Richards, and Ulrich W. Paetzold. Drying and coating of perovskite thin films: How to control the thin film morphology in scalable dynamic coating systems. *ACS applied materials & interfaces*, 14(9):11300–11312, 2022. doi:10.1021/acsami.1c22363.

[131] Shangshang Chen, Xuezeng Dai, Shuang Xu, Haoyang Jiao, Liang Zhao, and Jinsong Huang. Stabilizing perovskite-substrate interfaces for high-performance perovskite modules. *Science (New York, N.Y.)*, 373(6557):902–907, 2021. doi:10.1126/science.abi6323.

[132] Xiaodan Gu, Leo Shaw, Kevin Gu, Michael F. Toney, and Zhenan Bao. The meniscus-guided deposition of semiconducting polymers. *Nature Communications*, 9(1):534, 2018. ISSN 2041-1723. doi:10.1038/s41467-018-02833-9.

[133] J. Clay Hamill, Jeffrey Schwartz, and Yueh-Lin Loo. Influence of solvent coordination on hybrid organic–inorganic perovskite formation. *ACS Energy Letters*, 3(1):92–97, 2018. ISSN 2380-8195. doi:10.1021/acsenergylett.7b01057.

[134] Viktor Gutmann. Solvent effects on the reactivities of organometallic compounds. *Coordination Chemistry Reviews*, 18(2):225–255, 1976. ISSN 00108545. doi:10.1016/S0010-8545(00)82045-7.

[135] Shambhavi Pratap, Elisabeth Keller, and Peter Müller-Buschbaum. Emergence of lead halide perovskite colloidal dispersions through aggregation and fragmentation: insights from the nanoscale to the mesoscale. *Nanoscale*, 11(8):3495–3499, 2019. doi:10.1039/C8NR09853K.

[136] Yixin Zhao and Kai Zhu. Ch 3 nh 3 cl-assisted one-step solution growth of ch 3 nh 3 pbi 3 : Structure, charge-carrier dynamics, and photovoltaic properties of perovskite solar cells. *The Journal of Physical Chemistry C*, 118(18):9412–9418, 2014. ISSN 1932-7447. doi:10.1021/jp502696w.

[137] Mengjin Yang, Taiyang Zhang, Philip Schulz, Zhen Li, Ge Li, Dong Hoe Kim, Nanjie Guo, Joseph J. Berry, Kai Zhu, and Yixin Zhao. Facile fabrication of large-grain ch3nh3pbi3-xbrx films for high-efficiency solar cells via ch3nh3br-selective ostwald ripening. *Nature Communications*, 7:12305, 2016. ISSN 2041-1723. doi:10.1038/ncomms12305.

[138] Li-Hui Chou, Julian M. W. Chan, and Cheng-Liang Liu. Progress in spray coated perovskite films for solar cell applications. *Solar RRL*, 6(4):2101035, 2022. ISSN 2367-198X. doi:10.1002/solr.202101035.

[139] Qiang Wu, Jie Guo, Rui Sun, Jing Guo, Shuangfeng Jia, Yaowen Li, Jianbo Wang, and Jie Min. Slot-die printed non-fullerene organic solar cells with the highest efficiency of 12.9% for low-cost pv-driven water splitting. *Nano Energy*, 61:559–566, 2019. ISSN 22112855. doi:10.1016/j.nanoen.2019.04.091.

[140] Nicholas Rolston, William J. Scheideler, Austin C. Flick, Justin P. Chen, Hannah Elmaraghi, Andrew Sleugh, Oliver Zhao, Michael Woodhouse, and Reinhold H. Dauskardt. Rapid open-air fabrication of perovskite solar modules. *Joule*, 4(12):2675–2692, 2020. ISSN 25424351. doi:10.1016/j.joule.2020.11.001.

[141] Xinyu Jiang, Pauline Chotard, Kexun Luo, Felix Eckmann, Suo Tu, Manuel A. Reus, Shanshan Yin, Julija Reitenbach, Christian L. Weindl, Matthias Schwartzkopf, Stephan V. Roth, and Peter Müller-Buschbaum. Revealing donor–acceptor interaction on the printed active layer morphology and the formation kinetics for nonfullerene organic solar cells at ambient conditions. *Advanced Energy Materials*, 12(14):2103977, 2022. ISSN 16146832. doi:10.1002/aenm.202103977.

[142] Tamara Merckx, Aranzazu Aguirre, Yinghuan Kuang, Arvid van der Heide, Ali Hajjiah, Yaser Abdulraheem, Anurag Krishna, Jef Poortmans, and Tom Aernouts. Stable device architecture with industrially scalable processes for realizing efficient 784 cm 2 monolithic perovskite solar modules. *IEEE Journal of Photovoltaics*, 13(3):419–421, 2023. ISSN 2156-3381. doi:10.1109/JPHOTOV.2023.3259061.

[143] Yulong Wang, Changyu Duan, Pin Lv, Zhiliang Ku, Jianfeng Lu, Fuzhi Huang, and Yi-Bing Cheng. Printing strategies for scaling-up perovskite solar cells. *National science review*, 8(8):nwab075, 2021. doi:10.1093/nsr/nwab075.

[144] Rahul Patidar, Daniel Burkitt, Katherine Hooper, David Richards, and Trystan Watson. Slot-die coating of perovskite solar cells: An overview. *Materials Today Communications*, 22:100808, 2020. ISSN 23524928. doi:10.1016/j.mtcomm.2019.100808.

[145] Dong Seok Ham, Woo Jin Choi, Hongseok Yun, Min Kim, Dong-Hyun Yeo, Seungjin Lee, Bumjoon J. Kim, and Jae Heung Lee. Influence of drying conditions on device performances of antisolvent-assisted roll-to-roll slot die-coated perovskite solar cells. *ACS Applied Energy Materials*, 4(8):7611–7621, 2021. ISSN 2574-0962. doi:10.1021/acsaem.1c00892.

[146] Xiaoyu Ding, Jianhua Liu, and Tequila A. L. Harris. A review of the operating limits in slot die coating processes. *AIChE Journal*, 62(7):2508–2524, 2016. ISSN 0001-1541. doi:10.1002/aic.15268.

[147] Chi-Feng Lin, David S. Hill Wong, Ta-Jo Liu, and Ping-Yao Wu. Operating windows of slot die coating: Comparison of theoretical predictions with experimental observations. *Advances in Polymer Technology*, 29(1):31–44, 2010. ISSN 07306679. doi:10.1002/adv.20173.

[148] Xiuxiu Niu, Nengxu Li, Qi Chen, and Huanping Zhou. Insights into large–scale fabrication methods in perovskite photovoltaics. *Advanced Energy and Sustainability Research*, 2(2): 2000046, 2021. ISSN 2699-9412. doi:10.1002/aesr.202000046.

[149] L. Landau and B. Levich. Dragging of a liquid by a moving plate. In *Dynamics of Curved Fronts*, pages 141–153. Elsevier, 1988. ISBN 9780125503556. doi:10.1016/B978-0-08-092523-3.50016-2.

[150] Severin Siegrist, Pranjal Nandi, Radha K. Kothandaraman, Aribia Abdessalem, Ayodhya N. Tiwari, and Fan Fu. Understanding coating thickness and uniformity of blade–coated sno 2 electron transport layer for scalable perovskite solar cells. *Solar RRL*, 2023. ISSN 2367-198X. doi:10.1002/solr.202300273.

[151] Jueng-Eun Kim, Yen-Sook Jung, Youn-Jung Heo, Kyeongil Hwang, Tianshi Qin, Dong-Yu Kim, and Doojin Vak. Slot die coated planar perovskite solar cells via blowing and heating assisted one step deposition. *Solar Energy Materials and Solar Cells*, 179:80–86, 2018. ISSN 0927-0248. doi:10.1016/j.solmat.2018.02.003.

[152] Donmin Lee, Yen-Sook Jung, Youn-Jung Heo, Sehyun Lee, Kyeongil Hwang, Ye-Jin Jeon, Jueng-Eun Kim, Jiyoon Park, Gun Young Jung, and Dong-Yu Kim. Slot-die coated perovskite films using mixed lead precursors for highly reproducible and large-area solar cells. *ACS applied materials & interfaces*, 10(18):16133–16139, 2018. doi:10.1021/acsami.8b02549.

[153] Mengjin Yang, Zhen Li, Matthew O. Reese, Obadiah G. Reid, Dong Hoe Kim, Sebastian Siol, Talysa R. Klein, Yanfa Yan, Joseph J. Berry, Maikel F. A. M. van Hest, and Kai Zhu. Perovskite ink with wide processing window for scalable high-efficiency solar cells. *Nature Energy*, 2(5), 2017. ISSN 2058-7546. doi:10.1038/nenergy.2017.38.

[154] Christoph Gernot Lindenmeir. *Optimization of Morphology and Efficiency of Slot-Die Printed Perovskite Solar Cells*. M.Sc. thesis, Technical University of Munich, 2023.

[155] I. M. Lifshitz and V. V. Slyozov. The kinetics of precipitation from supersaturated solid solutions. *Journal of Physics and Chemistry of Solids*, 19(1-2):35–50, 1961. ISSN 00223697. doi:10.1016/0022-3697(61)90054-3.

[156] Hanlin Hu, Zhiwei Ren, Patrick W. K. Fong, Minchao Qin, Danjun Liu, Dangyuan Lei, Xinhui Lu, and Gang Li. Room–temperature meniscus coating of >20% perovskite solar cells: A film formation mechanism investigation. *Advanced Functional Materials*, 29(25): 1900092, 2019. ISSN 1616-301X. doi:10.1002/adfm.201900092.

[157] Alexander R. Pascoe, Qinying Gu, Mathias U. Rothmann, Wei Li, Yupeng Zhang, Andrew D. Scully, Xiongfeng Lin, Leone Spiccia, Udo Bach, and Yi-Bing Cheng. Directing nucleation and growth kinetics in solution-processed hybrid perovskite thin-films. *Science China Materials*, 60(7):617–628, 2017. ISSN 2095-8226. doi:10.1007/s40843-017-9043-y.

[158] Zihui Liang, Yuchen Hou, Yidong Ming, Zhaoyang Wei, Shashank Priya, Kai Wang, and Congcong Wu. Paradigm ink with a temporally controllable processing-window for perovskite modules. *Journal of Materials Chemistry A*, 10(28):14989–14999, 2022. ISSN 2050-7488. doi:10.1039/D2TA03437A.

[159] Wen Liang Tan and Christopher R. McNeill. X-ray diffraction of photovoltaic perovskites: Principles and applications. *Applied Physics Reviews*, 9(2):021310, 2022. doi:10.1063/5.0076665.

[160] D. S. Sivia. *Elementary scattering theory: For X-ray and neutron users / D.S. Sivia.* Oxford University Press, Oxford, 2011. ISBN 9780199228676.

[161] Carmelo Giacovazzo. *Fundamentals of crystallography.* 1992. ISBN 0198555784.

[162] Christoph Schaffer. *Morphological Degradation in Polymer-Fullerene Solar Cells.* Physik. Universitätsbibliothek der TU München, München, 2017. ISBN 978-3-8439-3059-8.

[163] William Henry Bragg and William Lawrence Bragg. The reflection of x-rays by crystals. *Proceedings of the Royal Society of London. Series A, Containing Papers of a Mathematical and Physical Character*, 88(605):428–438, 1913. ISSN 0950-1207. doi:10.1098/rspa.1913.0040.

[164] Koichi Momma and Fujio Izumi. Vesta 3 for three-dimensional visualization of crystal, volumetric and morphology data. *Journal of applied crystallography*, 44(6):1272–1276, 2011. ISSN 0021-8898. doi:10.1107/S0021889811038970.

[165] SCHERRER P. Nachr ges wiss goettingen. *Math. Phys.*, 2:98–100, 1918. URL https://cir.nii.ac.jp/crid/1571417126345362048.

[166] G.K Williamson and W.H Hall. X-ray line broadening from filed aluminium and wolfram. *Acta Metallurgica*, 1(1):22–31, 1953. ISSN 00016160. doi:10.1016/0001-6160(53)90006-6.

[167] Detlef-M Smilgies. Scherrer grain-size analysis adapted to grazing-incidence scattering with area detectors. *Journal of applied crystallography*, 42(Pt 6):1030–1034, 2009. ISSN 0021-8898. doi:10.1107/S0021889809040126.

[168] Peter Müller-Buschbaum. The active layer morphology of organic solar cells probed with grazing incidence scattering techniques. *Advanced materials (Deerfield Beach, Fla.)*, 26 (46):7692–7709, 2014. doi:10.1002/adma.201304187.

[169] Alexander Hexemer and Peter Müller-Buschbaum. Advanced grazing-incidence techniques for modern soft-matter materials analysis. *IUCrJ*, 2(Pt 1):106–125, 2015. ISSN 2052-2525. doi:10.1107/S2052252514024178.

[170] M. A. Reus, L. K. Reb. Insight: The in situ gixs heuristic tool for efficient reduction of grazing-incidence scattering data. URL https://www.ph.nat.tum.de/en/functmat/forschung-research/insight/.

[171] Jessy L. Baker, Leslie H. Jimison, Stefan Mannsfeld, Steven Volkman, Shong Yin, Vivek Subramanian, Alberto Salleo, A. Paul Alivisatos, and Michael F. Toney. Quantification of thin film crystallographic orientation using x-ray diffraction with an area detector. *Langmuir : the ACS journal of surfaces and colloids*, 26(11):9146–9151, 2010. doi:10.1021/la904840q.

[172] Zhang Jiang. Gixsgui : a matlab toolbox for grazing-incidence x-ray scattering data visualization and reduction, and indexing of buried three-dimensional periodic nanostructured films. *Journal of Applied Crystallography*, 48(3):917–926, 2015. doi:10.1107/S1600576715004434.

[173] Victoria Savikhin, Maxime Babics, Marios Neophytou, Shengjian Liu, Stefan D. Oosterhout, Hongping Yan, Xiaodan Gu, Pierre M. Beaujuge, and Michael F. Toney. Impact of polymer side chain modification on opv morphology and performance. *Chemistry of Materials*, 30(21):7872–7884, 2018. ISSN 0897-4756. doi:10.1021/acs.chemmater.8b03455.

[174] Martin Etter and Robert E. Dinnebier. A century of powder diffraction: a brief history. *Zeitschrift für anorganische und allgemeine Chemie*, 640(15):3015–3028, 2014. ISSN 00442313. doi:10.1002/zaac.201400526.

[175] J. Paul Goode. The homolosine projection: A new device for portraying the earth's surface entire. *Annals of the Association of American Geographers*, 15(3):119, 1925. ISSN 00045608. doi:10.2307/2560812.

[176] Claudia Maria Palumbiny. *Polymeric PEDOT:PSS electrodes for organic electronics: Understanding the conductivity-structure relation.* Dissertation, Universitätsbibliothek der TU München, München, 2015.

[177] R. W. Cheary, A. A. Coelho, and J. P. Cline. Fundamental parameters line profile fitting in laboratory diffractometers. *Journal of research of the National Institute of Standards and Technology*, 109(1):1–25, 2004. ISSN 1044-677X. doi:10.6028/jres.109.002.

[178] M. v. Laue. Vi. lorentz-faktor und intensitätsverteilung in debye-scherrer-ringen. *Zeitschrift für Kristallographie - Crystalline Materials*, 64(1-6):115–142, 1926. ISSN 2194-4946. doi:10.1524/zkri.1926.64.1.115.

[179] H. Dosch, B. W. Batterman, and D. C. Wack. Depth-controlled grazing-incidence diffraction of synchrotron x radiation. *Physical review letters*, 56(11):1144–1147, 1986. doi:10.1103/PhysRevLett.56.1144.

[180] Mario Birkholz. *Thin Film Analysis by X–Ray Scattering.* Wiley, 2005. ISBN 9783527310524. doi:10.1002/3527607595.

[181] Dag W. Breiby, Oliver Bunk, Jens W. Andreasen, Henrik T. Lemke, and Martin M. Nielsen. Simulating x-ray diffraction of textured films. *Journal of applied crystallography*, 41(2):262–271, 2008. ISSN 0021-8898. doi:10.1107/S0021889808001064.

[182] T. A. Ezquerra. *Applications of synchrotron light to scattering and diffraction in materials and life sciences*, volume 776 of *Lecture notes in physics, 0075-8450*. Springer, Berlin, 2009. ISBN 9783540959670.

[183] P. Müller-Buschbaum. Grazing incidence small-angle x-ray scattering: an advanced scattering technique for the investigation of nanostructured polymer films. *Analytical and bioanalytical chemistry*, 376(1):3–10, 2003. ISSN 1618-2642. doi:10.1007/s00216-003-1869-2.

[184] Y. Yoneda. Anomalous surface reflection of x rays. *Physical Review*, 131(5):2010–2013, 1963. ISSN 0031-899X. doi:10.1103/PhysRev.131.2010.

[185] J. R. Levine, J. B. Cohen, Y. W. Chung, and P. Georgopoulos. Grazing-incidence small-angle x-ray scattering: new tool for studying thin film growth. *Journal of applied crystallography*, 22(6):528–532, 1989. ISSN 0021-8898. doi:10.1107/S002188988900717X.

[186] Gilles Renaud, Rémi Lazzari, and Frédéric Leroy. Probing surface and interface morphology with grazing incidence small angle x-ray scattering. *Surface Science Reports*, 64(8): 255–380, 2009. ISSN 01675729. doi:10.1016/j.surfrep.2009.07.002.

[187] R. Hosemann. Der ideale parakristall und die von ihm gestreute kohrente rntgenstrahlung. *Zeitschrift fr Physik*, 128(4):465–492, 1950. ISSN 1434-6001. doi:10.1007/BF01330029.

[188] Rolf Hosemann. Rntgeninterferenzen an stoffen mit flssigkeitsstatistischen gitterstrungen. *Zeitschrift fr Physik*, 128(1):1–35, 1950. ISSN 1434-6001. doi:10.1007/BF01339555.

[189] Lennart K. Reb, Michael Böhmer, Benjamin Predeschly, Sebastian Grott, Christian L. Weindl, Goran I. Ivandekic, Renjun Guo, Christoph Dreißigacker, Roman Gernhäuser, Andreas Meyer, and Peter Müller-Buschbaum. Perovskite and organic solar cells on a rocket flight. *Joule*, 4(9):1880–1892, 2020. ISSN 25424351. doi:10.1016/j.joule.2020.07.004.

[190] Benjamin Predeschly. *Design and Realization of a Measuring Setup for Characterizing Organic and Hybrid Solar Cells in Space*. M.Sc. thesis, Technical University of Munich, 2019.

[191] Dorian-David Percheron. *Optimizing the Compact TiO_2 Electron Transport Layer for High Efficiency Perovskite Solar Cells*. B.Sc. thesis, Technical University of Munich, 2019.

[192] Nicola Taffertshofer. *Improving the Efficiency of Perovskite Solar Cells by Blocking Layer Optimization*. B.Sc. thesis, Technical University of Munich, 2019.

[193] Alexander D. Taylor, Qing Sun, Katelyn P. Goetz, Qingzhi An, Tim Schramm, Yvonne Hofstetter, Maximillian Litterst, Fabian Paulus, and Yana Vaynzof. A general approach to high-efficiency perovskite solar cells by any antisolvent. *Nature Communications*, 12 (1):1878, 2021. ISSN 2041-1723. doi:10.1038/s41467-021-22049-8.

[194] Martin Stolterfoht, Christian M. Wolff, Yohai Amir, Andreas Paulke, Lorena Perdigón-Toro, Pietro Caprioglio, and Dieter Neher. Approaching the fill factor shockley–queisser limit in stable, dopant-free triple cation perovskite solar cells. *Energy & Environmental Science*, 10(6):1530–1539, 2017. ISSN 1754-5692. doi:10.1039/C7EE00899F.

[195] Jinzhao Li, Janardan Dagar, Oleksandra Shargaieva, Marion A. Flatken, Hans Köbler, Markus Fenske, Christof Schultz, Bert Stegemann, Justus Just, Daniel M. Többens, Antonio Abate, Rahim Munir, and Eva Unger. 20.8% slot–die coated mapbi 3 perovskite solar cells by optimal dmso–content and age of 2–me based precursor inks. *Advanced Energy Materials*, 11(10):2003460, 2021. ISSN 16146832. doi:10.1002/aenm.202003460.

[196] Hsu Thazin Myint. *Fabrication and Characterization of Semiconducting Carbon Nitride Thin Films for Application in Perovskite Photovoltaics*. M.Sc. thesis, Technical University of Munich, 2022.

[197] Constantin Harder, Alexandros E. Alexakis, Yusuf Bulut, Shuxian Xiong, Benedikt Sochor, Guangjiu Pan, Huaying Zhong, Korneliya Goordeyeva, Manuel A. Reus, Volker Körstgens, Arno Jeromin, Thomas F. Keller, L. Daniel Söderberg, Eva Malmström, Peter Müller-Buschbaum, and Stephan V. Roth. Optical properties of slot–die coated hybrid colloid/cellulose–nanofibril thin films. *Advanced Optical Materials*, 11(13), 2023. ISSN 2195-1071. doi:10.1002/adom.202203058.

[198] Manuel A. Reus, Ahmed Krifa, Quinten A. Akkerman, Alexander Biewald, Zehua Xu, David P. Kosbahn, Christian L. Weindl, Jochen Feldmann, Achim Hartschuh, and Peter Müller-Buschbaum. Layer–by–layer printed metal hybrid (cs:fa)pbi 3 perovskite nanocrystal solar cells. *Advanced Optical Materials*, 2023. ISSN 2195-1071. doi:10.1002/adom.202301008.

[199] Sih-Hao Liao, Hong-Jyun Jhuo, Po-Nan Yeh, Yu-Shan Cheng, Yi-Lun Li, Yu-Hsuan Lee, Sunil Sharma, and Show-An Chen. Single junction inverted polymer solar cell reaching power conversion efficiency 10.31% by employing dual-doped zinc oxide nano-film as cathode interlayer. *Scientific Reports*, 4(1):6813, 2014. ISSN 2045-2322. doi:10.1038/srep06813.

[200] E. Abbe. Beiträge zur theorie des mikroskops und der mikroskopischen wahrnehmung. *Archiv für Mikroskopische Anatomie*, 9(1):413–468, 1873. ISSN 0176-7364. doi:10.1007/BF02956173.

[201] Weili Zhou and Zhong Lin Wang. *Scanning microscopy for nanotechnology: Techniques and applications / edited by Weilie Zhou and Zhong Lin Wang*. Springer, New York and London, 2007. ISBN 9780387333250.

[202] LOUIS de BROGLIE. Waves and quanta. *Nature*, 112(2815):540, 1923. doi:10.1038/112540a0.

[203] Adeline Buffet, André Rothkirch, Ralph Döhrmann, Volker Körstgens, Mottakin M. Abul Kashem, Jan Perlich, Gerd Herzog, Matthias Schwartzkopf, Rainer Gehrke, Peter Müller-Buschbaum, and Stephan V. Roth. P03, the microfocus and nanofocus x-ray scattering (minaxs) beamline of the petra iii storage ring: the microfocus endstation. *Journal of synchrotron radiation*, 19(Pt 4):647–653, 2012. doi:10.1107/S0909049512016895.

[204] Julian A. Steele, Eduardo Solano, David Hardy, Damara Dayton, Dylan Ladd, Keith White, Peng Chen, Jingwei Hou, Haowei Huang, Rafikul Ali Saha, Lianzhou Wang, Feng Gao, Johan Hofkens, Maarten B. J. Roeffaers, Dmitry Chernyshov, and Michael F. Toney. How to giwaxs: Grazing incidence wide angle x–ray scattering applied to metal halide perovskite thin films. *Advanced Energy Materials*, 13(27), 2023. ISSN 16146832. doi:10.1002/aenm.202300760.

[205] Li-Qiang Xie, Liang Chen, Zi-Ang Nan, Hai-Xin Lin, Tan Wang, Dong-Ping Zhan, Jia-Wei Yan, Bing-Wei Mao, and Zhong-Qun Tian. Understanding the cubic phase stabilization and crystallization kinetics in mixed cations and halides perovskite single crystals. *Journal of the American Chemical Society*, 139(9):3320–3323, 2017. ISSN 0002-7863. doi:10.1021/jacs.6b12432.

[206] Y. Shigesato, R. Koshi-ishi, T. Kawashima, and J. Ohsako. Early stages of ito deposition on glass or polymer substrates. *Vacuum*, 59(2-3):614–621, 2000. ISSN 0042207X. doi:10.1016/S0042-207X(00)00324-9.

[207] Stephen Seltzer. Tables of x-ray mass attenuation coefficients and mass energy-absorption coefficients, nist standard reference database 126.

[208] Johannes Schlipf, Pablo Docampo, Christoph J. Schaffer, Volker Körstgens, Lorenz Bießmann, Fabian Hanusch, Nadja Giesbrecht, Sigrid Bernstorff, Thomas Bein, and Peter Müller-Buschbaum. A closer look into two-step perovskite conversion with x-ray scattering. *The journal of physical chemistry letters*, 6(7):1265–1269, 2015. doi:10.1021/acs.jpclett.5b00329.

[209] Gerd Wedler. *Lehrbuch der physikalischen Chemie*. VCH Verlagsgesellschaft, Weinheim, 2., bearb. und erw. aufl. edition, 1985. ISBN 3527258809.

[210] J. Tauc. Optical properties and electronic structure of amorphous ge and si. *Materials Research Bulletin*, 3(1):37–46, 1968. ISSN 00255408. doi:10.1016/0025-5408(68)90023-8.

[211] Franz Urbach. The long-wavelength edge of photographic sensitivity and of the electronic absorption of solids. *Physical Review*, 92(5):1324, 1953. ISSN 0031-899X. doi:10.1103/PhysRev.92.1324.

[212] Paul Pucknus. *Optimization of Perovskite Solar Cells for Space Application using Quantum Efficiency and I-V Measurements*. B.Sc. thesis, Technical University of Munich, 2022.

[213] Michael Saliba and Lioz Etgar. Current density mismatch in perovskite solar cells. *ACS Energy Letters*, 5(9):2886–2888, 2020. ISSN 2380-8195. doi:10.1021/acsenergylett.0c01642.

[214] Sandheep Ravishankar, Clara Aranda, Pablo P. Boix, Juan A. Anta, Juan Bisquert, and Germà Garcia-Belmonte. Effects of frequency dependence of the external quantum efficiency of perovskite solar cells. *The journal of physical chemistry letters*, 9(11):3099–3104, 2018. doi:10.1021/acs.jpclett.8b01245.

[215] Lennart K. Reb, Michael Böhmer, Benjamin Predeschly, Sebastian Grott, Christoph Dreißigacker, Jörg Drescher, Andreas Meyer, and Peter Müller-Buschbaum. An experiment for novel material thin-film solar cell characterization on sounding rocket flights. *The Review of scientific instruments*, 92(7):074501, 2021. doi:10.1063/5.0047346.

[216] Alexander Kallenbach. Atek flight requirements plan: V 1.5, 2019.

[217] Christian Spannfellner. *Development of pathfinder missions and instruments for the Pacific Ocean Neutrino Experiment*. Masterthesis, Technical University of Munich, 2020. URL https://www.ph.nat.tum.de/fileadmin/w00bya/cosmic-particles/Thesis/masterthesis_final_christian_spannfellner.pdf.

[218] Immacolata Carmen Rea. *The Pacific Ocean Neutrino Experiment: feasibility study for a new Neutrino Telescope at Cascadia Basin, NE Pacific Ocean*. Universitätsbibliothek der TU München, München, 2021.

[219] Henry J. Snaith, Antonio Abate, James M. Ball, Giles E. Eperon, Tomas Leijtens, Nakita K. Noel, Samuel D. Stranks, Jacob Tse-Wei Wang, Konrad Wojciechowski, and Wei Zhang. Anomalous hysteresis in perovskite solar cells. *The journal of physical chemistry letters*, 5(9):1511–1515, 2014. doi:10.1021/jz500113x.

[220] Lennart K. Reb, Michael Böhmer, Benjamin Predeschly, Lukas V. Spanier, Christoph Dreißigacker, Andreas Meyer, and Peter Müller-Buschbaum. Attitude determination in space with ambient light sensors using machine learning for solar cell characterization. *Solar RRL*, 6(11):2200537, 2022. ISSN 2367-198X. doi:10.1002/solr.202200537.

[221] Rohm Co., Ltd. Datasheet. digital 16bit serial output type ambient light sensor ic. URL https://www.mouser.com/datasheet/2/348/bh1750fvi-e-186247.pdf.

[222] Benjamin Braun and Jochen Barf. Image processing based horizon sensor for estimating the orientation of sounding rockets, launch vehicles and spacecraft. *CEAS Space J*, 15(3):509–533, 2022. doi:10.1007/s12567-022-00461-0.

[223] Guido VanRossum and Fred L. Drake. *The Python language reference*, volume / Guido van Rossum; Fred L. Drake [ed.] ; Pt. 2 of *Python documentation manual*. Python Software Foundation and SoHo Books, [Hampton, NH] and [Redwood City, Calif.], release 3.0.1 [repr.] edition, 2010. ISBN 1441412697.

[224] Charles R. Harris, K. Jarrod Millman, Stéfan J. van der Walt, Ralf Gommers, Pauli Virtanen, David Cournapeau, Eric Wieser, Julian Taylor, Sebastian Berg, Nathaniel J. Smith, Robert Kern, Matti Picus, Stephan Hoyer, Marten H. van Kerkwijk, Matthew Brett, Allan Haldane, Jaime Fernández Del Río, Mark Wiebe, Pearu Peterson, Pierre Gérard-Marchant, Kevin Sheppard, Tyler Reddy, Warren Weckesser, Hameer Abbasi, Christoph Gohlke, and Travis E. Oliphant. Array programming with numpy. *Nature*, 585(7825): 357–362, 2020. doi:10.1038/s41586-020-2649-2.

[225] Matthew Newville, Till Stensitzki, Daniel B. Allen, and Antonino Ingargiola. Lmfit: Non-linear least-square minimization and curve-fitting for python, 2014.

[226] Pauli Virtanen, Ralf Gommers, Travis E. Oliphant, Matt Haberland, Tyler Reddy, David Cournapeau, Evgeni Burovski, Pearu Peterson, Warren Weckesser, Jonathan Bright, Stéfan J. van der Walt, Matthew Brett, Joshua Wilson, K. Jarrod Millman, Nikolay Mayorov, Andrew R. J. Nelson, Eric Jones, Robert Kern, Eric Larson, C. J. Carey, İlhan Polat, Yu Feng, Eric W. Moore, Jake VanderPlas, Denis Laxalde, Josef Perktold, Robert Cimrman, Ian Henriksen, E. A. Quintero, Charles R. Harris, Anne M. Archibald, Antônio H. Ribeiro, Fabian Pedregosa, and Paul van Mulbregt. Scipy 1.0: fundamental algorithms for scientific computing in python. *Nature methods*, 17(3):261–272, 2020. doi:10.1038/s41592-019-0686-2.

[227] Jeff Reback, jbrockmendel, Wes McKinney, Joris Van den Bossche, Matthew Roeschke, Tom Augspurger, Simon Hawkins, Phillip Cloud, gfyoung, Patrick Hoefler, Sinhrks, Adam Klein, Terji Petersen, Jeff Tratner, Chang She, William Ayd, Richard Shadrach, Shahar Naveh, Marc Garcia, JHM Darbyshire, Jeremy Schendel, Torsten Wörtwein, Andy Hayden, Daniel Saxton, Marco Edward Gorelli, Fangchen Li, Matthew Zeitlin, Vytautas Jancauskas, Ali McMaster, and Thomas Li. pandas-dev/pandas: Pandas 1.4.4, 2022.

[228] John D. Hunter. Matplotlib: A 2d graphics environment. *Computing in Science & Engineering*, 9(3):90–95, 2007. ISSN 1521-9615. doi:10.1109/MCSE.2007.55.

[229] Jonathan Goodman and Jonathan Weare. Ensemble samplers with affine invariance. *Communications in Applied Mathematics and Computational Science*, 5(1):65–80, 2010. ISSN 1559-3940. doi:10.2140/camcos.2010.5.65.

[230] Daniel Foreman-Mackey, David W. Hogg, Dustin Lang, and Jonathan Goodman. emcee : The mcmc hammer. *Publications of the Astronomical Society of the Pacific*, 125(925): 306–312, 2013. ISSN 00046280. doi:10.1086/670067.

[231] Brian Olson, Irina Hashmi, Kevin Molloy, and Amarda Shehu. Basin hopping as a general and versatile optimization framework for the characterization of biological macromolecules. *Advances in Artificial Intelligence*, 2012:1–19, 2012. ISSN 1687-7470. doi:10.1155/2012/674832.

[232] Simo Särkkä. *Bayesian Filtering and Smoothing*. Cambridge University Press, 2014. ISBN 9781107030657. doi:10.1017/CBO9781139344203.

[233] Lennart K. Reb, Michael Böhmer, Benjamin Predeschly, Sebastian Grott, Christian L. Weindl, Goran I. Ivandekic, Renjun Guo, Lukas V. Spanier, Matthias Schwartzkopf, Andrei Chumakov, Christoph Dreißigacker, Roman Gernhäuser, Stephan V. Roth, Andreas Meyer, and Peter Müller-Buschbaum. Space– and post–flight characterizations of perovskite and organic solar cells. *Solar RRL*, 7(9), 2023. ISSN 2367-198X. doi:10.1002/solr.202300043.

[234] Nutifafa Y. Doumon, Mikhail V. Dryzhov, Félix V. Houard, Vincent M. Le Corre, Azadeh Rahimi Chatri, Panagiotis Christodoulis, and L. Jan Anton Koster. Photostability of fullerene and non-fullerene polymer solar cells: The role of the acceptor. *ACS applied materials & interfaces*, 11(8):8310–8318, 2019. doi:10.1021/acsami.8b20493.

[235] Philip Calado, Andrew M. Telford, Daniel Bryant, Xiaoe Li, Jenny Nelson, Brian C. O'Regan, and Piers R. F. Barnes. Evidence for ion migration in hybrid perovskite solar cells with minimal hysteresis. *Nature Communications*, 7(1):13831, 2016. ISSN 2041-1723. doi:10.1038/ncomms13831.

[236] Antonio Abate, Tomas Leijtens, Sandeep Pathak, Joël Teuscher, Roberto Avolio, Maria E. Errico, James Kirkpatrik, James M. Ball, Pablo Docampo, Ian McPherson, and Henry J. Snaith. Lithium salts as "redox active" p-type dopants for organic semiconductors and their impact in solid-state dye-sensitized solar cells. *Physical chemistry chemical physics : PCCP*, 15(7):2572–2579, 2013. doi:10.1039/C2CP44397J.

[237] C. R. Brown, G. E. Eperon, V. R. Whiteside, and I. R. Sellers. Potential of high-stability perovskite solar cells for low-intensity–low-temperature (lilt) outer planetary space missions. *ACS Applied Energy Materials*, 2(1):814–821, 2019. ISSN 2574-0962. doi:10.1021/acsaem.8b01882.

[238] Surampudi S., Blosiu J., Stella P., Elliott. J, Castillo J., Yi. T., Lyons J, . M.Piszczor, J.McNatt, C.Taylor, E.Gaddy, S.Liu, E.Plichta, and C.Iannello. Solar power technologies for future planetary science missions, jpl d-101316. 2017. URL https://solarsystem.nasa.gov/resources/548/solar-power-technologies-for-future-planetary-science-missions/.

[239] Marko Jošt, Benjamin Lipovšek, Boštjan Glažar, Amran Al-Ashouri, Kristijan Brecl, Gašper Matič, Artiom Magomedov, Vytautas Getautis, Marko Topič, and Steve Albrecht. Perovskite solar cells go outdoors: Field testing and temperature effects on energy yield. *Advanced Energy Materials*, 10(25):2000454, 2020. ISSN 16146832. doi:10.1002/aenm.202000454.

[240] E. A. Katz, D. Faiman, S. M. Tuladhar, J. M. Kroon, M. M. Wienk, T. Fromherz, F. Padinger, C. J. Brabec, and N. S. Sariciftci. Temperature dependence for the photovoltaic device parameters of polymer-fullerene solar cells under operating conditions. *Journal of Applied Physics*, 90(10):5343–5350, 2001. ISSN 0021-8979. doi:10.1063/1.1412270.

[241] Yongju Park, Seunguk Noh, Donggu Lee, Jun Young Kim, and Changhee Lee. Temperature and light intensity dependence of polymer solar cells with moo3 and pedot:pss as a buffer layer. *Journal of the Korean Physical Society*, 59(2):362–366, 2011. ISSN 0374-4884. doi:10.3938/jkps.59.362.

[242] N. Bristow and J. Kettle. Outdoor performance of organic photovoltaics: Diurnal analysis, dependence on temperature, irradiance, and degradation. *Journal of Renewable and Sustainable Energy*, 7(1), 2015. doi:10.1063/1.4906915.

[243] Liuxing Guo, Yi Chen, Ge Wang, Yiqiu Xia, Dongxu Luo, Zihan Zhu, Chen Wang, Wei Dong, and Shanpeng Wen. Efficient perovskite solar cells achieved using the 2-methoxyethanol additive: Morphology and composition control of intermediate film. *ACS Applied Energy Materials*, 4(3):2681–2689, 2021. ISSN 2574-0962. doi:10.1021/acsaem.0c03227.

[244] Sebastian Svanström, T. Jesper Jacobsson, Gerrit Boschloo, Erik M. J. Johansson, Håkan Rensmo, and Ute B. Cappel. Degradation mechanism of silver metal deposited on lead halide perovskites. *ACS applied materials & interfaces*, 12(6):7212–7221, 2020. doi:10.1021/acsami.9b20315.

[245] Sebastian Grott, Amir Kotobi, Lennart K. Reb, Christian L. Weindl, Renjun Guo, Shanshan Yin, Kerstin S. Wienhold, Wei Chen, Tayebeh Ameri, Matthias Schwartzkopf, Stephan V. Roth, and Peter Müller-Buschbaum. Solvent tuning of the active layer morphology of non–fullerene based organic solar cells. *Solar RRL*, 6(6):2270065, 2022. ISSN 2367-198X. doi:10.1002/solr.202270065.

[246] Christoph J. Schaffer, Claudia M. Palumbiny, Martin A. Niedermeier, Christian Burger, Gonzalo Santoro, Stephan V. Roth, and Peter Müller-Buschbaum. Morphological degradation in low bandgap polymer solar cells - an in operando study. *Advanced Energy Materials*, 6(19):1600712, 2016. ISSN 16146832. doi:10.1002/aenm.201600712.

[247] Dominik M. Schwaiger, Wiebke Lohstroh, and Peter Müller-Buschbaum. The influence of the blend ratio, solvent additive, and post-production treatment on the polymer dynamics in ptb7:pcbm blend films. *Macromolecules*, 54(13):6534–6542, 2021. ISSN 0024-9297. doi:10.1021/acs.macromol.1c00313.

[248] Zhengguo Xiao, Qingfeng Dong, Cheng Bi, Yuchuan Shao, Yongbo Yuan, and Jinsong Huang. Solvent annealing of perovskite-induced crystal growth for photovoltaic-device efficiency enhancement. *Advanced materials (Deerfield Beach, Fla.)*, 26(37):6503–6509, 2014. doi:10.1002/adma.201401685.

[249] Markus W. Heindl, Tim Kodalle, Natalie Fehn, Lennart K. Reb, Shangpu Liu, Constantin Harder, Maged Abdelsamie, Lissa Eyre, Ian D. Sharp, Stephan V. Roth, Peter Müller-Buschbaum, Aras Kartouzian, Carolin M. Sutter-Fella, and Felix Deschler. Strong induced circular dichroism in a hybrid lead–halide semiconductor using chiral amino acids for crystallite surface functionalization. *Advanced Optical Materials*, 10(14), 2022. ISSN 2195-1071. doi:10.1002/adom.202200204.

[250] Suo Tu, Ting Tian, Anna Lena Oechsle, Shanshan Yin, Xinyu Jiang, Wei Cao, Nian Li, Manuel A. Scheel, Lennart K. Reb, Shujin Hou, Aliaksandr S. Bandarenka, Matthias Schwartzkopf, Stephan V. Roth, and Peter Müller-Buschbaum. Improvement of the thermoelectric properties of pedot:pss films via dmso addition and dmso/salt post-treatment resolved from a fundamental view. *Chemical Engineering Journal*, 429:132295, 2022. ISSN 13858947. doi:10.1016/j.cej.2021.132295.

[251] Maximilian T. Sirtl, Melina Armer, Lennart K. Reb, Rik Hooijer, Patrick Dörflinger, Manuel A. Scheel, Kristofer Tvingstedt, Philipp Rieder, Nadja Glück, Pallavi Pandit, Stephan V. Roth, Peter Müller-Buschbaum, Vladimir Dyakonov, and Thomas Bein. Optoelectronic properties of cs 2 agbibr 6 thin films: The influence of precursor stoichiometry. *ACS Applied Energy Materials*, 3(12):11597–11609, 2020. ISSN 2574-0962. doi:10.1021/acsaem.0c01308.

[252] Renjun Guo, Ali Buyruk, Xinyu Jiang, Wei Chen, Lennart K. Reb, Manuel A. Scheel, Tayebeh Ameri, and Peter Müller-Buschbaum. Tailoring the orientation of perovskite crystals via adding two-dimensional polymorphs for perovskite solar cells. *Journal of Physics: Energy*, 2(3):034005, 2020. doi:10.1088/2515-7655/ab90d0.

[253] Lennart Reb, Juan A. Fernández-Ontiveros, M. Almudena Prieto, and Klaus Dolag. A lower limit to the accretion disc radius in the low-luminosity agnngc 1052 derived from high-angular resolution data. *Monthly Notices of the Royal Astronomical Society: Letters*, 478(1):L122–L126, 2018. ISSN 1745-3925. doi:10.1093/mnrasl/sly079.

List of publications

Publications related to the dissertation

- Lennart K. Reb, Michael Böhmer, Benjamin Predeschly, Sebastian Grott, Christian L. Weindl, Goran I. Ivandekic, Renjun Guo, Lukas V. Spanier, Matthias Schwartzkopf, Andrei Chumakov, Christoph Dreißigacker, Roman Gernhäuser, Stephan V. Roth, Andreas Meyer, and Peter Müller-Buschbaum, *Space-and Post-Flight Characterizations of Perovskite and Organic Solar Cells*, *Solar RRL*, 7 (9), 2300043, 2023, doi:10.1002/solr.202300043 [233]
- Lennart K. Reb, Michael Böhmer, Benjamin Predeschly, Lukas V. Spanier, Christoph Dreißigacker, Andreas Meyer, and Peter Müller-Buschbaum, *Attitude determination in space with ambient light sensors using machine learning for solar cell characterization*, *Solar RRL*, 6 (11), 2200537, 2022, doi:10.1002/solr.202200537 [220]
- Lennart K. Reb, Michael Böhmer, Benjamin Predeschly, Sebastian Grott, Christoph Dreißigacker, Jörg Drescher, Andreas Meyer, and Peter Müller-Buschbaum, *An experiment for novel material thin-film solar cell characterization on sounding rocket flights*, *Review of Scientific Instruments*, 92(7), 074501, 2021, doi:10.1063/5.0047346 [215]
- Lennart K. Reb, Michael Böhmer, Benjamin Predeschly, Sebastian Grott, Christian L. Weindl, Goran I. Ivandekic, Renjun Guo, Christoph Dreißigacker, Roman Gernhäuser, Andreas Meyer, and Peter Müller-Buschbaum, *Perovskite and organic solar cells on a rocket flight*, *Joule*, 4 (9), 1880–1892, 2020, doi:10.1016/j.joule.2020.07.004 [189]

Further publications

- Manuel A. Reus[1], Lennart K. Reb[1], David P. Kosbahn, Stephan V. Roth, and Peter Müller-Buschbaum, *INSIGHT: In situ GIXS heuristic tool for the efficient reduction of grazing-incidence scattering data*, in preparation
- Renjun Guo, Qiu Xiong, Aleksander Ulatowski, Saisai Li, Zijin Ding, Tianxiao Xiao, Suzhe Liang, Julian E. Heger, Tianfu Guan, Xinyu Jiang, Kun Sun, Lennart K. Reb, Manuel A. Reus, Andrei Chumakov, Matthias Schwartzkopf, Minjian Yuan, Yi Hou, Stephan V. Roth, Laura M. Herz, Peng Gao, and Peter Müller-Buschbaum, *Trace water in lead iodide limits the performance of perovskite solar cells*, submitted

[1]Equal contribution.

- Markus W. Heindl, Tim Kodalle, Natalie Fehn, Lennart K. Reb, Shangpu Liu, Constantin Harder, Maged Abdelsamie, Lissa Eyre, Ian D. Sharp, Stephan V. Roth, Peter Müller-Buschbaum, Aras Kartouzian, Carolin M. Sutter-Fella, and Felix Deschler, *Strong Induced Circular Dichroism in a Hybrid Lead-Halide Semiconductor Using Chiral Amino Acids for Crystallite Surface Functionalization*, *Advanced Optical Materials* 10 (14), 2200204, 2022, doi:10.1002/adom.202200204 [249]
- Sebastian Grott, Amir Kotobi, Lennart K. Reb, Christian L. Weindl, Renjun Guo, Shanshan Yin, Kerstin S. Wienhold, Wei Chen, Tayebeh Ameri, Matthias Schwartzkopf, Stephan V. Roth, and Peter Müller-Buschbaum, *Solvent Tuning of the Active Layer Morphology of Non-Fullerene Based Organic Solar Cells*, *Solar RRL* 6 (6), 2101084, 2022, doi:10.1002/solr.202101084 [245]
- Manuel A. Reus, Lennart K. Reb, Alexander F. Weinzierl, Christian L. Weindl, Renjun Guo, Tianxiao Xiao, Matthias Schwartzkopf, Andrei Chumakov, Stephan V. Roth, and Peter Müller-Buschbaum, *Time–resolved orientation and phase analysis of lead halide perovskite film annealing probed by in situ giwaxs*, *Advanced Optical Materials*, 10 (14), 2102722, 2022, doi:10.1002/adom.202102722 [123]
- Suo Tu, Ting Tian, Anna Lena Oechsle, Shanshan Yin, Xinyu Jiang, Wei Cao, Nian Li, Manuel A. Scheel, Lennart K. Reb, Shujin Hou, Aliaksandr S. Bandarenka, Matthias Schwartzkopf, Stephan V. Roth, and Peter Müller-Buschbaum, *Improvement of the thermoelectric properties of PEDOT: PSS films via DMSO addition and DMSO/salt post-treatment resolved from a fundamental view*, *Chemical Engineering Journal*, 429, 132295, 2022, doi:10.1016/j.cej.2021.132295 [250]
- Renjun Guo, Dan Han, Wei Chen, Linjie Dai, Kangyu Ji, Qiu Xiong, Saisai Li, Lennart K. Reb, Manuel A. Scheel, Shambhavi Pratap, Nian Li, Shanshan Yin, Tianxiao Xiao, Suzhe Liang, Anna Lena Oechsle, Christian L. Weindl, Matthias Schwartzkopf, Hubert Ebert,Peng Gao, Kai Wang, Mingjian Yuan, Neil C. Greenham, Samuel D. Stranks, Stephan V. Roth, Richard H. Friend, and Peter Müller-Buschbaum, *Degradation mechanisms of perovskite solar cells under vacuum and one atmosphere of nitrogen*, *Nature Energy*, 6 (10), 977–986, 2021, doi:10.1038/s41560-021-00912-8 [43]
- Maximilian T. Sirtl, Melina Armer, Lennart K. Reb, Rik Hooijer, Patrick Dörflinger, Manuel A. Scheel, Kristofer Tvingstedt, Philipp Rieder, Nadja Glück, Pallavi Pandit, Stephan V. Roth, Peter Müller-Buschbaum, Vladimir Dyakonov, and Thomas Bein, *Optoelectronic Properties of $Cs_2AgBiBr_6$ Thin Films: The Influence of Precursor Stoichiometry*, *ACS applied energy materials*, 3 (12), 11597-11609, 2020, doi:10.1021/acsaem.0c01308 [251]
- Renjun Guo, Ali Buyruk, Xinyu Jiang, Wei Chen, Lennart K. Reb, Manuel A. Scheel, Tayebeh Ameri, and Peter Müller-Buschbaum, *Tailoring the orientation of perovskite crystals via adding two-dimensional polymorphs for perovskite solar cells*, *Journal of Physics: Energy*, 2 (3), 034005, 2020, doi:10.1088/2515-7655/ab90d0 [252]

- Lennart Reb, Juan A. Fernández-Ontiveros, M. Almudena Prieto, and Klaus Dolag, *A lower limit to the accretion disc radius in the low-luminosity AGN NGC 1052 derived from high-angular resolution data*, Monthly Notices of the Royal Astronomical Society, 478 (1), 122-126, 2018, doi:10.1093/mnrasl/sly079 [253]

Releases and awards related to this work

- Press release of the Technical University of Munich (TUM), *New solar cells for space – Perovskite and organic solar cells prove successful on a rocket flight in space*, https://www.tum.de/en/news-and-events/all-news/press-releases/details/36193-1, 13 August 2020
- Press release of the German Aerospace Center (DLR), *New solar cells for space*, https://www.dlr.de/en/latest/news/2020/03/20200813_new-solar-cells-for-space, 13 August 2020
- Press release of the Deutsches Elektronen-Synchrotron DESY *Atmosphere has strong influence on stability of novel solar cells*, https://www.desy.de/aktuelles/news_suche/index_ger.html?openDirectAnchor=2178&two_columns=1 , 19 October 2021
- Episode *Solar cells in space* in the podcast *Your friendly physicist and other Nerds* by Dr. Lucas Kreuzer, https://open.spotify.com/episode/0zy5BUmKt2sL37eI1NZU6x?si=64cc027f18c14686, 2 May 2023
- Best Presentation Award 2021 (2nd place), in recognition of the presentation "Emerging Thin-Film Solar Cell Technologies Reaching Space", 11th Colloquium of the Munich School of Engineering, Garching (Germany), 28 – 29 July 2021
- Best Poster Award 2022 (2nd place), in recognition of the poster "Solar incidence determination using ambient light sensors and a machine learning approach for space solar cell characterization", NanoGe: PVSPACE, Rome (Italy), 21 – 22 June 2022
- Best Poster Award 2023 (1st place), in recognition of the poster "Overview of the First Spaceflight Experiment of Perovskite and Organic Solar Cells", NanoGe: PVSPACE, Rome (Italy), 5 – 7 July 2022

Scientific reports

- L. K. Reb, L. V. Spanier, M. Böhmer, C. Dreißigacker, R. Gernhäuser, A. Meyer, and P. Müller-Buschbaum, *Organic and hybrid solar cells in space – the experiment*, Lehrstuhl für Funktionelle Materialien, Annual Report, 2022
- L. K. Reb, M. A. Reus, C. Rosemann, M. Schwartzkopf, S. V. Roth, and P. Müller-Buschbaum, *INSIGHT – methodology of the scattering data analysis tool*, Lehrstuhl für Funktionelle Materialien, Annual Report, 2021

- L. K. Reb, M. Böhmer, C. Dreißigacker, R. Gernhäuser, A. Meyer, and P. Müller-Buschbaum, *A further step to space — perovskite and organic solar cells on a rocket flight*, Lehrstuhl für Funktionelle Materialien, Annual Report, 2020
- L. K. Reb, M. A. Scheel, R. Guo, and P. Müller-Buschbaum, *Perovskite: effects of cesium-incorporation investigated with GIWAXS*, Lehrstuhl für Funktionelle Materialien, Annual Report, 2019
- L. Reb, M. Schwartzkopf, S. V. Roth, and P. Müller-Buschbaum, *In-situ GISAXS investigation of gold sputter deposition on perovskite films*, Lehrstuhl für Funktionelle Materialien, Annual Report, 2018

Conference talks

- L. K. Reb, M. Böhmer, B. Predeschly, S. Grott, Lukas V. Spanier, C. L. Weindl, G. I. Ivandekic, R. Guo, C. Dreißigacker, M. Schwartzkopf, A. Chumakov, R. Gernhäuser, S. V. Roth, A. Meyer, P. Müller-Buschbaum, *Post-Flight Analysis of Space-Probed Perovskite and Organic Solar Cells with Means of Grazing-Incidence X-ray-Scattering*, DPG Jahrestagung, Dresden, 27 – 31 March 2023
- L. K. Reb, A. Vitaloni, H. T. Myint, C. G. Lindenmeir, C M. Reus, P. Müller-Buschbaum, *Testing Next-Generation Thin-Film Solar Cells in Space*, ATUMS: Annual Meeting, Bernried, 6 – 11 November 2022
- L. K. Reb, M. Böhmer, B. Predeschly, S. Grott, C. L. Weindl, G. I. Ivandekic, R. Guo, C. Dreißigacker, Jörg Drescher, R. Gernhäuser, A. Meyer, P. Müller-Buschbaum, *Perovskite and Organic Solar Cells Generate Power in Space*, DPG Jahrestagung, Regensburg, 4 – 9 September 2022
- L. K. Reb, M. Böhmer, B. Predeschly, S. Grott, L. V. Spanier, C. L. Weindl, G. I. Ivandekic, R. Guo, C. Dreißigacker, Jörg Drescher, R. Gernhäuser, A. Meyer, P. Müller-Buschbaum, *Characterization of Perovskite and Organic Solar Cells In and Post Spaceflight*, ACS Fall Meeting (virtual), 18 – 22 August 2022
- L. K. Reb, M. Böhmer, B. Predeschly, S. Grott, C. L. Weindl, G. I. Ivandekic, R. Guo, C. Dreißigacker, Jörg Drescher, R. Gernhäuser, A. Meyer, P. Müller-Buschbaum, *Perovskite and Organic Solar Cells Generate Power in Space*, DPG Jahrestagung (virtual), Regensburg, 27 September – 1 October 2021
- L. K. Reb, M. Böhmer, B. Predeschly, S. Grott, C. L. Weindl, G. I. Ivandekic, R. Guo, C. Dreißigacker, Jörg Drescher, R. Gernhäuser, A. Meyer, P. Müller-Buschbaum, *Emerging Thin-Film Solar Cell Technologies Reaching Space*, 11th MSE Energy Colloquium (virtual), Garching, 28 – 29 July 2021
- L. K. Reb, M. Böhmer, B. Predeschly, S. Grott, C. L. Weindl, G. I. Ivandekic, R. Guo, C. Dreißigacker, Jörg Drescher, R. Gernhäuser, A. Meyer, P. Müller-Buschbaum, *Perovskite Solar Cells for Space Application*, MRS Spring Meeting (virtual), 17 – 23 April 2021

- L. K. Reb, M. Böhmer, B. Predeschly, S. Grott, C. L. Weindl, G. I. Ivandekic, R. Guo, C. Dreißigacker, Jörg Drescher, R. Gernhäuser, A. Meyer, P. Müller-Buschbaum, *Characterizing Organic Solar Cells in Space*, ACS Spring Meeting (virtual), 5 April – 1 May 2021
- B.-J. Niebuur, L. Reb, D. Schwaiger, *Raman spectroscopy*, Polymer Physics Summer School, Obertauern, Austria, 12 — 15 Jun 2018

Conference poster presentations

- L. K. Reb, M. Böhmer, B. Predeschly, S. Grott, L. V. Spanier, C. L. Weindl, G. I. Ivandekic, R. Guo, C. Dreißigacker,J. Drescher, R. Gernhäuser, A. Meyer, P. Müller-Buschbaum, *Overview of the First Spaceflight Experiment of Perovskite and Organic Solar Cells*, NanoGe: PVSPACE, Rome (Italy), 5- – 8 July 2023
- L. K. Reb, M. A. Reus, M. Schwartzkopf, C. Rosemann S. V. Roth, P. Müller-Buschbaum, *INSIGHT – A new GIXS analysis software tool*, 21st SAXS/WAXS/GISAXS satellite workshop of DESY photon science users' meeting (virtual), 21 – 28 January 2022
- L. K. Reb, M. A. Reus, M. Schwartzkopf, C. Rosemann S. V. Roth, P. Müller-Buschbaum, *The in-situ GIXS heuristic tool*, DKG Spring Meeting (virtual), 14 – 17 March 2022
- L. K. Reb, M. Böhmer, B. Predeschly, S. Grott, C. L. Weindl, G. I. Ivandekic, R. Guo, L. V. Spanier, C. Dreißigacker,J. Drescher, R. Gernhäuser, A. Meyer, P. Müller-Buschbaum, *A Space Experiment for Novel Solar Cell Technologies*, MEP Colloquium, 28 July 2022
- L. K. Reb, M. Böhmer, B. Predeschly, S. Grott, C. L. Weindl, G. I. Ivandekic, R. Guo, L. V. Spanier, C. Dreißigacker,J. Drescher, R. Gernhäuser, A. Meyer, P. Müller-Buschbaum, *Solar incidence determination using ambient light sensors and a machine learning approach for space solar cell characterization*, NanoGe: PVSPACE, Rome (Italy, virtual), 21 – 22 June 2022
- L. K. Reb, M. A. Reus, M. Schwartzkopf, S. V. Roth, P. Müller-Buschbaum, *GIWAXS In-Situ Analysis of MAPI Perovskite Annealing*, DESY Photon Science Users' Meeting (virtual), 24 – 28 January 2021
- L. K. Reb, M. Böhmer, B. Predeschly, S. Grott, C. L. Weindl, G. I. Ivandekic, R. Guo, C. Dreißigacker, Jörg Drescher, R. Gernhäuser, A. Meyer, P. Müller-Buschbaum, *A Further Step Towards Space: Perovskite and Organic Solar Cells on a Rocket Flight*, DPG Spring Meeting (virtual), 15 – 26 March 2021
- L. K. Reb, A. Vitaloni, M. Reus, P. Müller-Buschbaum, *Tuning Composition and Morphology of Printed Perovskite Films for Photovoltaic Applications*, ATUMS: Annual Meeting (virtual), 12 November 2021
- L. K. Reb, M. A. Reus, M. Schwartzkopf, C. Rosemann, S. V. Roth, P. Müller-Buschbaum, *The In-Situ GIWAXS Heuristic Tool for Efficient Reduction of High-Quality Big Data*, MLZ User Meeting (virtual), 7 – 8 December 2021

- L. K. Reb, M. Böhmer, B. Predeschly, S. Grott, C. L. Weindl, G. I. Ivandekic, R. Guo, C. Dreißigacker, R. Gernhäuser, A. Meyer, P. Müller-Buschbaum, *Perovskite and Organic Solar Cells on a Rocket Flight*, ATUMS: Annual Meeting (virtual), 09 November 2020
- L. K. Reb, M. Böhmer, B. Predeschly, S. Grott, C. L. Weindl, G. I. Ivandekic, R. Guo, C. Dreißigacker, R. Gernhäuser, A. Meyer, P. Müller-Buschbaum, *Perovskite and Organic Solar Cells on a Rocket Flight*, 9th SolTech Conference (virtual), 05 – 06 October 2020
- L. K. Reb, W. Chen, S. J. Schaper, X. Jiang, M. Schwartzkopf, P. Pandit, M. Gensch, J. Drewes, O. Polonskyi, T. Strunskus, F. Faupel, S. V. Roth, P. Müller-Buschbaum, *Following the Interface Formation During Sputter Deposition on Perovskite Films*, MLZ User Meeting 2020 (virtual), 08 – 09 December 2020
- L. Reb, W. Chen, S. Schaper, X. Jiang, M. Schwartzkopf, P., M. Gensch, J. Drewes, O. Polonskyi, T. Strunskus, F. Faupel, S. V. Roth, P. Müller Buschbaum, *The 2-step deposition method of mixed perovskites as a route to highly tuneable optoelectronic properties*, DPG-Frühjahrstagung, Regensburg, 31 Mar – 05 Apr 2019
- L. Reb, P. Müller-Buschbaum, *Tailoring optoelectronic properties of mixed halide perovskites via the versatile 2-Step deposition method*, 4th internal biennial science meeting of the MLZ, Grainau, 24 -– 27 Jun 2019
- L. Reb, P. Müller-Buschbaum, *Challenging Silicon: Perovskite Based Solar Cells*, 4th German SNI Conference, Garching, 17 – 19 Sep 2018

Acknowledgements

This thesis represents more than just a report of the hard work at the Chair of Functional Materials, also known as E13 that I went through in the last years. All the amount of work would not have been possible without the unwavering support I received from numerous individuals, both on a scientific and personal level. I want to thank those people and for all the guidance that fostered my personal development to make me a better scientist.

I am profoundly indebted to Peter Müller-Buschbaum for his unwavering support, guidance, and belief in my abilities to cope with the challenges of pursuing such a complex project. I am still marveling at how you could manage to be permanently available for all my questions and doubts despite your very busy schedule and still fill hours with explanations – no matter whether scientifically or strategically. The freedom I was granted allowed me to pursue my ideas and passion, such as the INSIGHT project that Manuel Reus and I pursued during endless homeworking coding sessions during Covid.

I am especially grateful to the colleagues and friends who were there when my time started at E13 and for turning the following years into a wonderful time. With Julian Heger, Xinyu Jiang, and Shanshan Yin, it all began in the big office, and till the end, we shared the office to become best office mates. Happy moments during countless days and nights will remain in my memory, in the Coffice with Dominik Schwaiger, Christina Geiger, Renjun Guo, Anna Lena Oechsle, going together through all the intense and fun times, as well as Manuel Reus (INSIGHT Jedi Master) and Christian Weindl (competent Pizzaiolo).

A special appreciation goes to all the Perovsguys, the Weird-Flex People, the Printing Crew, the INSIGHT Jedis, the Hamburg Guys, and the Glovebox Chiefs, who have made this a great time, as well as Apostolos Vagias, Yusuf Bulut, Suo Tu, Peixi Wang, Zhuijun Xu, Huaying Zhong, Yuxin Liang, Suzhe Liang, Zerui Li, Yanan Li, Kun Sun, Kerstin Wienhold, Xiongzhuo Jiang, Tianfu Guan, Dominik Petz, Pablo Alvarez Herrera, Fabian Apfelbeck, Christopher Everett, Tobias Hölderle, Linus Huber, Morgan Le Dü, Thien An Pham, Ivana Pivarnikova, Julija Reitenbach, Lukas Spanier, Constantin Harder, Marc Gensch, with whom we had fun times and exciting discussions during numerous group activities, such as summer schools, conferences, beer garden, or just spontaneous late-work Pizza at the Black to Gold or from la Pergola. Unforgettable were especially the in-person conferences in the last years after Covid, cheers to the Quintet Grande and Power Napoleon and our Stammtisch. I also want to express my thanks to the old generation of colleagues, Johannes Schlipf, Shambhavi Pratap, Sebastian Grott, Lorenz Bießmann, Nitin Saxena, Simon Schaper, Nuri Hohn, Franziska Löhrer, Bart-Jan Niebuur, Florian Jung, Wei Chen, Tobias Widmann, Stephan H. Pröller, Jenny M. Lebert, Mihael Čorić,

and Oliver Filonik who relentlessly answered my numerous questions, tried to sharpen my focus to the important things, and their lightheartedness and spontaneity when having the one beer. I am thankful for the time spent with my mentor Volker Körstgens, an institution at E13. I will miss his unagitated sense of humor and dry comments regarding our music taste when we suddenly started playing loud music on Friday evenings in our office next to his. I would also like to express my appreciation for the future generation of colleagues, including Christoph Lindenmeir, Simon Wegener, Thomas Baier, Altantulga Buyan-Arivjikh, and David Kosbahn, who have injected fresh perspectives into our work. My gratitude extends to Christine Papadakis and her group, who have always dedicated their precious time to improving our science and all our laboratories.

Much of the work presented in this thesis has its foundation in the successful rocket experiment. None of this would have been achievable without Michael Böhmer and Benjamin Predeschly. Michael from the Central Technology Laboratory is a genuine expert in electronics. Retrospective, it felt like he produced all the electronics out of thin air. Benjamin, my first master's student, invested endless time and energy during the stressful project phase twisting his mind to make the parts fit each other. Without his workforce, it hadn't worked out. Michael, Benjamin, and I pushed beyond our limits. The teamwork was the perfect mix of performing and understanding – my gratitude for making such an awesome team! I am indebted to our workshop, in particular Reinhold Funer, who played a central role in manufacturing various parts for the project. His µm-precision work and educated eye could compensate for our lack of expertise in the technical drawings and I appreciate the hospitality during various hearty snacks. Many ideas would not have worked out without Sebastian Grott, who often helped me make the right choices during the project, using his penetrative way of finding the weak spots in concepts and always having a backup plan, especially during the campaign in Sweden. A very big thank goes to the numerous individuals who provided helping hands or a mental shoulder during the hot phases of solar cell manufacturing with the rocket flight ahead. I appreciate the work the Master students Goran Ivandekic and Christian Weindl put into manufacturing the organic solar cells. I also thank the other TUM workshops involved in manufacturing parts for the project, highlighting the Central Workshop in the Department of Physics, the Medicine Technics workshop, and the E15 workshop with greetings to Thomas Richter. Furthermore, I would like to thank the people in the background of the project, Roman Gernhäuser (invaluable input during the design phase), Christian Fruck (3D printer), Terry Weinmann (with his electronics treasure), Egon Lenker (professional soldering), and the crystal and material laboratory.

During the meetings and pretests in Cologne, the bench tests and environmental tests in Oberpfaffenhofen, and the campaign in Sweden, I got to know great people and rocket scientists from the DLR. A very big thanks to Andreas Meyer, Christoph Dreißigacker, and Jörg Drescher for an exciting collaboration. I am grateful to have met Raphael Keßler from DLR-MP, Jens Hauslage, and Christian Liemersdorf from DLR-ME with numerous philosophical discussions about life and science. I extend my gratitude to the MORABA team including Alexander Kallenbach (who accompanied our experiment through the project design phase), Jürgen Knof (late-access

comrade), Jochen Barf, Thaddäus Stromsky, Dorian Hargarten, Martin Huber, Martin Reinold, Frank Scheuerpflug, and Benjamin Braun.
I want to particularly thank our good soules Carola Kappauf Marion Waletzki for not only only doing an incredible job in ensuring the smooth operation of our group. Carola, thank you for your patience and guidance in navigating through numerous Reisekostenabrechnungsformulare. I am grateful for all the help provided by Anke Friebel and Sergei Vagin to maneuver through the qualification elements of graduate school.
Delegating tasks is essential when faced with a substantial workload, and I extend my gratitude to my students who not only contributed significantly to this thesis but also lent a hand in the lab in stressful times and displayed remarkable motivation and dedication to their own projects. My heartfelt thanks go to Benjamin Predeschly, Dorian Perecheron, Nicola Taffertshofer, Andrea Vitaloni, Hsu Tazin Myint, Christoph Lindenmeir, Paul Pucknus, and Lukas Bauer. I highly appreciate the work performed by the IDP students, who helped make INSIGHT a better software.
Within the ATUMS program, I could enjoy my research exchange in Edmonton, Canada. I am very grateful for this opportunity and my special appreciation goes to the Canadian ATUMS family who made this possible, Jon Veinot, Leah Veinot, Vladimir Michaelis, Frank Hegmann, and Karthik Shankar. My thanks go to my Canadian colleagues Nils Refvik, Riley Hooper, and many more inspiring people who made this an awesome experience.
I appreciate all the proofreaders who dedicated their time to rectifying errors and typos hidden within the text. My thanks extend to Manuel Reus, Michael Böhmer, and Christoph Lindenmeir for their valuable assistance.
Last but certainly not least, my most profound gratitude goes to my family. In particular, I owe a debt of gratitude to my parents Carina and Rainald, who have been providing me the privilege to pursue my path with unwavering support and belief in me throughout my life. I extend my heartfelt thanks to them and to my brother Rudyard. Finally, to my dear Anna-Lena, who has been by my side through all the ups and downs of my neverending journey as a Ph.D. candidate, I am immensely grateful for your patience, support, and being an integral part of my life.